Optimal sizing and design of electric drive systems for aerospace actuation applications considering centralised and distributed topologies

Patrick Xie

A thesis presented for the degree of
Doctor of Philosophy



Faculty of Engineering
University of Nottingham
United Kingdom

Date of submission: 31st May 2021

Abstract

The aviation industry is moving towards more electric aircraft. This involves the replacement of conventional mechanical, pneumatic, and hydraulic systems with electrical solutions. The motivation for this is to reduce system mass and operating costs, increase efficiency and availability while maintaining reliability and performance. This thesis presents a multifaceted design toolbox for optimal sizing of aerospace electric drive systems with long feeder cables. The design tool is applied to a flap actuation sizing case study. The drive components considered are the power electronics, EMI input filter, LC output filter, cable, machine, and gearbox. The toolbox's inputs are design requirements defined by the system's power, lifetime profile, failure rate, operating environment, and power quality. Models and procedures for each component within the toolbox determine their respective mass, volume, efficiency, thermals, failure rate, dynamics, power quality, and component parameters. The models are coupled with one another such that variation of one parameter lead to a change in another. The system is sized with the main objective of minimising its overall mass while ensuring design requirements are met. Analytical sizing and parameter determination procedures have been developed for all considered components. The capabilities of the proposed toolbox are demonstrated by using it to optimally size and design the electrical flap actuation drive system of an Airbus A320-200. Two different topologies are compared, centralised and distributed. Through the analysis and results, it was concluded that distributed is superior to the centralised topology, offering less mass and reduced complexity. The novelties of this research include:

- A new sizing algorithm for surface mounted permanent magnet synchronous machines suitable.
- Development of design toolbox for optimal aerospace electric drive system design consisting of high fidelity inter-domain dependent models that explicitly considers the relationship between mass, volume, electrical, electromechanical, thermal, mechanical, failure rate, and lifetime profile. The considered components are the machine, cable, LC output filter, inverter, parallel plate finned heat sink, EMI input filter, inductors, and capacitors.
- Utilisation of aforementioned toolbox to assess the merits and drawbacks of optimised aerospace electric drive designs for both centralised and distributed topologies.

Acknowledgements

I would like to thank Dr. Gaurang Vakil, and Prof. Chris Gerada for giving me the opportunity to embark on my PhD studies. Without them, I would not have been able to start the four and half year journey through to its completion.

I would like to thank the members of the Power Electronics, Machines, and Control group who have helped me out, Dr. David Dewar, Dr. Muhammad Khowja, Dr. Ramkumar Ramanathan, Dr. Shaohong Zhu. I would like to thank the help from the technical staff, Colin Blackburn, John Hinchliffe, Matt Cooper, Chris Varley, Daniel Bathgate.

I would also like to thank my internal and external assessors, Dr. Rishad Ahmed, and Dr, Mike Willers respectively for taking their time to read through my thesis and provide their expert input on it.

I am forever grateful to my family who have supported me emotionally and financially. I would like to thank my friends who have cheered me on and encouraged me through the difficult times.

Last but not least, I would like to thank my partner Dr. Melissa Courtney for being there and supporting me in every possible manner, all the way through.

Contents

1 Introduction **1**

1.1 About optimal design for aerospace electric drive systems 1
1.2 Centralised and Distributed topology 4
1.3 Objective 5
1.4 Thesis structure 5
1.5 Publications 6

2 Literature review **7**

2.1 More electric aircraft trends and existing systems 7
2.2 Flight control surfaces actuators 10
2.2.1 Conventional hydraulic actuators 12
2.3 Electric actuators - power-by-wire 13
2.3.1 Electro-hydrostatic actuators 13
2.3.2 Electro-mechanical actuators 16
2.4 Redundant topologies 17
2.4.1 Fault-tolerant electrical topology 17
2.4.1.1 “n+1” 18
2.4.1.2 “n×3” 18
2.4.2 Fault-tolerant mechanical topology 20
2.4.2.1 Torque summing 20
2.4.2.2 Velocity summing 22
2.5 System sizing and modelling techniques 22
2.6 Failure rate 26
2.6.1 System failure rate 28
2.7 Electric drive systems with long feeder cables 29
2.8 Conclusion 30

3 Problem Definition **33**

3.1 Flap actuation functional description 33
3.2 Flap actuation mechanical description 35
3.2.1 Actuation Requirement and mechanical system representation . . 35

3.2.2 Speed reducer gearbox, electromagnetic brakes, and torque tube scaling laws . . . 37
3.2.2.1 Speed reducer gearboxes . . . 38
3.2.2.2 Electromagnetic brakes . . . 41
3.2.3 Torque tube sizing . . . 41
3.2.4 Flap mechanical model . . . 42
3.2.4.1 Flap kinematics and dynamics . . . 42
3.2.4.2 Flap mechanism model parameter estimation . . . 44
3.2.5 Flap actuation mechanism dynamic model . . . 45
3.3 Failure rate requirements . . . 49
3.4 Conclusion . . . 50

4 Model and Toolbox Realisation 53
4.1 Introduction . . . 53
4.1.1 High level design concept . . . 53
4.1.2 System design steps overview . . . 54
4.2 MATLAB global optimization toolbox . . . 60
4.3 Failure rate . . . 61
4.3.1 General Model for electrical and electronic components . . . 61
4.3.2 Lifetime profile . . . 62
4.3.3 Capacitor and Inductor . . . 63
4.3.4 Discrete semiconductors . . . 65
4.3.5 Insulation failure rate . . . 66
4.3.6 Results . . . 68
4.4 Passive component sizing . . . 69
4.4.1 Inductor - static and low band . . . 69
4.4.1.1 Geometry . . . 70
4.4.1.2 Magnetic operating point . . . 71
4.4.1.3 Losses . . . 72
4.4.1.4 Thermal . . . 73
4.4.1.5 Mass and volume . . . 74
4.4.1.6 Inductor mass minimisation . . . 74
4.4.1.7 Empirical fitting and inductor look up table generation . . . 76
4.4.2 Capacitor - static and low band . . . 77
4.5 Enclosure volume and mass - static band . . . 78
4.6 Machine - static and low band . . . 79
4.6.1 Specification . . . 80
4.6.2 Slot/pole combination selection . . . 81
4.6.3 Stator and rotor sizing . . . 81

4.6.4 Windings, conductors, and stator resistance . . . 84
4.6.5 Operating point, stator inductance, and magnetic flux linkage . . 85
4.6.6 Mass . . . 87
4.6.6.1 Losses and power factor . . . 88
4.6.7 System level candidate machine design selection . . . 89
4.6.7.1 Preliminary machine sizing function . . . 89
4.6.7.2 Preliminary system mass estimation for machine design selection . . . 89
4.6.8 Air gap and magnet sizing . . . 93
4.6.8.1 Inductance . . . 93
4.6.8.2 Permanent magnet . . . 97
4.6.8.3 Air gap, tooth tip, and magnet sizing . . . 98
4.6.8.4 Demagnetisation limit . . . 100
4.6.9 Thermal modelling . . . 101
4.6.9.1 Overview . . . 101
4.6.9.2 Lumped parameter thermal network . . . 102
4.6.9.3 Machine to ambient heat transfer . . . 103
4.6.10 Electrical machine model validation . . . 105
4.6.10.1 Experimental set-up . . . 105
4.6.10.2 Utilised existing machines for validation . . . 109
4.6.10.3 Air gap, tooth tip, and magnet sizing . . . 109
4.6.10.4 Thermal model . . . 111
4.7 Cable sizing - static band . . . 113
4.8 LC Output filter . . . 115
4.8.1 Parameter selection . . . 117
4.8.2 LC output filter failure rate vs. mass . . . 120
4.9 Inverter sizing - static and low band . . . 121
4.9.1 Power electronics losses . . . 122
4.9.2 Heat sink sizing . . . 125
4.9.2.1 Geometry . . . 126
4.9.2.2 Convection . . . 126
4.9.2.3 Radiation . . . 128
4.9.2.4 Equivalent thermal resistance . . . 129
4.9.2.5 Mass and volume . . . 129
4.9.2.6 Heat sink look-up table generation . . . 129
4.9.3 Inverter failure rate vs. heat sink mass . . . 130
4.10 Input EMI filter design . . . 133
4.10.1 Conducted Emissions Requirements - MIL-STD-461F . . . 133
4.10.2 Multi-stage LC inverter topology . . . 134

4.10.3 Determination of common mode voltage and dc-link current harmonics . . . 135
4.10.4 EMI filter parameter selection . . . 139
4.10.4.1 Example EMI filter design . . . 143
4.10.5 Inverter input EMI filter and dc-link capacitor - failure rate vs. mass 143
4.11 Conclusion . . . 148

5 Drive level - dynamic modelling and control 153
5.1 Overview . . . 153
5.2 Electrical system dq representation . . . 155
5.3 Electrical system state-space representation . . . 157
5.3.1 Continuous state-space representation . . . 157
5.3.2 Discrete state-space representation . . . 159
5.4 Gain-scheduled state feedback current controller . . . 159
5.4.1 The need for gain-scheduling . . . 159
5.4.1.1 State-feedback controller with integral action reference tracking . . . 160
5.4.1.2 Linear quadratic regulator design and gain selection . . . 161
5.4.2 Gain-scheduling . . . 164
5.5 Gain-scheduled full state observer . . . 165
5.6 Controller and observer simulation with switching model . . . 168
5.7 Cascaded speed and position control loop . . . 169
5.8 Conclusion . . . 172

6 Drive level - high-frequency 175
6.1 Overview . . . 175
6.2 Single-line transmission line model . . . 176
6.2.1 Source . . . 177
6.2.2 Differential mode model . . . 178
6.3 Transmission line model parameter extraction . . . 180
6.4 High-frequency machine model . . . 185
6.4.1 Machine winding per-turn equivalent circuit . . . 186
6.4.2 Per-turn resistance and inductance . . . 186
6.4.3 Inter-turn and turn-to-stator capacitance . . . 189
6.4.4 Eddy current resistor . . . 192
6.4.5 HF machine model from measurement . . . 193
6.5 Experimental validation . . . 194
6.5.1 Cable . . . 195
6.5.2 Differential mode and common mode machine impedance . . . 197

6.5.3 High frequency cable and machine model - time domain comparison 197
6.6 Conclusion . . . 198

7 Topology Comparison 201
7.1 Introduction . . . 201
7.2 Design search space . . . 202
7.3 Results - Centralised topology . . . 206
7.3.1 System level . . . 206
7.3.2 Machine . . . 210
7.3.3 Gearbox . . . 212
7.3.4 Cable . . . 213
7.3.5 LC output filter . . . 213
7.3.5.1 Initial design parameters . . . 213
7.3.5.2 Filtering effectiveness . . . 214
7.3.5.3 Inductor design . . . 215
7.3.6 Power electronics . . . 216
7.3.7 LC input filter . . . 217
7.3.8 Current control . . . 218
7.3.9 Summary . . . 220
7.4 Results - Distributed topology . . . 221
7.4.1 System level . . . 221
7.4.2 Machine . . . 222
7.4.3 Gearbox . . . 223
7.4.4 Cable . . . 225
7.4.5 Control . . . 226
7.4.6 Power electronics and heat sink . . . 226
7.4.7 LC input filter . . . 227
7.4.8 Summary . . . 229
7.5 Centralised vs. distributed topology . . . 230
7.5.1 System level . . . 230
7.5.2 Machine . . . 231
7.5.3 Cable . . . 232
7.5.4 LC output filter . . . 232
7.5.5 Power electronics and heat sink . . . 233
7.5.6 EMI LC input filter . . . 235
7.5.7 Control . . . 236
7.5.8 Conclusion . . . 236

8 Conclusion **239**

8.1 Summary 239

8.2 Critiques and future work 241

8.3 Contributions 244

List of Figures

1.1 Mass vs. failure rate Pareto frontier example. 4
1.2 Centralised (top) and distributed (bottom) electrical topologies. 5

2.1 Commercial aircraft electrical generation with respect to first year of flight. [1] 8
2.2 Conventional electrical system with centralised distribution and Boeing 787's electrical system with distributed distribution [2]. 8
2.3 Airbus A350 electrical system [3]. 10
2.4 Airbus A350 flight control surfaces [3]. 11
2.5 Airbus A350 hydraulic and actuator system [3]. 11
2.6 EHA system (a) Overview of EHA system. (b) Axial piston pump diagram [4]. 14
2.7 F-18 Electro-hydrostatic actuator [5]. 14
2.8 Airbus A350 electro-hydrostatic actuators [6]. 15
2.9 Airbus A380's aileron electro-hydrostatic actuator (left) and hydraulic actuator (right) [7]. 15
2.10 Moog electro-mechanical servo actuator [8]. 16
2.11 2+1 fault-tolerant machine topology [9]. 19
2.12 Current reshaping of phase a and b currents after phase c current failure at 0.02 seconds for a 2+1 fault-tolerant machine [9]. 19
2.13 2×3-ph fault-tolerant machine topology [10]. 19
2.14 ELGEAR operation before and after single-lane open circuit fault [11]. . 20
2.15 Four lane torque summer with clutches [12]. 21
2.16 Circumferential and axial dual-lane segmentation [13]. 21
2.17 Calculated drag torque for short-circuit fault of axially (Ax) and circumferentially (Circ) segmented lanes with single layer (SL) and double layer winding schemes (DL) [13]. 21
2.18 Velocity summing with a differential gearbox [12]. 22
2.19 A320 flap actuation system with a differential gearbox [14]. 23
2.20 Failure rate vs. time bathtub curve [15]. 27
2.21 Paschen's curve for air [16]. 30

3.1 Flap lever and indicator [14]. 34
3.2 Flap retracted and fully-extended [14]. 34
3.3 A320 slat and flap transmission system [14]. 35
3.4 A350XWB flap transmission system with active differential gearbox for differential flap settings [17]. 35
3.5 A320-200 outboard flap actuation definition provided by [18]. 36
3.6 Proposed mechanical flap actuation topology. 36
3.7 Flap actuation mechanical analogous circuit. 37
3.8 Mass of single stage gearbox with respect to nominal low speed side output torque. [19] 40
3.9 Moment of inertia of single stage gearbox with respect to nominal low speed side output torque. [19] 40
3.10 Calculated and fitted friction coefficient for single stage gearbox with respect to high speed input side for nominal output torque. [19] 41
3.11 A320 trailing edge flap mechanism and link-track kinematic modelled as a slider-crank mechanism. 43
3.12 Estimated A320-200 outboard flap's mechanism parameters and slider position with respect to crank arm position θ for constant torque tube speed of 25RPM. 46
3.13 Dual machine with electric brakes (E/B) driving open differential gearbox topology, (a) nominal operation with both machines 1 and 2 are active and either respective E/B are off, sun and ring driving carrier gear at $\omega_c = \omega_s = \omega_r$, (b) faulted operation with machine 2 faulted, E/B 2 is on, machine 1 is driving load carrier gear at $\omega_c = 2\omega_s$. 46
3.14 Simplified flap actuation mechanical analogous circuit with equivalent low speed side lumped moment of inertia, friction coefficient, and equivalent torque. 47
3.15 Mechanical system representation for nominal operation. 48
3.16 Mechanical system representation for faulted operation. 49

4.1 System sizing and design process overview. 57
4.2 Commercial class 200 polyester/polyamideimide coated winding wire lifetime vs. temperature [20]. 67
4.3 Dry tantalum capacitor with axial metal packaging predicted failure rate vs. applied over rated voltage ratio for internal and external lifetime profiles of Table 4.1 and 4.2. 68
4.4 D3pack silicon MOSFET discrete semiconductor predicted failure rate vs. junction temperature for internal and external lifetime profiles of Table 4.1 and 4.2. 68

4.5 Commercial 200 class winding wire insulation predicted failure rate with respect to operating temperature for external stores lifetime profile of Table 4.2. 69
4.6 EI inductor core and coil assembly [21]. 71
4.7 Core material magnetic permeability μ_m vs. flux density B. 71
4.8 Inductor design process illustration of a 1mH inductor I_{dc} = 5A, ΔI = 0.5A, f_c = 15kHz, T_{amb} = 40°C, altitude = 20,000ft, amorphous core. Lighter shade markers represent higher values. Red "×" represents infeasible designs whose parameters exceed their respective limits. Feasible design of minimum mass is highlighted with a cyan (light blue) dot. . . . 76
4.9 Bisection method iteration values of inductor dimension D with respect to calculated temperature rise T_r. 76
4.10 Empirical curve fitting for inductor volume vs. inductance and current. Dots represent specific designed point, line represents empirical equation fit. Inductor specification: f_c = 15kHz, current ripple= 10%, T_{amb} = 40°C, altitude = 20,000ft, temperature rise = 30°C, amorphous core. 77
4.11 Empirical curve fitting for capacitor volume vs. capacitance and voltage for commercial capacitors capacitor range. 78
4.12 Demonstrator inverter internal view. 79
4.13 Inverter case dimensions. 79
4.14 Permanent magnet synchronous machine dimensions. 82
4.15 Non-salient permanent magnet synchronous machine's operating range represented on the dq current axis. 86
4.16 System level machine sizing, 1.1kW rating, f_{mac1} outputs $|v_{dq}|$ and machine mass. 91
4.17 Preliminary estimation of system mass with respect machine phase current I_{ph} and torque per rotor volume TRV of a centralised 1.1kW system considering, machine, cable, and LC output filter, semiconductor, and heat sink. 93
4.18 System level candidate machine design and selection. 94
4.19 Slot teeth dimensions and leakage flux permanence paths [22]. 95
4.20 Magnet's open-circuit equivalent reluctance circuit [23]. 97
4.21 System level candidate machine design and selection. 100
4.22 Lumped parameter thermal network [24]. 101
4.23 System level candidate machine design and selection. 102
4.24 Machine to ambient convective, conductive, and radiative heat transfer paths. 103
4.25 Test set-up overview 106
4.26 Mechanical loading rig. 107

4.27 Dual-lane axially-segmented HEMAS machine. 107
4.28 Inverter power electronics [6]. 108
4.29 Impedance analyser to measure SHAO machine. 108
4.30 Electrical machine cross section - HEMAS single layer design. 110
4.31 Electrical machine cross section - HEMAS double layer design. 110
4.32 Electrical machine cross section - SHAO design. 110
4.33 Measured differential mode impedance plots for HEMAS-SL, HEMAS-DL, and SHAO machines. 111
4.34 Measured back-EMF plots for HEMAS-SL, HEMAS-DL, and SHAO machines. 112
4.35 Lumped parameter thermal model validation using HEMAS dual stator/rotor machine. 113
4.36 Measured thermal profiles for HEMAS machine, 41W copper losses for each stator. 114
4.37 LC output filter with dc-link mid-point balancing capacitors and resistors. 116
4.38 Simplified common mode equivalent circuit of LC output filter and dc-link mid-point. 117
4.39 Inverter output phase voltage spectrum and MIL-STD-704F distortion spectrum limit. 118
4.40 MIL-STD-704F variable frequency power system distortion spectrum limit. 118
4.41 Simulated filter output phase voltage spectrum and MIL-STD-704F distortion spectrum limit. 119
4.42 Simulated inverter output phase current. 119
4.43 Simulated LC filter's output phase voltage and machine side terminal voltage. 120
4.44 Output LC filter inductance and capacitance for desired inverter line output current ripple. 120
4.45 LC output filter failure rate vs. mass for capacitor voltage rating and current ripple. 121
4.46 LC output filter's mass breakdown with respect to current ripple and capacitor voltage rating 122
4.47 On-state voltage/current characteristics with respect to temperature for Microsemi's silicon carbide power MOSFET MSC080SMA120S. 124
4.48 Turn on and turn off losses for Microsemi's silicon carbide power MOSFET MSC080SMA120S. 124
4.49 Equivalent inverter thermal network. 125
4.50 Parallel plate natural convection heat sink geometry. 126
4.51 Equivalent thermal resistance vs. heat sink mass for ambient temperature 70°C, equivalent pressure at an altitude of 20,000ft, base temperature 120°C, base thickness = 5mm. 130

4.52 Inverter failure rate vs. junction temperature. 131
4.53 Heat sink thermal resistance vs. junction temperature. 132
4.54 Corresponding heat sink thermal resistance vs. mass. 132
4.55 Inverter failure rate in time vs. heat sink mass. 133
4.56 MIL-STD-461 CE101 and CE102 conducted emissions, power leads, limits for aircraft applications at different operating voltages (AD or DC). . . . 134
4.57 MIL-STD-461 Line impedance stabilisation network (LISN). 134
4.58 Line impedance stabilisation network (LISN) connection to power source and equipment under test (EUT). 135
4.59 Proposed multi-stage LC EMI filter consisting of n differential mode (DM) stages. 135
4.60 Multi-stage LC EMI filter, differential mode (DM) equivalent circuit. . . 136
4.61 Two-level inverter diagram. 136
4.62 Equivalent circuit to determine baseline differential mode (DM) attenuation requirement. 140
4.63 Differential mode (DM) baseline voltage spectrum, MIL-STD-461F limits, -6dBuV margin, V_{dc} = 270V, M = 0.39, f_o = 150Hz, f_c = 15kHz, C_{dc} = 40uF, attenuation $A_{tt,dm}$ of -23.535dBuV at 30kHz. 140
4.64 Simulated power lead voltage spectrum, MIL-STD-461F limits, -6dBuV margin, n = 2, L_{dm} = 278uH, C_{dm} = 3.265uF, V_{dc} = 270V, M = 0.9, f_o = 483.3Hz, f_c = 15kHz, I_o = 9.29A, C_{dc} = 1uF, $C_{dc,cm}$ = 47.1uF. 143
4.65 Inverter input EMI filter and dc-link capacitor design process. 145
4.66 EMI filter and dc-link capacitor with silicon steel core inductors for 1.1kVA inverter - failure rate vs. mass. 146
4.67 Failure rate vs. mass of Pareto-efficient 1.1kVA inverter designs. 147
4.68 Mass breakdown by failure rate for internal and external lifetime profiles with silicon steel, 1.1kVA inverter. 147
4.69 Volume breakdown by failure rate for internal lifetime profiles, 1.1kVA inverter. 148

5.1 Full actuator overview for control analysis. 154
5.2 System dq equivalent circuit considering inverter, LC output filter, and machine. 155
5.3 System dq equivalent circuit considering inverter, LC output filter, cable, and machine. 157
5.4 Discrete state-space system representation and state feedback controller with integral action. 160

5.5 Calculated (a) bode and (b) step responses for gain-scheduled closed loop current control at fixed electrical speeds $\omega_o = \{2\pi(133.33), 2\pi(400), 2\pi(666.67)\}$, with unity dc gain and 450Hz bandwidth for $i^*_{md} \rightarrow i_{md}$ and $i^*_{mq} \rightarrow i_{mq}$. . 163

5.6 Performance error function $f_{\min}$ versus q_a and q_b for $\omega_o = 2\pi(400)$ and $r_a = 1$. 164

5.7 Gain-scheduled $\mathbf{K}_1$ and $\mathbf{K}_2$ matrix parameters with respect to operating electrical speed ω_o, "x" and "o" markers represent test points for matrix parameters of $\mathbf{K}_1$ and $\mathbf{K}_2$ respectively, line plots represent second degree polynomial fit. 166

5.8 Gain-scheduled full state feedback machine current controller with gain-scheduled full-state observer. 166

5.9 State-space matrix values (a) $\mathbf{A}_z$ and (b) $\mathbf{B}_z$ with respect to operating speed ω_o, "x" markers represent discrete test points, line plots represent second degree polynomial fit. 168

5.10 State-space matrix values (a) $\mathbf{E}_z$ and observer state feedback gains matrix (b) $\mathbf{G}_z$ with respect to operating speed ω_o, "x" markers represent discrete test points, line plots represent second degree polynomial fit. 168

5.11 Poles of total system considering plant, controller, and observer plotted in z-domain for different operating electrical speeds ω_o. 168

5.12 Real and estimated states with rotor speed ramp and step current command $i^*_{md} = 0$A, $i^*_{mq} = 7$A. 170

5.13 Phase voltage for rotor speed ramp and step current command $i^*_{md} = 0$A, $i^*_{mq} = 7$A. 170

5.14 Cascaded speed and position loop for mechanical system. 170

5.15 Open loop and closed loop bode plot of the machine speed for nominal and faulted operation. 171

5.16 PI controller with integral clamping anti-windup. 171

5.17 Mechanical system response for actuator arm, slider positions, and machine speed with respect to time for nominal and faulted operation. 173

6.1 Spectrum of symmetric and asymmetric trapezoidal waveform for $f_0 =$ 15kHz, d = 0.4, A = 270V. 177

6.2 Fourier series expansion coefficient maximum magnitude envelope for symmetrical trapezoid waveform, blue line where $\tau < \frac{T}{2}$, red line where $\tau > \frac{T}{2}$. 178

6.3 Γ-type single-line transmission line model. 179

6.4 Bode response plot of source side to load side voltage v_{Ldm}, source side trapezoidal waveform's Fourier expansion coefficients c_n, and resultant product of $c_n v_{Ldm}$ for a 10m long cable, fundamental frequency of f_0 = 20kHz, DC bus voltage of A = 100V, source side trapezoidal rise time τ_r = 0.03us and fall time τ_f = 0.08ns. 180
6.5 Time series of source side and load side voltages for a 10m long cable, fundamental frequency of f_0 = 20kHz, DC bus voltage of A = 100V, source side trapezoidal rise time τ_r = 0.03us. 181
6.6 Lumped continuous shield and stranded shield representation. 181
6.7 Cable differential mode single phase measurement arrangement. 182
6.8 Flux density $|B|$ and current density $|J|$ plots for different frequencies of M27500-10SD3T23 cable's cross section in three-phase differential model arrangement determined using FEMM. 183
6.9 Equivalent three-phase cable capacitance network. 183
6.10 Finite element electrostatic voltage plot for common mode three-phase and single phase arrangements of M27500-10SD3T23 cable. 184
6.11 Per unit length FEM calculated resistance and inductance with respect to frequency for three-phase differential mode cable arrangement for different conductor gauges. 184
6.12 Three-phase permanent magnet machine's common mode and differential mode impedance measurement arrangements. 185
6.13 Equivalent machine winding per-turn network. 186
6.14 FEMM determined real, imaginary impedance and inductance with respect to frequency for 12s10p HEMAS machine. 187
6.15 RLC equivalent circuit from vector fitting admittance. 188
6.16 Three conductor in grounded box example with labelled inter-conductor and conductor to ground capacitances. 190
6.17 Resultant voltage field plot of conductor filled stator slot where charge of one conductor is set to 1 coulomb. 191
6.18 FEMM determined turn to stator (diagonal) and inter-turn (off-diagonal) capacitances. 192
6.19 Per-phase equivalent circuit considering eddy current resistor [25]. 192
6.20 Vector-fitting of measured differential mode impedance. 193
6.21 Per phase high frequency permanent machine model. [26] 194
6.22 Measured vs. fitted differential mode and common mode impedance. . . . 195
6.23 M27500-10SD3T23 10AWG cable cross section. 195
6.24 Per unit length FEM-calculated vs. measured resistance and inductance with respect to frequency for three-phase differential mode cable arrangement. 196

6.25 Cable common mode three-phase and single phase measurement arrangements. . . . 197
6.26 Comparison between measured and FEMM, vector fitted, LTspice calculated differential and common mode impedances. . . . 198
6.27 Calculated and measured differential mode voltages of source and load side for 10m cable. . . . 199

7.1 Machine designs 12s/10p, 12s/14p with respect to failure rate and mass. 206
7.2 All system designs for centralised topology - per lane failure rate vs. mass. 207
7.3 Centralised systems, down-selected designs' failure rate vs. mass. . . . 208
7.4 Per-lane failure rate vs. per component failure rate for centralised systems. 208
7.5 Optimal system design for centralised topology - per-lane component mass breakdown. . . . 209
7.6 Optimal system design for centralised topology - per-lane mass and failure rate of each electrical component. . . . 210
7.7 Optimal system design for centralised topology - machine winding scheme and flux density plot at nominal load. . . . 211
7.8 Optimal system design for centralised topology - FEMM calculated torque and torque ripple vs electrical angle. . . . 212
7.9 LC output filter phase voltage at nominal operating condition and distortion spectrum. . . . 215
7.10 Source-side vs. load-side phase voltage and inverter output current. . . . 215
7.11 LC output filter inductor design FEMM determined flux density plot. . . 216
7.12 Optimal system design for centralised topology - EMI filter spectrum. . . 218
7.13 Optimal system design for centralised topology - current controller second-order polynomial gain-scheduled state feedback and observer gains. . . . 219
7.14 Optimal system design for centralised topology - current control test for step current step and speed ramp. . . . 219
7.15 Distributed topology system designs - per lane mass vs. failure rate. . . . 222
7.16 Optimised distributed system - per-lane component mass breakdown. . . 222
7.17 Optimised distributed system - electrical component mass and failure rate breakdown. . . . 223
7.18 Optimised distributed system - machine designs. . . . 224
7.19 Optimal system design for distributed topology - FEMM calculated torque nd torque ripple vs electrical angle. . . . 225
7.20 PI current controller with cross decoupling terms. . . . 227
7.21 PI current controller with system diagram. . . . 227
7.22 Optimised design for a distributed topology - current control test for current command step and speed ramp. . . . 228

7.23 Optimal design for distributed system - EMI filter spectrum. 229
7.24 Centralised vs. distributed topology comparison - per-lane mass vs. carrier frequency. 232
7.25 Centralised vs. distributed topology comparison - current control step response during speed ramp. 236

List of Tables

2.1 Comparison between conventional systems and the Boeing 787's no-bleed-air architecture systems, and resultant improvements [2]. 9

3.1 Mechanical-electrical impedance analogy. 37
3.2 Trailing-edge flap specific weights as weight per flap area for single-slotted link-track mechanism [27] and calculated weights for A320-200 outboard flap with area of 5.45m^2. 44
3.3 Estimated flap mechanism model parameters for A320-200 outboard trailing edge flap. 45
3.4 Moments of inertia and friction coefficients from differential gear box's high-speed side for gear box ratio k of 220. 48

4.1 Medium haul civil aircraft internal avionics bay lifetime profile [15]. . . . 62
4.2 Inferred medium haul civil aircraft external stores lifetime profile [15]. . . 63
4.3 Parameters for inductor and capacitor predicted failure rate calculation. . 65
4.4 Parameters for discrete semiconductor predicted failure rate calculation [15]. 66
4.5 Core material properties [28]. 73
4.6 Inductor design parameter comparion for $L = 1$mH, $I_{dc} = 5$A, $\Delta I = 0.5$A, $f_c = 15$kHz, $T_{amb} = 40$°C, altitude = 20,000ft, grid calculated minimum and bisection method improved. 75
4.7 Inductor volume and mass empirical equation constants look up table sample. 77
4.8 Empirical fitted capacitor volume equation constants k_{C1} and k_{C2}. . . . 78
4.9 Machine design process outputs. 80
4.10 Typical values of torque per rotor volume and current densities (continuous operation) [29]. 83
4.11 Material densities. 88
4.12 Case study machine for system level candidate design selection - f_{mac1} input. 90
4.13 Nominal operating parameters used in preliminary system mass estimation of centralised and distributed topologies. 92
4.14 Case study machine for system level candidate design selection - f_{mac1} input. 93

4.15 Geometric limits for air gap, magnet height, and tooth tip dimensions. . 99
4.16 Measurement equipment and power supply specifications. 106
4.17 Dual-lane axially-segmented HEMAS machine specifications. 107
4.18 Specifications of surface mounted permanent magnet synchronous machine utilised in experimental validation. 109
4.19 Measured, FEA, and analytical determined stator inductance and magnetic flux linkage comparison. 112
4.20 HEMAS steady state temperature with 41W of copper loss per stator at ambient temperature at 18°C. 113
4.21 Wire gauge sizes and corresponding current rating [16]. 114
4.22 Aircraft cable specifications [30]. 115
4.23 Case study for inverter failure rate vs. heat sink mass. 131
4.24 Section references for the Figure 4.65. 145
4.25 Input variables of input EMI filter and dc-link capacitor design process for 1.1kVA inverter case study. 146

5.1 Controller and observer simulation with switching model and transmission line parameters. 169

6.1 Per unit length FEE determined cable capacitance with respect to cable gauge. 185
6.2 Vector-fitted RL parameters for FEMM determined differential mode complex admittance 189
6.3 Vector-fitted RL parameters for measured differential mode impedance. . 193
6.4 M27500-10SD3T23 10AWG dimensions. 196
6.5 M27500-10SD3T23 10AWG materials. 196
6.6 Per unit length measured and FEE determined cable capacitances for M27500-10SD3T23 cable. 197

7.1 Centralised vs. distributed topology - system level functional definition and design search space. 203
7.2 Centralised vs. distributed topology - machine functional definition and design search space. 204
7.3 Centralised vs. distributed topology - EMI LC input filter functional definition and design search space. 204
7.4 Centralised vs. distributed topology - inductor functional definition and design search space. 205
7.5 Centralised topology - LC output filter definition and design search space. 205
7.6 Optimal system design for centralised topology - machine specifications. . 211

7.7 Optimal system design for centralised topology - FEMM determined machine specifications. 212
7.8 Optimal system design for centralised system - gearbox specifications. . . 213
7.9 Optimal system design for centralised system - cable specifications. . . . 213
7.10 Optimal system design for centralised topology - LC output filter and dc-link mid-point capacitor parameters. 214
7.11 Optimal system design for centralised topology - LC output filter inductor specifications. 216
7.12 Optimal system design for centralised topology - power electronics and heat sink specifications. 217
7.13 Optimal system design for centralised topology - EMI LC input filter specifications. 217
7.14 Optimal system design for distributed topology - machine specifications . 224
7.15 Optimal system design for centralised system - gearbox specifications. . . 225
7.16 Optimal system design for distributed system - cable. 226
7.17 Optimal system design for a distributed topology - power electronics and heat sink specifications. 228
7.18 Optimal system design for distributed topology - EMI LC input filter specifications. 229
7.19 Centralised vs. distributed topology comparison - system level mass and failure rate. 231
7.20 Centralised vs. distributed topology comparison - machine design. 233
7.21 Centralised vs. distributed topology comparison - cable design. 233
7.22 Centralised vs. distributed topology comparison - LC output filter design. 234
7.23 Centralised vs. distributed topology comparison - power electronics and heat sink design. 235
7.24 Centralised vs. distributed topology comparison - EMI LC input filter design. 235

8.1 Modelling of basic components and their relevant domains. 240
8.2 Subsystems and their contributing basic components. 240
8.3 Modelling of basic components and their relevant domains. 242

Acronyms

- AC - Alternating current
- ACE - Actuator control electronics
- AGB - Actuator gearbox
- AGBIB - Actuator gearbox inboard
- AGBOB - Actuator gearbox outboard
- APU - Auxiliary power unit
- ATU - Autotransformer unit
- AWG - American wire gauge
- BGB - Bevel gearbox
- CM - Common mode
- CPU - Central processing unit
- CSA - Cross-section area
- DC - Direct current
- DEAWS - Distributed electrically actuated wing system
- DGB - Differential gearbox
- DM - Differential mode
- EB - Electric brake
- EBHA - Electrical backup hydraulic actuator
- ECS - Environmental control system
- EHA - Electro-hydrostatic actuator
- ELGEAR - Electric Landing Gear Extend and Retract
- EMA - Electromechanical actuator
- EMC - Electromagnetic compatibility
- EMF - Electromotive force
- EMI - Electromagnetic interference
- EUT - Equipment under test
- FCS - Flight control system
- FEA - Finite element analysis
- FEM - Finite element methods
- FEMM - Finite element methods magnetics
- FIT - Failure in time
- GaN - Gallium Nitride
- GB - Gearbox
- HA - Hyrdaulic actuator
- HEMAS - Helicopter electro-mechanical actuation system
- IGBT - Insulated-gate bipolar transistor
- IPS - Ice protection system

- LISN - Line impedance stabilization network
- LQR - Linear quadratic regulator
- MLT - Mean length per turn
- MPL - Mean path length
- MOSFET - Metal–oxide–semiconductor field-effect transistor
- MTBF - Mean time between failure
- PCME - Power, control, and monitor electronics
- PCU - Power control unit
- PE - Power electronics
- PM - Permament magnet
- PU - Per unit
- PUL - Per unit length
- PWM - Pulse width modulation
- RAT - Ram air turbine
- RNM - Reluctance network model
- RPM - Rotations per minute
- SFCC - Slats flaps control computer
- Si - Silicon
- SiC - Silicon Carbide
- TDFS - Time domain frequency separation
- TRL - Technology readiness level
- TRV - Torque per rotor volume
- UUV - Unmanned underwater vehicle

Chapter 1

Introduction

1.1 About optimal design for aerospace electric drive systems

Optimal design of electromechanical aerospace electric drive systems for actuation is a complex multi-objective, multi-variable, multi-domain design problem. At a high-level, the considered design domains are actuation demand, reliability, thermal, power quality, mass, volume, mechanical, and electromechanical. Objective criteria may be categorised into one of these domains. Elements/items are defined by domain-specific parameters. Parameters of one domain may be coupled with parameters of another. Some parameters have constraints, whereby elements must reside within a given design space. Some parameters are dependent on others. Some parameters require minimisation. The design process, from objective to solution, can be streamlined by reducing the number of independent variables through coupling of two or more different parameters; thus, creating dependency between previously independent variables. This is achieved by appropriate design algorithms. All design solutions have negative side-effects or consequence. These negative side-effects are also known as the cost or the sum of weighted costs. The ultimate objective of an actuation system is to actuate a given demand, be it a flight control-surface, landing gear or any other arbitrary load. Negative side effects of the developed solution include losses, intrinsic mass, and added inertia. Thus, solving the electromechanical optimal design problem can be considered as finding a solution for a required actuation demand with minimal cost, within constraints, using developed design algorithms.

In the context of aerospace application design solutions, the most prominent negative side-effect to be minimised is mass. Consider the objective of moving a given payload from point A to point B by flying. Transport by aircraft is a solution to do this. The negative side-effect of the aircraft as a solution is that energy is needed to move itself, as well as the payload. The required energy is in the form of jet fuel which has intrinsic

monetary cost, mass, and environmental impact. The effectiveness of an aircraft to do this task is known as the payload fraction and is determined by dividing the payload mass by the aircraft's take-off mass. For a fixed payload, an increase in the aircraft take-off mass leads to a decrease in payload fraction and an increase in its fuel requirements. To maximise the payload fraction, the mass of solution (i.e. the aircraft) and its components should be minimised.

Let us consider how an arbitrary component's mass relates to the other design domains/parameters for a given technology level and topology while assuming continuity of material properties (e.g. density, Young's modulus, thermal conductivity) and dimensional/geometric ratios:

- Electrical/electromechanical – in this study, electromagnetic forces are utilised for actuation. This involves the manipulation of magnetic fields by way of designed electromagnetic mechanisms through voltage and current control and conditioning. The considered electromechanical mechanisms is the electrical machine/motor, converting electrical energy into actuating torque. Generally, an electrical machine's current is proportional to its torque, and its voltage is proportional to its operating speed. Control of the current leads to control of the torque. Voltage and current control and conditioning are done by power electronic inverters and output filters. Electrical power routing is done by electrical cables. The electrical machine's operating point with respect voltage/current, and torque/speed need to be considered simultaneously. Naturally, all components in the electrical and electromechanical system have intrinsic mass, volume, losses, reliability, thermal characteristics, and effect system level power quality. All components are dependent on electrical machine's operating point, as described by its voltage/current and torque/speed.
- Volume – generally, an increase in component's mass leads to an increase in its volume. In the context of aerospace actuation solutions; volume, space, and geometric limitations exist for a given aircraft design. Reduction in volume of a given component can increase the space for payload or other components.
- Mechanical – increase in force/torque load leads to increased component volume, and thus increased mass. For a fixed power demand, an increase in rotational/linear speed leads to a reduction in force/torque load and a reduction in component mass. Increased mass leads to increased inertia, and slower actuation dynamics or the requirement of a greater actuation force/power.
- Thermal – consider the thermal characteristics of electrical components designed for minimal mass i.e., maximum power density. Increasing power density leads to a decrease in mass and a decrease in volume. Consequently, for electrical components, this also leads to an increase in conduction losses and component temperature due to the reduced conductor cross sectional area. Reduction in mass leads to lower heat capacity, and shorter thermal time constants, thus a component can overheat

faster. Reduction in volume also reduces external surface area. In the case of convection and radiation, this in turn increases the effective component to ambient thermal resistance. Increased component to ambient thermal resistance leads to an increased operating temperature.

- Failure rate – failure rate of a component is dependent on thermals, its functional loading (be it electrical, mechanical) and ensuring it operates within its designed range. Failure rate requirements can be defined as mean time between failure (MTBF). Decreased failure rate refers to an increase in the MTBF value. Components can be oversized to decrease failure rates for exceptional loading circumstances or faults at the cost of increased physical mass/volume and cost. Generally, an increase in operating temperature leads to an increase in failure rate. Higher temperature leads to faster component degradation as described by Arrhenius's law. Higher operating temperature with respect to ambient temperature leads to more pronounced thermocycling due to repeated thermal expansion and contraction stresses.
- Power quality – electrical power quality can be described by power factor, crest factor, total harmonic distortion, and distortion spectrum. EMI and EMC power quality constraints for the input and output voltage/current of electrical devices are set by MIL-STD-704F and MIL-STD-461F for aerospace applications. Converter/Inverter switching can create un-wanted harmonics and distortion. Filters, consisting of resistors, inductors, and/or capacitors in combination, can be used to attenuate unwanted harmonics and condition the voltage/current at the cost of added mass, volume, losses. Generally, the greater the attenuation required, the greater the mass of the resultant filter.
- Functional requirement definition – mechanical actuation demand is part of the actuator's functional requirement definition. An increase in force/torque demand leads to increase in mass. Power quality and reliability constraints are considered a part of the functional requirement definition. The understanding is that for this system to function properly, it must also abide by these reliability and power quality constraints.

Lower failure rates is desirable as is minimum mass. These design objectives implicitly conflict with each other as it has been deduced that a reduction in failure rate generally leads to an increase in mass for a given technology level. This phenomenon can be illustrated by plotting the respective mass's and failure rates of a set of valid design cases in Figure 1.1. The unit for failure rate is FIT where 1 FIT is equivalent to one failure per 1×10^9 hours. As mass reduces, failure rate increases. Consider that a subset of design cases can be generated with each design case of the subset having failure rates below a threshold. Within that subset exists a single design of minimum mass. The subset's failure rate threshold is iterated for each design cases' respective failure rate,

from which a design of minimum mass is selected. These selected designs are plotted and joined to create the Pareto frontier. Any design that is an element of the Pareto frontier is considered Pareto efficient. Any design that is not an element of the Pareto frontier is considered suboptimal as another design exists with a lower failure rate for the same mass, or a lower mass for the same failure rate. Determination of the Pareto frontier relationship is key to determining an optimal compromise between failure rate and mass.

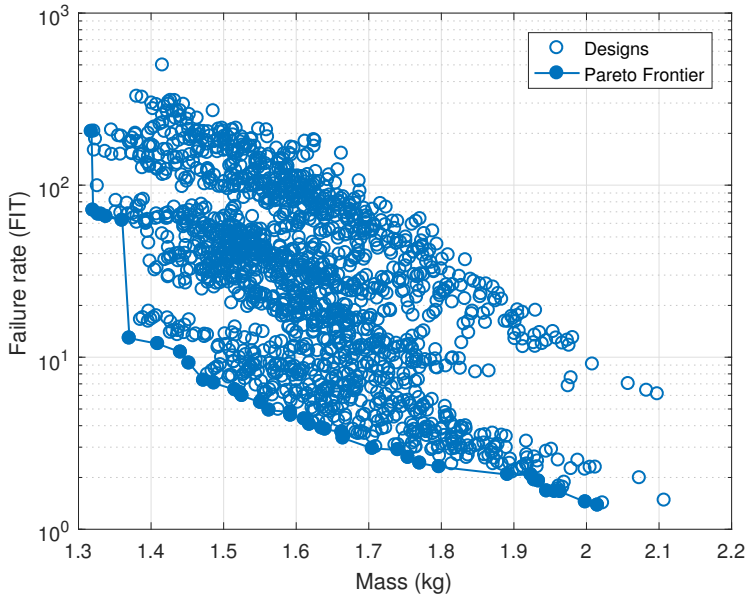


Figure 1.1: Mass vs. failure rate Pareto frontier example.

1.2 Centralised and Distributed topology

As mentioned in the thesis title, centralised and distributed electrical topologies are analysed. Both are shown in Figure 1.2. In the centralised topology, the inverter and its associated EMI and LC output filters are located within the pressurised fuselage. It is connected to the machine, which drives the actuator in the unpressurised wing environment via a long feeder cable. The advantage of this topology is that the power electronics and associated filters operate in the more hospitable environmental-controlled environment. To mitigate transmission line effects and power quality issues, the inverter's switched voltages are conditioned by an LC output filter. In the distributed topology, both the inverter and the machine are at the point of actuation in the less hospitable unpressurised environment. The inverter is supplied by the dc supply network via a long cable. Environment conditions affect the failure rate and operating temperatures of components. Components located in the unpressurised wing environment experiences larger amplitudes of thermal cycling, greater vibration, variation in pressure, and exposure to weather. Components need to be appropriately sized and designed to account for these

environmental stress effects.

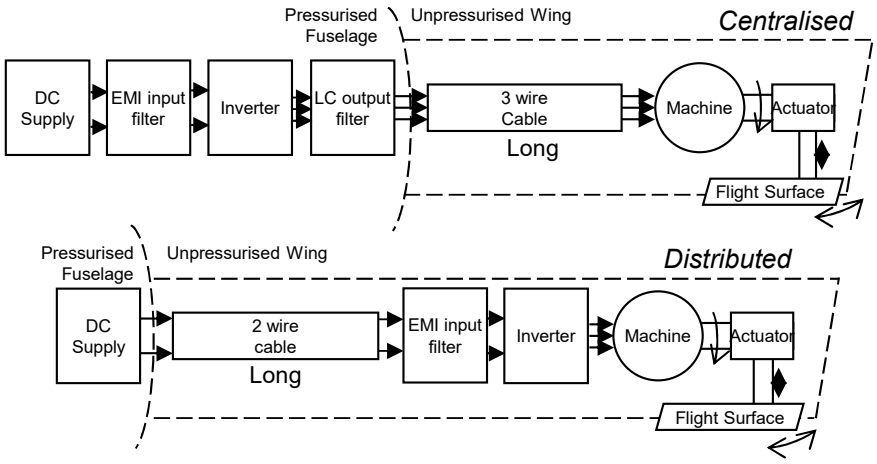


Figure 1.2: Centralised (top) and distributed (bottom) electrical topologies.

1.3 Objective

The ultimate objective is to create a toolbox for optimal sizing and design of electric drive systems for aerospace actuation applications considering centralised and distributed topologies. The toolbox is a collection of models and design procedures for each of the systems' component and for the system as a whole considering every relevant domain.

To demonstrate the toolbox's abilities, it will be used to optimally size the flap actuation system of an Airbus A320-200 for centralised and distributed topologies.

1.4 Thesis structure

The thesis structure is outlined below. This outline summarises the steps taken to achieve the objective of section 1.3.

- Chapter 2 covers the relevant background literature review considering more electric aircraft, its motivation, recent trends in aircraft electric systems, power-by-wire actuation systems, fault-tolerant topologies, demonstrators, and case studies. Methods of electric drive design and sizing are investigated.
- Chapter 3 provides the details of the problem definition (i.e. *what* is the problem that needs to be solved). The aim is optimally size and design a flap actuation drive system for an Airbus A320-200. The flap function is described. A mechanical and kinematic representation is formulated. The failure rates and failure modes requirements are outlined.

- Chapter 4 outlines the toolbox models and procedures utilised to optimal size and design electric drive systems (i.e. *how* is the problem solved). The considered components are inductors, capacitors, heat sinks, semiconductors, electric machine, cable, and gearbox. The subsystems are the inverter, inverter output filter, and EMI input filter. The modelling domains are electrical, electromechanical, power quality, volume, thermal, failure rate.
- Chapter 5 covers the drive system control scheme where a gain-scheduled LQR controller for the centralised topology is presented.
- Chapter 6 covers high-frequency modelling of the inverter, feeder cable, and machine for the centralised topology.
- In Chapter 7, the presented toolbox of Chapter 4 is utilised to optimally size and design the flap actuation drive systems; one design for centralised topology and another for distributed. These designs are compared and contrasted with each other.
- Chapter 8 provides the concluding summary of the work, critiques, identification of future work based on highlighted shortcomings, and the novel contributions.

1.5 Publications

The following publications related to the research topic written by the author are listed in chronological order as follows:

- P. Xie, D. Dewar, G. Vakil and C. Gerada, "Gain-scheduled LQR control of an aerospace drive system with LC filter and long feeder cable," *2020 23rd International Conference on Electrical Machines and Systems (ICEMS)*, 2020, pp. 656-661.
- P. Xie, G. Vakil and C. Gerada, "Electric drive systems with long feeder cables," *IET Electric Power Applications*, 2020, pp. 16-30.
- P. Xie, G. Vakil and C. Gerada, "Sizing, Design, and Modelling of Aerospace Electric Drive System with Long Feeder Cables," *2019 IEEE International Electric Machines & Drives Conference (IEMDC)*, 2019, pp. 993-1000.
- P. Xie, R. Ramanathan, G. Vakil and C. Gerada, "Simplified Analytical Machine Sizing for Surface Mounted Permanent Magnet Machines," *2019 IEEE International Electric Machines & Drives Conference (IEMDC)*, 2019, pp. 751-757.

Chapter 2

Literature review

The aviation industry is tending towards more electric aircraft. This involves replacement of conventional hydraulic, pneumatic, and mechanical systems with electrical solutions. The motivations for this movement are mass reduction leading to reduced fuel burn and reduced environmental impact, ease of maintenance leading to increased availability, and reduced operating costs leading to increased profits. This chapter discusses the background in more electric aircraft. General more electric aircraft design trends are presented. This is followed by an investigation focused on aerospace actuation applications. Conventional hydraulic actuation systems and their supporting systems are presented. Electrical actuators are then introduced, and their characteristics are compared with each other. Demonstrators and case studies for the presented actuator types are shown. Different electrical actuation topologies are discussed, considering redundancy, failed operation, and power quality. Existing design and modelling methodologies for electrical actuators are shown.

2.1 More electric aircraft trends and existing systems

Recent trends have shown an increase in commercial aircraft's electrical generation as shown in Figure 2.1 [1]. The largest leap in electrical power generation is with the Boeing 787, attributed to its no-bleed architecture [2].

The increase in electrical generation capability is clearly seen when a conventional electrical system and the Boeing 787's electrical system are compared, as shown in Figure 2.2. The conventional system has a centralised distribution system and the 787 has a distributed system. The conventional electrical system has 115Vac and 28Vdc networks. Boeing 787 has 230Vac, 115Vac, 28Vdc, and ±270Vdc networks. Both the distributed nature of the 787's electrical system and its higher voltages leads to a reduction in power feeder cable mass. The 787 has a total of six electrical generators, two 250kVA per engine

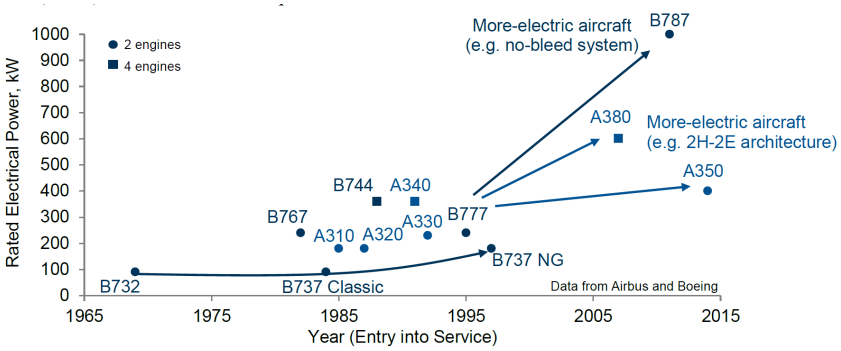


Figure 2.1: Commercial aircraft electrical generation with respect to first year of flight. [1]

and two 225kVa auxiliary power unit (APU) generators. This gives a total 1450kVA of on-board electrical generation.

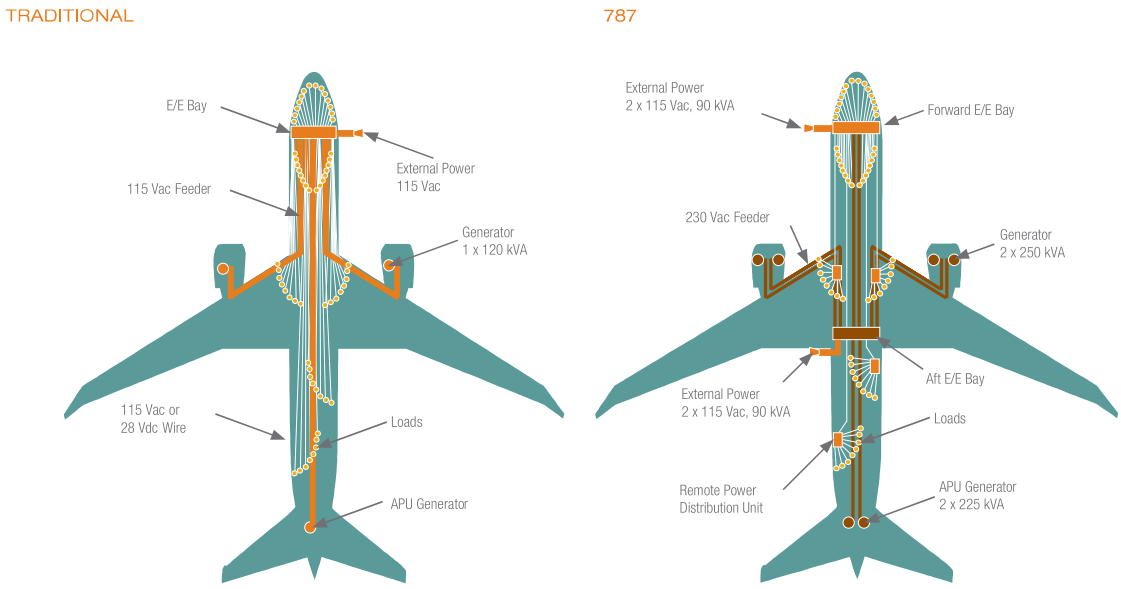


Figure 2.2: Conventional electrical system with centralised distribution and Boeing 787's electrical system with distributed distribution [2].

The generated electric power is utilised by various aircraft systems. A portion of the total power generated by the aircraft's engine is converted into different usable forms, such as pneumatic, hydraulic, and electrical. These power forms are known as secondary power and are required for the operation of aircraft's supporting systems. The major supporting systems include the Environmental Control System (ECS), the Ice Protection System (IPS), and the Flight Control System (FCS). Conventional aircraft utilise bleed air from the engine for IPS and ECS. Hydraulic system is utilised for FCS. The electrified systems in the Boeing 787 are the ECS, IPS, engine starting, and driving of the hydraulic pumps. A comparison between conventional systems and the 787's no-bleed-air architecture systems is shown in Table 2.1. Improvements between the no-bleed-system and conventional systems include improved efficiency, reduced complexity, and reduced

maintenance.

Table 2.1: Comparison between conventional systems and the Boeing 787's no-bleed-air architecture systems, and resultant improvements [2].

System	Conventional	No-bleed-air system	Result
Environmental control	Bleed-air energy extraction from engines requiring pre-coolers and modulating valves.	Output of the cabin pressurisation compressor flows through low pressure air conditional packs. Variable speed motors avoid excess supplied compressed air and further downstream down regulation losses.	Improved efficiency by using minimum energy required.
Ice protection	Hot bleed-air is distributed through piccolo tubes to the leading edges of the wing, then venting it to lower surface of wing/slat.	Electric blankets under the leading edge are utilised.	Energy usage is halved, removal of bleed-air ducting, reduced drag and reduced noise.
Hydraulic system centre lane	2 large 50 gallon per minute (gpm), 3000psi air-turbine driven hydraulic pumps for peak loads during take-off and landing. 2 small 6gpm electric-driven pumps for remainder of flight.	2 large 30gpm, 5000psi electric- driven hydraulic pumps. One runs throughout the entire flight, the other only runs during take-off and landing.	Higher pressure results in smaller hydraulic components for both mass and volume saving. Smaller part count.
Auxiliary power unit	Provides both pneumatic and electrical power.	Only provides electrical power.	Improved reliability, reduced maintenance, reduced complexity with elimination of pneumatic system.
Engine secondary power.	Majority of secondary systems power is in the form of bleed air.	Majority of secondary systems power is electrical.	1 to 2% reduction in fuel consumption during cruising, reduced engine complexity with the elimination of pneumatic system.

Other recent released aircraft such as the Airbus A350, A380, and Boeing 777X still rely on bleed air systems. Airbus 350 has adopted a 2H-2E architecture. Its electrical system is shown in Figure 2.3 [3]. There are two 230Vac 100kVA variable-frequency engine-driven generators per engine. The APU can supply 230Vac at 400Hz, 150kVA. There are three electrical distribution networks, 230Vac, 115Vac, and 28Vdc. Auto Transformer Units (ATUs) convert the 230Vac supply to 115Vac. When all generators fail, a drop out Ram Air Turbine (RAT) is deployed to power essential systems.

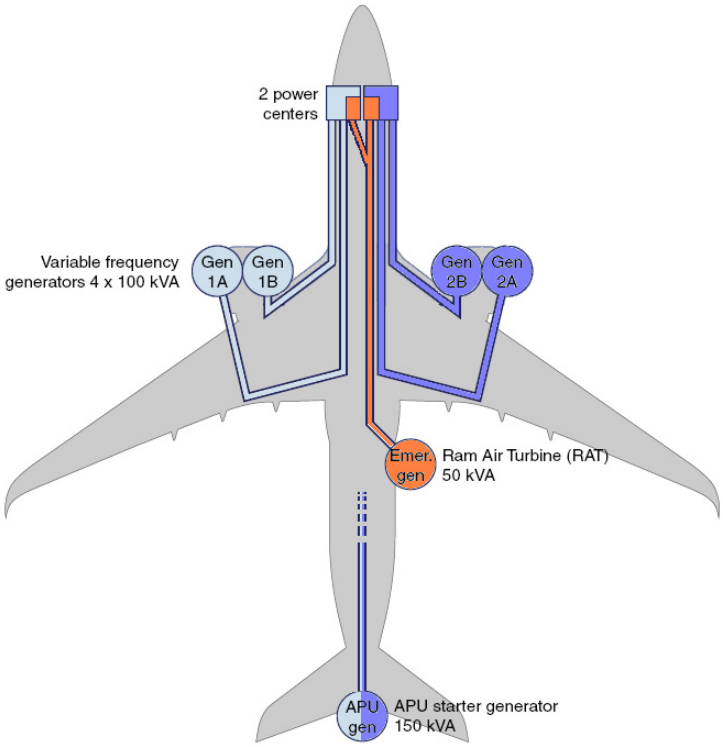


Figure 2.3: Airbus A350 electrical system [3].

2.2 Flight control surfaces actuators

Actuators are required to move flight control surfaces so the aircraft can change velocity, pitch, yaw, altitude, and direction. Actuators are also required to deploy and retract the landing gear, open and close cargo doors, and move the stator vanes in the turbo fan engines [31]. Generally, flight control surfaces fall into two categories; primary and secondary. Primary flight control surfaces are critical flight surfaces which must be operational and active at all times. They control the three main axis of rotation for flight: yaw, pitch, and roll. These surfaces include the elevators (for pitch), the ailerons and spoilers (for roll), and the rudder (for yaw). Secondary flight control surfaces control the amount of lift and drag and are utilised at take-off and landing. These surfaces are the leading-edge slats and the trailing-edge flaps. Upon final-approach for landing, the flaps and slats are extended in increments to increase both lift and drag so that the plane can land at slower speed. The flight control surfaces of an A350 is shown in Figure 2.4.

The A350's hydraulic system and actuator grouping is shown in Figure 2.5. There are four engine drive pumps (EDPs) in total, two per engine. One of them pressurises the green hydraulic systems and other powers the yellow. If one of the engines fails, both hydraulic systems can still be pressurised by the remaining functioning engine. The nominal pressure is 5000psi which is higher than the 3000psi of previous Airbus aircraft. The A350 is equipped with both hydraulic and electro-hydrostatic actuators (EHA) and electrical backup hydraulic actuators (EBHA). In the event of one or both hydraulic

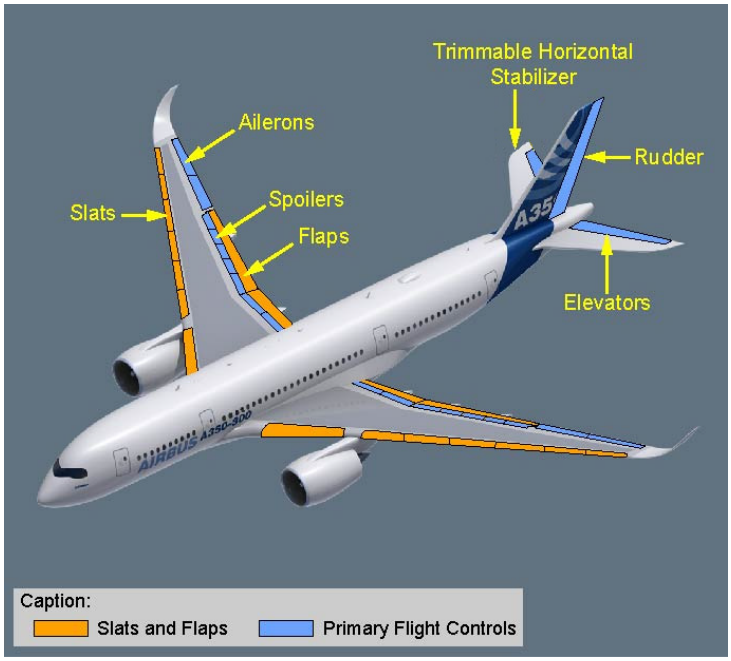


Figure 2.4: Airbus A350 flight control surfaces [3].

systems failing, EHA's and EBHA's are utilised for flight control surface actuation.

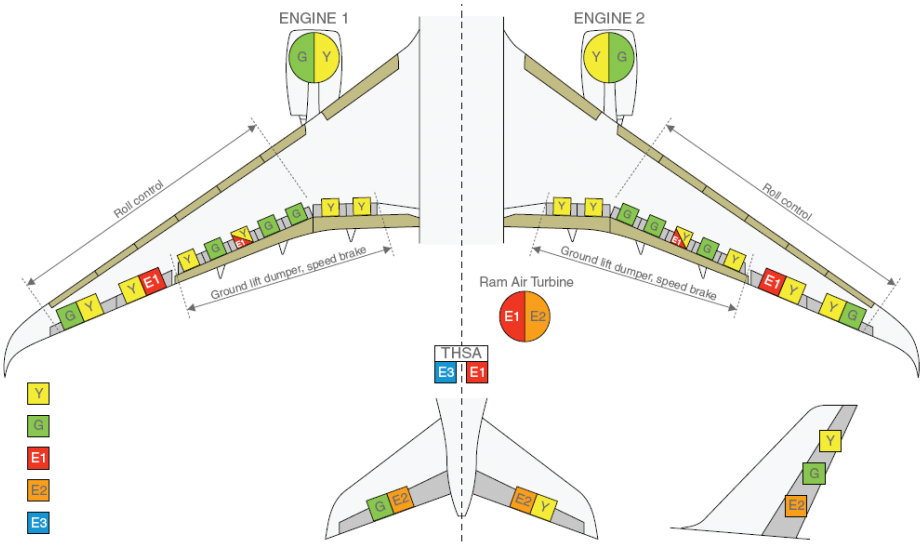


Figure 2.5: Airbus A350 hydraulic and actuator system [3].

Typical flight control surface actuator requirements can by defined by the following descriptors [32]:

- Type of motion - linear/rotary.
- Control - position controlled (primary flight surfaces), end-stop to end-stop movement (landing gear deployment/retraction), pressure to force control (braking).
- Operating duration - continuous (primary flight surface), transient (slats/flaps deployment).

- Power capability - force/velocity, torque/speed.
- Dynamics - 1Hz to 15Hz.
- Operating environment - temperature, altitude, humidity, vibrations, EMI
- Life time - 135000 flight hours for large commercial aircraft.
- Failure rate - 1×10^{-5} failures per flight hour for secondary flight controls, 1×10^{-9} failures per flight hour for primary flight controls.
- Failure mode - fail-operative with reduced output, fail-operate with full output, fail safe (passive/frozen/neutral).
- Maturation - >98%.

The lifespan of developed flight surface actuators need to be considered. NASA introduced technology readiness levels (TRL) which describe the degree of progress made to bring a product from concept to full operational readiness [33]. TRL2 represents formulation of concept idea, TRL4 is validation of concept by realised demonstrator, and TRL9 is fully operational and is put into service. The development of aerospace EHA took 15 years to go from TRL4 to TRL9 [32]. The same model of aircraft with the same actuators may be manufactured for thirty years and stay operational for another thirty years. Thus, it can take 75 years to go from concept formulation to retirement.

2.2.1 Conventional hydraulic actuators

Conventional hydraulic actuators require pressurised hydraulic fluid from a centralised hydraulic system. The pressurised hydraulic fluid in the actuator is controlled by valves and acts on a piston to drive a linear or rotary motion. Their use has been well established in aerospace for more than 50 years and are utilised as the main primary flight control surface actuators for all current generation large passenger aircraft. The advantages of hydraulic actuator systems are as follows [32]:

- High power density at the actuator level.
- Ease of heat dissipation due to the hydraulic fluid carrying the heat away.
- Moving parts have low inertia and thus high actuator bandwidth is possible.
- High force/low speed easily achievable.
- No issues with EMI.
- Can hold constant max torque/force without additional requirement of power.

The disadvantages of hydraulic actuator systems are as follows:

- Low power density at the system level, this includes both hydraulic power generation and distribution by fluid lines.
- Hydraulic fluid pollutants are not environmentally friendly.
- Difficulty of identifying leaks.

- Hydraulic fluid requires conditioning (filling, filtering, charging, clearing).
- Low efficiency on a system level as full force needs to be constantly generated, regardless of the immediate demand.

The development of electric powered alternatives is motivated by addressing the disadvantages of the hydraulic powered system.

2.3 Electric actuators - power-by-wire

Electric actuators for aerospace generally fall into two categories, electro-hydrostatic actuators (EHA) and electro-mechanical actuators (EMA). Recent developments in both are discussed in this section. Note that all presented case studies in sections are examples of distributed systems unless otherwise stated.

2.3.1 Electro-hydrostatic actuators

EHA transform supplied electrical power to hydraulic power to mechanical power. Typical EHA system consist of a bi-directional axial piston pump driven by an electric motor, a hydraulic actuator piston, and bypass valves as shown in Figure 2.6 (a). A diagram of the axial piston pump is shown in Figure 2.6 (b). The axial piston pump consists of pistons mounted in displacement chambers of the cylinder block. The pistons and cylinder block rotate with the drive shaft rotation. The drive end of the pistons are attached by ball-and-socket joints to slippers which are in contact with an angled swash plate. As the pistons rotate about the drive shaft axis, their respective displacement chamber volumes vary due to the reciprocating motion of the pistons as it tracks the angled swash plate. The displacement chambers' volume at the flow inlet Q_{in} is greater than the displacement chambers' volume at flow outlet Q_{out}. This creates negative pressure at the inlet side and positive pressure at the outlet. Axial piston pumps are fixed displacement pumps. Assuming incompressible fluid, flow rate is directly proportional to the speed of rotation.

US programs investigating the use of EHA's for aerospace have mainly focused on military applications. The F-35 fighter aircraft has a full electro-hydrostatic actuator system for all control surfaces with no centralised hydraulic system. [5] investigated replacing the standard aileron hydraulic actuator with an EHA on the F-18 fighter aircraft. The EHA system consisted of the EHA as shown in Figure 2.7, two independent interface boxes, one power control and monitoring electronics unit, one power conversion unit, pilot control panel. The EHA consists of an axial piston pump driven by a three-phase permanent magnet motor. Its total weight is 18.8kg and requires no active cooling. The power converter unit converts 115VAc to $\pm$135Vdc for the power, control, and monitor electronics (PCME). The PCME weighs 9.1kg and has 115Vac cooling fan.

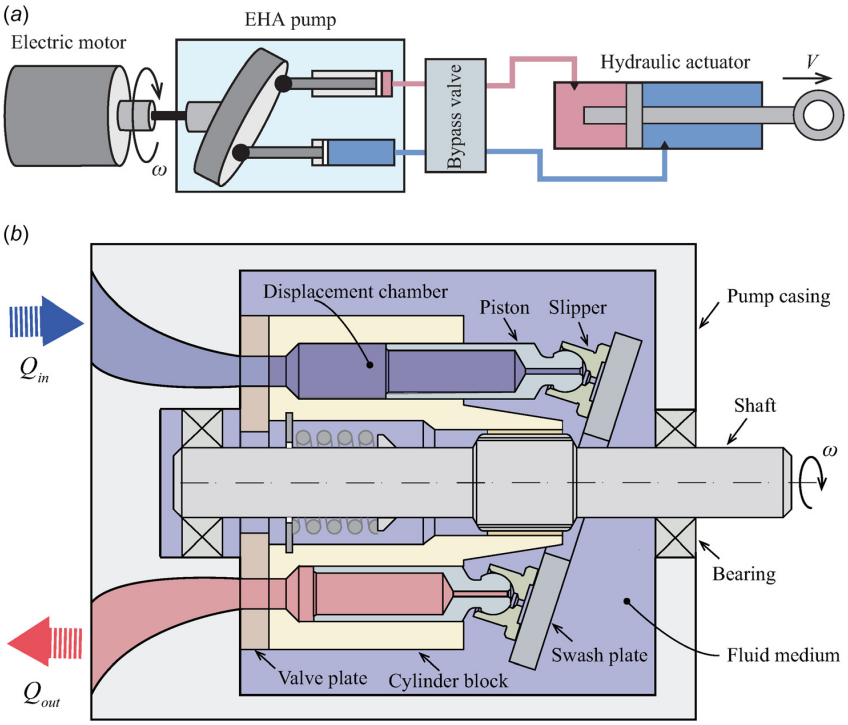


Figure 2.6: EHA system (a) Overview of EHA system. (b) Axial piston pump diagram [4].

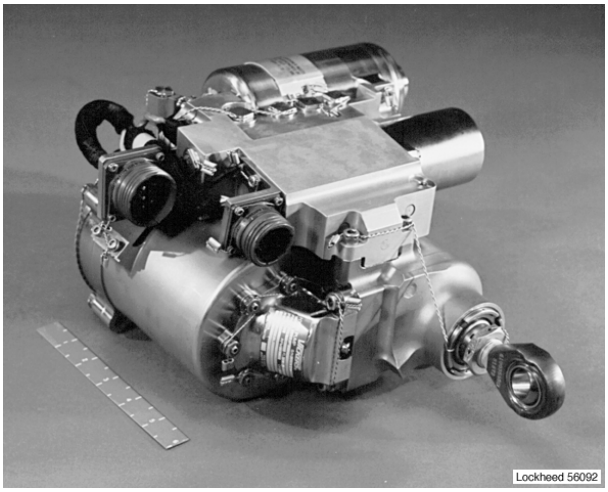
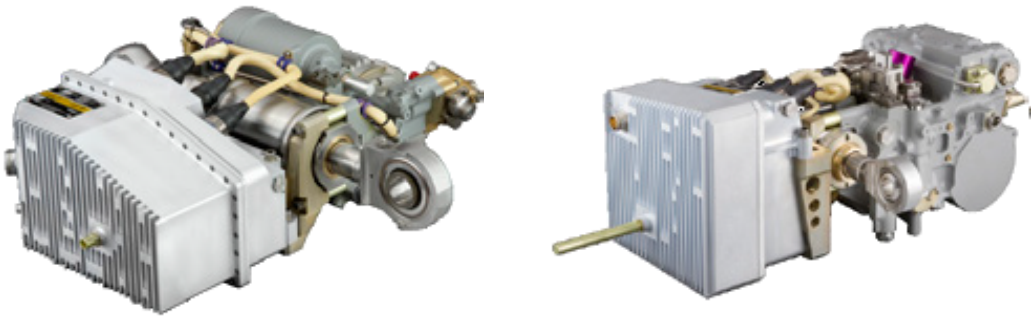


Figure 2.7: F-18 Electro-hydrostatic actuator [5].

European programs investigated EHA's for large commercial aircraft. Recent Airbus aircraft, such as the A380 [7], A350, and A400M utilises electro-hydrostatic backup actuator (EHBA) and electro-hydrostatic actuators (EHA) in support of the conventional hydraulic systems for their ailerons, elevators, rudders, and spoilers. Exact actuator specifications for in-service aircraft are not publicly available. The A350's inboard aileron EHA and spoiler EBHA are shown in Figure 2.8.

[7] highlighted the lessons learnt in the development of the A380 EHA's. The A380's 2H/2E arrangement improves on redundancy compared to the conventional 3H systems as two electrical systems has replaced one hydraulic system. The dissimilarity between



(a) Inboard aileron EHA.

(b) Spoiler EBHA.

Figure 2.8: Airbus A350 electro-hydrostatic actuators [6].

the two systems reduces the chances of common mode failure, such as maintenance errors which can effect one of the two kinds of systems. The EHA design requirements are high speed, low displacement pumps and low losses, as it cannot eject heat easily like a centralised hydraulic system can via its hydraulic fluid. EHA produce losses while generating a static holding force. The only form of heat dissipation is natural convection. The reliability of a forced cooling solution is of concern and the nature of forced cooling would contribute to drag forces on the aircraft. Because of the relative lower reliability of the power electronics, they are to be designed as line replaceable units, easily replaceable without the removal of the entire actuator. The Airbus A380's aileron EHA and HA are shown in the left and right of Figure 2.9 respectively. Here, the relative size between EHA and HA can be seen. The weight of the EHA is double that of the hydraulic actuator but weight savings on the overall system level is achieved with the removal of one hydraulic system. The motors of the EHA were designed with a wet rotor configuration, allowing better integration of motor and pump and elimination of the low reliability dynamic shaft seal. The EHA dynamics are 1-1.5Hz.



Figure 2.9: Airbus A380's aileron electro-hydrostatic actuator (left) and hydraulic actuator (right) [7].

2.3.2 Electro-mechanical actuators

Electro-mechanical actuators directly transfer electrical power into mechanical power, resulting in linear or rotary motion/actuation. Typical linear electro-mechanical actuators consists of an electric motor and a mechanism, such as a ball-screw or roller-screw, that converters the motor's rotation motion into linear motion as seen in Figure 2.10. The tailstock and rod end is where the load and the anchor point are attached. The ball nut and ball screw transforms rotational motion of the output gear into linear motion of the output shaft. A DC brushless motor drives transforms electrical energy into rotary mechanical energy. It drives the pinion gear which itself is meshed with the the output gear. Linear Variable Differential Transformer (LVDT) is used to determine output shaft linear position. The tachometer determines the rotary speed of the motor. Hall effect sensors are used in the electrical commutation of the dc brushless motor. The bearing plate holds the bearing to the actuator's casing. The bearing spacer ensures proper alignment of the bearings. The snubber is used to reduce excess force during actuation. The sleeve bearing ensures a seal between the output shaft and the actuators casing.

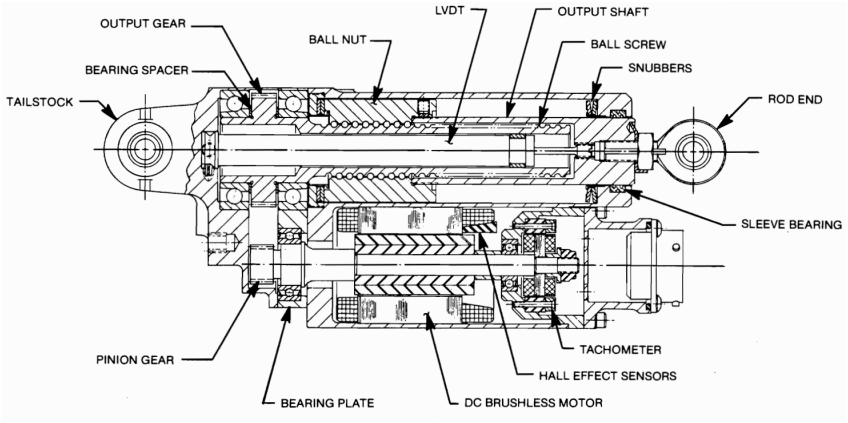


Figure 2.10: Moog electro-mechanical servo actuator [8].

The main advantage of EMA's compared to EHA's are that they are inherently lighter and less complex as there is no intermediate transform from electrical to hydraulic power. The main downside is their safety concern during failure. Jamming is a major concern and methods of dealing with jam failures have not reached a level of maturity for widespread adoption of EMA's for primary flight control surfaces. EHA's are not at the same risk of jamming as by-pass valves can be engaged to bring it to a fail-passive damped state. Recent European investigations into EMA's for primary flight control surfaces include COVADIS [34] and ACTUATION2015 [35] programs.

COVADIS [34] developed a TRL6 (technology readiness level 6) aileron EMA for the A320. It was tested both on an iron-bird and in flight on an A320. The EMA is a direct drive design, consisting of a PM DC brushless motor, position and force sensors, satellite roller screw, and power electronics.

ACTUATION2015 [35] investigated EMA for future all-electric aircraft. Its main aim was to develop catalogues of standardised, modular, and scalable EMA components for all types of aircraft. The objectives are to reduce overall life cycle costs, reduce mass, improve reliability, and mature technologies from TRL3 to TRL5. It is predicted that the outcomes from this project leads to a reduction of life cycle costs by 30%, reduce failure rate by 30% and aircraft mass of 500kg for an Airbus A320 sized aircraft.

DEAWS [9] and ELGEAR [36] developed EMAs for flap/slats actuation and landing gear nose wheel steering respectively. Details of these systems in the context of their topologies will be presented in successive sections.

2.4 Redundant topologies

Consider the problem of designing flight control surface actuation. Its actuation, failure rate, and faulted-operation mode requirements are defined. A potential solution is to use a single lane electro-mechanical actuator, consisting of an electric machine, power electronics, gearbox, and ball-screw mechanism. If however a single-lane solution cannot deliver on the actuation, failure rate, and faulted-operation mode requirements for a given technology level, then multi-lane redundant topologies would need to be adopted. Here, different redundant topologies and their design considerations are discussed.

2.4.1 Fault-tolerant electrical topology

First, let's consider a standard single-lane electric drive consisting of a two-level inverter and three-phase machine. This electric drive is used to drive an actuator. Together they make up an actuation system. The inverter consists of six switches and the machine consists of three windings, one for each phase. One of its six switches can fail (fail open-circuit or short-circuit) or one of its windings can short (degradation of insulation due to overheating, causing turn-to-turn fault and loss torque). This design is not fault-tolerant because a single failure of any of its subcomponents would ultimately lead to the failure of the drive and the entire actuation system. If each components' probability of failure is known, then the probability of failure for this single-lane is the sum of the probability values of each of its components.

Now, consider the use of two-lanes instead of a single lane to drive the same actuator. A fault occurs one of the two lanes. The faulty lane can restrict the operation of the healthy lane if a decoupling mechanisms is not present. The lanes have been sized such that if one of the lanes fail, the remaining healthy lane can still deliver the required actuation and overcome damping effects of coupled faulty lanes. Using two-lanes makes the actuation system fault-tolerant as actuation can be sustained after a lane failure. The actuator system will ultimately fail if both lanes fail. Assuming the probability of each

lane is equal to the single-lane case, the probability for both lanes failing is the square of the probability of a single-lane failing. Thus, failure rate probabilities can be reduced through multiple-lane design.

[37] presents two different fault-tolerant electric drive design concepts using multiple electrical lanes. They are known as "n+1" and "n×3".

2.4.1.1 "n+1"

The "n+1" topology is where each phase winding of one machine is driven by its own isolated inverter. The "2+1" arrangement, where n=2, is utilised in the "distributed electrically actuated wing system" (DEAWS) [9] as shown in Figure 2.11. Three windings are present, each connected to its own inverter and control electronics. Their current commands are generated and synchronised by the flap control computer. During healthy operation, each phases' current is sinusoidal with a phase difference of 120° with respect to each other. If the winding or the inverter of one of the lanes fail, the remaining two healthy lanes will drive the current to deliver the required torque. Generating smooth torque requires reshaping of the currents in the healthy lanes. This phase-fault compensation action is shown in Figure 2.12. Healthy operation is seen between 0.01 and 0.02 seconds as phases a, b, and c deliver sinusoidal current. At 0.02 seconds, an open circuit fault in phase c is induced and the remaining phases current is reshaped to compensate for the phase c current loss. The generated torque is maintained before and after the fault. If faulted full-output operation is required, each phase would need to be sized to deliver 50% of the total power. The reshaped current's peak value is 1.87 times that of nominal [37] .

The downside of this topology is that the instantaneous power drawn for each lane is sinusoidal and requires considerable input filtering. This adds excessive mass and volume to the system. For the 1.5kW DEAWS system, the total inductor mass of the input filter required to attenuate its input current distortion spectrum within DO-160F limits is 3.6kg. Increasing the number of lanes from beyond three may not be possible as each lane requires an isolated power source to avoid common mode failures. Most large commercial passenger aircraft have two engines and one APU, giving a total of three independent power sources. The APU typically isn't operated after take-off, with the exception of backing up the electrical system, backing up the air conditioning, or to restart the main engines [38].

2.4.1.2 "n×3"

The "n×3" topology consist of n-lanes where each lane has one set of 3-phase windings and powered by its respective isolated inverter. The "2×3-phase" topology as shown in Figure 2.13 was utilised in the ELGEAR project for electric landing gear nose wheel steering [11].

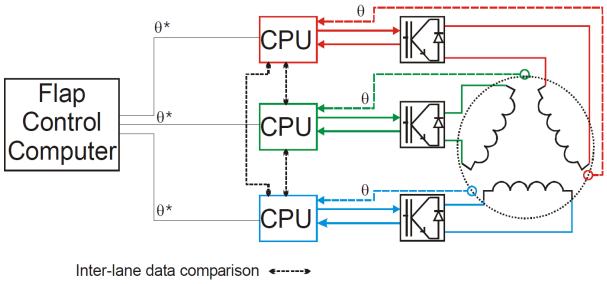


Figure 2.11: 2+1 fault-tolerant machine topology [9].

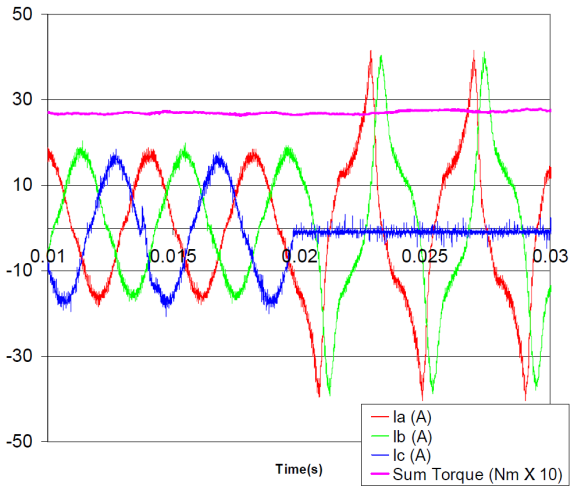


Figure 2.12: Current reshaping of phase a and b currents after phase c current failure at 0.02 seconds for a 2+1 fault-tolerant machine [9].

The advantages of this topology over "n+1" is that the power draw from each lane's power source is constant and not oscillating sinusoidally at the motor's fundamental frequency. Less filtering is required to get the input current distortion spectrum to be within DO-160F limits. Smooth torque is intrinsically generated by each lane, making it easier to implement during both healthy and faulted operation. During nominal operation, each lane delivers half of the total required power as shown in Figure 2.14. Upon an open circuit failure in lane B at 0.03 seconds, lane A's output power doubles with respect to its nominal value to maintain the same constant torque.

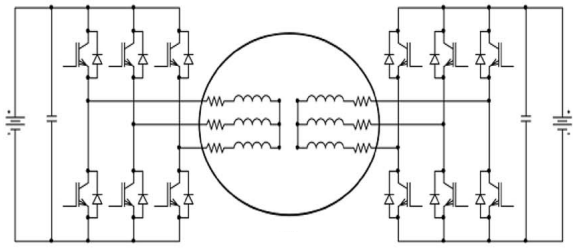


Figure 2.13: 2×3-ph fault-tolerant machine topology [10].

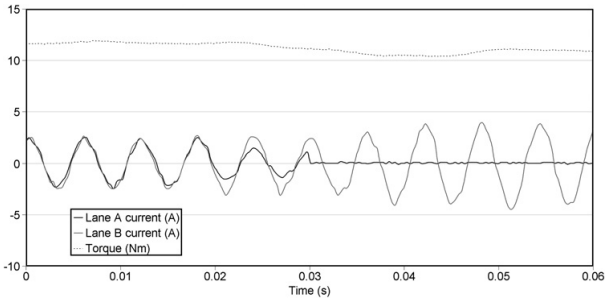


Figure 2.14: ELGEAR operation before and after single-lane open circuit fault [11].

2.4.2 Fault-tolerant mechanical topology

It has been established that multiple lanes can be utilised to create electrical redundancy in an actuation system. Methods to establish mechanical redundancy is now presented. The electric machine is the interface between the electrical domain and the mechanical domain. Broadly speaking, the mechanical output of two or more lanes can be combined by torque summing or speed summing [12].

2.4.2.1 Torque summing

Torque summing is where the total output torque is the sum of each lane's torque. Each lane's rotor shaft is mechanically coupled together by a gearbox or common drive shaft such that the relationship between their respective speeds is constant. The advantage of this is that it avoids speed run-away in one of the lanes. This can also be considered a disadvantage during a lane fault scenario. Depending on the failure manner of the machine and the machine type, the faulted lane's machine can create a drag torque that the remaining healthy lanes must overcome. This phenomenon occurs with permanent magnet motors that have a shorted phase or phase set. The rotation of the rotor in the faulted machine by the motion of the healthy lanes' machines creates a back-EMF voltage which in turn induces a current and drag torque [39]. This drag torque can be addressed in two ways: isolation or over-sizing. De-clutching of the faulted machine, as shown in Figure 2.15, is required to isolate the healthy lanes from faulted lane's drag torque. The addition of a clutch mechanism adds to the system's mass and complexity. The failure rate of the clutching mechanism needs to be accounted for to determine the total actuation system's failure rate. If de-clutching is not feasible, as is the case for lanes sharing a common drive shaft, then the remaining lanes need to be oversized to overcome the drag torque. [39] provides over-sizing scaling factors for torque summed "n+1" and "n×3" lane topologies.

"n+1" phase machines are intrinsically torque summed topologies with no option for de-clutching. Each lane's winding is magnetically coupled to the rotor. The same can be said for "2×3" machines investigated in [13]. Circumferential and axial segmentation

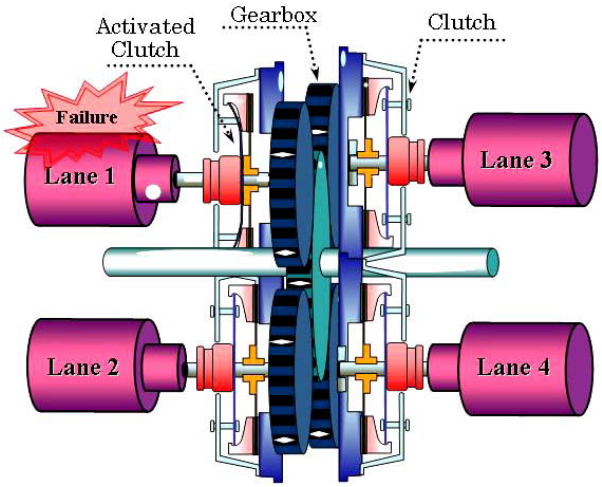


Figure 2.15: Four lane torque summer with clutches [12].

of the lanes' respective three-phase windings was investigated as shown in Figure 2.16. Optimised machine designs for both segmentation strategies were synthesised. The drag torque for short-circuited three-phase windings with respect to speed was calculated as shown in Figure 2.17.

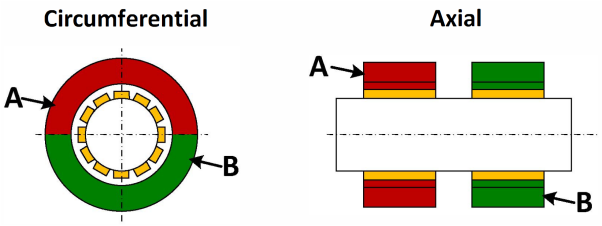


Figure 2.16: Circumferential and axial dual-lane segmentation [13].

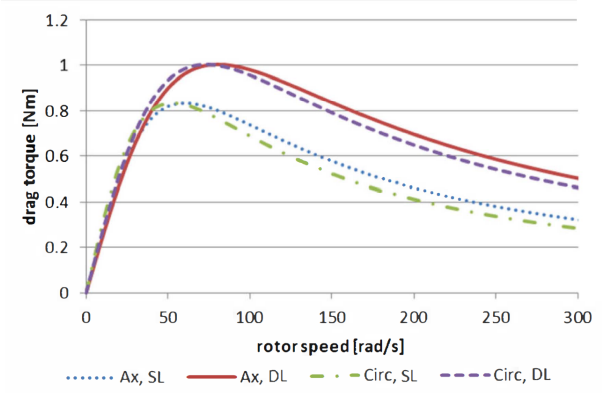


Figure 2.17: Calculated drag torque for short-circuit fault of axially (Ax) and circumferentially (Circ) segmented lanes with single layer (SL) and double layer winding schemes (DL) [13].

2.4.2.2 Velocity summing

Velocity summing is where the total output velocity is the sum or average of each lane's velocity. This is typically done through the use of a differential gearbox as shown in Figure 2.18. The main advantage is that it eliminates force fighting between the lanes if there is disagreement. If one of the lanes fails and its speed becomes uncontrollable, the remaining healthy lanes would need to compensate by increasing or reducing their speed to maintain constant output speed. The faulty lane would then need to be mechanically isolated by locking it in place. The remaining lanes would then need to increase their output to compensate for the loss in speed. For a two lane velocity summing configuration, both lanes deliver half the output power at their nominal torque and speed. If one of the lanes fail, the faulted lane's brake is activated and the healthy lane would need to double its power by doubling its speed to maintain the same output torque and speed. Isolating the faulted lane eliminates drag torque on the healthy lanes.

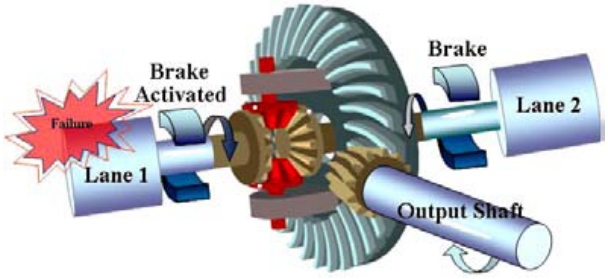


Figure 2.18: Velocity summing with a differential gearbox [12].

Velocity summing using a differential gearbox is utilised for the hydraulic actuation of the Airbus A320's flaps and slats as shown in Figure 2.19 for the flaps. Two hydraulic motors powered by the green and yellow hydraulic lanes respectively drive one differential gearbox. Each motor has its own pressure off brake (POB). If one of the lanes fail, its brake is engaged and the remaining healthy lane drives the flap or slat extension/retraction at half speed [14]. A loss of secondary flight control surface extension/retraction speed is acceptable for large commercial aircraft as it would not explicitly mean a loss in control of the aircraft's trajectory. A loss in dynamics of primary flight control surface may not be acceptable as it can lead to loss of aircraft control. [40] investigated a two-lane velocity summing topology for high-temperature EMA application. A planetary gear set is utilised as the velocity summing component and its output drives a ball-screw via a three stage gearbox set.

2.5 System sizing and modelling techniques

In this section, a review of published literature into aerospace electric drive actuation system sizing and modelling techniques are presented. Any relevant insights gathered

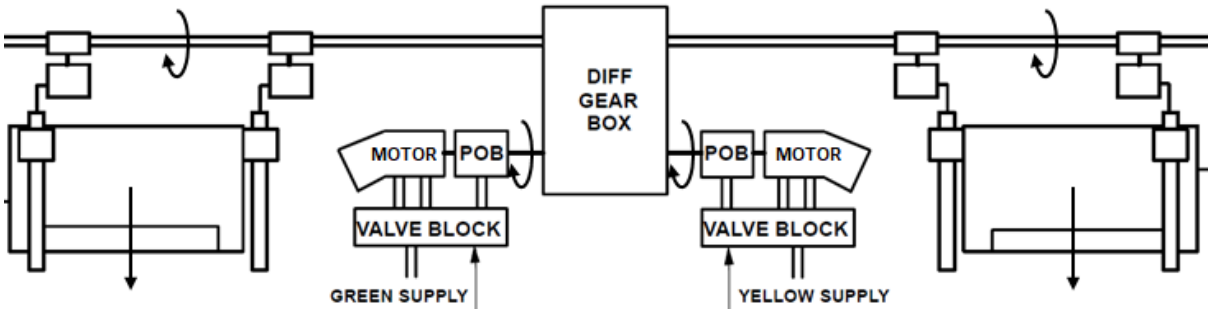


Figure 2.19: A320 flap actuation system with a differential gearbox [14].

from the reviewed literature are highlighted.

[41] and [42] presented easy to use mechanical component scaling laws that can be utilised in preliminary actuator sizing. Optimal EMA/EHA design is a multi-domain problem. Often is the case that a system level designer may lack knowledge in a specific field. This is where scaling laws can be used to aid the system designer. It allows the estimation of all relevant parameters for preliminary calculations and basic simulations from a small amount of inputs. The scaling law is based on the assumption of similarity of material properties and dimensional/geometric ratios. Knowing the specifications of one component in a product range, the specifications of another component of that product range can be easily deduced using the presented scaling laws.

[43] presented a multifaceted methodology for optimal preliminary design and sizing of EMA's. It stated that conventional "static sizing" based on one operating point is not sufficient and instead proposed sizing based on transient mission profiles considering all major design drivers (maximum torque/speed, vibration, temperature, duty cycle, failure rate, operating modes). Estimation, simulation, evaluation, and meta-models were utilised and the inter-model coupling relationships are described. Scaling laws and surface response methods is utilised to develop meta-models from which the design space can be computationally efficiently explored. Time domain simulation was done in Modelica. The methodology was demonstrated by sizing of a spoiler EMA.

[44] presented a dimensioning tool for MEA (more electric aircraft) actuator systems considering modelling, analysis, and technology comparison. Preliminary drive sizing was done for architecture comparison. Empirical inverter power loss and mass equations for IGBTs as function of dc-link voltage, switching frequency, and input power were used [45]. Empirical equations of a similar form were derived for the electrical machine as a function of input power, output torque, technology factor, and fundamental frequency, and for gearbox as a function of input power, nominal diameter, technology factor, and input rotation speed. The parameters determined from the preliminary design were utilised as starting points for detailed inverter, machine, and gearbox design. The electric machine design is analysed and validated using a combination of Finite Element Method (FEM) and Reluctance Network Model (RNM). The modelling principle of Time Domain

Frequency Separation (TDFS) is utilised whereby only quasi-stationary electrical state variables are simulated. Thermal, mechanical, control, and electrical dynamics differ in orders of magnitude. Here, any fast dynamics that occur within a switching cycle are ignored, thus improving simulation run time. Time domain simulations utilising these TDFS models was done in Modelica.

[46] presented a multi-level integrated mass optimisation method for electric drives. It addresses the issue that most existing literature related to electric drive optimisation focuses exclusively on either the power electronics or the machine. The considered drive consisted of an AC/DC rectifier, dc-link capacitor, six-switch inverter, inverter heat sink, and machine. The four modelling levels are listed as follows in order of decreasing bandwidth: component (>100kHz), behavioural (10kHz - 100kHz), functional (10Hz – 10kHz), and architectural (<10Hz). The multi-level approach separates the optimisation into level-segregated runs. Particle swarm optimisation (PSO) from MATLAB's global optimization toolbox was utilised for the system mass minimisation. Parameter variables associated to a given level are optimised and then passed on as input constants to the level below. This process is repeated iteratively until no improvements are seen in the objective function. This reduces the number of dimensions for each run, in turn reducing runtime and increases robustness. This approach was compared with a single-level optimisation were all parameters across all levels are considered for optimisation simultaneously. The best objective function optimisation results for multi-level and single-level are 11.96kg and 11.85kg respectively. The average for computation times for multi-level and single-level are 793.35 seconds and 113.1 seconds respectively. The single-level approach took approximately 50% longer to simulate but achieved a superior design of lesser mass compared to the multi-level approach. However, the difference between minimal mass of the single-level and multi-level approaches was small that it could be neglected. One may select the multi-level optimisation approach for improved optimisation robustness and the faster simulation time at the expense of a slightly heavier design.

[47] presented a multi-objective optimisation technique for electric machine design considering electromagnetic, electrical, mechanical, and thermal characteristics. Multi-objective optimisation allows for the exploration of the design space by generating the Pareto frontier and comparing multiple objectives which may be in contradiction with each other. The multi-objective optimisation was completed using distributed heterogeneous optimization [48] with genetic algorithm. The considered objectives parameters were mass, phase voltage, and winding temperature.

[49] presented a computational efficient design procedure for permanent magnet synchronous machines using the RNM of [50] and thermal resistance networks of [51]. The RNM parameters are determined from the geometry and material specifications of the stator, rotor, magnet, and windings. The RNM is used to solve the torque/stator current relationship while considering material non-linearities. There is a good match between

RNM- and finite element method (FEM)-calculated torque/current relationships and torque ripple. Solving of RNM networks is faster than FEM equivalent models. The RNM is integrated as a part of an optimisation scheme utilising particle swarm optimisation as presented in [52]. The "2×3" fault tolerant 12 slot, 10 pole HEMAS (Helicopter Electro-Mechanical Actuation System) machine is realised from this study.

[53] presented modelling and simulation of flight control electromechanical actuators considering multi-disciplinary effects. Multidisciplinary energy flow was represented explicitly using the Bond graph formalism [54]. This facilitated the implementation of an in-depth multi-disciplinary simulation model. The model considers thermals, response to failure, and power quality. The considered components of the studied actuation system includes a direct drive EMA with a nut-screw mechanism, actuator control electronics, power drive electronics, permanent magnet motor, flight control surface, and sensors for current, speed, and position. The multi-disciplinary domain coupling facilitated energy balance modelling and thermal effects on magnetic properties, friction, and dimensions. Non-linear effects considered include magnetic saturation, compliance effects (preload, backlash), friction, structural dampening, and cogging torque. The simulation was implemented in AMEsim.

[55] determined optimal designs with respect to power (volumetric) density for DC-DC converter, single phase AC-DC converter, three phase unit power factor PWM rectifier, and a sparse matrix converter. The analysis determined the power density limits for these four topologies as 28kW/dm^3, 35kW/dm^3, 45kW/dm^3, and 71kW/m^3 respectively. The design paradigm considered power semiconductor modules and their losses, power passives (transformers, inductors, capacitors), cooling system (finned air heat sink and fan), and EMI filter. Optimal finned air heat design is outlined in [56]. Optimal EMI filter sizing is achieved by deriving an empirical relationship between inductor, capacitor volume of a multi-stage EMI filter with respect to required attenuation. The paper declared that power density has been doubling every decade since 1970. To double the power density, the switching frequency would been to be increased by approximately a factor of 10. Increase in switching frequency leads to a reduction in EMI filter sizing. To facilitate this increase in switching frequency, a proportional decrease in switching times is required to preserve the comparable switching losses. This poses challenges for semiconductor manufacturers to reduce the switches drain-source capacitance. Thermally coupling passive components to the heat sink using heat pipes can increase the passive components' power density. Increasing the allowable junction temperature of semiconductors increases the effectiveness of heat sink to dissipate the losses to ambient, noting that heat flow is directly proportional to temperature difference for a constant thermal resistance.

[57] presented a multi-objective optimised design for an unmanned underwater vehicle (UUV) propulsion drive. The UUV is 53cm in diameter with a requirement to

move 1.54m/s at a thrust of 152N. The components considered were the surface mounted permanent magnet synchronous machine, propeller, power electronics, and battery. Considered system losses included propeller losses, semiconductor losses, machine copper losses and core losses. 33 design constraints were set. These include machine geometry and mass limits, minimum conductor width, propeller geometry limits, flux density, machine magnet demagnetisation limits and maximum input power. Genetic algorithm was utilised for the optimisation from which the Pareto efficient designs were determined with respect to system mass and range.

[58] determined Pareto-optimal designs for three 10kW AC-DC generation systems with Silicon, Silicon Carbide (SiC), and Gallium Nitride (GaN) semiconductors respectively. The considered system components were the permanent magnet AC machine, a passive rectifier, DC-DC converter, inductors, and capacitors. The Pareto-efficient optimisation with respect to total losses and total mass by genetic algorithm. For the same system loss of 300W, the GaN based system's mass is 93.6% that of SiC based system, and 60.8% that of the Si based system.

[59] presented a generalised process for drive train optimisation of industrial robots. The presented design paradigm considered the relationship between cost, lifetime, and performance. The payload's trajectory was considered in the design loop. The considered drive train components were the machine, and gearbox and were modelled empirically. The Complex algorithm [60] was utilised for optimisation as it was suitable to be used for discrete-set input data and is non-gradient dependent. The design process was demonstrated by sizing a dual axes industrial robot, each axes having six degrees of freedom. A total of 12 optimisation variables were determined, 6 for each axes. The design process is applicable for more joints, though [59] stated that problems with more than 25-30 optimisation problems (i.e. 4-5 axes with 6 degrees of freedom each) may require an alternative optimisation algorithm to the Complex algorithm.

2.6 Failure rate

Low failure rates are a requirement for aerospace actuators. The failure rates for primary and secondary control surfaces are $<1 \times 10^{-9}$ and $<1 \times 10^{-5}$ failures per flight hour respectively. To understand what failure rates are and to assess an actuation topology's failure rate; methods of determining its components' failure rates and the system's overall failure rate are required. An electrical component's failure rate with respect to time are often represented by the bathtub curve as shown in Figure 2.20. It consists of three different regions, infant mortality, maturity, and wear out. During the infant mortality period, failure rates reduce with time. Failures during this period are typically attributed to the setting up and debugging process. After that, failure rates are approximately constant during the maturity period. The length of this period is known as its normal

life. After this is the wear out period, where the component's failure rate increases. Often when "failure rates" are mentioned, it is implicitly referring to the constant failure rate of the bath tub curve's mature period.

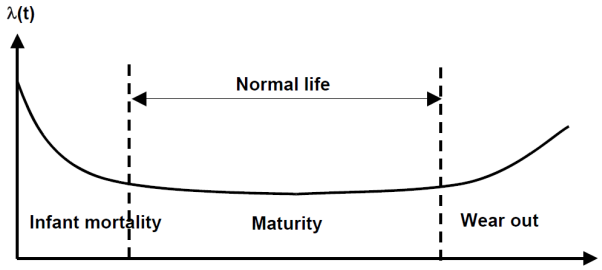


Figure 2.20: Failure rate vs. time bathtub curve [15].

The MIL-HDBK-217 handbook [61] is one of the most cited references of reliability calculation of electronic components. The general equation for the failure rate λ_p model of a component p is a product of the base failure rate λ_b, temperature factor π_T, power rating factor π_R, voltage factor π_S, quality factor π_Q and environmental factor π_E,

$$\lambda_p = \lambda_b \pi_T \pi_R \pi_S \pi_Q \pi_E. \tag{2.1}$$

The latest update of the MIL-HDBK-217 was 1995 and it is now considered obsolete and has been shown to be highly inaccurate. [62] compiled a collection of critical articles from government research bodies, academics, and industry. [63] [64] stated that there was no scientific foundation upon which MIL-HDBK-217 models are based and that results are highly inaccurate. The failure rates are determined from statistical curve fitting of failures gathered from field data. It does not take into consideration different environmental and operational loading conditions and assumes the same failure rate for all loading conditions.

Many alternative methods of determining component reliability have been developed to address the short comings of the MIL-HDBK-217 [62]. These include physics of failure model-based prediction, data-driven prognostics, similarity analysis-based prediction, field data-based prediction, and test data-based prediction.

FIDES (meaning faith in Latin) Guide 2009 [15] was created to address the shortcomings of MIL-HDBK-217. Its development was instigated by the French Ministry of Defence in collaboration with Airbus France, Eurocopter, Nexter Electronics, MBDA missile systems, and Thales. It provides realistic failure rates of the electronic components considering physical factors, life profile, electrical, mechanical, and thermal overstresses, failure related to development, production, operation, and supplier determination factor for components. It adopts a physics of failure approach. The methodology has been shown to provide good results and the existing models have been expanded upon in the PISTIS project to consider new technologies, such as sub-30nm semiconductor nodes,

and GaN power modules [65].

2.6.1 System failure rate

[11] and [66] utilised fault tree analysis in comparing different electrical actuator architectures. Component failure rates are assumed to be constant and taken from literature. The developed fault tree is used to identify the cause and effect of different failure types.

[67] utilised Markov analysis to determine drive level reliability of an induction motor drive under field-orientated control. The considered components were power electronics, induction machine, speed encoder, and current sensors. The considered modes of failures include omission, gain, and bias errors for the speed encoder and current sensors, open-circuit, short-ciruit to ground or dc-bus for the phase legs, and machine phase to phase and rotor bar break. It identified the dominant failure modes are due to the speed encoder. Markov analysis also allows the inclusion of maintenance scheduling in the analysis and to determine its effect on a system's failure rate [68].

[69] analysed the relationship between cost and reliability of a $N+X$ parallel inverter system for power distribution, where N is the number of parallel inverters required to deliver full load, and X is the number of inverters for redundancy. The case study considered a parallel inverter system delivering 100kW. For this scenario, it was found that increasing X increases system reliability significantly up to a point, where $X > 3$ for $N = 3$ returned negligible increase in overall system reliability. The paper investigated the effects of dynamic power distribution and time sharing between the inverters. M out of N inverters were utilised at a time to deliver the required load to optimise efficiency at lower, non-nominal loads. Effects of this scheme was an increase in system up time, increased efficiency, lower operating thermals, and thus increase reliability. Total system cost included hardware, operating and maintenance, downtime, and power loss. An optimised minimal cost solution of $N = 6$ and $X = 2$ was determined.

[70] presented system-level reliability analysis for a 5kW backup power dc/dc converter based on the system's mission profile. The analysis addressed the short-comings of common reliability analysis assumptions, such as assuming constant failure rate, and taking no consideration of realistic mission profile. This leads to overestimation of unreliability and over engineering. Component-level and system-level reliability is determined as function of mission profile. The ambient temperature and power load of the mission profile is described by bins of a histogram lifetime frequency distribution. The considered components of the dc/dc converter were the power electronics and dc capacitors. The considered electronic component stress factors are voltage, current, and temperature, from which the components' lifetimes are determined. The steps of predicting component lifetime are as follows. First, component loading is determined with respect to loading profile and ambient temperature. The current and voltage is determined and

the losses are calculated. Loss data is fed into component thermal models to determine temperature. The component's voltage, current, and temperature stress factors are used to determine component lifetime. This is repeated to determined the equivalent lifetime for each bin of the histogram lifetime frequency distribution. The effective lifetime is determined from the sum of the inverted lifetimes for each bin, weighted by their respective bin frequency. Sensitivity analysis is completed considering variation in base component lifetime. System level reliability is determined using a series/parallel reliability block diagram.

2.7 Electric drive systems with long feeder cables

An investigation into electric drive systems with long feeder cables was completed by the author and published as [71]. The motivation behind the investigation is the proposal of a new centralised electric drive topology for aerospace actuation, whereby the inverter is located in the fuselage and the actuator is located on the wing, at the point of actuation. An understanding of the design concerns and modelling methods is required to both qualitatively and quantitatively assess this topology. High dv/dt switched inverter voltages applied to long cable feeders whose surge impedance matches poorly with that of the machine can lead to high-frequency high-amplitude oscillations through out the cable, at the machine's terminals and through out the machine's windings. This phenomenon is known as the transmission line effect. These effects can lead to high EMI, corona discharge, differential mode current, common-mode current, bearing current. The issue of corona discharge is of particular concern for aerospace application. The amplitude of the voltage oscillation can be more than 2× that of the dc-link voltage value for short pulse widths [72]. As altitude increases, atmospheric pressure reduces and with that, the breakdown threshold voltage for corona discharge reduces as well. This has been described by the Paschen's curve as shown in Figure 2.21. The x-axis is pressure times distance in units of Pascals metres. The y-axis is the peak ac/dc breakdown voltage in units of volts. Corona discharge can lead to degradation of the insulation system and bearing currents lead to breakdown of the bearing track race surface.As utilisation of wide-band gap semiconductors with high dv/dt and faster switching frequencies increases, these high-voltage high-frequency phenomena and associated issues will become more prevalent and must be addressed correctly. High-frequency cable and machine models are required to model this high-frequency transmission line phenomenon. The presented methodology can be extended to other applications, such as renewable energy and drive systems.

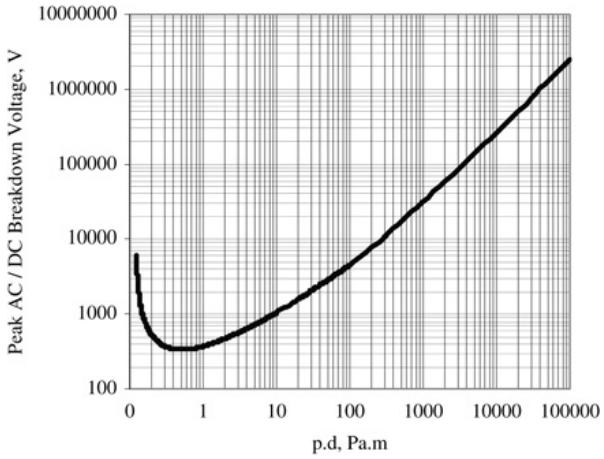


Figure 2.21: Paschen's curve for air [16].

2.8 Conclusion

The aim of this thesis to develop an optimal electrical actuation sizing toolbox for aerospace applications. The relevant literature to help achieve this goal has been presented in this chapter. The key points are summarised here.

Recent trends have shown an increase in commercial aircraft's electrical generation such as the Boeing 787's no-bleed architecture and Airbus A350's and A380's 2H-2E architecture. Development of EHA have reached a level of maturity that they have been adopted for primary control surface use, albeit in a support or back-up role in the A350 and A380. The increased electrification trend will eventually lead to an all-electric secondary power systems aircraft. It is predicted by Actuation2015 that full utilisation of EMA's can lead to a reduction of life cycle costs by 30%, reduce failure rate by 30% and total mass reduction of 500kg for an Airbus A320 sized aircraft. Sagem has successfully demonstrated and te sted a TRL6 aileron EMA on the A320.

Fault-tolerant electrical topologies "n+1" and "n×3" were presented. The issues of the "n+1" topology have been highlighted: non-constant power draw from each lane, high input filtering requirement, and the need for current re-shaping during lane failure. This makes "n×3" the better electrical topology candidate as each lane draws constant power, thereby reducing input filtering requirements. Moreover, current reshaping is not required in the event of a lane failure.

The concepts of torque and velocity summing are presented along with their redundant failure-mode operating requirements. Torque summing topologies without the option of de-clutching experience pulsating drag torque from the failed lane due to machine phase short. This drag torque would need to be compensated for by the remaining healthy lanes. "n+1" topologies are intrinsically torque summing topologies as multiple lanes are magnetically coupled to the same rotor. "n×3" topologies can be torque or velocity summing topologies. A dual-lane velocity summing topology with differential gearbox

and per-lane pressure off brakes is already utilised in conventional hydraulic actuation systems for flaps and slats. The added advantage of this topology is the faulted lane can be easily mechanically isolated with a brake, thus eliminating the effects of drag torque on the healthy lanes' operation.

System sizing and modelling techniques have been presented. The effective utilisation of scaling laws to quickly and easily size mechanical drive train components was demonstrated in literature. The importance of a holistic approach to electrical actuator design and sizing, spanning multiple domains and bandwidth levels, has been highlighted by many authors. The adoption of heuristic search algorithms such as particle swarm and genetic algorithm for both component and system level optimisation has been prolific and can be accredited to the ease of accessibility for academics via MATLAB's global optimization toolbox. The bundled optimisation algorithms allows for easy implementation and exploration of the optimal design space for a multi-objective optimisation problems by generation of the Pareto frontier. Computationally efficient analytically based sizing procedures are required for the effective utilisation of heuristic search algorithms. An example of this is using RNM instead of FEM to determine the torque/current relationship for machine sizing optimisation.

Design for actuation system failure rate is of equal importance as designing for mechanical actuation requirement and power quality. Conventionally, MIL-HDBK-217 was used to determine component reliability but numerous publications have outlined its obsolescence, inaccuracies, and lack of consideration for difference in environment, operating loads, and loading conditions. FIDES guide 2009 is the preferred method of determining component reliability due to its physics of failure approach and its continued development ties with reputable aerospace engineering companies. Fault tree analysis and Markov analysis are two common methods of determining the system level reliability. Fault tree analysis is comparatively easier to implement while Markov can include the effects of maintenance scheduling into its analysis.

A thorough investigation into electric drive systems with long feeder cables was conducted by the author and published in [71]. The motivation behind this investigation was the proposal of a centralised topology with long feeder cables. Steep-fronted switched voltages with high dv/dt applied to long feeder cables with high cable-machine surge impedance mismatch leads to high-frequency high-amplitude voltage oscillations. This phenomena is known as transmission line effects and can lead to corona discharge, high EMI, bearing currents, and eventual system failure if not properly considered. High-frequency cable and machine models are required to analyse this effect.

Chapter 3

Problem Definition

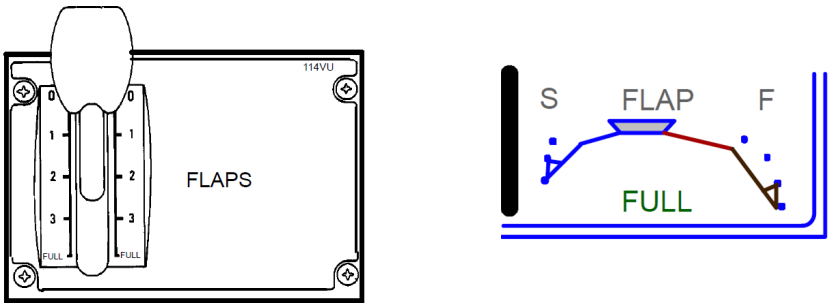
Before the solution to a problem can be developed, the problem itself needs to be understood and defined. The considered problem is optimal sizing and design of the flap actuation drive system for an Airbus A320-200. The flap's function is described. A mechanical and kinematic representation is formulated. The failure rates and failure mode requirements are outlined.

3.1 Flap actuation functional description

Flaps, as well as slats, are part of an aircraft's high-lift system. The slats and flaps are secondary flight control surfaces. The high-lift system increases both the lift and the drag of the aircraft. This allows for slower speed landings and take-off's, thus shorter runaways and reduced wear on the landing gear. The flaps and slats extend and retract to discrete positions. In the Airbus 320, there are five discrete flap positions, named 0, 1, 2, 3, and FULL. The positions are labelled on the A320's flap position lever and shown on its slat/flap indicator display as seen in Figure 3.1.

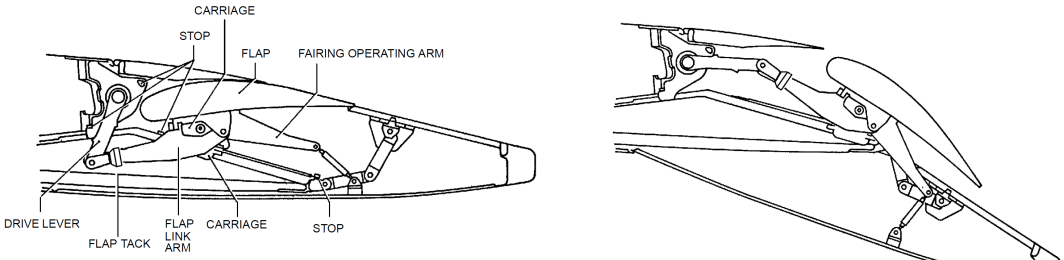
The A320's flap retracted and fully-extended positions are shown in Figure 3.2. When the flaps are extended or retracted, they need to overcome the aerodynamic forces acting upon the surface. The drive arm rotates about the pivot point of the rotary actuator. This in term, moves the flap link arm, the flap carriage, and the flap along the track.

The Airbus A320's conventional slat and flap transmission system is shown in Figure 3.3. The flap actuation system is controlled using two slats flaps control computer, SFCC1 and SFCC2. Electrically controlled hydro-mechanical Power Control Unit (PCU) controls power to drive the hydraulic motors. Two motors, supplied by the green and yellow hydraulic supply, drive torque to the common flap transmission system for a differential gearbox. The gear position of the differential gearbox is monitored by the feedback position pickup unit (FPPU) and instrument position pick up unit (IPPU). The flap actuators are connected to the common flap transmission system. As the transmission



(a) Lever. **(b)** Indicator.

Figure 3.1: Flap lever and indicator [14].



(a) Retracted.

(b) Fully-extended.

Figure 3.2: Flap retracted and fully-extended [14].

shaft rotates, both the outer and inner flaps are actuated in synch. Slat actuation is achieved using the same concept. A centrally located slat power control unit and two motors powered by the blue and green supply drive a common transmission system, via a differential gearbox, from which all slat actuators are connected to. Asymmetry position pick-up off units (APPU) are located at either ends of flap and slat transmission systems respectively. Wing-tip brakes (WTB) are present to stop flap or slat movement in the event of a fault, over-speeding, or asymmetry. Feedback Position Pick-Off Unit provides position information to the power control unit (PCU). Flaps position and proximity signals are sent to the Landing Gear Control Interface Units (LGCIU) as deployment and retraction of the landing gear coincides with use with flaps during take-off and landing. The disadvantage of this transmission system using torque shafts and mechanical links is that it is difficult to install, is heavy, and doesn't allow for differential setting of the inboard and outboard flaps.

The Airbus A350XWB implements an additional active differential gear box between the inboard and outboard flaps, as shown in Figure 3.4. This allows for differential flap settings (DFS) and variable chamber (VC) [3]. These features allows for reduction of wing load by alleviating aerodynamic and structural loads on the wing, leading to weight savings on the order of half a tonne in the wing box [73].

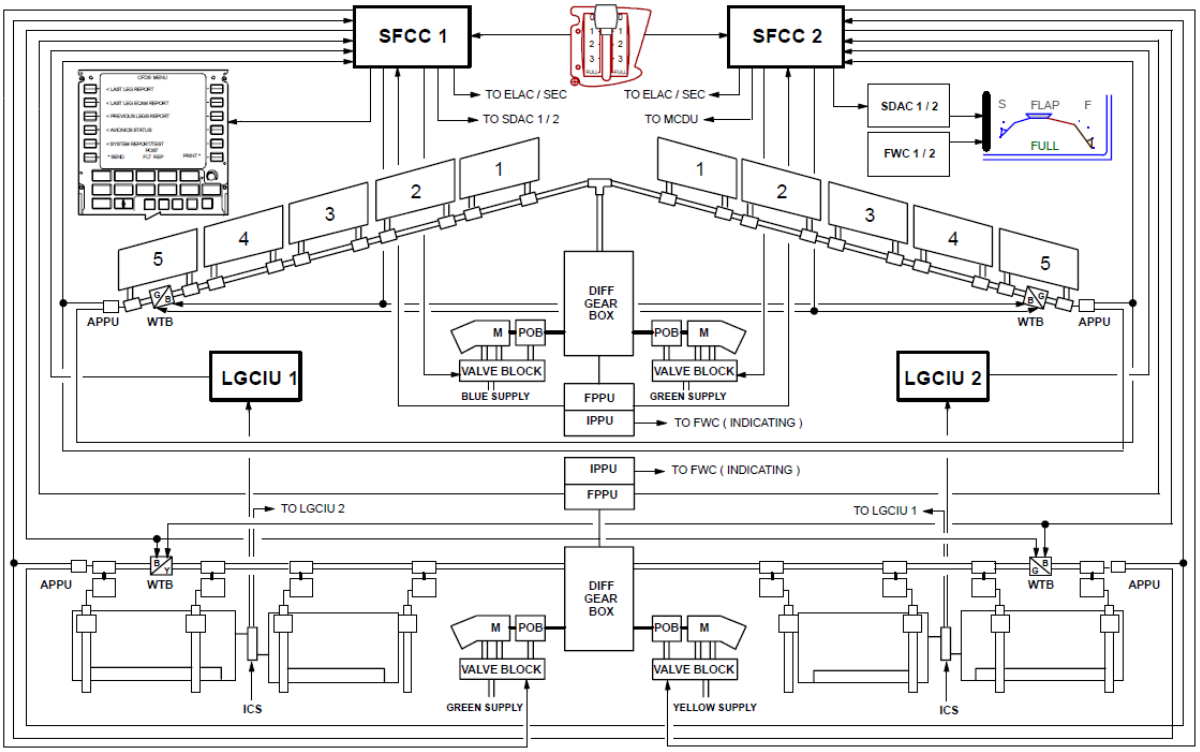


Figure 3.3: A320 slat and flap transmission system [14].

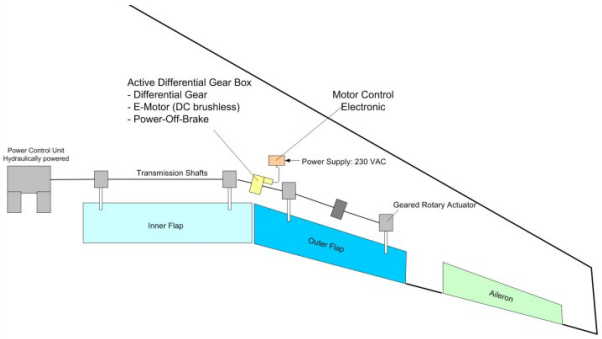


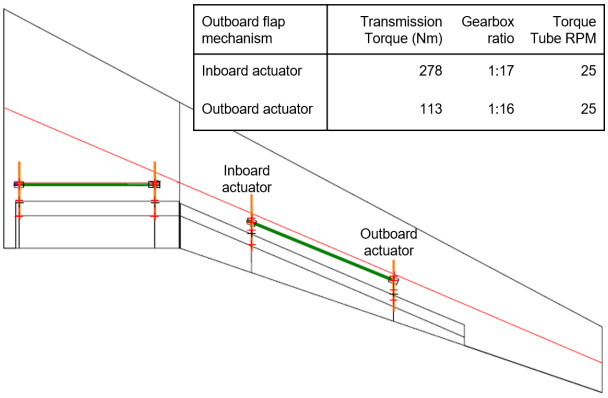
Figure 3.4: A350XWB flap transmission system with active differential gearbox for differential flap settings [17].

3.2 Flap actuation mechanical description

3.2.1 Actuation Requirement and mechanical system representation

A distributed flap system is proposed where by the actuation of each flap can be independently controlled. This allows for differential flap setting and variable camber. [18] determined the flap actuation loads for the Airbus A320-200. The actuation load for the outboard trailing edge flap is shown in Figure 3.5. There are four flap surfaces, two for each wing. Each flap is actuated by an inboard and outboard mechanisms. These mechanisms are link-track systems driven by rotary actuators. The inboard and outboard

rotary actuators are driven by a torque tube rotating nominally at 25RPM via their respective gearboxes of 1:17 and 1:16 gearbox ratios respectively. The total actuation power requirement for the outboard flap is determined as 1.1kW when rounding up to the nearest 0.1kW. It is proposed an electric drive system is designed for this load.



Outboard flap mechanism	Transmission Torque (Nm)	Gearbox ratio	Torque Tube RPM
Inboard actuator	278	1:17	25
Outboard actuator	113	1:16	25

Figure 3.5: A320-200 outboard flap actuation definition provided by [18].

To deliver the required mechanical power for the flap actuation load in a fault-tolerant manner, the velocity summing topology of Figure 3.6 is considered. It consists of two three-phase machines, labelled M1 and M2 rotating at speeds ω_1 and ω_2 respectively, electrical brakes EB1 and EB2, and a differential gearbox DGB. When the flap is not being actuated and its position matches that desired by the slats flaps control computer (SFCC), both EB1 and EB2 are locked to hold the flap in place. This means no energy is expended by applying the holding torque while the flap is stationary. During nominal non-faulted actuating operation, the flap is moved from one position to another, EB1 and EB2 are unlocked and both M1 and M2 are controlled to rotate at the same speed such that $\omega_1 = \omega_2$. This drives the actuation load via the 1:k gear ratio differential gearbox DGB. The output shaft of DGB drives a 1:1 gear ratio 90° bevel gearbox, rotating the torque tube TT which drive the inboard actuation gearbox AGB,IB and outboard actuation gearbox AGB,OB. Gear ratio k of DGB is a design variable.

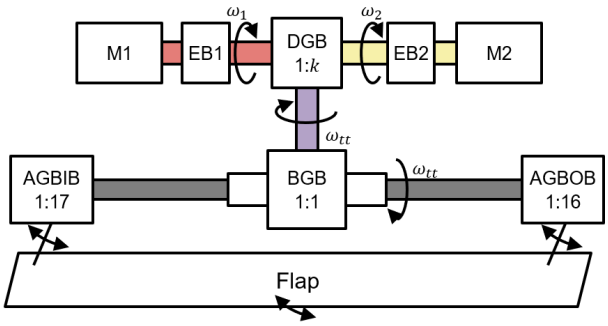


Figure 3.6: Proposed mechanical flap actuation topology.

A mechanical system can be represented by an analogous electrical circuit using the method of impedance analogy as described in Table 3.1.

Table 3.1: Mechanical-electrical impedance analogy.

Mechanical rotation variable	Analogous electrical variable
Torque	Voltage
Angular velocity	Current
Angular momentum	Flux linkage
Angle	Charge
Rotational resistance	Resistance
Moment of inertia	Inductance
Rotational compliance	Capacitance

A simplified analogous circuit for the flap mechanical system of Figure 3.6 is shown in Figure 3.7. Gearboxes are represented by transformers in the analogous circuit. Variables J and F represent moments of inertia and friction coefficients respectively. The differential gearbox consist of ns number of stages. The moment of inertia's differential gearbox's input gears is $J_{DGB,1}$. The moment of inertia for the remaining gears is represented by $J_{DGB,2\rightarrow ns}$. The load torque applied on the inboard and outboard rotary actuators are represented by $T_{F,IB}$ and $T_{F,OB}$ respectively. The lumped moment of inertia $J_{F,IB}$ and $J_{F,OB}$ includes that of the rotary actuator arm, the flap mechanism and the flap.

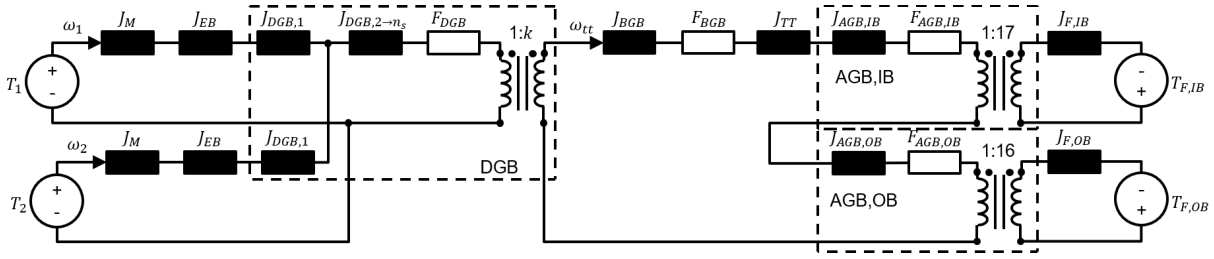


Figure 3.7: Flap actuation mechanical analogous circuit.

Methods for determining appropriate values for analogous circuit's parameters in Figure 3.7 is presented in section 3.2.2.

3.2.2 Speed reducer gearbox, electromagnetic brakes, and torque tube scaling laws

[41] presented estimation models suitable for preliminary system-level design of electromechanical actuators and mechanical systems. The proposed estimation model for a given component directly links the component's primary characteristics, which describes its main function, to its secondary characteristics. For example, consider a torque tube. Its function is to deliver drive torque from a rotational source to a rotational load by mechanically linking them. A torque tube's primary characteristic is defined by its nominal operating torque. Examples of secondary characteristics are its mass, moment of inertia, and maximum speed.

Scaling laws are used to describe the association between primary and secondary characteristics of components. The scaling law ratio of a given parameter x^* is calculated as

$$x^* = x/x_{ref}, \tag{3.1}$$

where x_{ref} is reference parameter and x is the parameter under study. The scaling law is based on assumptions of similarity where the considered reference component and components under study have the same,

1. Material properties (e.g. density, Young's modulus)
2. Dimensional and geometric ratios.

3.2.2.1 Speed reducer gearboxes

The established scaling laws for speed reducers with one stage are as follows [41]. For single stage speed reducer, the definition parameter is nominal output torque T_{nom} and transmission reduction ratio k. The scaling law with respect to dimensions length l^* and diameter d^*, and mass M^* are,

$$d^* = T_{nom}^{*1/3}, \tag{3.2}$$

$$l^* = T_{nom}^{*1/3}, \tag{3.3}$$

$$M^* = T_{nom}^*. \tag{3.4}$$

The relationship between the moment of inertia and torsional stiffness to the definition parameter are as follows,

$$J^* = T_{nom}^{*5/3}, \tag{3.5}$$

$$K^* = T_{nom}. \tag{3.6}$$

The operating torque and speed limits are related to the definition parameter as shown,

$$T_{max}^* = T_{nom}^*, \tag{3.7}$$

$$\omega_{max}^* = T_{nom}^{-1/3}. \tag{3.8}$$

For multi-stage planetary gearbox speed reducers with high overall stage reduction ratio k, the maximum reduction ratio for each stage is limited by geometrical restrictions. It is assumed that the overall reduction ratio k is shared equally among the n_s stages such that each i^{th} stage's reduction ratio k_i is equal to $k^{(1/n_s)}$. The last stage (where $\mathrm{i} = n_s$) is sized for its nominal output torque in the exact same manner as the single stage speed reducer. The supplementary stages' ($\mathrm{i} < n_s$) torque load is significantly reduced but rotational speed increases and with that fatigue. Thus, both fatigue and transmission are drivers for supplementary stage sizing. These stages are sized such that their fatigue

lifetime is the same as that of the last stage. The fatigue lifetime is represented by an associated cumulated damages term Q_h and is a function of nominal torque ω_{nom} where p is a bearing constant equal to 3 or 10/3 depending on bearing type [74],

$$Q_h = T_{nom}^p \omega_{nom}. \tag{3.9}$$

Thus, the nominal torque of the i$^{\text{th}}$ stage with respect to the nominal output torque of the final stage $i = n_s$ and per stage efficiency η can be derived as follows,

$$T_{i,nom}^* = \frac{T_{ns,nom}^*}{k^{(1-\frac{1}{p})(1-\frac{i}{n_s})}\eta^{n_s-i}}. \tag{3.10}$$

This $T_{i,nom}^*$ value is used to size the i$_{\text{th}}$ stage using the aforementioned single stage equations (3.2-3.8).

The mass M_i of each i$^{\text{th}}$ stage is determined for $T_{i,nom}^*$ using (3.4). The total mass of the multi-stage gearbox is the sum of all of the stages. The moment of inertia J_i for each ith stage is determined using (3.5). The total equivalent inertia J_{eq} considering all stages of the multi-stage gearbox with respect to the high-speed input side is as follows,

$$J_{eq} = \sum_{i=1}^{n_s} \frac{J_i}{k^{2(i-1)/n_s}}. \tag{3.11}$$

The torsion stiffness K_i for each ith stage is determined using (3.6). The total equivalent torsion stiffness K_{eq} with respect to the low speed shaft is as follows,

$$K_{eq} = \left(\sum_{i=1}^{n_s} K_{i,eq}^{-1} \right)^{-1}, \tag{3.12}$$

where,

$$K_{i,eq} = K_i k^{2(n_s-i)/n_s}. \tag{3.13}$$

Mechanical torque limit is considered with respect to the last stage as this is where the maximum torque is experienced. Inversely, the rotational speed limit is considered with respect to the first stage as that is where the maximum rotational speed occurs,

$$T_{max}^* = T_{n_s,nom}^*, \tag{3.14}$$

$$\omega_{max}^* = T_{1,nom}^{-1/3}. \tag{3.15}$$

The equivalent per stage gearbox friction coefficient term F was estimated from data sheet nominal operating conditions for single-stage gearbox with reducer ratio k and

efficiency η,

$$F = \frac{T_{nom}(1-\eta)}{\omega_{nom}\eta}. \tag{3.16}$$

The fitted relationship between single stage gearbox's mass and moment of inertia with respect to torque are shown in Figures 3.8 and 3.9 respectively. The data points are taken from manufacturer datasheets [19]. Equation of the form (3.4) was fitted to the mass vs torque data points of Figure 3.8. Equation of the form (3.5) was fitted to data points of Figure 3.9. The empirical equations to calculate gear mass and moment of inertia derived from fitting manufacturer's data are hence forth utilised in gearbox sizing.

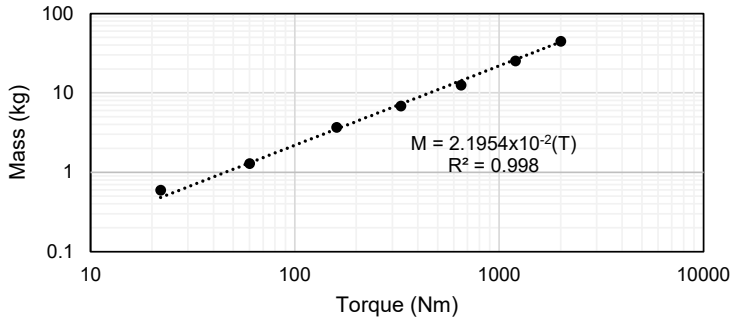


Figure 3.8: Mass of single stage gearbox with respect to nominal low speed side output torque. [19]

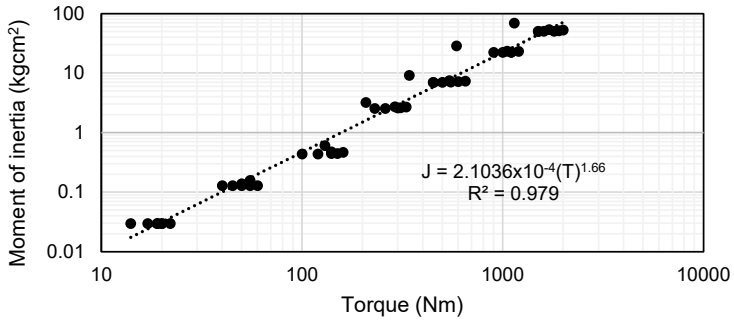


Figure 3.9: Moment of inertia of single stage gearbox with respect to nominal low speed side output torque. [19]

The F values determined using 3.16 for a given dataset [19] is plotted in Figure 3.10. A power curve is fitted to this data. The total equivalent friction coefficient F_{eq} considering

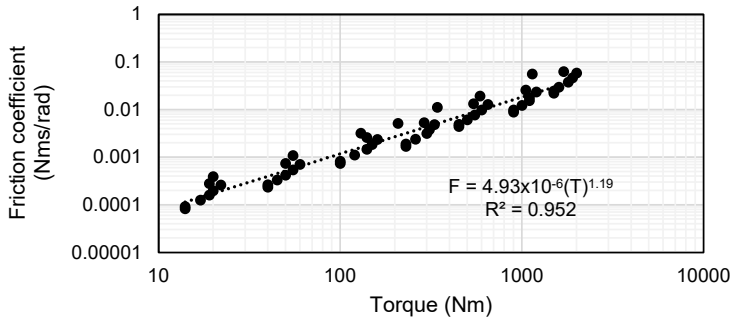


Figure 3.10: Calculated and fitted friction coefficient for single stage gearbox with respect to high speed input side for nominal output torque. [19]

all stages of a multi-stage gearbox with respect to the high-speed input side is as follows,

$$F_{eq} = \sum_{i=1}^{n_s} \frac{F_i}{k^{2(i-1)/n_s}}. \tag{3.17}$$

3.2.2.2 Electromagnetic brakes

The scaling laws for electromagnetic brakes are as follows [41]. The definition parameter is holding torque T^*. The scaling laws with respect to dimension length $l*$, mass M and moment of inertia J^* are as follows,

$$T^* = l^{*4}, \tag{3.18}$$

$$M^* = T^{*3/4}, \tag{3.19}$$

$$J^* = T^{*5/4}. \tag{3.20}$$

The relationship between the absolute maximum operating torque and speed to the definition parameter are as follows,

$$T^*_{em,peak} = T^*, \tag{3.21}$$

$$\omega^*_{abs,max} = T^{*-1/4}. \tag{3.22}$$

3.2.3 Torque tube sizing

Torque tubes are sized for maximum allowable shear stress τ due to torsion,

$$\tau = \frac{Tr}{I}, \tag{3.23}$$

where T is the torque, I is the second moment of area about the tube's axial axis, and r is the outer radius of the torque tube where the highest torsion is experienced. For a solid torque tube, $I = \frac{1}{2}\pi r^4$. Substituting I into (3.23) gives,

$$r = \sqrt[3]{\frac{2T}{\pi\tau}}. \tag{3.24}$$

The torque tube's volume V, mass M, and moment of inertia J are determined as follows for material density ρ and tube length l,

$$V = \pi r^2 l, \tag{3.25}$$

$$M = \rho V, \tag{3.26}$$

$$J = \frac{1}{2} M r^2. \tag{3.27}$$

3.2.4 Flap mechanical model

A link/track mechanism for the outboard flap of an A320-200 is considered. This is modelled by a slider-crank mechanism, the kinematic model of which is presented in section 3.2.4.1. Methods of estimating the model parameters is shown in section 3.2.4.2.

3.2.4.1 Flap kinematics and dynamics

The flap actuator's link-track kinematics of Figure 3.11a can be modelled by a slider-crank mechanism as shown in Figure 3.11b. The x-axis is aligned with the slider motion . The centre of crank rotation coincides with the origin. The slider-crank model consists of:

- the actuator crank arm OA highlighted in orange of mass m_1, length r, applying making a crank angle θ with respect to the x-axis, applying a torque T about O,
- a link arm AB highlighted in blue of mass m_2, length l making an angle ϕ with respect to the axis of slider motion,
- lumped slider highlighted in purpled of mass m_3 at B consisting of flap, pivot and roller masses with external force F_E applied along its axis.

The centres of mass for the crank arm (x_{1c}, y_{1c}), link arm (x_{2c}, y_{2c}), and slider (where centre of mass coincides with slider position) (x_{3c}, y_{3c}) are as follows,

$$(x_{1c}, y_{1c}) = \left(\frac{1}{2} r\cos(\theta), \frac{1}{2} r\sin(\theta)\right), \tag{3.28}$$

$$(x_{2c}, y_{2c}) = \left(r\cos(\theta) + \frac{1}{2} l\cos(\phi), \frac{1}{2} l\sin(\phi)\right), \tag{3.29}$$

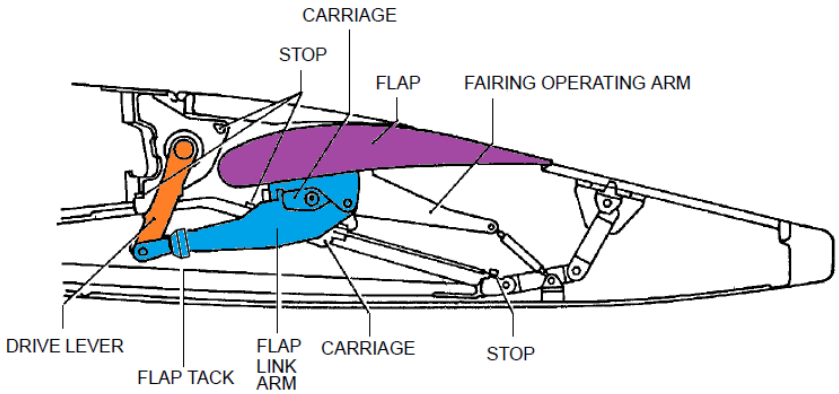
$$(x_{3c}, y_{3c}) = (r\cos(\theta) + l\cos(\phi), 0). \tag{3.30}$$

The relationship between crank angle θ and link angle ϕ is,

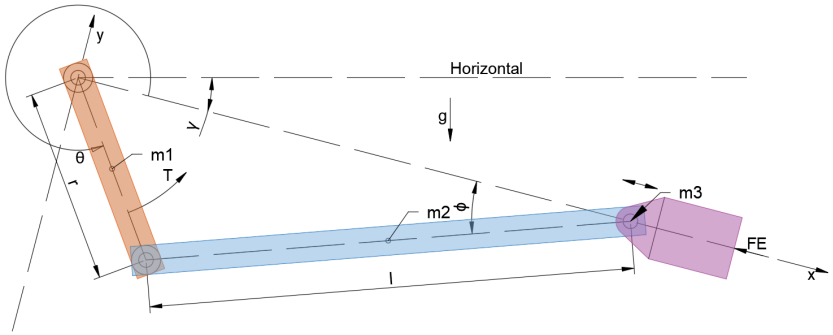
$$r\sin\theta = l\sin\phi. \tag{3.31}$$

An expression for slider position x_{3c} expressed exclusively with respect to θ is as follows,

$$x_{3c} = r\cos(\theta) + l\sqrt{1 - \left(\frac{r}{l}\sin(\theta)\right)^2}. \tag{3.32}$$



(a) Trailing edge flap mechanism in the retracted position [14].



(b) Slider-crank mechanism.

Figure 3.11: A320 trailing edge flap mechanism and link-track kinematic modelled as a slider-crank mechanism.

[75] derived the mechanical dynamic equations of the slider-crank mechanism as a function of crank angle θ. The presented equations of [75] have been modified to account for slider slope γ with the inclusion of reaction torque $\hat{G}(\theta)$ due to gravitation forces.

$$\hat{J}(\theta)\frac{d^2\theta}{dt^2} + \hat{B}(\theta, \frac{d\theta}{dt}) = \hat{F}(\theta) + \hat{G}(\theta), \tag{3.33}$$

where,

$$\hat{J} = \left[(2m_3 + m_2) + \frac{m_3}{c} r\cos\theta\right]\left(\frac{r^3}{c}\cos\theta\sin^2\theta\right) + (m_2 + m_3)r^2\sin^2\theta + \frac{1}{3}m_2\left(\frac{l}{c}\right)^2(r\cos\theta)^2 + \frac{1}{3}m_1r^2, \tag{3.34}$$

$$\hat{B} = \left[m_2r^2\sin\theta\cos\theta\left(1 - \frac{l^2}{3c^2} + \frac{r}{c}\cos\theta + \frac{(lr)^2}{3c^4}\cos^2\theta + \frac{r^3}{2c^3}\cos\theta\sin^2\theta\right) - m_2\frac{r^3}{2c}\sin^3\theta + m_3r^2\sin\theta\cos\theta\left(1 - \frac{r^2}{c^2}\sin^2\theta + \frac{r^2}{c^2}\cos^2\theta + 2\frac{r}{c}\cos\theta + \frac{(r^4\cos^2\theta\sin^2\theta)}{c^4} + \frac{r^3}{c^3}\sin^2\theta\cos\theta\right) - m_3\frac{r^3}{c}\sin^3\theta\right]\left(\frac{d\theta}{dt}\right)^2, \tag{3.35}$$

$$\hat{G} = -\frac{m_1gr}{2}(\cos\gamma\cos\theta - \sin\gamma\sin\theta) - \frac{m_2gr}{2}\left(\cos\gamma\cos\theta - \frac{r}{c}\sin\theta\sin\gamma\cos\theta - \sin\gamma\sin\theta\right) + m_3gr\left(\frac{r\sin\gamma\sin\theta\cos\theta}{c} + \sin\gamma\sin\theta\right), \tag{3.36}$$

$$\hat{F} = \tau - (F_E)r\sin\theta\left(1 + \frac{r}{c}\cos\theta\right), \tag{3.37}$$

$$c = \sqrt{l^2 - r^2\sin^2\theta}. \tag{3.38}$$

3.2.4.2 Flap mechanism model parameter estimation

[27] presents trailing edge flap's components' specific weight values with respect to projected area of nested flap(s) and flap type mechanism. The calculation method is based on weight estimation formulas determined by [76] and have been modified for the use of composites in flap construction. The trailing edge flap specific weights for a single slotted link-track mechanism and calculated weights for an A320-200's outboard flap of area 5.45m^2 are shown in Table 3.2. Given there are two flap actuator mechanism consisting of supports, actuation, and fairings, these particular values need to be halved to determine per actuator mechanism masses.

Table 3.2: Trailing-edge flap specific weights as weight per flap area for single-slotted link-track mechanism [27] and calculated weights for A320-200 outboard flap with area of 5.45m^2.

Single-slotted link/track	Specific weights kg/m^2 [27]	A320-200 OB flap weights (kg)
Flap panels	13.2	72.0
Supports	7.3	40.0
Actuation	9.8	53.3
Fairing	0.5	26.7
Total flap	30.8	167.9

The A320 single slot trailing edge flap mechanism in the retracted position is shown

in Figure 3.11a. Relative end-view areas of the drive lever and flap link arm are determined. These relative areas of the drive lever and flap link arm are used to estimate their respective components' masses assuming total calculated actuation arm mass of 26.65kg. Drive arm and link arm mass are estimated to be 7.2kg and 19.5kg respectively. It is assumed each flap actuator supports half of the flap panel mass, this being 36kg. The track slope is measured directly from the diagram and has been determined to be 15°.

The drive lever and flap track arm lengths were estimated to be 0.2m and 0.33m respectively. This was done by scaling the flap actuator diagram of Figure 3.11a such the flap chord and aft fairing distance matches that of plan view drawings taken from [77].

A summary of the estimated flap mechanism model parameters are shown in Table 3.3 for drive lever crank arm mass m_1, link arm mass m_2, per actuator flap mass m_3, drive lever length r, link arm length l, and slope track angle γ. These values are utilised in the flap slider-crank mechanism model equations (3.33-3.38) presented in section 3.2.4.1.

Table 3.3: Estimated flap mechanism model parameters for A320-200 outboard trailing edge flap.

Mechanism	m_1	m_2	m_3	r	l	γ
Inboard	10.23kg	27.73kg	51.19kg	0.2m	0.33m	15°
Outboard	4.16kg	11.27kg	20.81kg	0.2m	0.33m	15°

Inboard and outboard flap mechanism parameters in Table 3.3 were substituted into (3.34-3.36) to plot $\hat{J}$, $\hat{B}$, $\hat{G}$, and x_{3c} with respect to θ for a nominal torque tube speed of 25RPM as shown in Figure 3.12.

3.2.5 Flap actuation mechanism dynamic model

Consider the following topology shown in Figure 3.13 where two identical machines M1, M2 with electric brakes EB1, EB2 drive a flap load via the open differential gearbox DGB with gear ratio of k. The output of DGB drives a 90 degree bevel gear box BGB with unity gear ratio. Torque tubes drive the inboard and outboard actuator gearboxes respectively. During nominal actuating operation, the electric brakes are off and both machines drive the flap actuation load via the differential gearbox at the same torque and speed. If a fault develops in one of the machines, its respective electric brake locks that axle and the non-faulted machine drives the flap load. After the actuation motion is complete and the desired position is reached, both electric brakes are engaged to lock position into place.

The equivalent mechanical dynamic plant model is presented. Section 3.2.4 represented the full equivalent flap actuation system mechanical model as shown in Figure 3.7. This model is simplified by lumping the moments of inertia and friction coefficients on the output low-speed side of the differential gearbox to equivalent values J_{eq} and F_{eq}

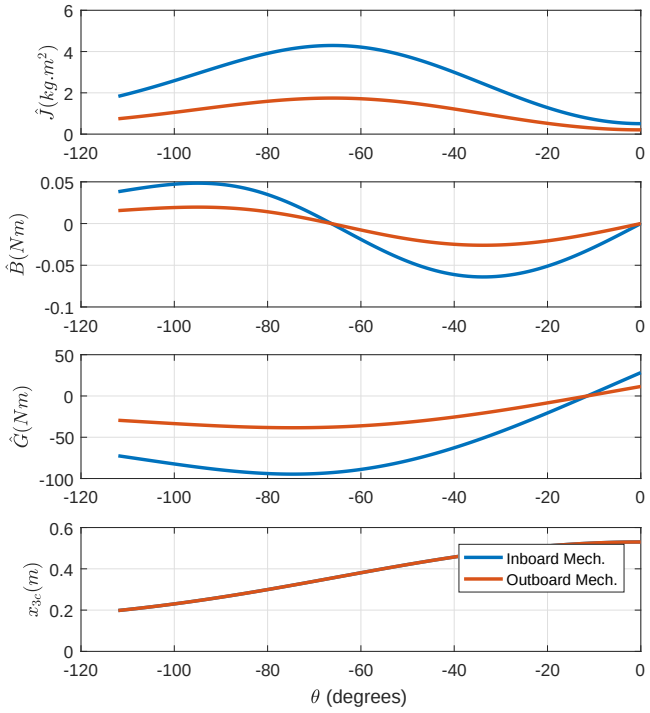


Figure 3.12: Estimated A320-200 outboard flap's mechanism parameters and slider position with respect to crank arm position θ for constant torque tube speed of 25RPM.

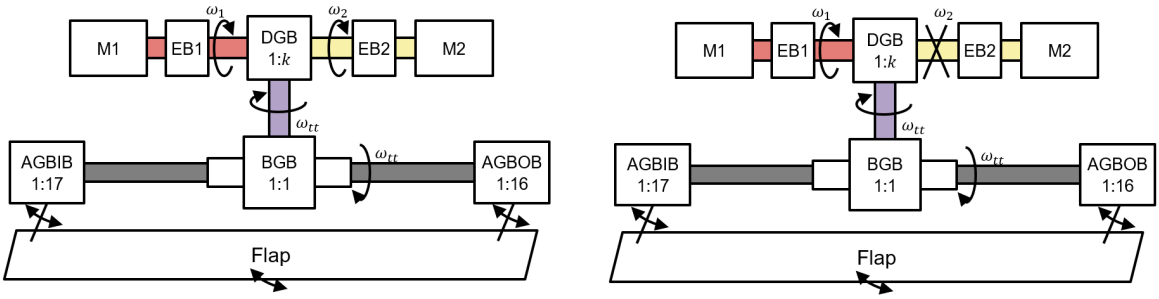


Figure 3.13: Dual machine with electric brakes (E/B) driving open differential gearbox topology, (a) nominal operation with both machines 1 and 2 are active and either respective E/B are off, sun and ring driving carrier gear at $\omega_c = \omega_s = \omega_r$, (b) faulted operation with machine 2 faulted, E/B 2 is on, machine 1 is driving load carrier gear at $\omega_c = 2\omega_s$.

respectively as shown in Figure 3.14,

$$J_{eq} = J_{\text{BGB}} + J_{\text{TT}} + J_{\text{AGB,IB}} + J_{\text{AGB,OB}} + \frac{J_{\text{F,IB}}}{17^2} + \frac{J_{\text{F,OB}}}{16^2}, \tag{3.39}$$

$$F_{eq} = F_{\text{BGB}} + F_{\text{AGB,IB}} + F_{\text{AGB,OB}}, \tag{3.40}$$

$$T_{eq} = \frac{T_{\text{AGB,IB}}}{17} + \frac{T_{\text{AGB,OB}}}{16}, \tag{3.41}$$

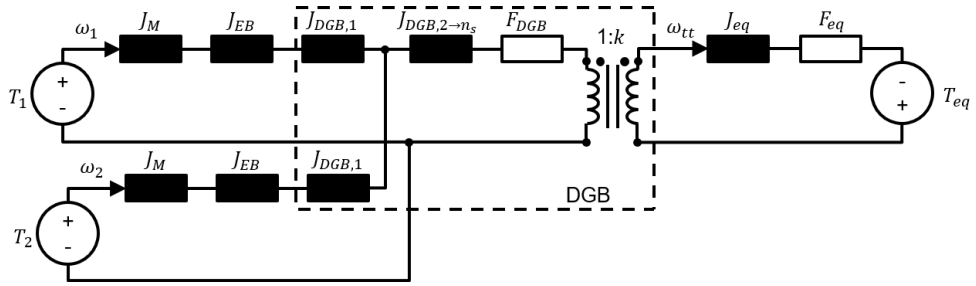


Figure 3.14: Simplified flap actuation mechanical analogous circuit with equivalent low speed side lumped moment of inertia, friction coefficient, and equivalent torque.

$$T_{\text{AGB,IB}}(\theta, \frac{d\theta}{dt}) = -\hat{B}_{\text{AGB,IB}}(\theta, \frac{d\theta}{dt}) - \hat{G}_{\text{AGB,IB}}(\theta) + \hat{F}_{\text{AGB,IB}}(\theta), \tag{3.42}$$

$$T_{\text{AGB,OB}}(\theta, \frac{d\theta}{dt}) = -\hat{B}_{\text{AGB,OB}}(\theta, \frac{d\theta}{dt}) - \hat{G}_{\text{AGB,OB}}(\theta) + \hat{F}_{\text{AGB,OB}}(\theta), \tag{3.43}$$

where:

- J_M is the machine moment of inertia,
- J_{EB} is the electric brake moment of inertia,
- $J_{DGB,1}$ is the first stage moment of inertia of the differential gearbox,
- $J_{DGB,2\to n_s}$ is lumped moment of inertia for remaining stages of the differential gearbox,
- J_{eq}, is the equivalent low speed side moment of inertia,
- F_{DGB} is the friction coefficient of the differential gearbox,
- F_{eq} is the equivalent low speed side friction coefficient,
- k is the differential gearbox gear ratio,
- T_{eq} is the equivalent low speed side load torque which includes flap reaction and gravitational loads.

From this an equivalent linear time invariant transfer function needs to be derived with which a control scheme can be designed. Given a nominal torque tube rotational speed of 25RPM and machine speeds in the range of 1000-8000RPM, the range for differential gear box ratio k is determined to be 40-320. It is observed that J_{eq} and F_{eq} vary as a function of θ but because k is high, the significance of J_{eq} and F_{eq} from the perspective of the differential gear box's high speed side are low. This is demonstrated for a design case of two 1kW machines, nominal 5500RPM connected to a differential gearbox with $k = 220$. The values J'_{eq} and F'_{eq} represent the equivalent differential gear box low speed side moment of inertia and friction coefficient respectively from the perspective of the high speed side as shown,

$$F'_{eq} = F_{eq}/k^2, \tag{3.44}$$

$$J'_{eq} = J_{eq}/k^2. \tag{3.45}$$

The moments of inertia and friction coefficients for this design case are shown in Table 3.4. The maximum lumped moment of inertia on the low-speed side of the differential gearbox reflected from the high-speed side is $J'_{eq(\max)}$. It can be seen that this value is approximately three orders of magnitude smaller than that of the machine's rotor moment of inertia. Similar can be said when comparing F_{DGD} to F'_{eq}, where $F'_{eq} << F_{DGD}$. Because J'_{eq} and F'_{eq} contribute so little to the high speed side total moment of inertia and friction coefficient, they are not accounted for in the control design. This assumption is made for this application where a high gear ratio is required. Only moments of inertia and friction coefficient on the high-speed side, which include J_M, J_{EB}, $J_{DGD,1}$, $J_{DGD,2\leftarrow n_s}$, F'_{DGD} are considered.

Table 3.4: Moments of inertia and friction coefficients from differential gear box's high-speed side for gear box ratio k of 220.

J_M	3.337×10^{-4} kg.m^2	$J_{DGD,2\leftarrow n_s}$	2.143×10^{-6} kg.m^2
J_{EB}	3.408×10^{-5} kg.m^2	$J_{eq(\max)}$	3.59×10^{-2} kg.m^2
$J_{DGD,1}$	0.92×10^{-5} kg.m^2	$J'_{eq(\max)}$	7.417×10^{-7} kg.m^2
F_{DGD}	4.125×10^{-4} Nm.s/rad	F'_{eq}	3.643×10^{-6} Nm.s/rad

Two operating conditions need to be considered from which equivalent transfer functions need to be derived:

1. Nominal operation - both machine 1 and machine 2 are driving T_1 and T_2 at speeds ω_1 and ω_2 respectively. Each machine delivers half of the total required load power. Control effort for each machine is weighted equally, thus $T_1 = T_2 = T_m$ and $\omega_1 = \omega_2 = \omega_m = \omega/(2kk_{act})$, where ω is the crank arm angular speed. The equivalent nominal operation mechanical transfer function $G_{nom}(s)$ is as follows,

$$G_{nom}(s) = \frac{\omega_m(s)}{T_m(s)} = \frac{1}{s\left(\frac{(J_M+J_{EB}+J_{DGB,1})}{2} + J_{DGB,2\leftarrow n_s}\right) + F_{DGB}} \tag{3.46}$$

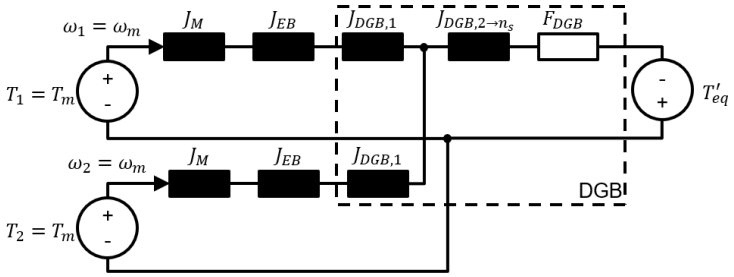


Figure 3.15: Mechanical system representation for nominal operation.

2. Faulted operation - Consider the case where machine 1 is operational and machine 2 is faulted. Machine 2's rotor is locked such that its respective speed remains zero,

$\omega_2 = 0$, and the machine 1 delivers the required load power at torque T_m at speed ω_1 such that $\omega_1 = \omega_m = \omega/(kk_{act})$. The equivalent faulted operation mechanical transfer function $G_{flt}(s)$ is as follows,

$$G_{flt}(s) = \frac{\omega_m(s)}{T_m(s)} = \frac{1}{s\left(J_M + J_{EB} + J_{DGB,1} + J_{DGB,2\leftarrow n_s}\right) + F_{DGB}} \tag{3.47}$$

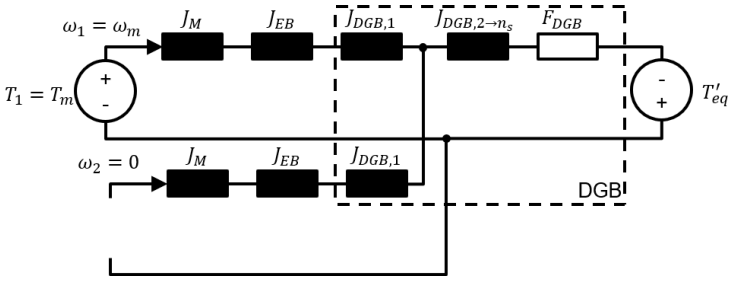


Figure 3.16: Mechanical system representation for faulted operation.

3.3 Failure rate requirements

Airbus has outlined the main slats and flap system failure modes and their respective failure rate limits as follows [36]:

1. Asymmetry: failure rate $<1 \times 10^{-10}$ per flight hour.
   - Asymmetry is when one flap extends further than the other flap on other side of the aircraft. Skew is when inboard and outboard panels do not extend at the same rate.
   - Flap/slat surfaces $\pm 5\%$ travel or else pilot would need to correct with 10% roll control via ailerons.
   - $>\pm 5\%$ variance can cause loss of control.
2. Un-commanded movement: failure rate $<1 \times 10^{-10}$ per flight hour.
   - $\pm 1\%$ flap/slat actuator travel. Related to breakage/erroneous actuator action/sudden control surface movement.
3. Inability to extend/retract flaps/slats: failure rate $<1 \times 10^{-5}$ per flight hour. The flap is fixed in position.
   - On ground failure: aborted take-off.
   - Post take-off: cannot retract flaps; must return to airport.
   - Pre landing: cannot extend flap; emergency landing and require extra runway distance.
   - Post landing: cannot retract; aircraft is grounded for repairs.

4. Incorrect indication to pilot: failure rate $<1 \times 10^{-9}$ per flight hour
    - Not being indicated about correct position of flaps/slats.
    - Can cause pilot to fly the aircraft out of its flight envelope if the erroneous flaps/slats position is assumed correct.

Failure modes 1, 2, and 4 are considered out of the scope of the project as their common root cause of fault, asymmetry, is addressed and managed by the asymmetry sensors and SFCC (slats flaps control computer) operating scheme. For example, the Boeing 777 has asymmetry sensors and indicators for flaps [78]. If flap asymmetry or skew is beyond a certain threshold, flaps are fixed by the electric brake. Failure mode 2 relates to a mechanical failure. Failure mode 4 relates to SFCC and sensor reliability. Failure mode 3 is directly linked to the reliability design constraint of this thesis. The focus of the design is flap actuation, not sensing, avionics, mechanical failures. Failure rates of modes 1, 2, and 4 are orders of magnitude greater than that of 3. The SFCC and sensing are responsible and active for all modes of operation. If the existing technology level SFCC's satisfy the higher reliability conditions of 1, 2, and 4, it will by extension satisfy the lower reliability condition of failure mode 3. Same can be said for actuator structural and mechanical design.

The reliability to extend/retract flaps/slats is greater than 1×10^{-5} failures per flight hour. The failure rate of the slats and flaps are assumed to be equal. The failure rate of the flap system is calculated as 5×10^{-6} per flight hour. The failure rate of each of the four flap systems is assumed to be equal for which a per flap failure rate of 1.25×10^{-6} failures per flight hour is determined. For a duplex-lane-per-flap fault-tolerant system, the per lane failure rate is 2.5×10^{-6} failures per flight hour. A typical medium haul civil aircraft spends 0.55 of the calendar year time flying. To determine Failure In Time (FIT) from the failure per flight hours value, the per lane failure in flight hours reliability value of 2.5×10^{-6} is multiplied by the proportion of flying time for the aircraft (i.e. 0.55), resulting in a value of 1.375×10^{-6} failures per hour, or 1375FIT where 1FIT is equal to 1 failure per 1×10^{9} hours. Thus, 1375FIT is the per-lane reliability design goal for a duplex-lane-per-flap fault-tolerant flap actuation system.

3.4 Conclusion

The problem definition specifications have been outlined in this document. The considered problem is optimal sizing and design of the flap actuation drive system for an Airbus A320-200.

Flaps are a part of an aircraft's high-lift system. The high-lift system allows for increase in both lift and drag of an aircraft, enabling slower landings and take-offs. Flap

actuation operation is intermittent whereby flap position is set and fixed in discrete positions during various stages of take-off and landing.

A distributed flap was proposed where by the actuation of each flap can be independently controlled, allowing for differential flap setting and variable camber. The considered design case was that of the outboard flap and its power requirements was determined to be 1.1kW.

For the actuation of each flap surface, a fault-tolerant, dual-lane, velocity-summing topology is proposed. It consists of two electric machines driven by their respective power electronics and powered from independent sources. Electrical brakes are present on each lane which allows for machine locking when the desired actuation position is reached and mechanical isolation in the event of lane fault. The mechanical output of the two machines drive a differential gearbox, the output of which drives the outboard and inboard rotary flap actuators via a bevel gear box, torque tube, and actuator gearboxes.

The link/track mechanism for the outboard flap of an A320-200 is modelled by a slider/crank mechanism. The kinematic and dynamic model has been derived. Mass estimation of the link/track mechanism's components was completed. Due to the speed reducer's high gear ratios, the reflected side moments of inertia and frictional coefficients from the low speed can be considered negligible compared to that of the high-speed side. Thus, the machine, the electric-brake, and differential gearbox dominate the rotational dynamics of the mechanical system and a simplified mechanical representation was formed.

The mechanical system is represented by an analogous circuit. The parameters were estimated using following scaling laws, based on the assumption of similarity whereby the considered reference component and component under study have the same material properties and dimensional/geometric ratios. These scaling laws were used to estimate the mass, and moment of inertia for single-stage and multi-stage speed reducer gearboxes, and electromagnetic brakes, and torque tubes.

The failure rate requirements were outlined for different failure modes. Failure rate for the inability to extend/retract flaps and slats was set at $< 1 \times 10^{-5}$ per flight hour, from which a per-lane reliability deign goal of 1375FIT was determined for a duplex-lane-per-flap fault tolerant flap actuation system.

Chapter 4

Model and Toolbox Realisation

The design problem has been defined in Chapter 3. This chapter describes how the aforementioned problem is solved. Just like a toolbox is collection of different tools to do different tasks, the presented realised solution is a figurative toolbox, within which is a collection of design procedures and models acting as the figurative tools. The high-level design concept is described. Design procedures and models are realised for different system components and modelling domains. The considered components are inductors, capacitors, heat sinks, semiconductors, electric machine, cable, and gearbox. The subsystems (a collection of components that work together to perform a task) are the inverter, inverter output filter, and EMI input filter. The modelling domains are electrical, electromechanical, power quality, mass, volume, thermal, and failure rate.

4.1 Introduction

4.1.1 High level design concept

The high-level design concepts are as follows. Let's start with the premise that an arbitrary system consists of subsystems and components. The aim is to design the optimal system. To do this, subsystems and components would also need to be optimally sized and designed. The subsystems and components need to be compatible with each other and function together so the system functions as a whole.

Consider the design at a subsystem or component level. Design algorithms are developed for each component and subsystem. Each component and subsystem design algorithm takes a functional definition as its independent input. The functional definition consists of the functional requirement (e.g., force, torque, current, inductance, operating environment, duty cycle) and cost/constraint limits (e.g., failure rate, power quality, geometric/manufacturing accuracy). From the component's inputs, the design algorithm determines all dependent parameter outputs in their domains (i.e., electrical, electromechanical, mass, volume, thermal, failure rate, and power quality, actuation de-

mand) while minimising the subsystem's/component's mass. The dependent parameter outputs are compared with their respective cost/constraint limits. A design is considered feasible if the costs/constraint limits are abided and the functional requirements are met. Thus, a set of mass-minimised feasible candidate designs is generated by the developed design algorithm for each component/subsystem.

Secondly, the mass and failure rates of all mass-minimised feasible candidate designs for a given component/subsystem are compared, from which the set's Pareto frontier is determined. The set of candidate designs is then down selected to only Pareto efficient designs. Thus, sets of mass-minimised feasible Pareto-efficient candidate designs are created for each component and subsystem. These sets act as a catalogue from which the full system design's components and subcomponents are selected from.

Thirdly, consider system level design using proposed design algorithms to generate sets of mass-minimised Pareto-efficient subsystem and component candidate designs. During the creation of the subsystem and component candidate design sets, the functional definition input of the respective component design algorithms have been coordinated at a system level to ensure both mutual compatibility between design sets and satisfaction of system level functionality (e.g., any designed inverter is compatible with any designed output filter, or input filter.) This allows for each subsystems and components' designs from their respective sets to be mixed and matched iteratively to generate every feasible design combination. Each combination's system level mass and failure rate are determined and compared with each other. Optimal system designs are feasible designs of minimum mass within constraints of failure rates.

Finally, the selected optimal system designs are simulated to check if electrical constraints are abided by and control scheme is stable. The relevant simulated voltage waveform's distortion spectrums are checked. Current controller stability is tested by a constant current command as electrical speed ramps from stand still to rated. Finite element analysis is utilised for validation of electromagnetic component designs.

4.1.2 System design steps overview

The sizing and design of one lane of a duplex-lane fault-tolerant system is described. Both lanes are identical. The considered electric drive topologies are centralised and distributed. The centralised topology has a long cable feeder connection between inverter and machine. The distributed topology is where the drive and the machine are both located at the point of actuation. Both topologies consist of a machine, cable, inverter, and inverter input filter. An inverter output filter is required in a centralised system to mitigate transmission line effects, but can be omitted in a distributed system due to the short distance connection between inverter and machine. Input filters and output filters consist of inductors and capacitors. Natural convection finned heat sinks are required for

inverter semiconductor thermal management. The considered component and subsystem design algorithms are for the machine, cable, inverter, inverter LC output filter, inverter EMI input filter, inductors, capacitors, and finned heat sinks. Each step in the design process ultimately leads to determining feasible, inter-compatible, and Pareto-efficient with respect to mass and failure rate designs of components or subsystems.

A basic overview of the per-lane system sizing procedure is shown in Figure 4.1. Key input and output variables for each sub-procedure are listed. Please note it is non-exhaustive list. The variables are as follows,

- T_{nom} - Nominal torque,
- RPM - Machine's rotor's mechanical speed in rotations per minute,
- V_{dc} - DC-link voltage,
- I_{ph} - Machine's phase current,
- f_c - Inverter carrier/switching frequency,
- R_s - Machine's stator resistance,
- L_s - Machine's stator inductance,
- λ_m - Machine's magnetic flux linkage,
- ω_o - Electrical frequency in radians per second,
- p - Number of pole pairs,
- R_c - Cable phase resistance,
- L_c - Cable phase inductance,
- C_c - Cable phase to phase capacitance,
- L_{fil} - Output filter inductance,
- C_{fil} - Output filter capacitance,
- P_T - Inverter's transistor losses,
- P_D - Inverter's diode losses,
- T_j - Inverter's semiconductor junction temperature,
- $\bar{v}_{dq,inv}$ - Inverter output dq voltage,
- $\bar{i}_{dq,inv}$ - Inverter output dq current,
- x_{mac} - Machine,
- x_{cable} - Cable,
- x_{fil} - Output filter,
- x_{inv} - Inverter,
- x_{hs} - Heatsink,
- x_{inv} - Inverter,
- x_{EMI} - Input EMI filter,
- $f(x)$ - Function f of variable x,
- L - Inductor inductance,
- I_L - Inductor current,
- T - Temperature,
- C - Capacitor capacitance,
- V_c - Capacitor voltage,
- V_{ce}/I_C - IGBT collector-emitter voltage to IGBT collect current relationship,
- E_{on}, E_{off} - IGBT on and off switching energy respectively,
- V_F/I_F - Forward diode voltage and forward diode conducting current relationship,
- E_{rr} - Diode reverse recovery energy,
- R_{hs} - Heat sink thermal resistance,
- FIT - Failure in time.

Multiple machine designs are generated from a given functional requirement, defined by its mission profile. These designs are down selected to only Pareto-efficient designs. For each machine design, a gearbox and cable are sized for it. Multiple LC-input filter, inverter, heat-sink, and EMI input filter designs are generated. Mass, volume, and failure rate data for inductors, capacitors, semiconductors, and heat sinks are provided to the LC-

input filter, inverter, heat-sink, and EMI input filter sizing. The inputs for the respective design processes were coordinated at a system level to ensure inter-compatibility between components. Unique combination of components were generated in an iterative serial process. The pseudo code to do this process is shown below. The empty list `sys_list` is created where system designs would be stored. The lists of designed machines, cables, outputs filters, inverters, and EMI input filter are `list_mac`, `list_cable`, `list_fil`, `list_inv`, and `list_emi` respectively. Nested `foreach` loops iterate through each item of each component list. A temporary variable `a_sys` representing a given system design is created to which each component is assigned. The system `a_sys` mass and failure rates are determined by the sum of its components mass and failure rate. This temporary system variable `a_sys` is added to storage list `sys_list`.

```
sys_list = list();
foreach mac in list_mac
  foreach cable in list_cable
    foreach fil in list_fil
      foreach inv in list_inv
        foreach emi in list_emi
          a_sys.mac = mac;
          a_sys.cable = cable;
          a_sys.fil = fil;
          a_sys.inv = inv;
          a_sys.emi = emi;
          a_sys.kg = sum(mac.kg,cable.kg,fil.kg,inv.kg,emi.kg);
          a_sys.fit = sum(mac.fit,cable.fit,fil.fit,inv.fit,emi.fit);
          sys_list.add(a_sys);
```

Unique per-lane system level designs are plotted with respect to mass and failure rate as shown in the "Optimal design selection" box of Figure 4.1. The optimal design is picked and has the minimum mass below a failure rate limit.

The selected Pareto efficient design is then validated and refined, as described in the "Control, validation, and refinement" box of Figure 4.1. The analysis procedures are categorised under "Dynamic modelling, and control", "Power quality","Finite element analysis", and "High-frequency". These steps are not included in the system level optimisation loop due to their relatively high computational effort. The purpose of these steps is to validate the design. For dynamic modelling and control, a gain-scheduled LQR state feedback controller is tuned and tested in a time series simulation with a full electrical system model implemented in Simulink and PLECs software. The outputs of the simulation is dynamic and controller performance, and electrical voltage waveforms from which the power quality is determined. FEA methods are used to validate machine

torque/current relationship, torque ripple, and inductance. High-frequency analysis investigates load side voltages due to inverter switching and transmission line effects. If it was discovered from the validation process that system power quality and machine electromagnetic/electromechanical performance marginally miss their respective design targets, the design can be refined until its respective design targets are met within a satisfactory margin. Passives components in filters maybe re-selected to address power quality issues. Machine geometry can be adjusted to address machine electromagnetic/-electromechanical issues. The manner in which this is done at this stage is at discretion of the designer.

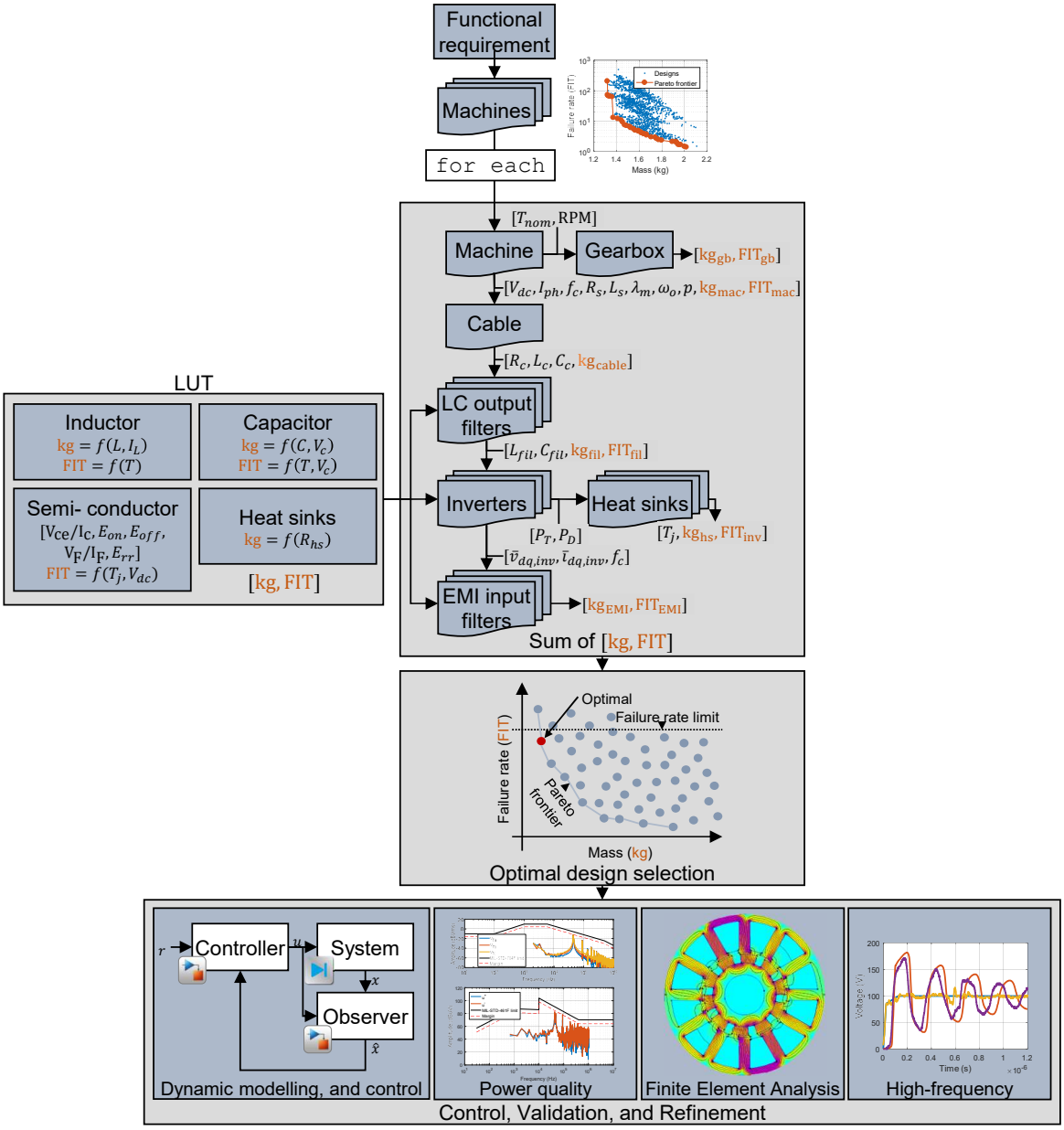


Figure 4.1: System sizing and design process overview.

Component failure rates are determined in section 4.3. Lifetime profile affects the

failure rate of all devices/components. Semiconductor's failure rate are mainly dependent on its operating junction temperature and thermocycling. As junction temperature increases, so too does failure rate. The inductor's failure rate is dependent on its internal temperature, ambient board temperature, and thermocycling. Thermocycling of greater amplitude and higher frequency leads to higher solder joint failure rates by thermal expansion [15]. Capacitor's failure rates are dependent on the ratio between the applied voltage and capacitor's rated voltage, rms current, and operating frequency. Capacitor failure rates increase with applied voltage for a constant rated voltage. Capacitor reliability can be increased with the increase of rated voltage at the expense of mass and volume. Winding insulation failure rate is determined with respect to its operating temperature and lifetime profile.

The overall mass and failure rate of a filter subsystem (e.g., the inverter output filter and EMI input filter) consisting of inductors, capacitors, and semiconductor switches is the contribution of their components' individual mass and failure rates.

The design procedure for passive components is shown in section 4.4. Inductors are designed with respect to inductance, operating current, current density, and operating environment. An increase in either operating current or inductance for the same current density leads to an increase in mass and volume. An increase in current density leads to smaller and lighter components with increased copper losses and higher temperature rise. Capacitors are sized with respect to rated voltage and capacitance. Capacitor's size and volume increases with rated voltage and capacitance.

The enclosure mass and volume sizing procedure is shown in section 4.5. The case mass enclosing inverter output filter (if present), power electronics, and input filter is considered. Larger total volume of components leads to larger and heavier cases.

The machine design procedure is shown in section 4.6. The machine is designed for minimal mass considering torque/speed requirements, minimum current ripple, inverter switching frequency, inverter dc-link voltage, operating environment, current density, and lifetime profile. The machine's phase resistance, phase inductance, and flux linkage constant, stator and rotor diameters, and stack length are determined from the torque/speed requirements, minimum current ripple, inverter switching frequency, inverter DC link voltage and current density. The machine's air gap, stator tooth tip geometry, and magnets are sized for the phase inductance and flux linkage. Knowing the full geometry of the machine and its steady state electrical operating point, copper losses, and core losses are determined. A lumped parameter thermal network is utilised to determine steady state operating temperature. The winding insulation failure rate is determined from the winding temperature and machine's lifetime profile. Thus, the relationship between machine mass and failure rate is determined.

The cable design selection procedure is shown in section 4.7. The cable is selected considering operating environment and required machine phase current. The cable pa-

rameter's phase resistance, phase inductance, phase-to-shield and phase-to-ground capacitance, mass, and dimensions are determined.

The passive LC output filter design procedure is shown in section 4.8. The passive LC inverter output filter is determined for the required harmonic attenuation, maximum allowable inverter output phase current ripple, and minimum mass. The cut-off frequency is selected to provide the required attenuation of inverter switching harmonics such that MIL-STD-704F's distortion spectrum limits for variable frequency systems are not exceeded. The inductor's inductance is determined to ensure the maximum allowable inverter output current ripple is not exceeded. The capacitor's capacitance can then be solved from the filter cut-off frequency and inductor's inductance.

The inverter semiconductor losses and heat sink design procedure is shown in section 4.9. The operating conditions of the inverter power electronics are determined. The operating modulation index, and line current, phase are calculated from the inverter load (i.e., the output filter (if present), cable, and machine). For given semiconductor transistor and diode, the switching and conduction power losses are determined for the operating conditions. Knowing the power losses, the relationship between the junction temperature and heat sink thermal resistance for a given ambient condition is determined. The relationship between failure rate and junction temperature is determined given the inverter's operating environment and lifetime profile. Natural convection finned heat sinks are used for inverter thermal management and are sized for minimum mass considering heat sink base temperature, ambient temperature, and atmospheric pressure. The relation between thermal resistance and heat sink mass is determined from which the relationship between heat sink mass and inverter failure rate can be correlated.

The inverter EMI input filter design procedure is shown in section 4.10. The inverter input filter is designed for MIL-STD-461F EMI requirements, using the inverter's nominal modulation index, nominal output phase current, phase, switching frequency, and switching scheme. The inverter dc link current is calculated analytically, from which the inverter input conducted emissions spectrum is determined in the absence of a filter. This is to determine a baseline from which the required attenuation is calculated. Parameters of a multi-stage LC filter are then calculated to deliver the required attenuation while minimising mass. Knowing the DC-link current draw and the multi-stage LC filter's parameters, the inverter's power leads conducted emissions is solved to check if EMI requirements have been met. Trivially, the inverter input filter's overall mass and failure rate is determined by the contribution of that of its components' individual mass and failure rate.

The current control scheme is presented in Chapter 5. A gain-scheduled LQR state feedback LQR current controller and state observer is implemented for the centralised topology. Gain tuning was done through the minimisation of a closed loop performance dependent cost function by pattern search algorithm. The controllability, stability were

tested in simulation.

Drive-level high frequency modelling is presented in Chapter 6. High-frequency models for the inverter, cable, and machine are presented. High-frequency lumped parameter network models are utilised for the cable and machine. Finite element analysis based methods are used to determine the high-frequency impedance characteristics of the cable and machine.

4.2 MATLAB global optimization toolbox

MATLAB global optimization toolbox was utilised at various points for component level optimisation. The toolbox contains a collection of global heuristic search algorithm solvers to find the solution of multi-variable problems through minimisation of a cost function. The solvers utilised were pattern search, and particle swarm. [79] compares different solvers from MATLAB's global optimization tool in terms of robustness, precision, calculation effort, and implementation difficulty. It provides example MATLAB code for each of different solvers. The two methods from this toolbox were used; pattern search, and particle swarm optimisation. Detailed analysis and these methods is beyond the scope of this thesis.

Pattern search is direct search numerical optimisation method. The algorithm for general pattern search is described in [80]. The merits of this algorithm is that it is derivative-free and doesn't require the cost function to be continuous or linear. Pattern search was utilised to determine the required stator tooth tip and magnet geometry to achieve desired stator inductance and magnetic flux linkage in section 4.6.8.3. This is done by minimisation of a cost error function defined in (4.156). Pattern search was also utilised for gain tuning of an LQR current controller through minimisation of a performance cost function defined by (5.57) in section 5.4.1.2.

Particle swarm optimisation is population based algorithm inspired by the social interaction of flock of birds or a school of fish. The basis of its algorithm can be found in [81]. The merits of this algorithm is that it is derivative-free and doesn't require the cost function to be continuous or linear. It was utilised to fit parameters of a per-phase high-frequency permanent machine model in a least squared manner to measured differential-mode and common-mode impedance data in section 6.4.5, by minimisation of the cost error function defined by (6.39).

4.3 Failure rate

4.3.1 General Model for electrical and electronic components

Predicted failure rates are determined in units of FIT where 1FIT is one failure per 10^9 calendar hours.

The failure rate of a non-redundant system λ_{system} is the sum of its components' failure rates. A non-redundant system in this context means if any one of its components fails, the system as a whole will fail. The proposed fault-tolerant duplex-lane actuation topology is considered redundant because if one lane fails, the other remaining lane can still drive the actuation. However, each lane is non-redundant if considered independently as any failure of any lane's components ultimately leads to failure of the lane.

$$\lambda_{\text{product}} = \sum_{\text{Item}} \lambda_{\text{item}}. \tag{4.1}$$

FIDES guide 2009 general reliability model is utilised to calculate the failure rate of discrete semiconductors, capacitors, and inductors [15]. All of the failure rate equations in sections 4.3.1 to 4.3.4 have been taken directly from FIDES guide 2009 [15]. The failure rate λ is expressed with respect to physical contributions $\lambda_{\text{Physical}}$, manufacturing quality and control contribution factor Π_{PM}, and development and usage process quality contribution Π_{Process}.

$$\lambda = \lambda_{\text{Physical}} \Pi_{\text{PM}} \Pi_{\text{Process}}. \tag{4.2}$$

To determine $\lambda_{\text{Physical}}$, per phase failure rates first need to evaluated. Components would experience different phases throughout the year, representing different periods of operation states. A phase of index "i" is period of time with constant failure rate $\lambda_{\text{phase-i}}$ due to the same condition being maintained through said phase. A lifetime profile is used to represent these phases throughout a calendar year. The physical contribution $\lambda_{\text{Physical}}$ is the time-weighted sum of all phases where 8760 presents the number of hours in a year,

$$\lambda_{\text{Physical}} = \sum_{i}^{\text{Phases}} \left(\frac{\text{Hours per year of phase-i}}{8760} \lambda_{\text{phase-i}} \right). \tag{4.3}$$

This is to account for deterioration and wear of components through the calendar year, including periods when it is not operational and is in storage or idle.

The per phase physical contribution in failure rate $\lambda_{\text{phase-i}}$ is the weighted sum of physical contribution stress accelerating factors temperature λ_{TH}, temperature cycling λ_{TCy}, humidity λ_{RH} and vibration λ_{Mech},

$$\lambda_{\text{phase-i}} = \left(\lambda_{\text{TH}} + \lambda_{\text{TCy}} + \lambda_{\text{RH}} + \lambda_{\text{Mech}}\right)_i \left(\Pi_{\text{induced}}\right)_i. \tag{4.4}$$

The calculation of $\lambda_{\text{Physical}}$ for capacitors and inductors is shown in section 4.3.3, and for discrete semiconductors in section 4.3.4.

The manufacturing quality and control contribution factor Π_{PM} is determined as follows,

$$\Pi_{\text{PM}} = e^{1.39(1-\text{Part\_Grade})-0.69} \tag{4.5}$$

where,

$$\text{Part\_Grade} = \frac{((\text{QA}_{\text{manufacturer}} + \text{QA}_{\text{component}}) \times f_{\text{xp}})}{24} \tag{4.6}$$

The values $\text{QA}_{\text{manufacturer}}$ and $\text{QA}_{\text{component}}$ represents manufacturer and component quality assurance levels respectively and f_{xp} represents component buyer's experience with their supplier. QA represents the components position relative to the state of the art when on a scale of 0 (much lower) to 3 (higher). A higher value of QA leads to a higher value of Part_Grade, and a lower value of Π_{PM}. Here, both $\text{QA}_{\text{manufacturer}}$ and $\text{QA}_{\text{component}}$ are set to 2, for equivalent level to state of the art. Experience factor f_{xp} varies from 1 to 4, where 4 represents component recognised reputable manufacturer with a matured process and 1 represents component from manufacturer with previous product disqualifications. Here, f_{xp} is set to 3, representing recognised manufacturer but process has not yet matured.

Finally, the term Π_{Process} represents the technical and quality control over reliability in the product life cycle and ranges from 1 (best case) to 8 (worst case). The default value of 4 was used as it was not evaluated. Further detail related to Π_{PM} and Part_Grade can be found in sections 1.8 and 1.9 of [15].

4.3.2 Lifetime profile

The typical life profile and environmental conditions in a medium haul civil aircraft avionics bay is provided by FIDES guide 2009, as shown in Table 4.1 for a calendar year [15]. The "On/off" column has been adjusted from the original lifetime profile as flap actuation only occurs during "Ground - taxiing" and "Flight - climb/descent" phases.

Table 4.1: Medium haul civil aircraft internal avionics bay lifetime profile [15].

Index (i)	Phase title	Calendar time (h)	On/off	Ambient temp. (C)	RH (%)	ΔT (°C)	Cycles/year	Cycle duration (h)	Max temp. during cycling (C)
1	Ground operation (on/off)	700	Off	40	30	25	350	2	40
2	Ground - operation (stopover)	1400	Off	55	30	15	700	2	55
3	Ground - taxiing	630	On	40	10	0	2100	0.3	40
4	Flight - climb/descent	1050	On	40	10	0	1050	1	40
5	Stable - flight	3150	Off	40	10	0	1050	3	40
6	Ground - dormant	1830	Off	15	70	10	365	5.01	20

Index (i)	Phase title	Random vibrations (Grms)	Saline pollution	Environmental pollution	Application pollution	Protection level	Π application	Equivalent altitude (ft)
1	Ground operation (on/off)	0.05	Low	Moderate	Moderate	Non-hermetic	4.8	0
2	Ground - operation (stopover)	0.05	Low	Moderate	Moderate	Non-hermetic	2	0
3	Ground - taxiing	5	Low	Low	Moderate	Non-hermetic	1.2	0
4	Flight - climb/descent	0.6	Low	Low	Moderate	Non-hermetic	1.1	8000
5	Stable - flight	0.6	Low	Low	Moderate	Non-hermetic	1.1	8000
6	Ground - dormant	0	Low	Moderate	Low	Non-hermetic	3.3	0

FIDES guide 2009 does not explicitly provide lifetime profile for components operating in the wing for a medium haul civil aircraft. It does provide a lifetime profile for external stores of multi-role fighter aircraft. A medium haul civil aircraft external stores lifetime profile is inferred by combining the phases, calendar hours, on/off periods, cycles/year, and cycle duration values of Table 4.1 with the ambient temperature, relative humidity, thermal cycling amplitude, maximum cycling temperature, random vibrations, saline, environmental, and application pollution, protection level, and $\Pi_{\text{Application}}$ of external stores multi-role fighter aircraft lifetime profile. Comparing the lifetime profiles of Table 4.1 and 4.2, the $\Pi_{\text{Application}}$ in the external stores profile is much higher, leading to higher failure rates for components operating in this environment.

Table 4.2: Inferred medium haul civil aircraft external stores lifetime profile [15].

Index (i)	Phase title	Calendar time (h)	On/off	Ambient temp. (C)	RH (%)	ΔT (C)	Cycles/year	Cycle duration (h)	Max temp. during cycling (C)
1	Ground operation (on/off)	700	off	35	20	20	350	2	40
2	Ground - operation (stopover)	1400	off	35	20	20	700	2	35
3	Ground - taxiing	630	on	35	20	0	2100	0.3	0
4	Flight - climb/descent	1050	on	35	20	0	1050	1	0
5	Flight - stable	3150	off	-2	10	37	1050	3	35
6	Ground - dormant	1830	off	15	70	10	365	5.01	20

Index (i)	Phase title	Random vibrations (Grms)	Saline Pollution	Environmental Pollution	Application Pollution	Protection level	Π application	Equivalent altitude (ft)
1	Ground operation (on/off)	0.05	Low	Moderate	Moderate	Non-hermetic	4.8	0
2	Ground - operation (stopover)	0.5	Low	Moderate	moderate	Non-hermetic	4.8	0
3	Ground - taxiing	8	Low	Moderate	Moderate	Non-hermetic	5	0
4	Flight - climb/descent	8	Low	Low	Moderate	Non-hermetic	5	20000
5	Flight - stable	4	Low	Low	Moderate	Non-hermetic	5	40000
6	Ground - dormant	0	Low	Moderate	Low	Non-hermetic	4.4	0

4.3.3 Capacitor and Inductor

All equations in this section have been taken directly from [15]. The general equation for capacitors and inductors predicted failure rate λ is as follows,

$$\lambda = \lambda_{\text{Physical}} \Pi_{\text{PM}} \Pi_{\text{Process}}. \tag{4.7}$$

The expression for physical applied stress contribution $\lambda_{\text{Physical}}$ is as follows where $\Pi_{\text{TH-EL}}$, Π_{TCy}, Π_{Mech} represent thermal-electrical, thermal-cycling, and mechanical stress acceleration factors respectively,

$$\lambda_{\text{Physical}} = \lambda_0 \sum_{i}^{\text{Phases}} \left(\frac{t_{\text{annual}}}{8760} \right)_i \left(\Pi_{\text{TH-EL}} + \Pi_{\text{TCy}} + \Pi_{\text{Mech}} \right)_i \left(\Pi_{\text{Induced}} \right)_i . \tag{4.8}$$

The capacitor thermal-electrical stress acceleration factors $\Pi_{\text{TH-EL,Cap}}$ is a function of applied voltage V_{applied}, rated voltage V_{rated}, reference level of electrical stress S_{ref}, activation energy Ea, and ambient board temperature $T_{\text{board ambient}}$. The term γ represents

the corresponding basic stress acceleration factor value and can be found in Table 4.3,

$$\Pi_{\text{TH-EL,Cap}} = \gamma_{\text{TH-EL,Cap}} \left(\frac{1}{S_{\text{ref}}} \times \frac{V_{\text{applied}}}{V_{\text{rated}}} \right)^3 e^{11604 \times Ea \times \left(\frac{1}{293} - \frac{1}{T_{\text{board ambient}} + 273} \right)}. \tag{4.9}$$

$\Pi_{\text{TH-EL,Cap}} = 0$ for non-operation phase(s).

The inductor thermal-electrical stress acceleration factors $\Pi_{\text{TH-EL,Ind}}$ is as follows where $T_{\text{board ambient}}$ is the ambient board temperature and ΔT is the component's temperature relative to ambient during operation,

$$\Pi_{\text{TH-EL,Ind}} = \gamma_{\text{TH-EL,Ind}} e^{11604 \times Ea \times \left(\frac{1}{293} - \frac{1}{T_{\text{board ambient}} + \Delta T + 273} \right)}. \tag{4.10}$$

$\Pi_{\text{TH-EL,Ind}} = 0$ for non-operation phase(s).

The thermal cycling accelerating factor Π_{TCy} is as follows where $N_{\text{annual-cy}}$ is number of cycles of the considered phase per year, t_{annual} is the total number of hours per year of the considered phase, θ_{cy} is the per cycle duration in hours, $\Delta T_{\text{cycling}}$ is amplitude in temperature variation for the phase in °C, and $T_{\text{max-cycling}}$ is the maximum temperature achieved during cycling in °C,

$$\Pi_{\text{TCy}} = \gamma_{\text{TCy}} \left(\frac{12 N_{\text{annual-cy}}}{t_{\text{annual}}} \right) \left(\frac{\min(\theta_{\text{cy}}, 2)}{2} \right)^{1/3} \left(\frac{\Delta T_{\text{cycling}}}{20} \right)^{1.9} e^{1414 \left(\frac{1}{313} - \frac{1}{T_{\text{max-cycling}} + 273} \right)}. \tag{4.11}$$

The mechanical stress acceleration factor is as follows where G_{rms} is the associated stress from random vibration,

$$\Pi_{\text{Mech}} = \gamma_{\text{Mech}} \left(\frac{G_{\text{rms}}}{0.5} \right)^{1.5}. \tag{4.12}$$

The induced overstress failure contributing factors Π_{Induced} is calculated for each phase as follows,

$$\Pi_{\text{Induced}} = (\Pi_{\text{Placement}} \Pi_{\text{Application}} \Pi_{\text{Ruggedising}})^{(0.511 \log(C_{\text{sensitivity}}))}, \tag{4.13}$$

where placement contributing factor $\Pi_{\text{Placement}}$ is 2.5 for analogue power interface function, application contributing factor $\Pi_{\text{Application}}$ can be found in the lifetime profile for a given phase. A default value of 1.7 is set for the ruggedising contributing factor $\Pi_{\text{ruggedising}}$ as it is not fully evaluated. Inherent overstress sensitivity factor $C_{\text{sensitivity}}$ values are found in Table 4.3.

Parameters for inductor and capacitor predicted failure rate calculations are shown in Table 4.3 for dry tantalum capacitor with axial metal packaging, and wire wound power inductors for basic failure rate λ_0, reference level of electrical stress S_{ref}, contribution sensitivity factor $C_{sensitivity}$, basic stress acceleration factors $\gamma_{\text{TH-EL}}$, γ_{TCy}, γ_{Mech},

for thermoelectric, thermocycling, and mechanical respectively, temperature rise ΔT and activation energy Ea.

Table 4.3: Parameters for inductor and capacitor predicted failure rate calculation.

Component	λ_0	$\gamma_{\text{TH-EL}}$	γ_{TCy}	γ_{Mech}	ΔT (°C)	S_{ref}	$\text{C}_{\text{sensitivity}}$	Ea (eV)
Dry tantalum capacitor axial metal packaging	0.25	0.94	0.04	0.02	N/A	0.4	6.95	0.15
Wirewound power inductor	0.05	0.09	0.79	0.12	30	N/A	8.05	0.15

4.3.4 Discrete semiconductors

The general equation for discrete semiconductors predicted failure rate λ is the same as shown in (4.2). The equations for this section were taken from [15]. The physical applied stress contribution $\lambda_{\text{Physical}}$ expression for discrete semiconductors is as follows,

$$\lambda_{\text{Physical}} = \sum_{i}^{\text{Phases}} \left(\frac{t_{\text{annual}}}{8760}\right)_i \left(\lambda_{\text{TH}} + \lambda_{\text{TCy}} + \lambda_{\text{RH}} + \lambda_{\text{Mech}}\right)_i \left(\Pi_{\text{induced}}\right)_i . \tag{4.14}$$

where

$$\lambda_{\text{TH}} = \lambda_{0\text{TH}} \Pi_{\text{Thermal}} \tag{4.15}$$

$$\lambda_{\text{TCy}} = \lambda_{0\text{TCycase}} \Pi_{\text{TCycase}} + \lambda_{0\text{TCysolder}} \Pi_{\text{TCysolder}} \tag{4.16}$$

$$\lambda_{RH} = \lambda_{0RH} \times \Pi_{RH} \tag{4.17}$$

$$\lambda_{Mech} = \lambda_{0Mech} \times \Pi_{Mech} \tag{4.18}$$

The terms λ_0 represent base failure rate while Π represents the acceleration factor.

The thermal-electrical stress acceleration factor is a function of junction temperature T_j in °C for power transistors,

$$\Pi_{\text{Thermal}} = e^{11604 \times 0.7 \times \left(\frac{1}{293} - \frac{1}{T_j + 273}\right)} \tag{4.19}$$

The thermal cycling stress acceleration factor considers both thermal cycling of the case Π_{TCycase} and of the solder $\Pi_{\text{TCysolder}}$,

$$\Pi_{\text{TCycase}} = \left(\frac{12 N_{\text{annual-cy}}}{t_{\text{annual}}}\right) \left(\frac{\Delta T_{\text{cycling}}}{20}\right)^4 e^{1414\left(\frac{1}{313} - \frac{1}{T_{\text{max-cycling}} + 273}\right)} \tag{4.20}$$

$$\Pi_{\text{TCysolder}} = \left(\frac{12 N_{\text{annual-cy}}}{t_{\text{annual}}}\right) \left(\frac{\min(\theta_{\text{cy}}, 2)}{2}\right)^{1/3} \left(\frac{\Delta T_{\text{cycling}}}{20}\right)^{1.9} e^{1414\left(\frac{1}{313} - \frac{1}{T_{\text{max-cycling}} + 273}\right)} \tag{4.21}$$

The mechanical and relative humidity acceleration factors, Π_{Mech} and Π_{RH}, are as follows where $\text{RH}_{\text{ambient}}$ is the ambient relative humidity in percentage,

$$\Pi_{\text{Mech}} = \left(\frac{G_{\text{rms}}}{0.5}\right)^{1.5}, \tag{4.22}$$

$$\Pi_{\text{RH}} = \left(\frac{\text{RH}_{\text{ambient}}}{70}\right)^{4.4} e^{11604\times 0.9\times\left(\frac{1}{293}-\frac{1}{(T_{\text{board ambient}}+273)}\right)}. \tag{4.23}$$

The induced overstress failure contributing factors Π_{Induced} is calculated in the same manner as (4.13). The contributing factor $\Pi_{\text{Placement}}$ and $\Pi_{\text{ruggedising}}$ were set to 2.5 and 1.7 respectively. The $C_{\text{sensitivity}}$ value is 5.2 for discrete semiconductors.

Parameters for discrete semiconductor basic failure rate calculation is found in Table 4.4. The basic failure rate for silicon carbide MOSFETs is not included in the FIDES but is assumed to be equal to that of silicon MOSFETs.

Table 4.4: Parameters for discrete semiconductor predicted failure rate calculation [15].

Case	$\lambda_{0\text{RH}}$	$\lambda_{0\text{TCycase}}$	$\lambda_{0\text{TCysolder}}$	$\lambda_{0\text{Mech}}$	Power transistors	λ_{0TH}
TO220	0.0589	0.00303	0.01515	0.0003	Silicon bipolar >5W	0.0478
D3PAK	0.0335	0.00413	0.02065	0.00041	Silicon MOS >5W	0.0202
ISOTOP	0.99	0.03333	0.16665	0.0033	IGBT	0.3021

Note the basic failure rate λ_{0TH} of IGBT's is an order of magnitude higher compared to silicon bipolar and silicon MOSFET. [82] determined the failure rate of the IGBT as the OR-gate combination of the silicon bipolar and silicon MOSFET. The basic failure rates for a low power silicon MOSFET, a silicon bipolar >5W, and a rectifying diode >3A from FIDES are 0.0145FIT, 0.0478FIT, and 0.1574FIT respectively. When N elements (e.g. diodes, transistors, etc.) are combined into a single case, the basic failure rate needs to be scaled by $\sqrt{(N)}$. Substituting the three failure rates and scaling the sum by $\sqrt{3}$ gives a calculated basic failure rate of 0.38FIT for an IGBT. This values is greater than the quoted IGBT failure rate of 0.3021FIT from Table 4.4 but is in the same order of magnitude. The IGBT failure rate from FIDES is what will be used going forward.

4.3.5 Insulation failure rate

The insulation lifetime L in hours operating at temperature T (in K) is as follows,

$$L = Ae^{\left(\frac{B}{T}\right)}, \tag{4.24}$$

where values A and B are characteristic constants of the insulation.

If the insulation is at a temperature T_i for a phase i of Δt_i hours duration per calendar

year, the proportion of the total insulation's lifetime m_i consumed by phase i is,

$$m_i = \frac{\Delta t_i}{L(T_i)} = \frac{\Delta t_i}{Ae^{(B/T_i)}}. \tag{4.25}$$

Insulation can experience different phases of operation throughout the year as described by its lifetime profile. Consider determining the failure in time of insulation for an electric machine. The operation of the machine is described by its lifetime profile. Assume the insulation reaches the machine winding's steady state for the entirety of its "on" phases. Assume the insulation is at ambient temperature during its "off" phases. Thus, the per phase insulation lifetime proportion consumption is determined using (4.25).

The total proportion of the lifetime consumed per calendar year M is thus the sum of the proportion consumption of all phases m_i,

$$M = \sum_{i}^{\text{Phases}} m_i. \tag{4.26}$$

The total lifetime hours is determined by inverting M and scaling by the number of hours for a year,

$$L_t = \frac{8760}{M}. \tag{4.27}$$

To determine insulation failure rate λ in units of FIT, L_t is inverted and scaled by 10^9,

$$\lambda = \frac{1}{L_t} \times 10^9. \tag{4.28}$$

Insulation constants A and B of (4.24) have been determined in a least square manner for a commercial class 200 polyester/polyamideimide coated winding wire as shown in Figure 4.2. The constants fitted were $A = 5.898{\times}10^{-17}$, and $B = 2.297{\times}10^4$. It can be observed that if temperature increases by 10°C, lifetime is approximately halved.

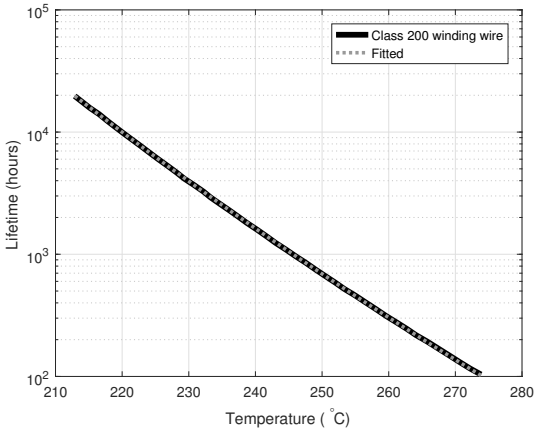


Figure 4.2: Commercial class 200 polyester/polyamideimide coated winding wire lifetime vs. temperature [20].

4.3.6 Results

The predicted failure rate of a dry tantalum capacitor with axial metal packaging vs. applied/rated voltage ratio is shown in Figure 4.3. As the applied/rated voltage ratio increases, failure rates increase. Failure rates of components in the external environment is higher than that of the internal for the same applied/rated voltage ratio. For the same operating voltage, the failure rate can be reduced by increasing the rated voltage.

The predicted failure rates of a power inductor with temperature rise ΔT of 30°C for internal and external lifetime profile of Table 4.1 and 4.2 are 18.67FIT and 54.98FIT respectively.

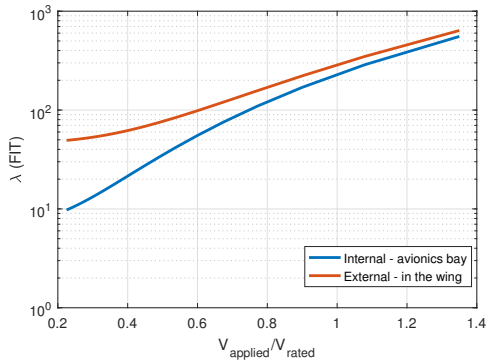


Figure 4.3: Dry tantalum capacitor with axial metal packaging predicted failure rate vs. applied over rated voltage ratio for internal and external lifetime profiles of Table 4.1 and 4.2.

The predicted failure rate of a discrete semiconductor vs. junction temperature is shown in Figure 4.4. The considered component is silicon MOSFET with a D3pack case. The considered lifetime profiles are the internal avionics bay and external - in the wing as shown in Tables 4.1 and 4.2 respectively. As temperatures increase, failure rates increase. Failure rates of components in the external environment is higher than that of internal for the same junction temperature.

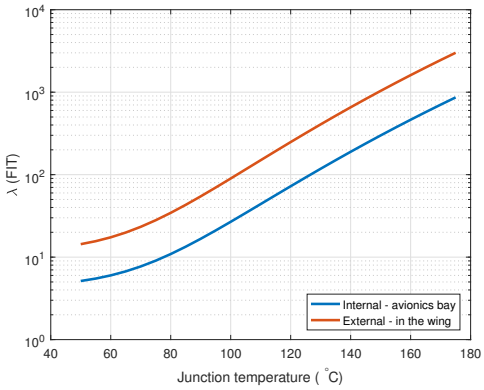


Figure 4.4: D3pack silicon MOSFET discrete semiconductor predicted failure rate vs. junction temperature for internal and external lifetime profiles of Table 4.1 and 4.2.

The insulation predicted failure rate has been determined with respect to operating temperature for external stores lifetime profile of Table 4.2 as shown in 4.5. The considered insulation is the commercial 200 class winding wire. The x-axis temperature corresponds to the "on" phases' insulation temperature of Table 4.2. During the "off" phases, insulation temperature is equal to that of ambient.

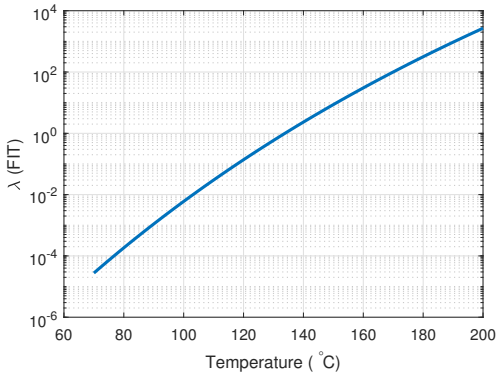


Figure 4.5: Commercial 200 class winding wire insulation predicted failure rate with respect to operating temperature for external stores lifetime profile of Table 4.2.

These calculated failure rate values for inductors, capacitors, discrete semiconductors, and winding wire insulation for internal and external lifetime profiles are used to determine subsystem-level and system-level failure rates going forward.

4.4 Passive component sizing

4.4.1 Inductor - static and low band

In this section, the fundamental inductor equations and design steps are presented. Using these equations and steps, an algorithm is realised to optimally design inductors with minimal mass within a maximum temperature rise. This algorithm is then used to generate a look-up table of inductor designs. This look-up table is then utilised at system level design to reduce computation demand. The key steps and procedures are listed below:

1. The core geometry and ratios are defined.
2. The magnetic operating point and coil parameters are determined considering core geometry, material magnetic properties, and gap fringing effect.
3. The copper losses and core losses are calculated from the coil parameters and magnetic operating point respectively.
4. The temperature rise is determined considering heat transfer by natural convection and radiation to ambient.
5. The mass and volume are determined.

6. An inductor is designed for minimal mass. A discrete set of core dimension and gap length combinations is created for which a corresponding inductor is designed. A preliminary optimal feasible inductor design of minimal mass is selected from a discrete set of design cases. This design is then improved with the use of bisection method.
7. A inductor design look-up table is generated from which system level design processes can pull inductor design data from, reducing computational load.

More information relating to each of these steps is found in the successive subsections.

4.4.1.1 Geometry

Inductors are sized based on methods outlined in [21], assuming an EI core as shown in Figure 4.6 with fixed geometric ratios,

$$E = D, \tag{4.29}$$

$$A_c = D^2, \tag{4.30}$$

$$\frac{W_a}{A_c} = 0.789, \tag{4.31}$$

$$G/F = 3, \tag{4.32}$$

$$F = \sqrt{\frac{W_a}{G/F}}, \tag{4.33}$$

$$\text{length} = 2(F + E), \tag{4.34}$$

$$\text{width} = D + F, \tag{4.35}$$

$$\text{height} = G + E, \tag{4.36}$$

$$A_t = 2(\text{length} \times \text{width} + \text{width} \times \text{height} + \text{height} \times \text{length}). \tag{4.37}$$

where W_a is the window area, A_c is core cross sectional area and A_t is equivalent external surface area. Thus, only D is required to define all of the core's dimensions.

The area product A_p is shown as follows where f_f is the core material fill factor,

$$A_p = \frac{W_a}{A_c}\left(\frac{A_c}{f_f}\right)^2. \tag{4.38}$$

The mean length per turn MLT and mean magnetic path length MPL are follows,

$$\text{MLT} = 4(D + F), \tag{4.39}$$

$$\text{MPL} = 2(E + G + F). \tag{4.40}$$

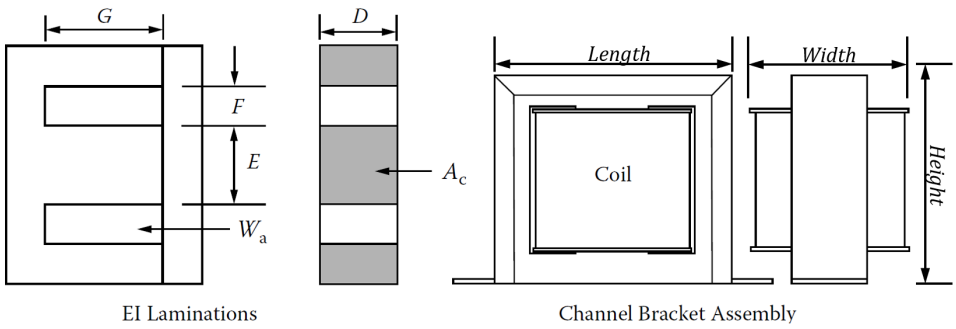


Figure 4.6: EI inductor core and coil assembly [21].

4.4.1.2 Magnetic operating point

The fringing factor F_r which accounts for the fringing flux at the air gap of length l_g is as follows,

$$F_r = 1 + \frac{l_g}{\sqrt{A_c}} \log\left(\frac{2G}{l_g}\right). \tag{4.41}$$

Consider core magnetic permeability μ_m varies with respect peak flux density B_{pk} as shown in Figure 4.7 for different materials. The number of turns N is a function of the peak magnetic flux B_{pk} as shown where L is the desired inductance and μ_0 is the magnetic permeability of free space,

$$N(B_{pk}) = \text{round}\left(\sqrt{\frac{L(l_g + \frac{\text{MPL}}{\mu_m(B_{pk})})}{(\mu_0 A_c F_r)}}\right) \tag{4.42}$$

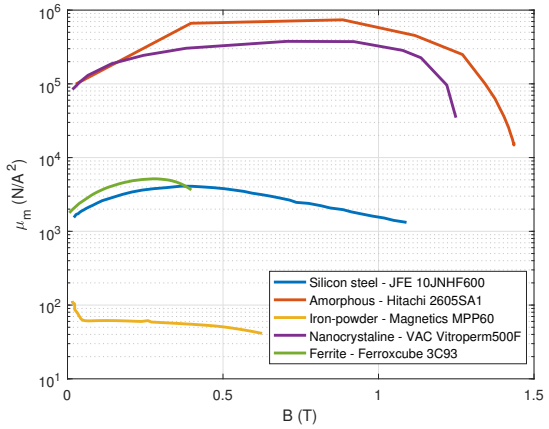


Figure 4.7: Core material magnetic permeability μ_m vs. flux density B.

The peak flux density B_{pk} is expressed with respect to turns as a function of peak flux density $N(B_{pk})$, peak current I_{pk}, and core magnetic permeability as function of peak flux density $\mu_m(B_{pk})$,

$$B_{pk} = \frac{F_r \mu_0 I_{pk} N(B_{pk})}{l_g + \frac{\text{MPL}}{\mu_m(B_{pk})}}, \tag{4.43}$$

where peak current I_{pk} is,

$$I_{pk} = I_{dc} + \frac{\Delta I}{2} \text{for dc inductors,} \tag{4.44}$$

$$I_{pk} = I_o + \frac{\Delta I}{2} \text{for ac inductors.} \tag{4.45}$$

I_{dc} is the average current, and ΔI is the ripple current for a dc inductor. I_o is the first harmonic's peak current, and ΔI is the ripple current of an ac inductor. Equation (4.42) is substituted into (4.43) to give the following expression,

$$B_{pk} = \frac{F_r \mu_0 I_{pk}}{l_g + \frac{\text{MPL}}{\mu_m(B_{pk})}} \text{round} \left(\sqrt{\frac{L(l_g + \frac{\text{MPL}}{\mu_m(B_{pk})})}{(\mu_0 A_c F_r)}} \right), \tag{4.46}$$

which is solved numerically for peak flux density B_{pk}.

Due to conductor number rounding by (4.42), the achieved inductance L' may not match that of the desired L. It is important to check this value as calculated from the rounded number of conductors,

$$L' = \frac{F_r \mu_0 N^2 A_c}{l_g + \frac{\text{MPL}}{\mu_m(B_{pk})}}. \tag{4.47}$$

The absolute relative inductance error with respect to desired inductance L_Δ is as follows,

$$L_\Delta = \text{abs} \left(\frac{L' - L}{L} \right). \tag{4.48}$$

4.4.1.3 Losses

The per wire copper cross sectional area A_{cu} is determined as follows for the copper fill factor $K_u = 0.4$,

$$A_{cu} = \frac{K_u W_a}{N}. \tag{4.49}$$

The inductor's phase resistance is determined where σ_{cu} is copper's electrical conductivity,

$$R_L = \frac{N\text{MLT}}{A_{cu}\sigma_{cu}}. \tag{4.50}$$

Proximity effects were not taken into consideration when calculation inductor's phase resistance.

The copper losses is determined for phase current I_{rms} as,

$$P_{cu} = I_{rms}^2 R_L. \tag{4.51}$$

For DC inductors, the ac flux density ripple B_{ac} due to current ripple ΔI is determined

as follows assuming $\mu_m(B_{pk}) \cong \mu_m(B_{pk} - B_{ac})$,

$$B_{ac} = \frac{\mu_0 N F_r \left(\frac{\Delta I}{2}\right)}{l_g + \frac{\text{MPL}}{\mu_m(B_{pk})}}. \tag{4.52}$$

Core loss P_{core} in units of watts for a core of volume $V_{\text{core,cm}^3}$ in cm^3 is determined using the Steinmetz equation with material constants k, α, and β,

$$P_{core} = V_{\text{core,cm}^3} k f^{\alpha} B_{ac}^{\beta} \times 10^{-3}. \tag{4.53}$$

The Steinmetz parameters for different core materials are shown in Table 4.5.

Table 4.5: Core material properties [28].

Index	Material type	Manufacturer	Name	B_s (T)	Density (g/cm^3)	f_f	k (mW/cm^3)	α	β
1	Silicon-steel	JFE	10JNHF600	1.87	7.53	0.9	0.05147	1.26	1.91
2	Amorphous	Hitachi	2605SA1	1.56	7.18	0.83	0.04668	1.67	1.79
3	Iron-powder	Magnetics	MPP60	0.75	8.2	1	0.10975	1.34	2.16
4	Nanocrystalline	VAC	Vitroperm500F	1.2	7.3	0.7	0.00347	1.71	2.09
5	Ferrite	Ferroxcube	3C93	0.5	4.8	1	0.00175	2.26	3.07

The core loss for ac inductors is determined as follows. It is assumed that the significant harmonics of the flux density are induced by the fundamental oscillating current I_o at a frequency f_o and the ripple current ΔI due to inverter switching at the carrier frequency f_c,

$$B_{ac}(t) = B_o \sin(2\pi f_o t) + B_c \sin(2\pi f_c t). \tag{4.54}$$

The Steinmetz equation is utilised to determine the core loss contribution of each of these harmonics,

$$P_{core} = V_{\text{core,cm}^3} K (f_o^{\alpha} B_o^{\beta} + f_c^{\alpha} B_c^{\beta}) \times 10^{-3}. \tag{4.55}$$

The total losses P_t are the sum of copper and core losses,

$$P_t = P_{core} + P_{cu}. \tag{4.56}$$

4.4.1.4 Thermal

Assuming an isothermal inductor, the total heat transfer rate q from itself to ambient is the sum of radiation q_r and convection q_c,

$$q = q_r + q_c = \epsilon \sigma A_t (T_s^4 - T_a^4) + h_c A_t (T_s - T_a), \tag{4.57}$$

where ϵ is the surface emissivity, $\sigma = 5.67 \times 10^{-8}$ $\text{W/m}^2\text{K}^4$ is the Stefan–Boltzmann constant, T_s is the surface temperature (K) and T_a is ambient temperature (K), and h_c is

the convective heat transfer coefficient, and A_t is the total surface inductors outer surface area.

An empirical equation for heat transfer coefficient h_c has been derived and provided by [83],

$$h_c = C\left(\frac{p}{p_{ref}}\right)^{0.477}\left(\frac{T_a}{T_{a,ref}}\right)^{-0.218}\left(\frac{(T_s - T_a)^{0.225}}{L_h^{0.285}}\right), \tag{4.58}$$

where C is equal to 1.53 for horizontal orientation, p is ambient atmospheric pressure (in pascals), p_{ref} is atmospheric pressure at sea level, $T_{a,ref}$ is 293.15K, and L_h is the considered hydraulic length,

$$L_h = \text{height} \times \text{width}. \tag{4.59}$$

Equation (4.58) shows convective heat transfer coefficient reduces with a decrease in ambient pressure and an increase in ambient temperature.

At thermal steady state, total power loss P_t is equal to total heat transfer rate from inductor to ambient q. Equation (4.58) is substituted into (4.57) and equated with (4.56) to give the following expression for which the solution T_s is numerically determined,

$$0 = -P_t + \epsilon\sigma A_t(T_s^4 - T_a^4) + C\left(\frac{p}{p_{ref}}\right)^{0.477}\left(\frac{T_a}{T_{a,ref}}\right)^{-0.218}\left(\frac{(T_s - T_a)^{0.225}}{L_h^{0.285}}\right)A_t(T_s - T_a). \tag{4.60}$$

The temperature rise T_r is calculated as the difference between T_s and T_a.

4.4.1.5 Mass and volume

The expressions for core volume V_{core} and copper volume V_{cu} are as follows,

$$V_{core} = 2D((F + E)(GE) - W_a), \tag{4.61}$$

$$V_{cu} = N(\text{MLT})A_{cu}. \tag{4.62}$$

The total inductor mass M_L is as follows where ρ_{core} and ρ_{cu} are the core and copper densities,

$$M_L = \rho_{core}V_{core} + \rho_{\text{cu}}V_{\text{cu}}. \tag{4.63}$$

The "box" volume considered for case volume calculations is as follows,

$$V_L = \text{height} \times \text{width} \times \text{length}. \tag{4.64}$$

4.4.1.6 Inductor mass minimisation

The design guideline is to minimise the inductor's mass for desired inductance, fundamental current, and ripple current while ensuring temperature rise T_r does not exceed a maximum $T_{r,\max}$ of 30°C, L_Δ is less than a threshold $L_{\Delta,\max}$, and peak flux density B_{pk}

does not exceed material's saturating flux density B_s.

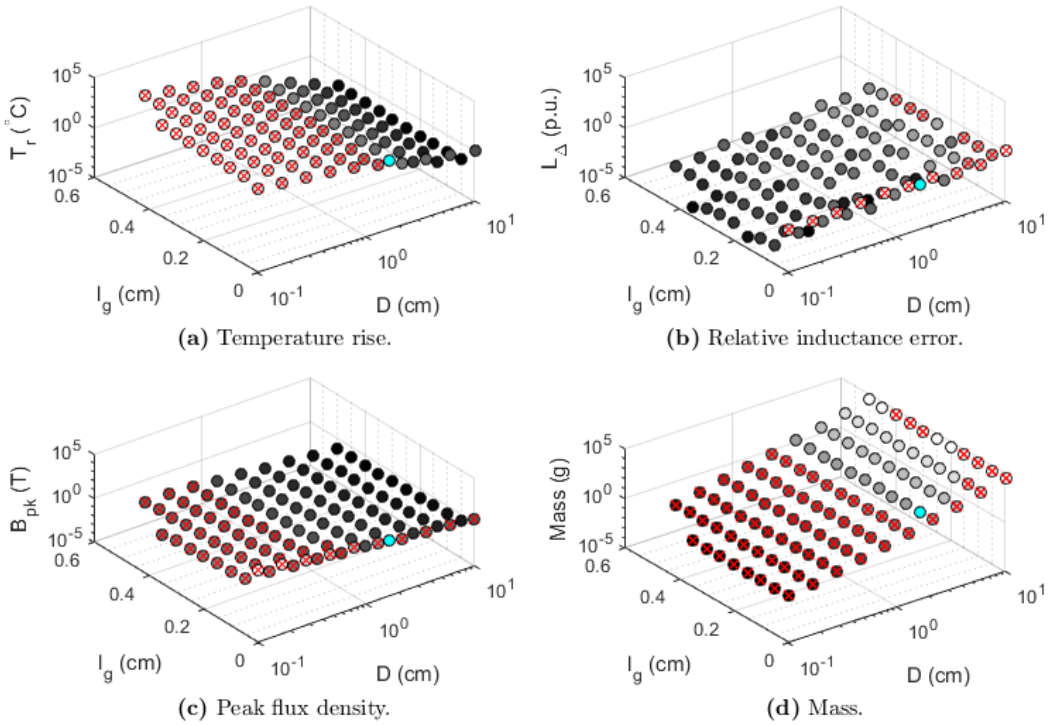
Assume desired inductance, fundamental current, and ripple current have been given. A set of core dimension D_i and gap length $l_{g,j}$ values, where i and j are the parameters' respective indexes, is created. The remaining core dimensions can be derived from 4.29 - 4.37. Each combination of $(D_i, l_{g,j})$ represents a unique candidate design for which its corresponding mass $M_L(D_i, l_{g,j})$, temperature rise $T_r(D_i, l_{g,j})$, absolute relative inductance error $L_\Delta(D_i, l_{g,j})$ and peak flux density $B_{pk}(D_i, l_{g,j})$ are calculated using procedure of Section 4.4.1.1 to 4.4.1.5. All designs with $T_r > T_{r,\max}$, $L_\Delta > L_{\Delta,\max}$, and $B_{pk} > B_s$ are removed from the set, after which the design of minimum mass is selected from the remaining designs. The selected design of minimum mass $(D_i, l_{g,j})$ is improved. Gap length $l_{g,j}$ is fixed while core dimension D is iterated between D_i and D_{i-1}, where $D_{i-1} < D_i$, using the bisection method. A feasible solution of minimum mass exists where T_r approaches $T_{r,\max}$.

This calculation process is demonstrated by sizing a 1mH inductor for I_{dc} = 5A, ΔI = 0.5A, and f_c = 15kHz, and amorphous core. A 10 x 10 grid on $(D_i, l_{g,j})$ values is created for which T_r, L_Δ, B_{pk}, and mass were determined as shown in Figure 4.8. Lighter shade data point markers represents higher values while darker shade represents lower. Each dataset $T_r(D_i, l_{g,j})$, $L_\Delta(D_i, l_{g,j})$, and $B_{pk}(D_i, l_{g,j})$ are checked with respect to their limits. The conditions for feasible designs are as follows: $T_r < 30°$C, $L_\Delta < 0.05$p.u., and $B_{pk} < 1.87$T. Any data points exceeding their respective limits is marked with a red "×" and are considered infeasible. The remaining feasible designs are left unmarked as shown in Figure 4.8 (d), out of which the design of lowest mass is selected and highlighted with a cyan (light blue) dot. This data point will be known as the "grid calculated minimum" design.

The grid calculated minimum design of Figure 4.8 is further improved by iterating D using the bisection method as shown in Figure 4.9. As the number of iterations increase, the temperature approaches that of the limit of 30°C. A comparison between the grid calculated minimum design and the bisection method improved design is shown in Table 4.6. Core dimension D has reduced from 2.154cm to 1.396cm. Overall mass has reduced from 400.79g to 142.89g. Temperature rise has increased from 5.06°C to 30.0°C.

Table 4.6: Inductor design parameter comparion for L = 1mH, I_{dc} = 5A, ΔI = 0.5A, f_c = 15kHz, T_{amb} = 40°C, altitude = 20,000ft, grid calculated minimum and bisection method improved.

	D (cm)	L_Δ (p.u.)	N	M_L (g)	T_r (°C)
Grid calculated minimum	2.154	0.0179	46	400.79	5.06
Bisection method improved	1.396	0.00051	51	142.89	30



(a) Temperature rise. **(b)** Relative inductance error. **(c)** Peak flux density. **(d)** Mass.

Figure 4.8: Inductor design process illustration of a 1mH inductor I_{dc} = 5A, ΔI = 0.5A, f_c = 15kHz, T_{amb} = 40°C, altitude = 20,000ft, amorphous core. Lighter shade markers represent higher values. Red "×" represents infeasible designs whose parameters exceed their respective limits. Feasible design of minimum mass is highlighted with a cyan (light blue) dot.

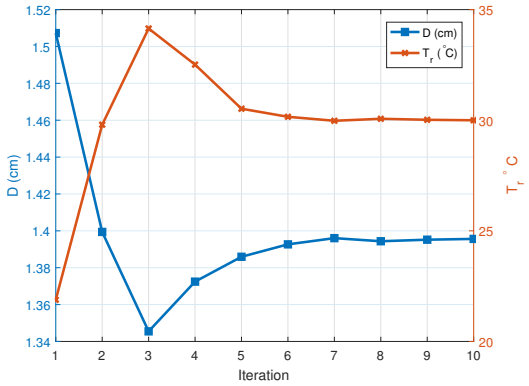


Figure 4.9: Bisection method iteration values of inductor dimension D with respect to calculated temperature rise T_r.

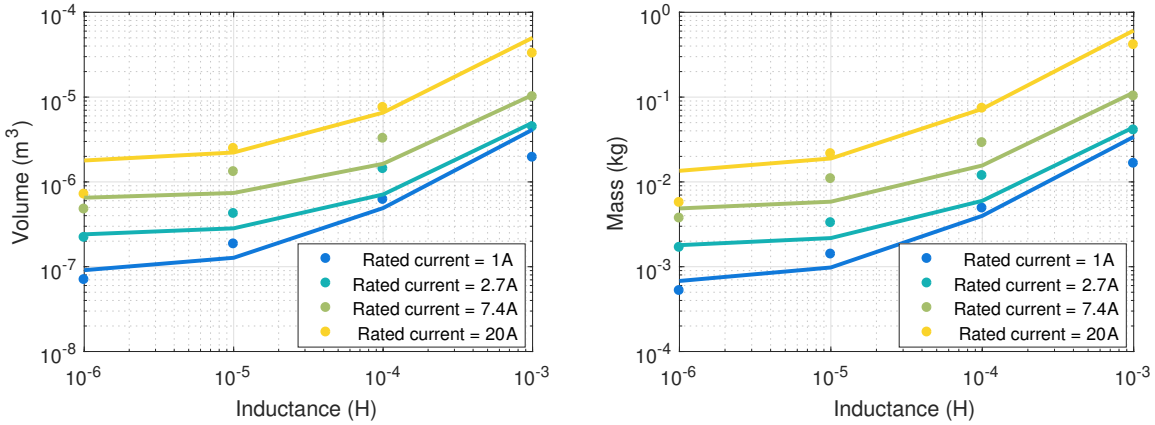
4.4.1.7 Empirical fitting and inductor look up table generation

Empirical equations for inductor volume V_L and mass M_L as a function of inductance L and rated current $\hat{I}_{in}$ have been provided by [84],

$$V_L(L, \hat{I}_{in}) = k_{L1} L \hat{I}_{in}^2 + k_{L2} L + k_{L3} \hat{I}_{in}, \tag{4.65}$$

$$M_L(L, \hat{I}_{in}) = m_{L1} L \hat{I}_{in}^2 + m_{L2} L + m_{L3} \hat{I}_{in}, \tag{4.66}$$

where k_{L1} and k_{L2} are volume constants and m_{L1} and m_{L2} are mass constants for fitting. An example of this fitting can be seen in Figure 4.10.



(a) Volume. **(b)** Mass.

Figure 4.10: Empirical curve fitting for inductor volume vs. inductance and current. Dots represent specific designed point, line represents empirical equation fit. Inductor specification: f_c = 15kHz, current ripple= 10%, T_{amb} = 40°C, altitude = 20,000ft, temperature rise = 30°C, amorphous core.

A look-up table of inductor volume and mass constants k_{L1}, k_{L2}, k_{L3} and m_{L1}, m_{L2}, m_{L3} for a range of switching frequencies, ambient temperature, environmental equivalent altitude, and material has been created using the inductor sizing procedure described. A portion of this look up table is shown in Table 4.7.

Table 4.7: Inductor volume and mass empirical equation constants look up table sample.

Inputs				Outputs					
Core material	T_a (°C)	Altitude (ft)	f_c (Hz)	k_{L1} ($\frac{m^3}{HA^2}$)	k_{L2} ($\frac{m^3}{H}$)	k_{L3} ($\frac{m^3}{A}$)	m_{L1} ($\frac{kg}{HA^2}$)	m_{L2} ($\frac{kg}{H}$)	($\frac{kg}{A}$)m_{L3}
			...	...	...	...	...	...	...
Amorphous	40	8000	15000	1.29×10^{-5}	9.31×10^{-3}	1.37×10^{-7}	2.65×10^{-1}	9.21×10^{1}	1.26×10^{-3}
			30000	1.29×10^{-5}	9.33×10^{-3}	1.37×10^{-7}	2.66×10^{-1}	9.25×10^{1}	1.26×10^{-3}
			45000	1.27×10^{-5}	9.03×10^{-3}	1.75×10^{-7}	2.62×10^{-1}	8.72×10^{1}	1.89×10^{-3}
			60000	1.27×10^{-5}	9.08×10^{-3}	1.75×10^{-7}	2.64×10^{-1}	8.78×10^{1}	1.89×10^{-3}
			75000	1.27×10^{-5}	9.14×10^{-3}	1.75×10^{-7}	2.65×10^{-1}	8.85×10^{1}	1.89×10^{-3}
			90000	1.51×10^{-5}	8.89×10^{-3}	1.67×10^{-7}	3.20×10^{-1}	8.18×10^{1}	1.70×10^{-3}
...	...	...	...	...	...	...	...	...	...

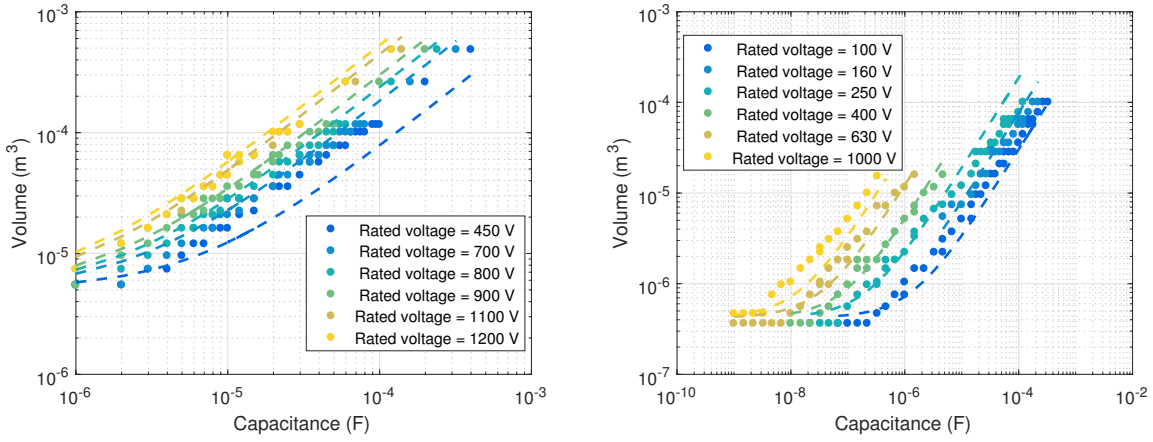
4.4.2 Capacitor - static and low band

Empirical equations for capacitor volume V_C as a function of capacitance C and rated voltage $\hat{U}_{in}$ have been provided by [84],

$$V_C(C, \hat{U}_{in}) = k_{C1} C \hat{U}_{in}^2 + k_{C2}, \tag{4.67}$$

where k_{C1} and k_{C2} are constants for fitting.

Two different sets of k_{C1}, k_{C2} values were determined for two different ranges of capacitors in a least square manner. For constant rated voltage, volume increases with capacitance. For constant capacitance, volume increases with rated voltage. The calculated constants are shown in Table 4.8. The data sheet values from [85] [86] and the calculated values are plotted in Figure 4.11.



(a) Vishay MKP1848. **(b)** Vishay MKT1820.

Figure 4.11: Empirical curve fitting for capacitor volume vs. capacitance and voltage for commercial capacitors capacitor range.

Table 4.8: Empirical fitted capacitor volume equation constants k_{C1} and k_{C2}.

Manufacturer	Name	k_{C1}	k_{C2}
Vishay	MKP1848	3.6329×10^{-6}	5.0137×10^{-6}
Vishay	MKT1820	2.9855×10^{-5}	4.2108×10^{-7}

To determine the capacitor's mass, their volume is multiplied by their density. The average density for both capacitor dataset is 1069.15kg/m^3.

4.5 Enclosure volume and mass - static band

An enclosure is required to house the input filter, inverter, and output filter (if present). The estimated case volume is the sum of the enclosed component's respective volumes, multiplied by a scaling factor k_{case},

$$V_{case} = k_{case} \sum V_{components}. \tag{4.68}$$

Here, a case scale factor of 2.5 is estimated from an in-house demonstrator inverter as shown in Figure 4.12.

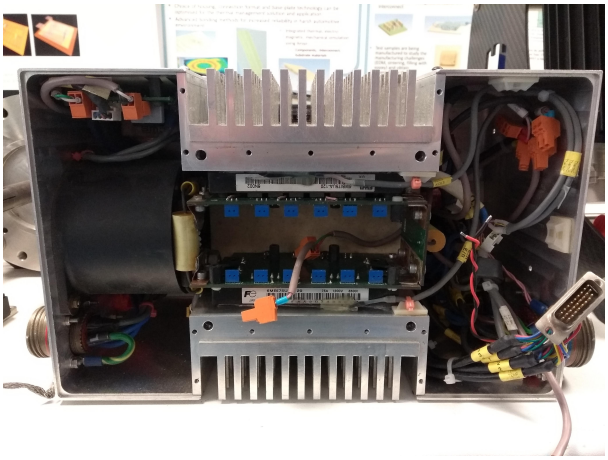


Figure 4.12: Demonstrator inverter internal view.

Consider a case with the following geometric ratios as shown in Figure 4.13. The case mass for this geometry M_{case} is,

$$M_{case} = \rho_{alu} 16 \left(\frac{V_{case}}{4} \right)^{\frac{2}{3}} t_{case}, \tag{4.69}$$

where ρ_{alu} is the density of aluminium and t_{case} is the case thickness, equal to 3mm.

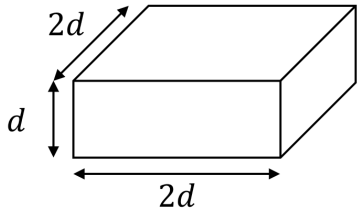


Figure 4.13: Inverter case dimensions.

4.6 Machine - static and low band

The surface mounted permanent magnet synchronous machine design process is presented in this section. The author has published the majority of the utilised procedure in [87]. The analytical algorithm generates candidate machine designs for electrical, electromechanical, material, and geometric specifications. The design procedure is divided into four mains sections,

- Initial stator and rotor sizing,
- Phase resistance R_s, phase inductance L_s, and magnetic flux λ_m linkage calculation,
- Air-gap, magnet, and tooth-tip sizing,
- Thermal calculation.

The following assumptions are made for the design process:

- Three-phase, outer-stator, inner-rotor, surface-mounted permanent magnets, non-salient, machine is considered.
- The permeability of the stator and rotor cores compared to that of air is considered infinite when determining stator inductance and magnet operating point.
- Magnetic saturation is not considered. The machine material is assumed and designed to operate in the linear B-H region.
- No forced cooling is utilised.

The full machine design process is divided into "System-level" and "Detailed". "System-level" encompasses initial stator and rotor sizing and calculation of electrical parameters R_s, L_s, and λ_m. "Detailed" includes air-gap, magnet, and tooth-tip sizing, and thermal calculations. The full stator, rotor, winding geometry is drawn up and the machine's electromagnetic properties and operating point is analysed using FEA. The machine design process outputs are shown in Table 4.9. This division is for the benefit of system-level designer reader who are concerned only with macroscopic drive level parameters.

Table 4.9: Machine design process outputs.

Parameter	System-level	Detailed
Mass/Volume	✓	✓
Phase resistance R_s	✓	✓
Phase inductance L_s	✓	✓
Magnetic flux linkage λ_m	✓	✓
Rotor moment of inertia	✓	✓
Losses and power factor	✓	✓
Tooth tip geometry		✓
Magnet geometry		✓
Air gap thickness		✓
Thermals		✓

4.6.1 Specification

The surface mounted permanent magnet machine design procedure's input specifications are grouped under the following categories:

- Mechanical - Nominal mechanical output power P_o, nominal operating speed RPM,
- Material - Density ρ, conductivity σ.
- Geometry ratio - slot number N_{sl}, pole number N_p, coil shortening n_r, rotor diameter to stack length aspect ratio x, slot tooth width to slot pitch ratio τ.
- Electrical - average flux density across the air gap B, current density J, switching carrier frequency f_c, torque per rotor volume TRV, slot fill factor F_{slot}, inverter dc link voltage V_{dc}, phase current I_{ph}.
- Magnet core - B-H curve, density Steinmetz properties k, α, β.

- Permanent magnet - Remnant reluctance B_r, relative recoil permeability μ_{rec}, intrinsic coercivity H_{cj}, density ρ.

These parameters need to be pre-defined before the design procedure can be executed.

4.6.2 Slot/pole combination selection

The slot/pole combination (i.e. the number of slots and poles) greatly influences the electromechanical characteristics of the machine. Reference [88] describes the effects of pole count and slot count on brushless machine's radial force, cogging torque, and back EMF. Zero net radial force on a rotor occurs when,

$$\gcd(N_p, N_s l) > 1, \tag{4.70}$$

where "gcd" stands for greatest common denominator. For $N_p = 10$, and $N_{sl} = 12$, the greatest common denominator is 2. Thus, radial forces are minimised. Minimising radial forces will minimise bearing loads and increase bearing longevity.

The least common multiple (lcm) between the $N_p, N_s l$ effects the cogging torque. As this value increases, the cogging torque decreases [89]. Thus, a high value of $\text{lcm}(N_p, N_s l)$ is desired. Cogging torque is the worst for integer slot pitch combination, i.e. when the value of N_{sl}/N_p is an integer [88].

Reference [90] has determined the winding factor amplitudes and back-EMF harmonics for different slot/pole combinations. The calculated data was utilised to make an informed choice on appropriate slot/pole combinations for low back-EMF harmonics and winding factor amplitudes

A fractional slot arrangements where $\gcd(N_p, N_s l) > 1$ and high value is $\text{lcm}(N_p, N_s l)$ is chosen. The advantages of fractional slot windings have been well documented in [91]. These include, short-end turns, high-power density, and fault tolerance due to phase separation for concentrated winding arrangements. The considered slot/pole combinations are 12/10 and 12/14.

4.6.3 Stator and rotor sizing

The considered machine dimensions and geometry are shown in Figure 4.14.

Fundamental electrical machine sizing equations have been provided by [29]. The average current density A around the air gap circumference is as follows for phase number m, number of turns per phase N_{ph}, and rotor diameter D,

$$A = \frac{2mN_{ph}I_{ph}}{\pi D}. \tag{4.71}$$

The magnet loading B is defined as the average flux density over the rotor surface and

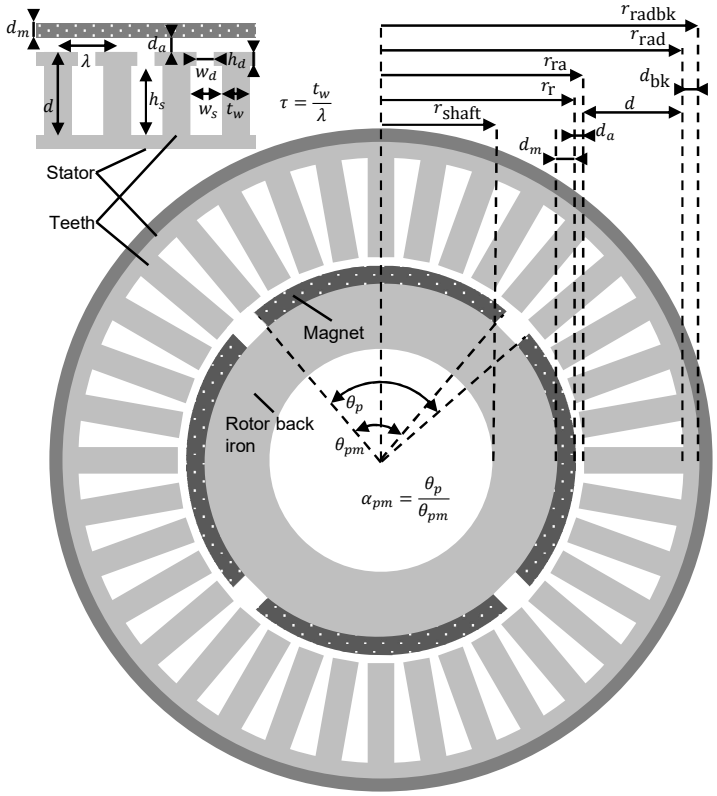


Figure 4.14: Permanent magnet synchronous machine dimensions.

is expressed for the stack length L_{stk}, fundamental component of the air gap flux linkage ϕ_1, and number of pole pairs p.

$$B = \frac{2p\phi_1}{\pi D L_{stk}}. \tag{4.72}$$

The per phase back-EMF E is expressed as follows for fundamental electrical frequency f_o, fundamental harmonic winding factor k_{w1},

$$E = \frac{2\pi}{\sqrt{2}} k_{w1} N_{ph} \phi_1 f, \tag{4.73}$$

The torque per rotor volume TRV can be expressed with respect to A, B, and rotor volume V_R for an ac machine,

$$\text{TRV} = \frac{T}{V_r} = \frac{\pi}{\sqrt{2}} k_{w1} AB. \tag{4.74}$$

Typical values for TRV have been provided by [29] and is shown in Table 4.10.

The slot fill factor F_{slot} is the ratio between cross sectional area of copper conductor compared to slots. The ratio of slot tooth width t_w to slot pitch λ is expressed by the variable τ. The current density J is expressed as shown with respect to F_{slot}, slot depth

Table 4.10: Typical values of torque per rotor volume and current densities (continuous operation) [29].

Class of machine	**TRV (kNm/m^3)**
Small totally-enclosed motor (Ferrite magnets)	7 - 14
Totally-enclosed motors (sintered rare earth or NdFeB)	14 - 42
Integral-hp industrial motors	7 - 30
High-performance servomotors	15 - 50
Aerospace machines	30 - 75
Condition	**J (A/mm^2)**
Totally-enclosed	1.5 - 5
Air-over, fan-cooled	5 - 10
Liquid cooled	10 - 30

d, and τ,

$$J = \frac{A}{F_{slot} d(1-\tau)}. \tag{4.75}$$

Typical values for current densities for available cooling conditions have been provided by [29] and is shown in Table 4.10.

The fundamental winding factor k_{w1} is the product of the fundamental pitch factor k_{p1}, distribution factor k_{d1}, and are expressed as follows [92],

$$k_{w1} = k_{p1} k_{d1}, \tag{4.76}$$

$$k_{p1} = \sin\left(\frac{y_Q - n_r}{y_Q}\frac{\pi}{2}\right), \tag{4.77}$$

$$k_{d1} = \frac{2\sin(\frac{\pi}{6})}{\frac{N_{sl}}{3p}\sin(\frac{\pi p}{N_{sl}})}. \tag{4.78}$$

The full pitch slot count y_Q is equal to the N_{sl}/N_p. The pitch shortening in number of slots is represented by n_r.

For a given TRV value, stack length, and rotor aspect ratio $x_r = L_{stk}/D$; the rotor volume V_r and diameter D are calculated. The relationship between the average magnetic loading B and the peak tooth magnet flux $B_{t(pk)}$ is as follows,

$$B = \frac{2\tau B_{t(pk)}}{\pi} \tag{4.79}$$

Typical values of $B_{t(pk)}$ is 1.6T and for $\tau = 0.5$, this gives $B \approxeq 0.5$. (4.74) is solved for A, giving

$$A = \frac{TRV\sqrt{2}}{\pi k_{w1} B}. \tag{4.80}$$

(4.71) is solved for N_{ph}, giving the following,

$$N_{ph} = \frac{A\pi D_r}{6 I_{ph}}. \tag{4.81}$$

Slot depth d is calculated from (4.75) giving the following expression,

$$d = \frac{A}{JF_{slot}(1-\tau)}. \tag{4.82}$$

Typical slot fill factor value is 0.4 [29].

The back-iron depth d_{bk} is expressed as follows,

$$d_{bk} = \frac{3N_{sl}}{N_p} t_w. \tag{4.83}$$

The stator dimensions r_{ra}, r_{rad}, and r_{radbk} are determined. An initial value of 1mm is set for the air gap d_a but will be corrected.

4.6.4 Windings, conductors, and stator resistance

Next, the stator windings need to be defined to determine the per phase stator resistance R_s. The total cross-sectional area (CSA) of copper $A_{cu(total)}$ is calculated from the product of F_{slot} with the slot's CSA A_{slots},

$$A_{cu(total)} = F_{slots} A_{slots}. \tag{4.84}$$

$$A_{slots} = \pi(r_{rad}^2 - r_{ra}^2) - N_{sl} d t_w, \tag{4.85}$$

The per conductor copper CSA $A_{cu(wire)}$ is determined,

$$A_{cu(wire)} = \frac{A_{cu(total)}}{(6N_{ph})}. \tag{4.86}$$

The maximum diameter of wire consisting of insulation and conductor assuming square packing pattern d_{wire} is expressed as follows. This value needs to be considered when determining the minimum value of the slot opening width w_d.

$$d_{wire} = \frac{d_{cu(wire)}}{2} \sqrt{\frac{\pi}{F_{slot}}} \tag{4.87}$$

Total length of wire for each phase l_{ph} is determined as follows for the per-turn mean end winding length for semi-circular end winding path l_{end} and pitch shortening in number of slots n_r [93],

$$l_{ph} = N_{ph}(l_{end} + 2L_{stk}). \tag{4.88}$$

$$l_{end} = \left(\frac{\pi^2}{2N_{sl}}\right)\left(1 - \frac{n_r N_p}{N_{sl}}\right)(r_{ra} + r_{rad}). \tag{4.89}$$

The stator resistance R_s can now be determined knowing the conductor's total length

and wire copper cross-sectional area,

$$R_s = \frac{l_{ph}}{\sigma_{cu} A_{cu(wire)}}, \tag{4.90}$$

where σ_{cu} is the copper electrical conductivity.

4.6.5 Operating point, stator inductance, and magnetic flux linkage

The steady state dq voltage equations in the synchronous reference frame for a non-salient surface mounted permanent magnet synchronous machine (SMPMSM) are as follows for d- and q- axis currents i_d and i_q , the d- and q- axis voltages v_d and v_q, d- and q- axis flux linkages λ_d and λ_q , permanent magnet flux linkage λ_m, and electrical speed $\omega_o = 2\pi f_o$. For a non-salient SPMSM, it is assumed that d- and q-axis stator inductances are equal such that $L_s = L_d = L_q$,

$$v_d = R_s i_d - \omega_o L_s i_q, \tag{4.91}$$

$$v_q = R_s i_q + \omega_o L_s i_d + \omega_o \lambda_m. \tag{4.92}$$

$$\lambda_d = L_s i_d + \lambda_m \tag{4.93}$$

$$\lambda_q = L_s i_q \tag{4.94}$$

$$|\lambda_{dq}| = \sqrt{\lambda_d^2 + \lambda_q^2} \tag{4.95}$$

The voltage and current magnitudes $|v_{dq}|$ and $|i_{dq}|$ are as follows,

$$|v_{dq}| = \sqrt{v_d^2 + v_q^2}, \tag{4.96}$$

$$|i_{dq}| = \sqrt{i_d^2 + i_q^2} = \sqrt{2} I_{ph}. \tag{4.97}$$

The relationship between mechanical speed ω_m and ω_o is follows,

$$\omega_o = \omega_m p, \tag{4.98}$$

The electromechanical torque T_{em} is,

$$T_{em} = \frac{3p}{2} \lambda_m i_q. \tag{4.99}$$

The voltage limit V_{max} need to taken into consideration and is expressed as follows

for linear modulation (i.e. modulation index $m \leq 1$),

$$V_{max} = \frac{V_{dc}}{2} \geq |v_{dq}|. \tag{4.100}$$

The machine's operating range is represented on the dq current axis as shown in Figure 4.15. The area enclosed by the blue arrows mark the dq current operating range. The voltage ellipses are marked by dotted lines. Typically, a current limit (represented by a circle) is imposed by the current control scheme to avoid excess machine copper losses and/or protect the power electronics. Compare the size of the voltage ellipse at electrical speed ω_o and ω_o^+ where $\omega_o < \omega_o^+$. As electrical speed increases, the voltage ellipse size decreases, limiting the current operating range. Torque is directly proportional to i_q as described by (4.99). Field-weakening is required during voltage limited operation to extend the operating range of the machine. This is done by injecting negative i_d which in turn reduces λ_d. The maximum required d-axis field weakening current can be solved by taking (4.93), setting $\lambda_d = 0$, and solving for i_d. The nominal operating point assumes no field-weakening (i.e., $i_d = 0$). The dq voltage equations (4.91-4.92) are simplified to,

$$v_d = -\omega_o L_s i_q, \tag{4.101}$$

$$v_q = R_s i_q + \omega_o \lambda_m. \tag{4.102}$$

The relationship between RMS phase current I_{ph} and i_q is simply,

$$i_q = \sqrt{2} I_{ph} \text{ for } i_d = 0. \tag{4.103}$$

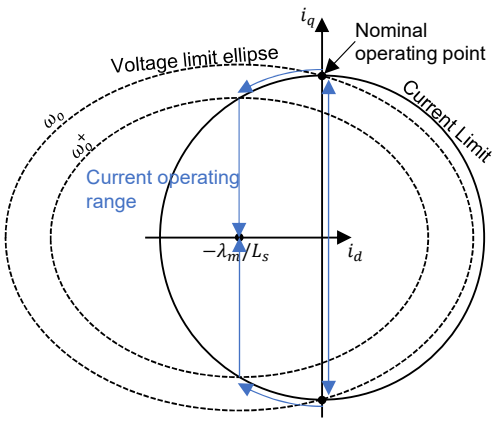


Figure 4.15: Non-salient permanent magnet synchronous machine's operating range represented on the dq current axis.

The desired stator inductance L_s is determined for a desired current ripple ΔI due to

switching at frequency f_c,

$$L_s = \frac{V_{dc}}{\pi^2 f_c \Delta I}. \tag{4.104}$$

The variable c for desired current ripple ratio is defined as,

$$c = \frac{\Delta I}{i_q} \tag{4.105}$$

Equation (4.105) is expressed with respect to ΔI and substituted into (4.104) to get an expression of L_s with respect to V_{dc}, f_c, c, and i_q,

$$L_s = \frac{V_{dc}}{\pi^2 f_c c i_q}. \tag{4.106}$$

The torque equation (4.99) is rearranged to get an expression of λ_m with respect to i_q and T_{em},

$$\lambda_m = \frac{2T_{em}}{3pi_q}. \tag{4.107}$$

Equations (4.104) and (4.107) are substituted into (4.101) and (4.102) and then into voltage limit equation (4.100) to get an expression of $|v_{dq}|$ as a function of i_q,

$$|v_{dq}| = \sqrt{\left(- \omega_o \frac{V_{dc}}{\pi^2 c i_q f_c} \right)^2 + \left(R_s i_q + \omega_o \frac{2T_{em}}{3pi_q} \right)^2}. \tag{4.108}$$

4.6.6 Mass

After determining dimensions of the stator, rotor, and windings; their respective mass is determined, given the material densities as seen in Table 4.11. The general equation for mass M_X of component "X" (e.g. stator core) is as follows, where ρ_X is the component's material density, CSA_X is its cross sectional area and l_X is its length.

$$M_X = \rho_X l_X \mathrm{CSA}_X. \tag{4.109}$$

The total mass of the copper conductor M_{cu} is determined in a similar manner,

$$M_{cu} = 3\rho_{cu} \mathrm{CSA}_{cu} l_{ph}. \tag{4.110}$$

The cylindrical case is assumed to be aluminium at a thickness t_{case} of 3mm and case length l_{case}. The case mass M_{case} is determined as follows,

$$M_{case} = \rho_{case}(\pi((r_{radbk} + t_{case})^2 - r_{radbk}^2) l_{case} + 2\pi(r_{radbk} + t_{case})^2 t_{case}) \tag{4.111}$$

Table 4.11: Material densities.

Component	Density (kg/m^3)
Steel laminations	8120
Copper conductor	8930
Aluminium case	2810
Insulation	1750
Magnet (NdFeB)	7500
Magnet (SmCo)	8300
Shaft	7800

The total machine mass M_{mac} is the sum of the mass of all components,

$$M_{mac} = M_{stator} + M_{rotor} + M_{cu} + M_{magnet} + M_{case} + M_{shaft}. \tag{4.112}$$

For system level analysis, rotor mass can be approximated by assuming magnet density is equal to that of the steel lamination. The air gap, magnet, and tooth tip will be fully dimensioned in section 4.6.8.

4.6.6.1 Losses and power factor

The total copper losses P_{cu} is determined as follows for rms phase current I_{ph}, and stator phase resistance R_s,

$$P_{cu} = 3I_{ph}^2 R_s. \tag{4.113}$$

The proportion of the total copper power loss dissipated in the end windings $P_{cu,ewdg}$ and in the slot windings $P_{cu,slot}$ are calculated as follows,

$$P_{cu,ewdg} = P_{cu}\frac{l_{end}}{l_{end} + 2L_{stk}}, \tag{4.114}$$

$$P_{cu,slot} = P_{cu}\frac{2L_{stk}}{l_{end} + 2L_{stk}}, \tag{4.115}$$

where l_{end} is the mean end-winding path length as given by (4.89) and L_{stk} is the stator stack length.

The per kg core losses is determined given the Steinmetz equation of the following form,

$$W_{kg} = K_h f B_{t(pk)}^{\alpha+\beta B_{t(pk)}} + 2\pi^2 K_{eddy} f_0^2 B_{t(pk)}^2, \tag{4.116}$$

where K_h, K_{eddy}, α, and β are core material Steinmetz constants.

It is assumed that rotor core losses are negligible, compared to that of the stator as the flux generated by the stator rotates in synch with the rotor at steady state. From the rotor's reference frame, the fundamental flux appears to be at dc. The back-iron stator core losses $P_{core,bk}$ and teeth core loss $P_{core,t}$ is estimated by multiplying the result

of (4.116) with their respective mass,

$$P_{core,bk} = M_{back-iron} W_{kg}. \tag{4.117}$$

$$P_{core,t} = M_{teeth} W_{kg}, \tag{4.118}$$

The power factor is determined from the operating dq voltages and currents,

$$PF = \cos\left(\arctan\left(\frac{v_q}{v_d}\right) - \arctan\left(\frac{i_q}{i_d}\right)\right). \tag{4.119}$$

4.6.7 System level candidate machine design selection

4.6.7.1 Preliminary machine sizing function

A function f_{mac1} is realised using equations (4.71-4.112) that calculates outputs $\{R_s,\ L_s,\ \lambda_m,\ |v_{dq}|,\ P_{cu},\ P_{core},\ M_{mac}\}$ from inputs $(I_{ph}, \text{TRV}, P_o, \text{RPM}, V_{dc}, x_r, J, B_{t(pk)}, N_{sl}, N_p, c, f_c, n_r, \tau)$.

$$\begin{aligned} &\{R_s, L_s, \lambda_m, |v_{dq}|, P_{cu}, P_{core}, M_{mac}\} = \\ &f_{mac1}(I_{ph}, \text{TRV}, P_o, \text{RPM}, V_{dc}, x_r, J, B_{t(pk)}, N_{sl}, N_p, c, f_c, n_r, \tau). \end{aligned} \tag{4.120}$$

The calculation process is demonstrated for a 1.1kW machine design. The design's input specifications for f_{mac1} are shown in Table 4.12. Inputs I_{ph} and TRV are iterated across a grid of values spanning 3.5-7Arms and 3-100kNm/m^3 respectively. The remaining input specifications are fixed. $R_s, L_s, \lambda_m, |v_{dq}|$, losses (as a sum of P_{cu} and P_{core}), and machine mass are plotted with respect to I_{ph} and TRV in Figures 4.16. Designs whose operating voltage magnitude is greater than the maximum allowable voltage, i.e. $|v_{dq}| > v_{max}$, were eliminated. For the given inputs, the labelled data point is considered the optimal machine design which will result in the minimum overall system mass. How this design is selected will be addressed later in this section. R_s, L_s, and λ_m increase with I_{ph} for a given value of TRV as seen in Figures 4.16 (a-c). L_s and λ_m do not vary with TRV as shown in (4.104-4.107) and in Figures 4.16 (b-c). For a given phase current; R_s and losses remain relatively constant with respect to TRV as seen in Figures 4.16 (a) and (d), with the exception of very low values of TRV. For a given phase current, there exists a minimum machine mass with respect to TRV as seen in Figure 4.16 (f). Phase current does not influence machine mass but it does greatly impact on the cable, output filter, and inverter mass. Thus, a machine design should be selected which would provide overall minimum system mass.

4.6.7.2 Preliminary system mass estimation for machine design selection

Preliminary estimation of the system mass for a given machine design assuming nominal component operating ranges is required. This will allow the selection of an optimal

Table 4.12: Case study machine for system level candidate design selection - f_{mac1} input.

Parameter	Value	Unit
Phase current I_{ph}	{3.5, ..., 7}	A_{rms}
Torque per rotor volume TRV	{3, ..., 100}	kNm/m^3
Mechanical output power P_o	1.1	kW
RPM	4000	
DC-link voltage V_{dc}	270	V
Rotor aspect ratio x_r	0.5	
Current density J	10	A/mm^2
Tooth peak flux density $B_{t(pk)}$	1.6	T
Slots/poles N_{sl}/N_p	12/10	
Current ripple c	0.1	p.u.
Switching carrier frequency f_c	15	kHz
Pitch shortening n_r	0	
Relative tooth width τ	0.5	

machine design which will result in minimum total system mass. The components considered for this preliminary estimation are the cable, LC output filter, inverter, and inverter heat sink. The mass calculation of these parameters require low computational demand compared to that of sizing the input EMI filter. EMI filter is done once machine designs are finalised and are down-selected to only Pareto-efficient designs.

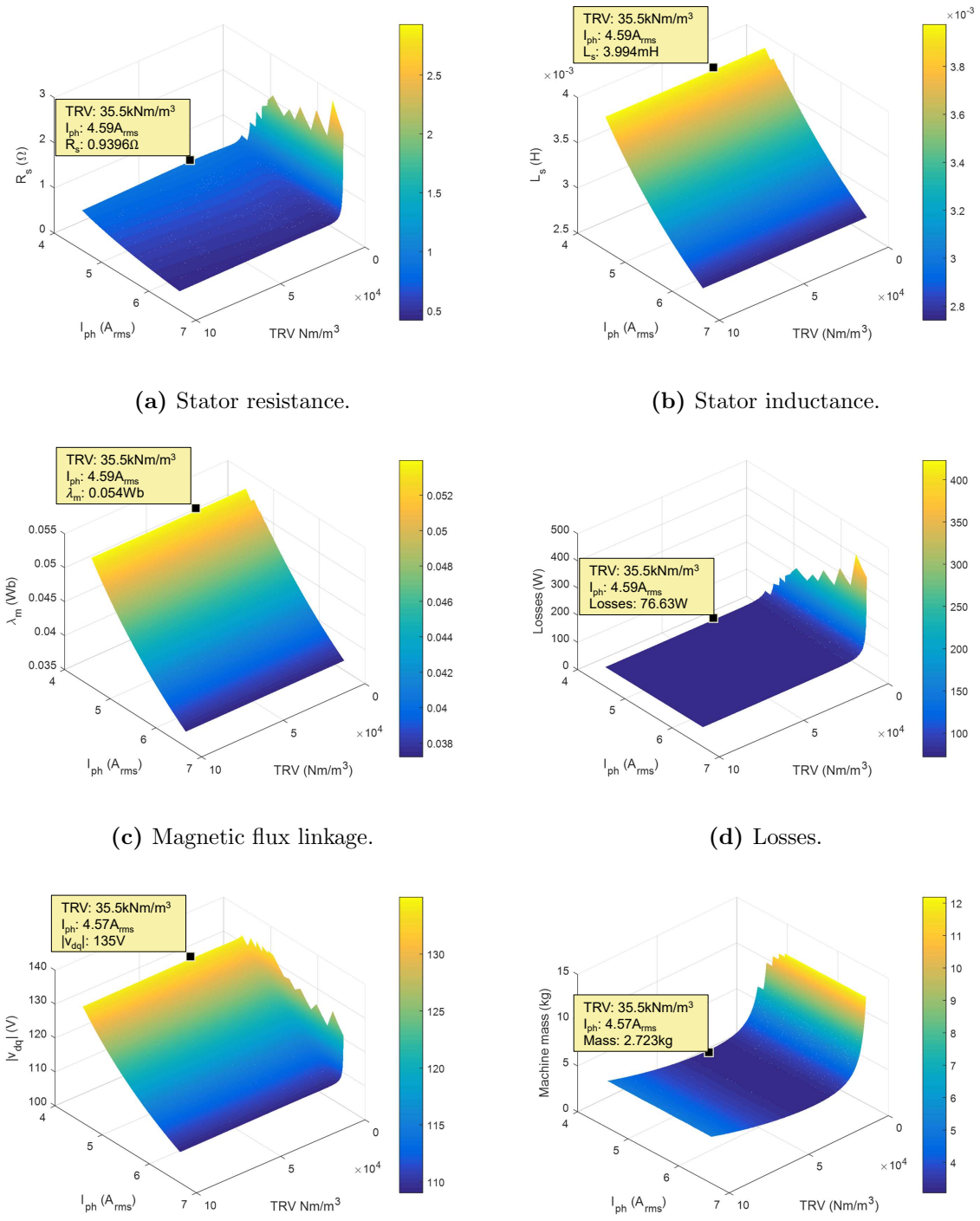
In section 4.7, the cable is sized considering the operating altitude, bundle number, phase current I_{ph}, cable length l_c, and voltage V_c. A function f_{cable} is created which returns its mass M_{cable}, line resistance R_{cs}, line inductance L_{cs}, and phase to ground C_{pg} capacitances,

$$\{M_{cable}, R_{cs}, L_{cs}, C_{pg}\} = f_{cable}(\text{Altitude}, \text{Bundle number}, I_{ph}, l_c, V_c). \tag{4.121}$$

In section 4.8, an LC output filter's inductance L_{fil} and capacitance C_{fil} are selected to attenuate the switching harmonics and its side-bands below that of the MIL-STD-704F distortion spectrum. The mass and volume of the inductors and capacitors are determined using sections 4.4.1.5, and 4.4.2 respectively. The case mass is determined from the component's volume as shown in section 4.5. A function $f_{LC,out}$ is created which returns its mass $M_{LC,out}$, the case mass M_{case}, inductance L_{fil}, and capacitance C_{fil},

$$\{M_{LC,out}, M_{case}, L_{fil}, C_{fil}\} = f_{LC,out}(V_{dc}, f_c, I_{ph}, V_{c,rated}). \tag{4.122}$$

The nominal inverter output voltage, modulation index M and current I_o, and phase angle ϕ can be determined given the parameters of the machine, cable, and output filter using section 5.2. In section 4.9.1, the power electronics losses is determined knowing M, I_o, ϕ, V_{dc}, and f_c from which the required heat-sink thermal resistance is determined for nominal junction operating temperature. The heat sink is then sized for the required heat-sink thermal resistance as described in section 4.9.2.6. Thus, a function $f_{Inverter}$ is



(a) Stator resistance.

(b) Stator inductance.

(c) Magnetic flux linkage.

(d) Losses.

(e) Voltage magnitude.

(f) Mass.

Figure 4.16: System level machine sizing, 1.1kW rating, f_{mac1} outputs $|v_{dq}|$ and machine mass.

realised which computes, heat sink mass $M_{heatsink}$ and semiconductor mass $M_{semiconductors}$.

$$\{M_{heatsink}, M_{semiconductors}\} = f_{Inverter}(M, I_o, \phi, f_c, V_{dc}) \tag{4.123}$$

The preliminary system mass is estimated as follows,

$$M_{total} = M_{mac} + M_{cable} + M_{LC,out} + M_{case} + M_{heatsink} + M_{semiconductors}. \quad (4.124)$$

Nominal operating conditions/parameters for preliminary system mass estimation for centralised and distributed topologies are shown in Table 4.13.

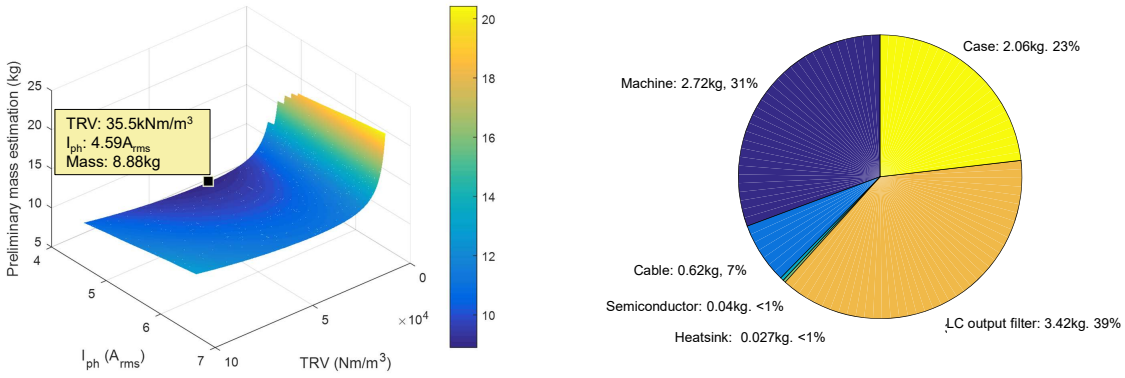
Table 4.13: Nominal operating parameters used in preliminary system mass estimation of centralised and distributed topologies.

Component	Parameter	Centralised	Distributed	Unit
Cable	Equivalent altitude	20000	20000	ft
	Bundle number	3	2	
	Length	10	10	°C
	Voltage rating	1000	1000	Vpk
LC output filter	Inductor temperature rise	30	n/a	°C
	Capacitor voltage rating	700	n/a	V
	Equivalent altitude	8000	n/a	ft
Power electronics	Junction temperature	125	125	°C
Heat sink	Ambient temperature	40	70	°C
	Equivalent altitude	8000	20000	ft

The preliminary estimated system mass values with respect I_{ph} and TRV are shown for a centralised system in Figure 4.17 (a). The machine design corresponding to the minimum system mass is labelled. Observe the optimal design is a design of minimum feasible phase current. Cable mass and inductor mass increases with respect to their current rating as described in section 4.7 and 4.4.1.7 respectively. Semiconductor switching and conduction losses increase with respect to current for a fixed voltage as seen in Figure 4.47 and Figure 4.48. Higher losses correspond to heat sinks with lower thermal resistance and higher mass as described in section 4.9.2.6. A mass breakdown of the optimal selected design of minimal system mass is shown in Figure 4.17 (b). Note that the mass of LC filter exceeds that of the machine.

Previously, only f_{mac1} inputs I_{ph} and TRV were iterated across a search space while the remaining inputs were constant. Now, the input variables RPM, dc-link voltage, rotor aspect ratio, current density, slots/poles combination, and switching carrier frequency are iterated within their respective search space range and resolution as specified in Table 4.14. For each combination of input, the optimal machine mass is determined by iteration of I_{ph} and TRV.

The design's are plotted with respect to machine mass, RPM, and current density in Figure 4.18 (a). Machine mass reduces with increase in speed and current density. Estimated system mass with respect to machine RPM, and inverter switching frequency is plotted in Figure 4.18 (b). Estimated system mass reduces with an increase in switching frequency and speed.



(a) Estimated system mass vs. I_{ph} and TRV. **(b)** Mass breakdown of optimal design.

Figure 4.17: Preliminary estimation of system mass with respect machine phase current I_{ph} and torque per rotor volume TRV of a centralised 1.1kW system considering, machine, cable, and LC output filter, semiconductor, and heat sink.

Table 4.14: Case study machine for system level candidate design selection - f_{mac1} input.

Parameter	Value	Unit
Phase current I_{ph}	{3.5, ..., 7}	A_{rms}
Torque per rotor volume TRV	{3, ..., 100}	kNm/m^3
Mechanical output power P_o	1.1	kW
RPM	{4000, 4250, ..., 8000}	
DC-link voltage V_{dc}	270	V
Rotor aspect ratio x_r	{0.5, 1, 2}	
Current density J	{10, 10.1, ..., 20}	A/mm^2
Tooth peak flux density $B_{t(pk)}$	1.6	T
Slots/poles N_{sl}/N_p	{12/10, 9/10, 12/14}	
Switching carrier frequency f_c	{15, 30, 45, 60}	kHz
Relative tooth width τ	0.5	

4.6.8 Air gap and magnet sizing

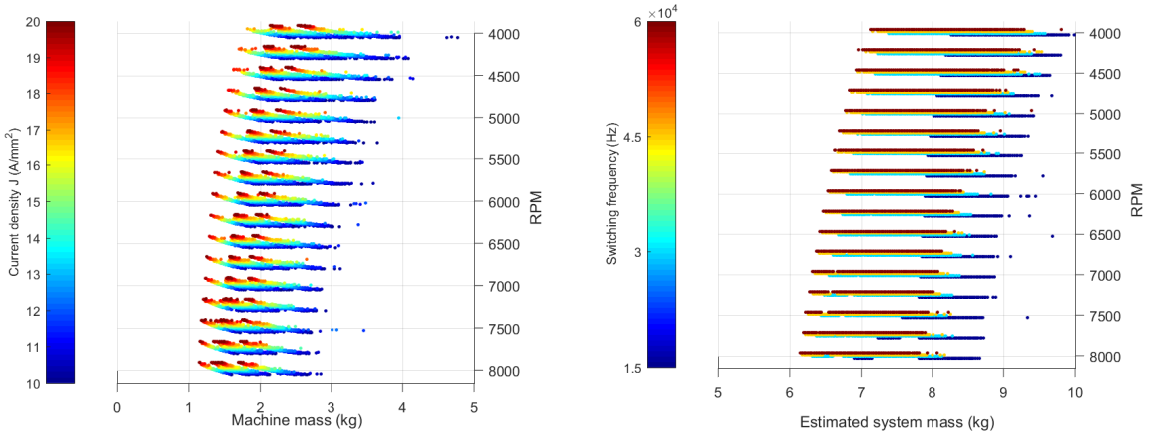
A set of machine designs have been created in the system level candidate machine design selection process. Basic stator and rotor dimensions such as tooth width t_w, number of slots N_{sl}, number of poles N_p, stack length L_{stk}, slot depth d, stator bore diameter r_{ra}, and stator outer diameter r_{radbk} have been defined. The air gap, tooth tip, and magnet need to be sized for desired stator inductance L_s and magnetic flux linkage λ_m.

4.6.8.1 Inductance

The calculated inductance L'_s is the sum of magnetising inductance L_{md} and leakage inductance L_{ls},

$$L'_s = L_{md} + L_{ls} \tag{4.125}$$

An expression for the Carter factor K_c is given by [94] which takes into account the



(a) Machine mass with respect to RPM, and current density.

(b) Estimated system mass with respect to machine RPM, and inverter switching frequency.

Figure 4.18: System level candidate machine design and selection.

lengthening of the air gap due to slotting,

$$K_c = \frac{w_d + w_{st}}{w_{st} + \frac{4d_a}{\pi} \ln\left(1 + \frac{\pi w_{ss}}{4d_a}\right)} \tag{4.126}$$

An effective stack length l' is utilised to account for lengthening of the air gap due to end-core field fringing effects [92],

$$l' = L_{stk} + 2(d_a + d_m) \tag{4.127}$$

The magnetising inductance L_{md} for a three-phase non-salient surface mounted permanent magnet synchronous machine is given by [92],

$$L_{md} = \frac{6\mu_0 \tau_p l' (k_{w1} N_{ph})^2}{p\pi^2 \left(K_c d_a + \frac{d_m}{\mu_{rec}}\right)} \tag{4.128}$$

Given air gap d_a, magnet thickness d_m, height h_d, and width w_d of slot opening depression, slot number N_{sl}, and stator bore radius r_{ra}; the tooth tip width w_{tt} and slot inner width w_{si} are determined as follows,

$$w_{tt} = \frac{2\pi r_{ra} - w_d N_{sl}}{N_{sl}} \tag{4.129}$$

$$w_{si} = \frac{2\pi r_{ra} - t_w N_{sl}}{N_{sl}} \tag{4.130}$$

The pole pitch τ_p and tooth pitch τ_t are as follows,

$$\tau_p = \frac{2\pi r_{ra}}{N_p}, \tag{4.131}$$

$$\tau_t = \frac{2\pi r_{ra}}{N_{sl}}. \tag{4.132}$$

The leakage inductance L_{ls} is determined as follows. [22] identified seven flux leakage paths as shown in Figure 4.19.

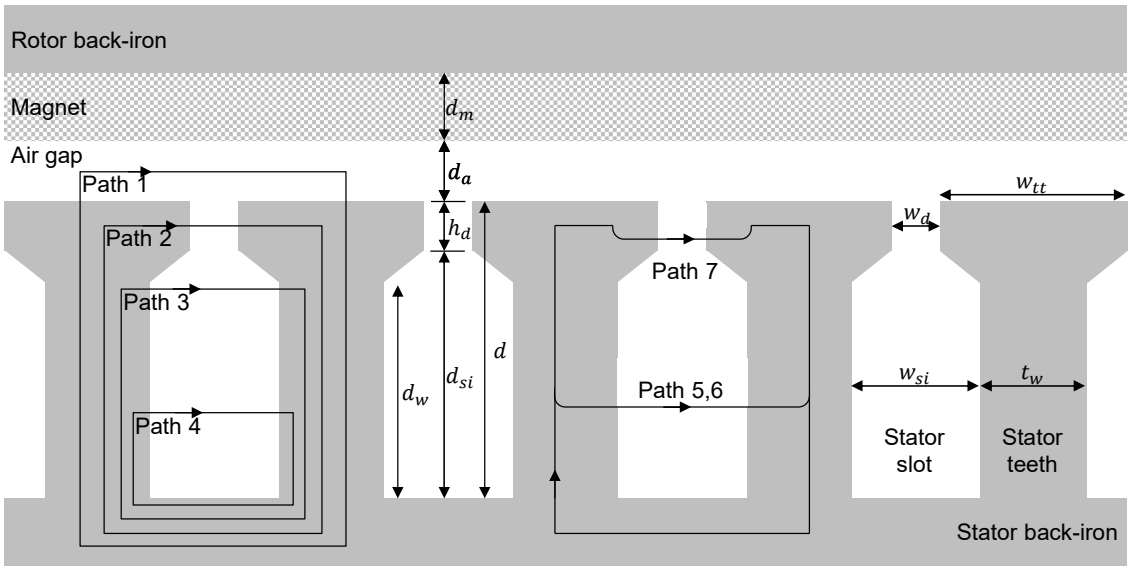


Figure 4.19: Slot teeth dimensions and leakage flux permanence paths [22].

The general equation for the permanence of a magnetically-uniform magnetic circuit element is as follows where d is length of the element, A is the element's cross sectional area, and μ is the material's magnetic permeability,

$$P = \frac{1}{R} = \frac{d}{\mu A} \tag{4.133}$$

Here, the permeability of the stator core is assumed to be infinite and the contribution from portions of the flux path which passes through the core to the overall path permanence are ignored.

Permanence of path 1 P_{sl1} is associated with the flux travelling from one tooth to the neighbouring tooth via the air gap and permanent magnet, without passing through the rotor back-iron,

$$P_{sl1} = \frac{\mu_0 L_{stk}}{\pi} \log\left(1 + \frac{\pi}{w_d} \min\left(\frac{w_{tt}}{2}, g'\right)\right). \tag{4.134}$$

Permanence of path 2 P_{sl2} is associated with the flux travelling from tooth tip to the neighbouring tooth tip in a transverse direction. The element CSA is $L_{stk} h_d$ and the element length is the slot opening depression width w_d.

$$P_{sl2} = \frac{\mu_0 L_{stk} h_d}{w_d}, \tag{4.135}$$

Permanence of path 3 P_{sl3} is associated with the flux travelling across the slot width, between the bottom of the tooth tip and the top of the winding,

$$P_{sl3} = \frac{\mu_0 L_{stk}(d_{si} - h_4)}{3w_{si}}. \tag{4.136}$$

Determination of permanence corresponding to path 4 P_{sl4} is based on an energy approach proposed by [90], as not all flux generated by the remaining path links all of conductors in that slot,

$$P_{sl4} = \frac{\mu_0 L_{stk} d_w}{3w_{si}}. \tag{4.137}$$

The permanence paths 5-7 are associated with the stator ends and have a component in the axial direction of the machine. The slot permanence for the winding region P_{sl5}, the region between the top of the winding and bottom of the tooth tip P_{sl6}, and region between tooth tips P_{sl7} are as follows,

$$P_{sl5} = \frac{\mu_0 d_w}{3\pi} \log\left(1 + \frac{\pi t_w}{w_{si}}\right), \tag{4.138}$$

$$P_{sl6} = \frac{\mu_0}{\pi} \log\left(1 + \pi \frac{t_w}{w_{si}}\right)(d_{si} - d_w), \tag{4.139}$$

$$P_{sl7} = \frac{\mu_0}{\pi} \log\left(1 + \pi \frac{w_{tt}}{w_d}\right) h_d. \tag{4.140}$$

The total leakage permanence P_{sl} is determined as the sum of the seven considered leakage permanence paths,

$$P_{sl} = P_{sl1} + P_{sl2} + P_{sl3} + P_{sl4} + 2P_{sl5} + 2P_{sl6} + 2P_{sl7}. \tag{4.141}$$

A magnetic permanence factor λ_{sl} associated with the total leakage permanence P_{sl} is introduced [92],

$$\lambda_{sl} = \frac{P_{sl}}{L_{stk}\mu_0}, \tag{4.142}$$

from which the equivalent leakage inductance L_{ls} is then determined,

$$L_{ls} = \frac{12\mu_0 l' N_{ph}^2 \lambda_{sl}}{N_{sl}}. \tag{4.143}$$

Thus, the total calculated stator inductance L'_s is determined as the sum of magnetising inductance L_{md} and leakage inductance L_{ls} as shown in 4.125.

4.6.8.2 Permanent magnet

A simplified open-circuit magnet reluctance circuit, as shown in Figure 4.20, is utilised to determine magnet operating point and the calculated magnetic flux linkage constant λ'_m. Subscripts "m", "L", and "g" refers to magnet, leakage, and air gap respectively.

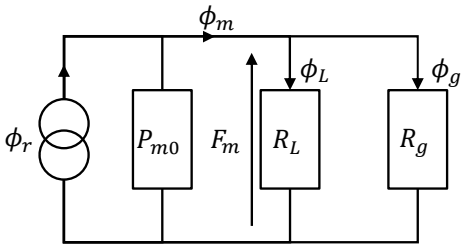


Figure 4.20: Magnet's open-circuit equivalent reluctance circuit [23].

The magnet area A_m is determined considering its cross section midway through the magnet to be its effective area,

$$A_m = \alpha_{pm} \frac{\pi}{p} \left(r_{ra} - d_a - \frac{d_m}{2} \right) L_{stk}, \tag{4.144}$$

where $\alpha_{pm} = \theta_{pm}/\theta_p$ as seen in Figure 4.14.

Optimal values for magnet pole-arc α_{pm} which minimise cogging torque is as follows [95],

$$\alpha_{pm} = \frac{N_{cp} - k_1}{N_{cp}} + k_2, \text{ for } k_1 = \{1, 2, \ldots, N-1\}, \tag{4.145}$$

where $N_{cp} = N_c/N_p$ and N_c is the lowest common multiple of N_{sl} and N_p, and k_2 is a correction factor to account for magnet fringing. Typical values for k_2 range from 0.01 - 0.03 and is dependent on the air gap.

The flux due to the magnet permanence ϕ_r is the product of the magnet's remnant reluctance B_r and magnet area A_m,

$$\phi_r = B_r A_m. \tag{4.146}$$

The magnet's self permanence P_{m0} is determined as follows for magnet's relative permeability μ_{rec} and magnet thickness d_m,

$$P_{m0} = \mu_{rec} \mu_0 \frac{A_m}{d_m} \tag{4.147}$$

The air gap area A_g is calculated as follows. The effects of fringing is approximated

by adding an air gap distance d_a to each of the four boundaries [23],

$$A_g = \left(\frac{\pi}{p}\left(r_{ra} - \frac{d_a}{2}\right)\alpha_{pm} + 2d_a\right)(L_{stk} + 2d_a). \tag{4.148}$$

The effective air gap g' considering slotting is determined as follows where K_c is the Carter's coefficient,

$$g' = K_c d_a. \tag{4.149}$$

The reluctance of the air gap is determined given g' and A_g,

$$R_g = \frac{g'}{\mu_0 A_g}. \tag{4.150}$$

The air gap flux linkage ϕ_g is determined as follows,

$$\phi_g = \frac{\phi_r}{\frac{1}{f_{lkg}} + P_{m0}R_g}, \tag{4.151}$$

where f_{lkg} is flux leakage factor defined as equal to ϕ_g/ϕ_m. Typical values for f_{lkg} are 0.9-0.95.

From (4.151), ϕ_m is determined given $\phi_m = \phi_g/f_{lkg}$. The magnet's operating point is calculated using $B_m = \phi_m/A_m$. The air-gap flux density B_g is determined as follows,

$$B_g = \frac{\phi_g}{A_g}, \tag{4.152}$$

from which the calculated fundamental magnet's flux linkage λ'_m is determined [96],

$$\lambda'_m = 8\frac{k_{w1}N_{ph}B_g r_{ra}L_{stk}}{\pi p}. \tag{4.153}$$

4.6.8.3 Air gap, tooth tip, and magnet sizing

A script function $f_{L'_s}$ is written from (4.125 - 4.143) which calculates L'_s for a set of inputs as shown,

$$L'_s = f_{L'_s}(d_a, d_m, w_d, h_d, t_w, d, \tau, L_{stk}, r_{ra}, p, k_{w1}, N_{ph}, N_{sl}, \mu_{rec}). \tag{4.154}$$

Similarly, a script function $f_{\lambda'_m}$ is written from (4.144 - 4.153) which calculates λ'_m for a set of inputs as shown,

$$\lambda'_m = f_{\lambda'_m}(d_a, d_m, w_d, N_{ph}, t_w, r_{ra}, L_{stk}, p, k_{w1}, f_{lkg}, B_r, \mu_{rec}, \tau, N_{sl}). \tag{4.155}$$

A set of machine designs have been created at system level candidate machine de-

sign selection as described in section 4.6.7.2. For each of these designs, the following parameters have already been determined,

- Tooth width t_w,
- Slot depth d,
- Tooth pitch τ,
- Stack length L_{stk},
- Stator bore radius r_{ra},
- Pole pairs p,
- Fundamental winding factor k_{w1},
- Number of turns per phase N_{ph},
- Number of slots N_{sl},
- Desired stator inductance L_s,
- Desired magnetic flux linkage λ_m.

The magnet properties B_r and μ_{rec} are defined by the selected magnet material. The only remaining undefined input variables required to solve $f_{L'_s}$ and $f_{\lambda'_m}$ are,

- Air gap d_a,
- Magnet thickness d_m,
- Width of slot opening w_d,
- Height of slot opening depression h_d.

An error function $f_{\min}$ to minimise consisting of $f_{L'_s}$ and $f_{\lambda'_m}$ is proposed as shown,

$$f_{\min}(d_a, d_m, w_d, h_d) = \frac{|f_{L'_s}(d_a, d_m, w_d, h_d, \dots) - L_s|}{L_s} + \frac{|f_{\lambda'_m}(d_a, d_m, w_d, \dots) - \lambda_m|}{\lambda_m}. \tag{4.156}$$

It can be seen that as calculated $L'_s = f_{L'_s}(d_a, d_m, w_d, h_d, \dots)$ and $\lambda'_m = f_{\lambda'_m}(d_a, d_m, w_d, \dots)$ approach desired L_s and λ_m respectively; $f_{\min}$ approaches 0. Minimisation of f_{min} is done using pattern search. Geometric limits are set for d_a, d_m, w_d, and h_d as shown in Table 4.15.

Table 4.15: Geometric limits for air gap, magnet height, and tooth tip dimensions.

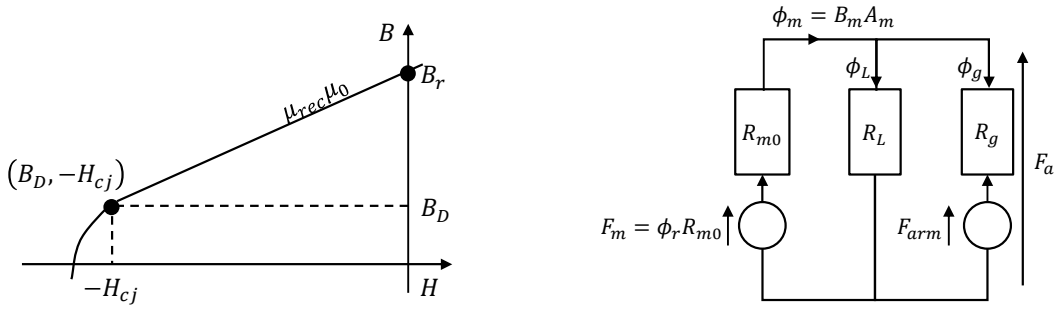
Variable	Lower limit	Upper limit	Unit
Air gap d_a	0.5×10^{-3}	$0.25 r_{ra}$	m
Magnet thickness d_m	1×10^{-3}	$0.25 r_{ra}$	m
Width of slot opening w_d	$2 d_{wire}$	$0.9 w_{si}$	m
Height of slot opening depression h_d	1×10^{-3}	$0.5 w_{si}$	m

The accuracy of the minimised solution is checked as a solution of $f_{\min} = 0$ may not exist for the predefined stator/rotor dimensions and geometric limitations. All designs whose $|L'_s - L_s|/L_s > 0.05$ and $|\lambda'_m - \lambda_m|/\lambda_m > 0.05$ are discarded.

4.6.8.4 Demagnetisation limit

During field-weakening operation, negative i_d current is injected to lower λ_d and increase the operating range at the voltage limit. However, excess negative i_d current can demagnetise the magnet. The magnet's operating point should never go below its knee point (B_D, H_{cj}) of demagnetisation curve, where H_{cj} is the magnet's intrinsic coercive force as shown in Figure 4.21 (a). The demagnetisation knee point flux density B_D is determined for given H_{cj},

$$B_D = \mu_{rec}\mu_0(-H_{cj}) + B_r. \tag{4.157}$$



(a) Permanent magnet BH curve.

(b) Equivalent magnetic circuit for demagnetisation calculation.

Figure 4.21: System level candidate machine design and selection.

The simplified equivalent magnetic circuit used to determine the magnet's demagnetisation operating point is shown in Figure 4.21 (b). The magnet flux ϕ_m for this operating point is determined by setting $B_m = B_D$ such that $\phi_m = B_D A_m$. The armature MMF F_{arm} for this condition is as follows,

$$F_{arm} = \phi_m R_L - (R_L + R_g)\left(\phi_m + (\phi_m - \phi_r)\frac{R_m 0}{R_L}\right). \tag{4.158}$$

The relationship between peak current I_{arm} and armature MMF F_{arm} is,

$$I_{arm} = \frac{p\pi F_{arm}}{3k_{w1}N_{ph}}. \tag{4.159}$$

Thus, (4.158) is substituted into (4.159) to give an expression for the demagnetisation current limit I_{demag},

$$I_{demag} = I_{arm} = \frac{p\pi}{3k_{w1}N_{ph}}\left(\phi_m R_L - (R_L + R_g)\left(\phi_m + (\phi_m - \phi_r)\frac{R_m 0}{R_L}\right)\right). \tag{4.160}$$

This value must be greater than λ_m/L_s so that the entire current operating range is

reachable. Thus, all designs whose $I_{demag} < \lambda_m / L_s$ are discarded.

4.6.9 Thermal modelling

4.6.9.1 Overview

Once all machine geometry designs have been finalised, the winding's operating temperatures are determined. To do this, the lumped parameter thermal network (LPTN) of [24] as shown in Figure 4.22 is utilised. This model was originally developed for inner rotor induction machines but has been modified by replacing the rotor winding properties with that of the permanent magnet. The represented components are the frame, stator back-iron, stator teeth, stator winding, air gap, end-winding, end-cap air, rotor magnet, rotor iron, and shaft. Each node represents a component's thermal potential, analogous to voltage of an electrical circuit. Heat flow between nodes is analogous to electrical current and thermal resistance is analogous to electrical resistance. Core losses and copper losses are modelled as power heat sources and are analogous to current sources. Ground potential is considered as ambient temperature.

Thus, to determine machine operating temperatures; the LPTN parameters, ambient to machine equivalent thermal resistance, and power losses are needed. The basis of the LPTN's component geometry to equivalent thermal network is presented in section 4.6.9.2. The ambient to machine surface equivalent thermal resistance R_{01} is determined in section 4.6.9.3. The power losses are calculated in section 4.6.6.1.

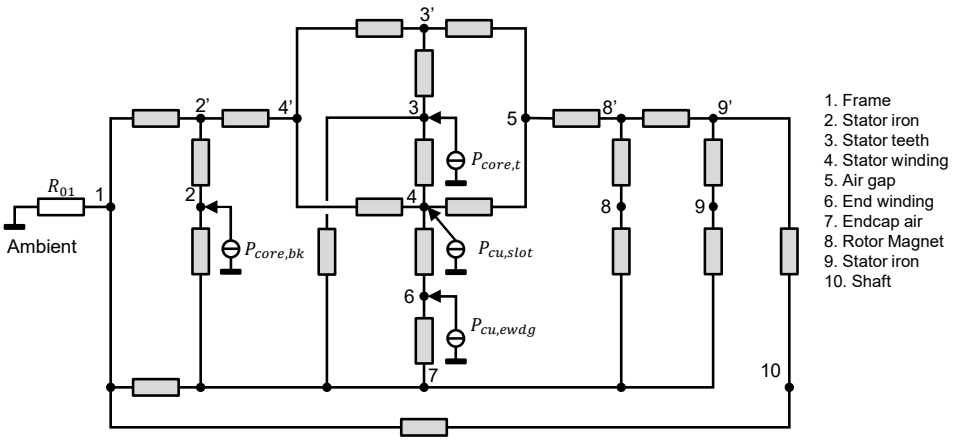


Figure 4.22: Lumped parameter thermal network [24].

4.6.9.2 Lumped parameter thermal network

The machine components' geometry is approximated by a cylinder as shown in Figure 4.23 (a). The axial and radial heat flows are assumed to be independent with respect to each other. A LPTN for each component is determined by its given geometry, and thermal properties. The corresponding cylindrical approximation LPTN is shown in Figure 4.23 (b). A single mean temperature T_m is determined for each component and used to calculate heat flow between components. The thermal resistance R_a, R_m, R_b, and R_c of Figure 4.23 (b) are as follows,

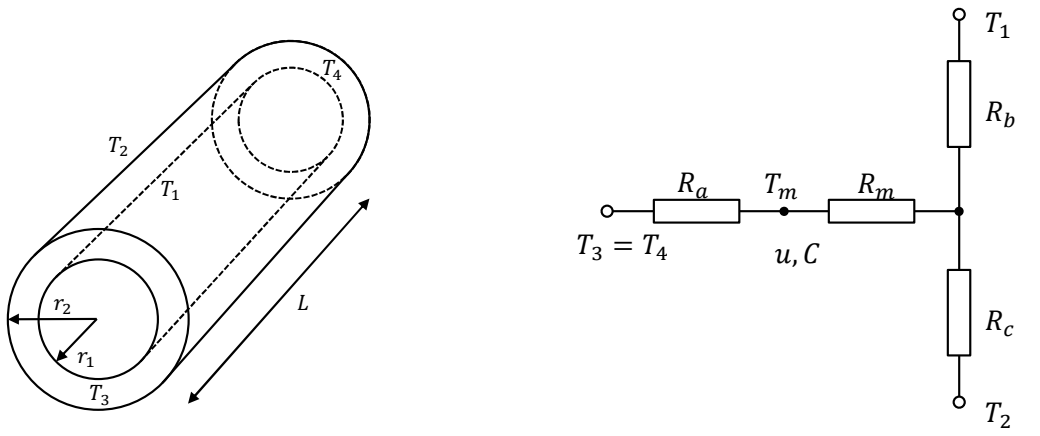
$$R_a = \frac{L}{6\pi k_a (r_1^2 - r_2^2)}, \tag{4.161}$$

$$R_b = \frac{1}{2\pi k_r L}\left(1 - \frac{2r_2^2 \ln\left(\frac{r_1}{r_2}\right)}{r_1^2 - r_2^2}\right), \tag{4.162}$$

$$R_c = \frac{1}{2\pi k_r L}\left(\frac{2r_1^2 \ln\left(\frac{r_1}{r_2}\right)}{r_1^2 - r_2^2} - 1\right), \tag{4.163}$$

$$R_m = \frac{-1}{4\pi (r_1^2 - r_2^2) k_r L}\left(r_1^2 + r_2^2 - \frac{4r_1^2 r_2^2 \ln\left(\frac{r_1}{r_2}\right)}{r_1^2 - r_2^2}\right), \tag{4.164}$$

where r_1 and r_2 are inner and outer cylinder radii, L is cylinder length, k_r and k_a are the radial and axial thermal conductivity. The extensive equations to determine each components' LPTN are outlined in [24].



(a) General cylinder geometry.

(b) Combined axial and radial network for symmetrical component.

Figure 4.23: System level candidate machine design and selection.

4.6.9.3 Machine to ambient heat transfer

Consider a machine horizontally mounted to a flange. Natural convection is assumed. The heat power flow from machine frame to ambient is the sum of heat transfer by convection q_{conv}, radiation q_{rad}, and conduction q_{cond} as shown in Figure 4.24. At steady state, this is equal to the total losses of the machine.

$$P_{core,bk} + P_{core,t} + P_{cu,slot} + P_{cu,ewdg} = q_{conv} + q_{rad} + q_{cond} = \frac{T_w - T_a}{R_{01}} \tag{4.165}$$

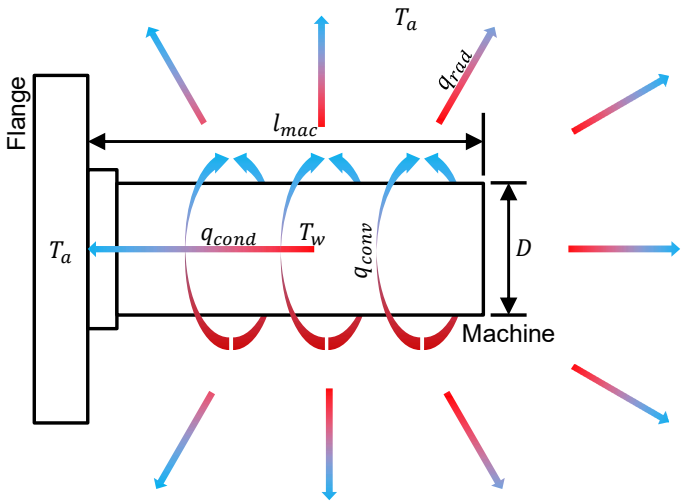


Figure 4.24: Machine to ambient convective, conductive, and radiative heat transfer paths.

Convection - to determine q_{conv}, the machine is approximated as a horizontal cylinder consisting of curved and vertical surfaces. The general equation for heat transfer by convection is as follows,

$$q_{conv} = hA(T_w - T_a). \tag{4.166}$$

This equation expresses heat flow q_{conv} flowing from the surface area with a heat transfer coefficient h, at a temperature T_w to an ambient temperature T_a.

The corresponding heat transfer coefficients for the curved surface and vertical surfaces h_{cylinder} and h_{vert} can be calculated from their respective Nusselt number as follows,

$$h_X = \frac{\text{Nu}_X k}{D}, \tag{4.167}$$

where X is replaced by "cylinder" or "vert", k is the thermal conductivity of the convection fluid, and D is the hydraulic length (in this case the diameter of outer case diameter

of the machine).

Total heat flow by natural convection is the sum of heat flow from the curved and vertical sides,

$$q_{\text{conv}} = \left(h_{\text{cylinder}} \pi D L_{stk} + h_{\text{vert}} 2\pi \left(\frac{D}{2} \right)^2 \right) (T_w - T_a) \tag{4.168}$$

The expressions of the Nusselt number for free natural convection of the curved isothermal surface of a cylinder $\text{Nu}_{\text{cylinder}}$ and an isothermal vertical plate Nu_{vert} are provided by [97][98] as shown,

$$\text{Nu}_{\text{cylidner}} = \left(0.6 + \frac{0.387 \text{Ra}_D^{\frac{1}{6}}}{\left(1 + \left(\frac{0.559}{\text{Pr}}\right)^{\frac{9}{16}}\right)^{\frac{8}{27}}} \right)^2, \tag{4.169}$$

$$\text{Nu}_{\text{vert}} = \left(0.825 + \frac{0.387 \text{Ra}_D^{\frac{1}{6}}}{\left(1 + \left(\frac{0.492}{\text{Pr}}\right)^{\frac{9}{16}}\right)^{\frac{8}{27}}} \right)^2, \tag{4.170}$$

where Pr is the Prandtl number.

The Rayleigh number Ra is expressed as follows,

$$\text{Ra}_D = \frac{g\beta(T_w - T_a)D^3}{v\alpha}, \tag{4.171}$$

where g is the acceleration due to gravity, β is the thermal expansion coefficient of the gas, v is the kinematic viscosity, and α is the thermal diffusivity.

Radiation - heat transfer rate by radiation q_{rad} is described by the Stefan-Boltzmann equation where ϵ is the emissivity of the surface, σ is the Stefan-Boltzmann constant $5.67\times10^{-8}\text{kg/s}^3/\text{K}^4$, A is the surface area, T_w is the surface temperature in K and T_a is the ambient temperature in K,

$$q_{\text{rad}} = \epsilon\sigma A(T_w^4 - T_a^4). \tag{4.172}$$

Conduction - to determine q_{cond}, consider heat transfer by conduction from frame to the mounting flange. The mounting flange is assumed to be a large thermal mass at constant ambient temperature. The general equation for thermal resistance by conduction R_{cond} of an element is expressed as,

$$R_{cond} = \frac{\Delta x}{Ak}, \tag{4.173}$$

where Δx is the element's thickness measured in the direction of heat flow, A is the cross sectional area in the plane perpendicular to the direction of the heat flow, and k is the element's thermal conductivity. In this scenario, the machine's case is acting as the conductive heat transfer path whereby heat flows axially from the machine towards the

flange. The considered Δx is approximated as half way along the length of the machine L_{mac} such that $\Delta x = L_{mac}/2$. The value A is the case's annular CSA $\pi(r^2_{radbkcs} - r^2_{radbk})$. The case thermal conductivity is that of aluminium. Substituting into (4.173) gives,

$$R_{cond} = \frac{L_{mac}/2}{\pi(r^2_{radbkcs} - r^2_{radbk})k_{cs}}. \tag{4.174}$$

Knowing the equivalent thermal resistance for the conductive path of frame to flange R_{cond}, the heat transfer rate by conduction for frame temperature T_w and ambient temperature T_a is as follows,

$$q_{cond} = \frac{(T_w - T_a)}{R_{cond}}. \tag{4.175}$$

The total heat transfer rate from the machine to ambient is the sum of natural convection and radiation. The equivalent thermal resistance as a function of T_w and T_a is determined,

$$R_{01}(T_w, T_a) = \frac{T_w - T_a}{q_{\text{rad}}(T_w, T_a) + q_{\text{conv}}(T_w, T_a) + q_{\text{cond}}(T_w, T_a)}. \tag{4.176}$$

4.6.10 Electrical machine model validation

In this section, the process of experimentally validating the electrical and thermal machine models is presented.

4.6.10.1 Experimental set-up

In this section, the details of the test set-up and hardware exclusively are presented. Experiments to validate specific aspects of the sizing and modelling tool can be found in their respective sections. An overview of the experimental set up is shown in Figure 4.25. The high voltage DC power supply and bench power supplies are labelled and highlighted in green. The high voltage DC power supply supplies 270Vdc to the inverter (highlighted in purple). The bench power supplies supply 28V to the DC/DC converters of the inverter's microcontroller board and supplies power to the magnetic brake. The oscilloscope is equipped with differential voltage probes and current probes. A 10m long cable connects the output of the inverter to the machine (which can not be seen from this angle, but is visible in Figure 4.26). Basic specifications for the equipment used are shown in Table 4.16.

The machine loading rig is shown in Figure 4.26. It consists of machine mounted on a flange, a torque sensor, a gearbox, and magnetic brake. It was built by "SpectraQuest Inc." as a drivetrain diagnostics simulator. The torque sensor, though labelled, was not used. Its torque nominal torque measurement is 100Nm and the torque output of the machine is 3Nm nominal. This gave a very low signal to noise ratio and thus was not

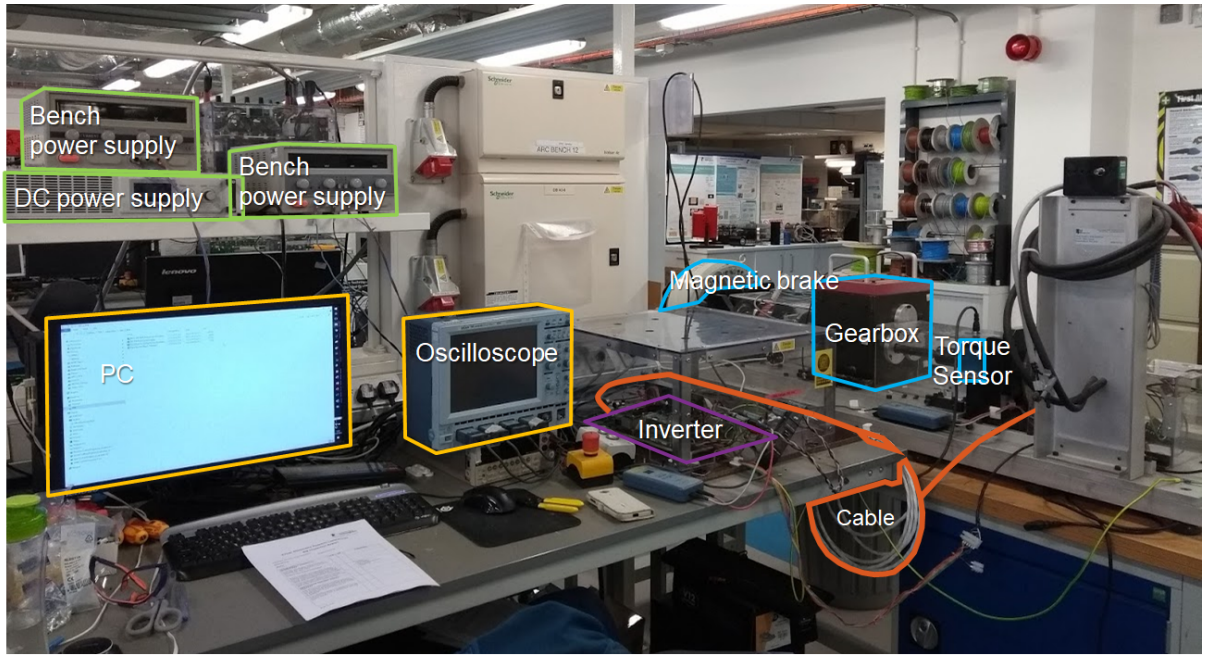


Figure 4.25: Test set-up overview

Table 4.16: Measurement equipment and power supply specifications.

Component	Name	Range	Bandwidth/Sampling rate
High voltage DC power supply	Electro-Automatik PSI 8720 2U	0 - 720V 0 - 15A	
Bench power supply	Digimess PM3006-2	0 – 30V 0 – 6A	
Impedance analyser	N4L PSM1735, Impedance Analysis Interface	10mΩ – 100MΩ 10pF – 1000uF 100nH – 10kH	10uHz - 35MHz
Oscilloscope	Lecroy 424 Waverunner		200MHz 2Gs/s
Voltage probes	LeCroy high voltage differential probe ADP300	1400Vpk differential voltage	20MHz
Current probes	LeCroy current probe CP150	150Arms	10MHz
Power analyser	NF4L PPA5500	300mVpk ∼3000Vpk (1000Vrms) 30mApk ∼300Apk(30Arms)	2.2Ms/s
Torque meter	Kistler Type 4502A	100Nm rated	100Nm = 5V output
Magnetic brake		2 - 43Nm	
Cable	M27500-10SD3T23	600Vrms, 10AWG	

used in this experiment. The torque from the magnetic brake is controlled directly by a bench power supply. Loading torque is directly proportional to the supplied current from the bench power supply to the magnetic brake. A fan is also mounted to aid in cooling.

The machine under test is the dual-lane axially-segmented HEMAS machine as shown in Figure 4.27. Both lanes are a 12 stator slot, 10 rotor pole design. Each lane has one set of three-phase windings connected in star. One lane has single layer windings, and the other has double layer windings. Multiple K-type thermocouples are embedded into the stator slots amongst the windings (two in the single layer stator and three in the double layer stator) though their exact placement is unknown. A resolver is used for rotor position measurement. The machine's basic specifications are shown in Table 4.17

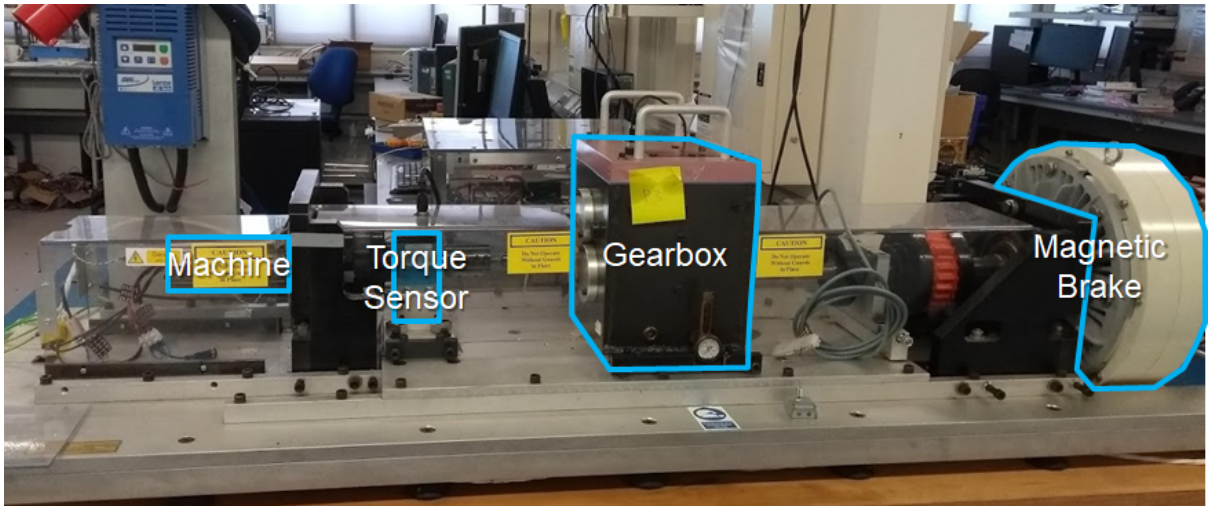


Figure 4.26: Mechanical loading rig.

with full specifications shown in Table 4.18.

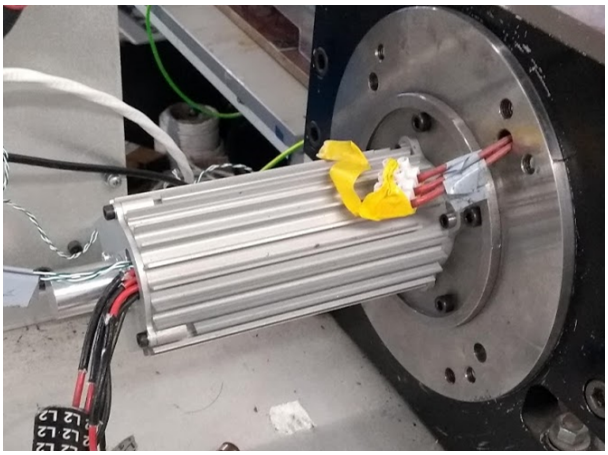


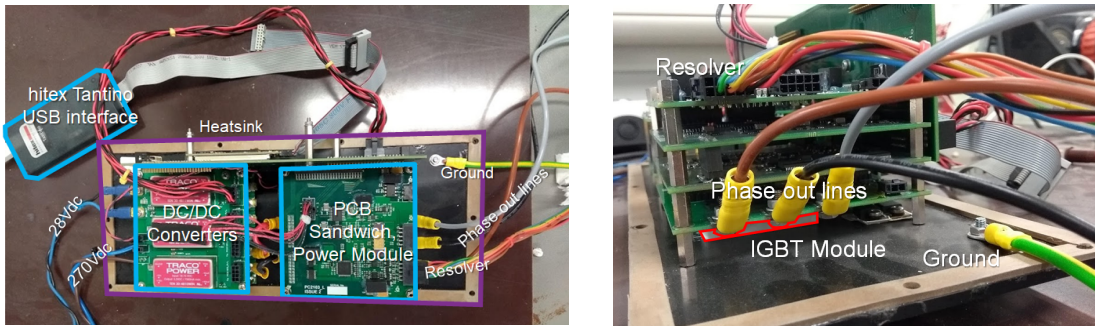
Figure 4.27: Dual-lane axially-segmented HEMAS machine.

Table 4.17: Dual-lane axially-segmented HEMAS machine specifications.

Parameter	Single-layer	Double-layer	Unit
Stator resistance R_s	0.297	0.412	Ω
Stator inductance L_s	1.416	1.455	mH
Magnetic flux linkage λ_m	0.0172	0.0198	Wb
Torque constant (k_t)	0.129	0.1485	Nm/Apk
Turns per phase	92	112	

The prototype inverter electronics and power electronics are shown in Figure 4.28. This hardware was developed by a previous student, Chintan Patel. Bench power supply supplies 28Vdc to the DC/DC converters. The output of the converters feeds the micro-controller and the switching circuit. The high voltage dc power supply supplies 270Vdc to the dc link located underneath the DC/DC converters. The resolver feed provides rotor position. There is one set of three-phase outputs. Thus only one of the two sets

of three-phase windings of the HEMAS machine can be energised at a time with this inverter. The power module is located on bottom PCB and is thermally bonded onto the heat sink. The power module is Infineon FS50R12KT4P_B11. It has six trench IGBT 4 switches and is rated for $V_{CES} = 1200V$ and $I_{C\ nom} = 50A$. It can be seen in the side view of Figure 4.28 (b). The heat sink is electrically bonded to ground. The microcontroller utilised is the Infineon TC1797. It is interfaced with the desktop computer via the Hitex Tantino USB box, allowing for debugging, monitoring, uploading of code, and control. The control scheme, safety checks, switching scheme, initialisation procedures are written in C, compiled, and then uploaded. The switching frequency was set at 10kHz.



(a) Top view. **(b)** Side view.

Figure 4.28: Inverter power electronics [6].

An example of the impedance analyser being used to measure the phase impedance of a machine is shown in Figure 4.29. The machine in this instance is the SHAO machine whose specifications can be found in Table 4.18.

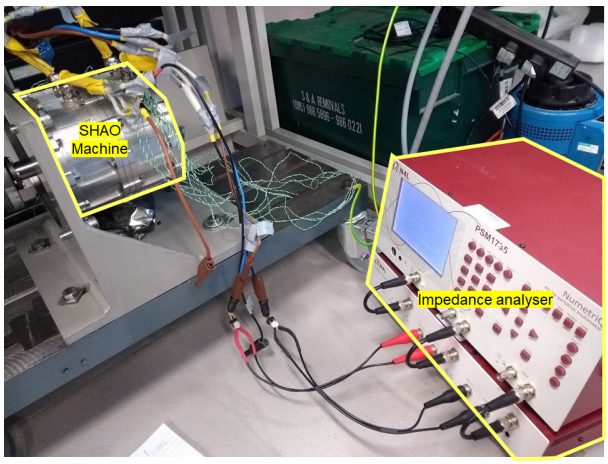


Figure 4.29: Impedance analyser to measure SHAO machine.

The machines electrical and thermal models were validated in section 4.6.10. The high-frequency cable and machine characterisation is outlined in section 6.3 for transmission line parameter extraction, section 6.5.2 for high-frequency machine model impedance calculation by FEA, and 6.5 for simulated voltage step response on long cable, and resultant machine side voltage overshoot.

4.6.10.2 Utilised existing machines for validation

Three different existing machines were utilised for validation, named HEMAS-SL, HEMAS-DL, and SHAO. HEMAS-SL and HEMAS-DL have the same stator and rotor but different winding schemes where SL stands for single layer and DL stands for double layer. SHAO is a fault tolerant machine with two sets of three-phase windings in the same stator. The specifications of the machines is shown in Table 4.18. Their winding schemes is shown in Figure 4.30-4.32. HEMAS-SL and SHAO both have concentrated single layer windings. HEMAS-DL has double layer windings. The machines' FEMM determined flux density plots are shown in Figure 4.30-4.32. For the SHAO machine, one of the two three-phase windings is considered when calculating for stator inductance and magnetic flux linkage.

Table 4.18: Specifications of surface mounted permanent magnet synchronous machine utilised in experimental validation.

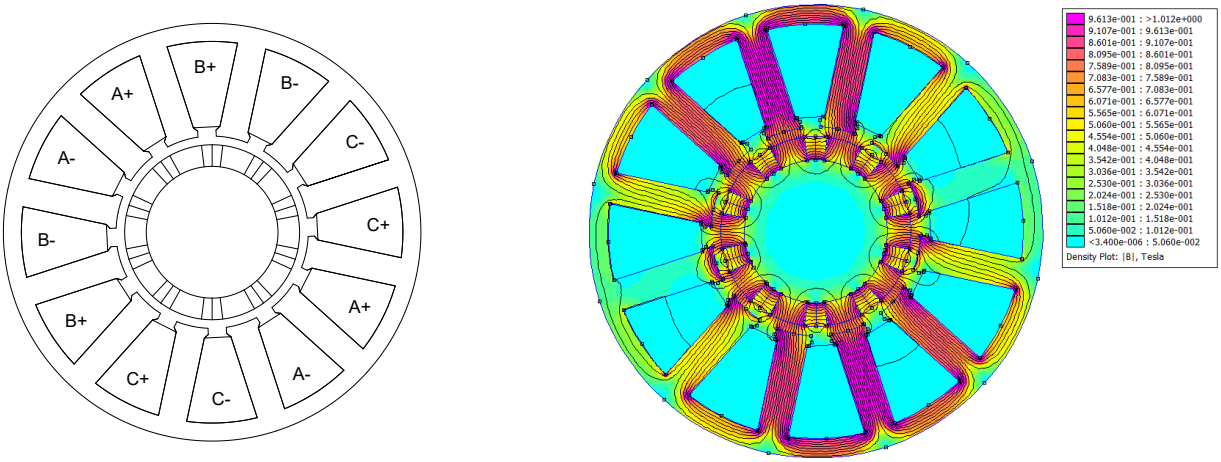
Parameter	Units	HEMAS-SL	HEMAS-DL	SHAO
Slots		12	12	24
Poles		10	10	22
Winding scheme		Single layer	Double layer	2× single layer
Stator diameter	mm	58	58	140
Stator bore	mm	26.7	26.7	84.4
Tooth width	mm	4	4	5.4
Slot depth	mm	13.15	13.15	21
Tooth tip depth	mm	0.85	0.85	1
Slot opening	mm	2.55	2.55	1.5
Stack length	mm	49.8	49.8	22
Magnet thickness	mm	3	3	5.3
Magnet arc	°E	110	110	165
Air gap	mm	1.2	1.2	0.8
Shaft diameter	mm	18.3	18.3	45
Turns per phase		92	112	108
Stator core material		Vacoflux-50	Vacoflux-50	Vacoflux-50
Rotor core material				DW270-35
Magnet material		Recoma 32	Recoma 32	N45SH

4.6.10.3 Air gap, tooth tip, and magnet sizing

The analytical procedure to determine stator inductance L_s and magnetic flux linkage λ_m for a given machine of known geometry and composition is validated using the aforementioned three machines. The stator inductance is measured using an impedance analyser. Each machine's differential mode impedance characteristic was measured and are plotted in Figure 4.33. The stator inductance is determined as follows,

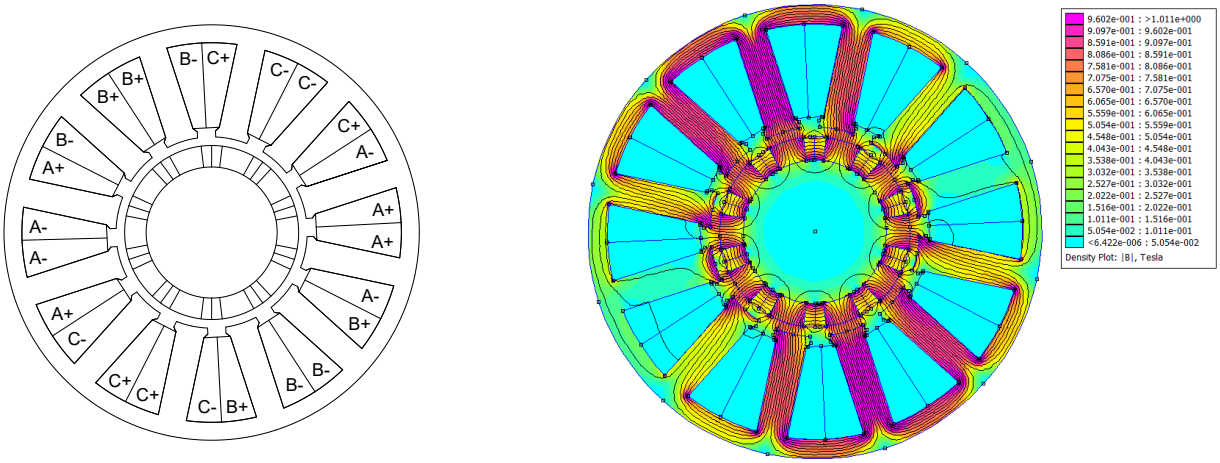
$$L_s = \frac{2}{3}\frac{A_{imp}\sin(\angle_{imp})}{2\pi f}, \tag{4.177}$$

where A_{imp} and $\angle_{imp}$ are the measured differential impedance amplitude and phase angle respectively at a frequency f. The stator inductance was calculated at a frequency f of



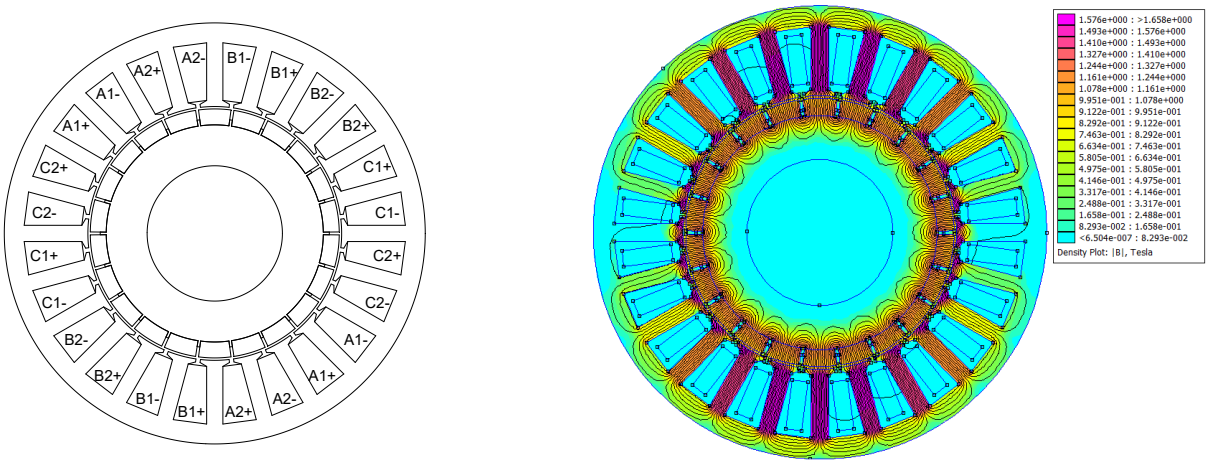
(a) Winding scheme. **(b)** FEMM determined flux density.

Figure 4.30: Electrical machine cross section - HEMAS single layer design.



(a) Winding scheme. **(b)** FEMM determined flux density.

Figure 4.31: Electrical machine cross section - HEMAS double layer design.



(a) Winding scheme. **(b)** FEMM determined flux density.

Figure 4.32: Electrical machine cross section - SHAO design.

1kHz.

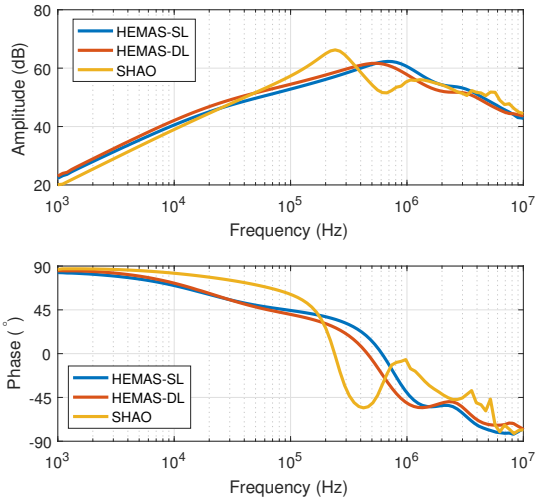


Figure 4.33: Measured differential mode impedance plots for HEMAS-SL, HEMAS-DL, and SHAO machines.

The magnetic flux linkage is determined from an open-circuit back-emf test. The line-to-line back emf profiles are shown in Figure 4.34. The magnetic flux linkage term is determined as follows,

$$\lambda_m = \frac{V_{ll,1}}{2\sqrt{3}\pi f_1}, \tag{4.178}$$

where $V_{ll,1}$ is the fundamental harmonic component of the measured line-to-line voltage at a frequency of f_1. The fundamental $V_{ll,1}$ is determined from the measured line-to-line back-emf voltage using Fourier analysis.

The measured, FEA, and analytically determined values are shown in Table 4.19. The error percentages are with respect to measured values. Results show a good match of calculated stator inductance values compared to measured for machines with single-layer windings, ranging from -3.8% for HEMAS-SL and 8.4% for SHAO. A larger stator inductance percentage error of 25.6% is observed for HEMAS-DL's results. The larger discrepancy in the HEMAS-DL result is because the inductance calculation method presented did not consider the flux interaction of different windings in the same slot. The inductance calculation method provided provides more accurate results for concentrated windings. Analytically determined magnetic flux linkage values are underestimated. The magnet flux linkage percentage errors are -21.5%, -13.7%, and -4.9% for HEMAS-SL, HEMAS-DL, and SHAO respectively.

4.6.10.4 Thermal model

The lumped parameter thermal network model of section 4.6.9 is validated using the HEMAS. HEMAS consists of two axially segmented stators, HEMAS-DL and HEMAS-

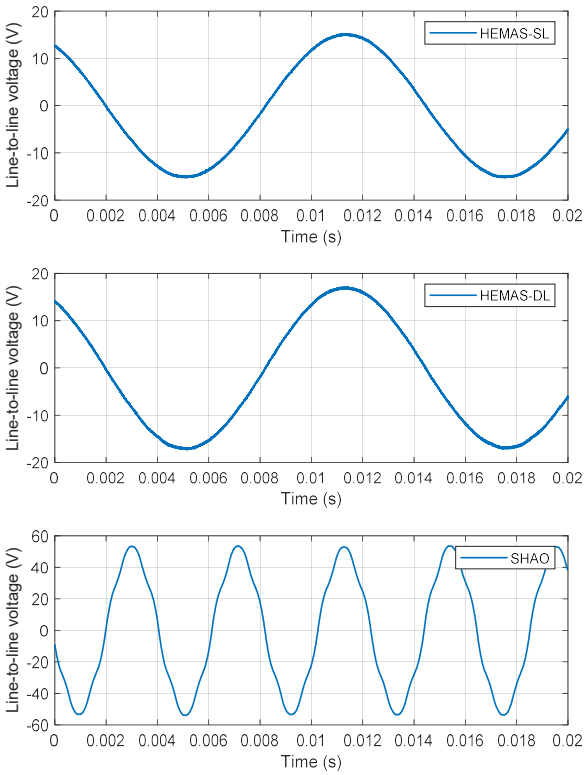
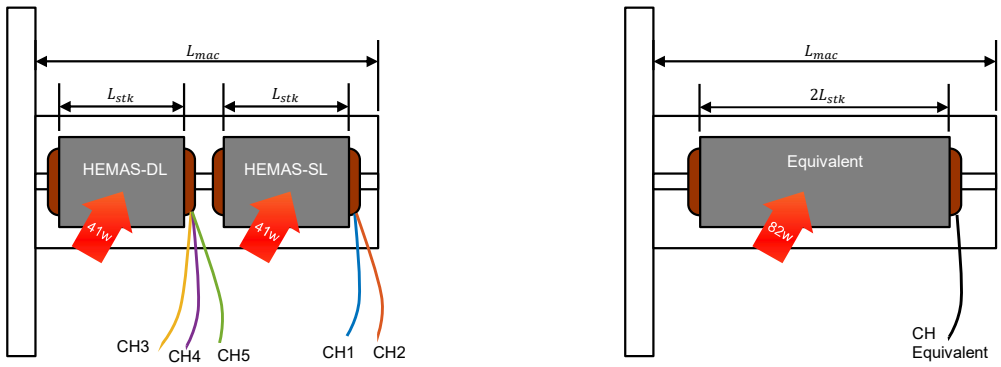


Figure 4.34: Measured back-EMF plots for HEMAS-SL, HEMAS-DL, and SHAO machines.

Table 4.19: Measured, FEA, and analytical determined stator inductance and magnetic flux linkage comparison.

Parameter	Method	HEMAS-SL		HEMAS-DL		SHAO	
L_s (mH)	Measured	1.416	[0.0%]	1.504	[0.0%]	0.988	[0.0%]
	FEMM	1.168	[-21.2%]	1.459	[-3.1%]	1.143	[13.6%]
	MotorCAD	1.200	[-18.0%]	1.482	[-1.5%]	n/a	
	Analytical	1.364	[-3.8%]	2.022	[25.6%]	1.078	[8.4%]
λ_m (Wb)	Measured	0.0172	[0.0%]	0.0196	[0.0%]	0.0198	[0.0%]
	FEMM	0.0180	[4.7%]	0.0211	[7.2%]	0.0197	[-0.3%]
	MotorCAD	0.0179	[4.2%]	0.0211	[7.1%]	n/a	
	Analytical	0.0142	[-21.5%]	0.0172	[-13.7%]	0.0189	[-4.9%]

SL as shown in Figure 4.35 (a). Their respective rotors are mechanically coupled onto the same shaft. HEMAS-DL is on the flange-side and HEMAS-SL is on the non-flange side. The stators' and rotors' stack lengths are all L_{stk}. For equal losses in both stators and rotors, the thermal characteristics of this dual stator, dual rotor machine is modelled simply as single stator, single rotor machine of stack length $2L_{stk}$ with the same cross sectional geometry as shown in Figure 4.35 (b). Two type-K thermocouples are located in HEMAS-SL's stator slots, labelled "CH1" and "CH2". Three type-K thermocouples are located in HEMAS-DL's stator slots, labelled "CH3", "CH4", and "CH5". The phases of HEMAS-DL and HEMAS-SL were connected to two seperate DC power supplies. Two out of the three machine phases are connected to the DC power supply's positive



(a) Experimental set-up. **(b)** Equivalent single stator/rotor machine.

Figure 4.35: Lumped parameter thermal model validation using HEMAS dual stator/rotor machine.

Table 4.20: HEMAS steady state temperature with 41W of copper loss per stator at ambient temperature at 18°C.

Channel	CH1	CH2	CH3	CH4	CH5	Mean	CH_{eq}
Absolute temperature (°C)	76.92	75.35	70.12	68.01	65.43	71.16	64.21 [-9.8%]
Temperature w.r.t. ambient (°C)	58.92	57.35	52.12	50.01	47.43	53.16	46.21 [-13.1%]

terminal, and the remaining phase is connected to the negative terminal. The power supplies voltage was adjusted to ensure equal ohmic losses is experienced in both stators' windings.

The measured thermal profiles for each thermocouple is shown in Figure 4.36. 41 watts in the form of copper losses are applied to each stator. Ambient temperature was 18°C. The measured steady state temperature of each thermocouple are shown in Table 4.20. Temperatures measured for HEMAS-DL are lower than that of the HEMAS-SL. This is because HEMAS-DL is closer to the flange which acts as a heat sink for conductive heat transfer through the machine's casing. The dimensions, heat loss, and ambient conditions of the equivalent machine in Figure 4.35 (b) were input into the lumped parameter thermal network model, from which the steady state stator winding temperature is determined. The calculated absolute steady state stator winding temperature of the equivalent model is 64.21°C, which is -9.8% that of the absolute mean measured stator winding temperature.

4.7 Cable sizing - static band

Cables are used to transmit electrical power from the aircraft dc power source to the inverter or from the inverter to the cable. A single core cable consists of a stranded

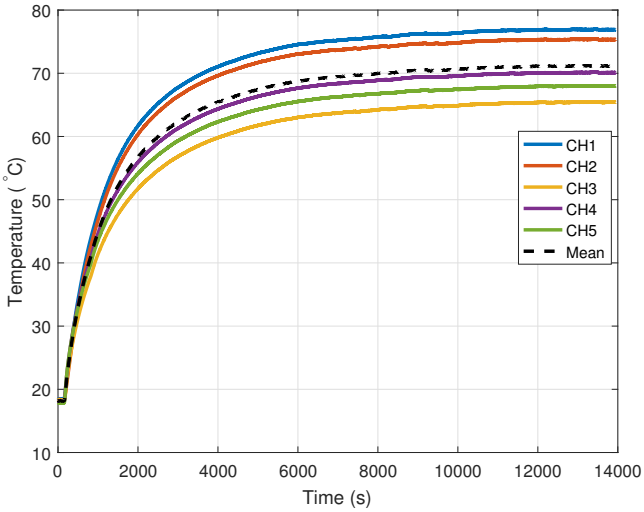


Figure 4.36: Measured thermal profiles for HEMAS machine, 41W copper losses for each stator.

copper conductor and two layers of insulation. Single-core cables are combined to make multi-phase cable bundle. The multi-phase cable bundle is shielded with a stranded aluminium shield. An outer jacket encases the entire cable structure and hold everything in place and to provide environmental protection.

[16] determined the current rating for standard wire gauge sizes and applied bundle derating factors for three-wire ac cable and four-wire dc cable bundles and altitude correction factor for operation at 40000ft as found in [99]. For the ac case, the derating factor for a three-wire bundle is 0.7375 and altitude correction factor at 40000ft is 0.7917. For the dc case, the four-wire bundle derating factor is 0.67 while the altitude corrector remains the same. The calculation results using this technique is shown in Table 4.21.

Table 4.21: Wire gauge sizes and corresponding current rating [16].

Wire gauge (AWG)	Conductor diameter (mm)	AC system current rating (A)	DC system current rating (A)
22	0.64	7.42	6.7
20	0.81	9.81	8.87
18	1.02	12.85	11.61
16	1.29	15.18	13.72
14	1.63	20.44	18.47
12	2.05	27.44	24.81
10	2.59	36.2	32.72
8	3.26	53.72	48.56
6	4.11	72.98	65.98
4	5.19	99.26	89.73
2	6.54	137.21	124.03
1	7.35	160.57	145.15
1/0	8.25	182.17	164.67
2/0	9.26	214.28	193.7

Once the conductor size has been selected for a given current rating, the appropriate cable is selected from a look-up table. Both Airbus ABS 1356 standard cables and M27500 standard cables are rated at 600Vrms or 1000Vpk. Their specifications are shown in Table 4.22 and are utilised for system level sizing. Determination of frequency-dependent cable parameters for high-frequency cable modelling is outlined in section 6.3.

Table 4.22: Aircraft cable specifications [30].

Part number	AWG	Cores	DC resistance (Ohms/km)	Diameter (mm)	Weight (g/m)
ABS1356VNC	24	3	149.4	2.45	11.14
	22	3	92.9	2.73	13.96
	20	3	51.1	3.35	20.34
	18	3	34.2	3.89	26.89
	16	3	23.7	4.62	38.23
	14	3	16	5.26	48.38
	12	3	11.2	6.25	70.04
	10	3	6	7.56	100.81
ABS1356VND	24	4	149.4	2.68	13.74
	22	4	92.9	2.99	17.37
	20	4	51.1	3.68	25.38
	18	4	34.2	4.29	33.83
	16	4	23.7	5.1	48.14
	14	4	16	5.92	66.67
M27500A	22	3	79.4	3.78	29.36
	20	3	51.1	4.73	42.83
	18	3	28.6	5.25	55.74
	16	3	22.3	5.65	66.72
	14	3	14.4	6.58	94.39
	12	3	9.3	7.53	131.47

4.8 LC Output filter

Consider the centralised topology where the inverter is located internally and a long cable connects the inverter to the machine.As discussed in a section 2.7, an LC filter is required to mitigate against transmission line effects associated with the long cable in a centralised system. Thus, the LC output filter is shown in Figure 4.37. The LC output filter is required to:

- Condition the inverter's output voltage such that transmission line effects are reduced by reducing its effective dv/dt,
- Attenuate the output phases' voltage harmonics so they do not exceed MIL-STD-704F distortion spectrums,
- Limit the output phase current ripple to ensure current control stability.

The LC output filter consists of three inductors, of series resistance R_{fil} and series

inductance L_{fil}, and three capacitors of capacitance C_{fil} connected in star. The star-arranged capacitors' neutral point is connected to the dc-link mid-point. This mid-point voltage is created by splitting the dc-link voltage in half with two capacitors $C_{dc,cm}$ and two damping balancing resistors R_d. At steady state, the mid point voltage is exactly half of the dc link voltage. R_d is appropriately selected to dampen the common mode voltage during switching as will be explained in 4.8.1.

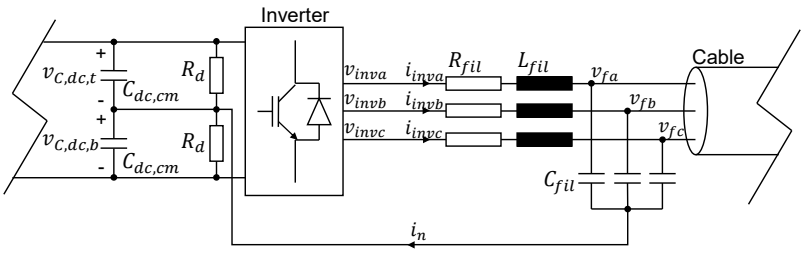


Figure 4.37: LC output filter with dc-link mid-point balancing capacitors and resistors.

A common mode current path exists starting from the output of the inverter, through the LC output filter's inductors and capacitors and back towards the dc-link midpoint. The simplified common mode equivalent circuit for this path is shown in Figure 4.38. The common mode inverter output voltage v_{cm} and common mode current i_n are as follows,

$$v_{cm} = \frac{v_{inva} + v_{invb} + v_{invc}}{3}, \tag{4.179}$$

$$i_n = i_{inva} + i_{invb} + i_{invc}. \tag{4.180}$$

The capacitor current flowing through capacitors C_{fil} is,

$$i_{C,fil} = \frac{i_n}{3}, \tag{4.181}$$

$$i_{C,dc,cm} = \frac{v_{cm2}}{s2C_{dc,cm}}. \tag{4.182}$$

The voltage difference v_{cm2} between the dc-link mid-point capacitors is as follows,

$$v_{cm2} = \frac{v_{C,dc,b} - v_{C,dc,t}}{2}. \tag{4.183}$$

When v_{cm2} is zero, the voltages of the top and bottom capacitors are the same and the mid-point voltage is exactly half that of the dc-link voltage, assuming balanced upper and lower bus capacitors. However, due to switching, this mid-point voltage will oscillate. An appropriate value of $C_{dc,cm}$ needs to be selected for given L_{fil} and C_{fil} to mitigate this voltage oscillation.

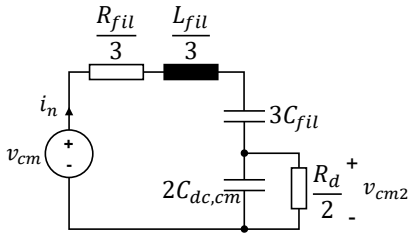


Figure 4.38: Simplified common mode equivalent circuit of LC output filter and dc-link mid-point.

4.8.1 Parameter selection

The output phase voltages' fundamental switching harmonic amplitude A_{10} at carrier frequency f_c is as follows,

$$A_{10} = \frac{2V_{dc}}{\pi}. \tag{4.184}$$

The required attenuation A_{tt} is determined by comparing this harmonic with the MIL-STD-704F distortion spectrum limit for variable frequency ac systems as shown in Figure 4.39. A margin of 6dB below the distortion spectrum limit is considered. The red-dots mark the harmonics that exceed the MIL-STD-704F limit. The output phase voltage spectrums were determined from the double Fourier-series solution of (4.232-4.237) for $V_{dc} = 270$V, $f_c = 15$kHz, and sinusoidal PWM.

The LC filter's cut-off frequency f_{fil} is determined as follows given the intrinsic attenuation of a second-order filter is -40dB/decade,

$$f_{fil} = \frac{f_c}{10^{\left(\frac{A_{tt}}{-40}\right)}}. \tag{4.185}$$

The inductor's inductance L_{fil} is determined for desired output phase current ripple ΔI,

$$L_{fil} = \frac{V_{dc}}{\pi^2 f_c \Delta I}. \tag{4.186}$$

The capacitor's capacitance C_{fil} is determined from L_{fil} and f_{fil},

$$C_{fil} = \frac{1}{(2\pi f_{fil})^2 L_{fil}}. \tag{4.187}$$

The voltage spectrum of v_{cm} is determined from the double Fourier-series solutions of (4.232-4.237). The resultant spectrum of common mode current i_n, and dc-link mid-point imbalance voltage v_{cm2} is determined using the simplified common mode equivalent circuit shown in Figure 4.38. The rms values of the common mode current and dc-link mid-point imbalance voltage is calculated from their respective spectrums. A function

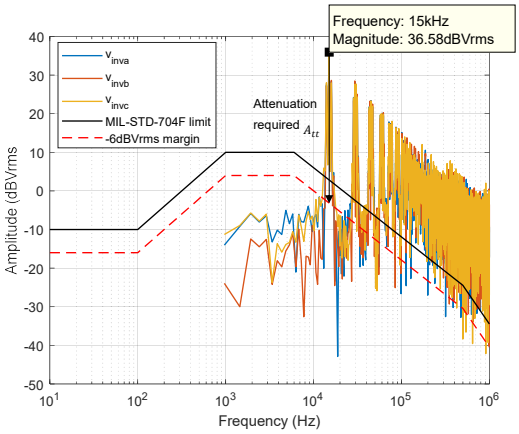


Figure 4.39: Inverter output phase voltage spectrum and MIL-STD-704F distortion spectrum limit.

$f_{C,dc,cm}$ is created from the aforementioned steps which determines the rms values of v_{cm2} and i_n from given inputs $\{v_{cm}, L_{fil}, C_{fil}, C_{dc,cm}, R_d, R_{fil}\}$. DC-link balancing capacitance $C_{dc,cm}$ is adjusted until the v_{cm2} is at or below a desired threshold voltage.

The MIL-STD-704F limit is used to determine the threshold rms value of v_{cm2}. The rms value of v_{cm2} can be determined from its voltage spectrum. The main contributor from v_{cm2}'s spectrum to its rms value is the fundamental switching harmonic. The desired v_{cm2} rms value is set equal to half of the interpolated rms voltage of the MIL-STD-704F limit at the switching harmonic frequency (consider 4.183). This is shown for a switching frequency of 15kHz in Figure 4.40. A 6dB margin below the limit is marked by the dashed red line. Its amplitude value at 15kHz is -4.864dBVrms or 0.5712Vrms. Halving this value gives a desired value for v_{cm2} equal to 0.2856Vrms.

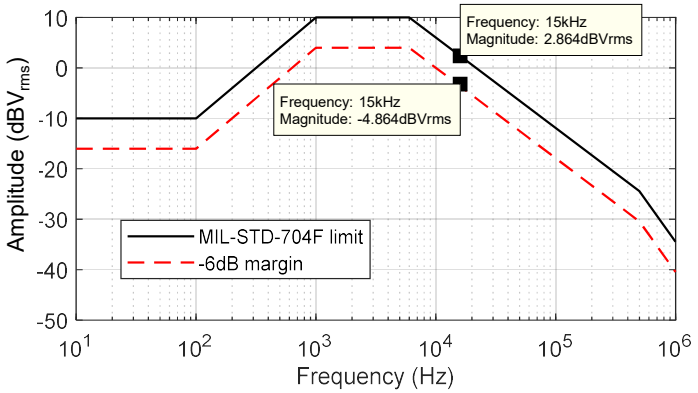


Figure 4.40: MIL-STD-704F variable frequency power system distortion spectrum limit.

The effectiveness of the designed LC filter at mitigating the switching harmonics and its side-bands is shown in the filter's output voltage spectrums from simulation in

Figure 4.41. The fundamental switching harmonic is attenuated to the margin. All other switching harmonics and their side bands are below the margin.

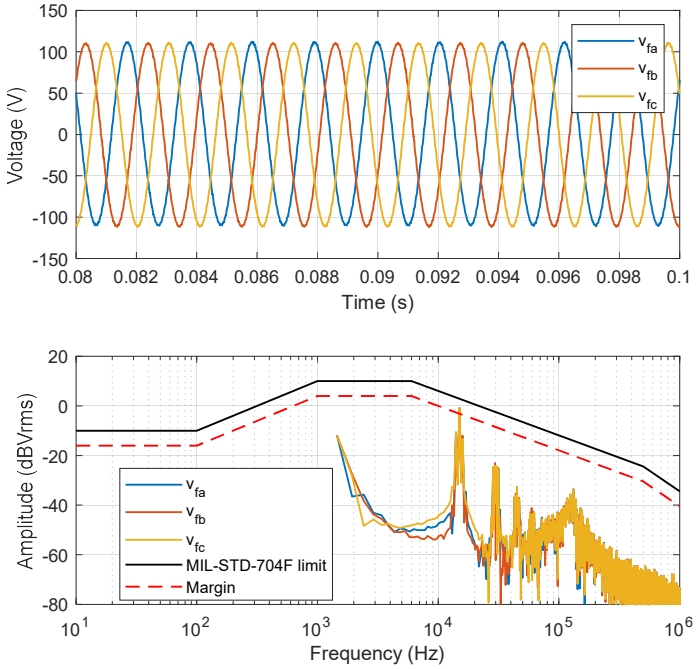


Figure 4.41: Simulated filter output phase voltage spectrum and MIL-STD-704F distortion spectrum limit.

The simulated inverter output current is shown in Figure 4.42. The desired peak to peak ripple $\Delta I = 0.2I_o$ is achieved. The simulated phase a filter output voltage v_{fa} and machine side voltage v_{ma} are plotted in Figure 4.43. Both are close to identical due to low voltage drop along the feeder cable. No transmission line effects occur due to low dv/dt of the source side applied voltage.

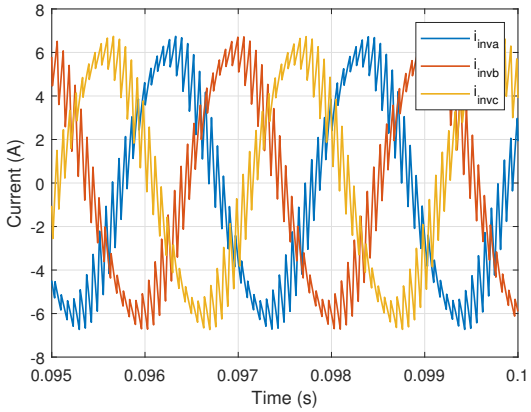


Figure 4.42: Simulated inverter output phase current.

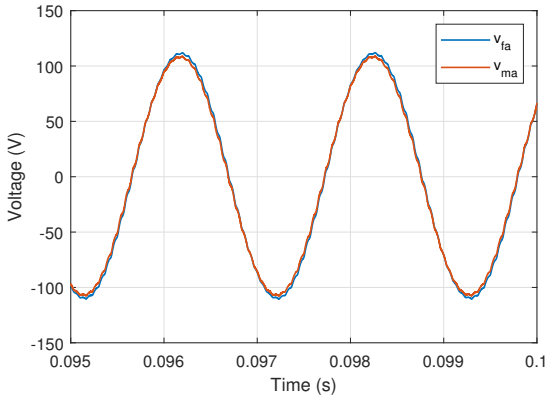


Figure 4.43: Simulated LC filter's output phase voltage and machine side terminal voltage.

4.8.2 LC output filter failure rate vs. mass

The inductor and capacitor failure rates are determined according to section 4.3.3 for given internal lifetime profile, inductor temperature rise T_r and voltage capacitor rating $V_{c,rated}$. The inductors' mass and volume are determined from its inductance, current rating, and operating environment according to the section 4.4.1.7. The capacitor's mass and volume are determined according to section 4.4.2 for capacitor voltage rating $V_{c,rated}$ and capacitance C_{fil}. The case mass is determined according to section 4.5 to enclose all LC output filter components.

The calculated inductances L_{fil} and capacitances C_{fil} vs. desired inverter line output current ripple ΔI for $f_c = 15$kHz, $V_{dc} = 270$V is shown in Figure 4.44. Here, the per unit value for current is set with respect to $I_0 = 5.15$A. As current ripple increases, inductance decreases and capacitance increases.

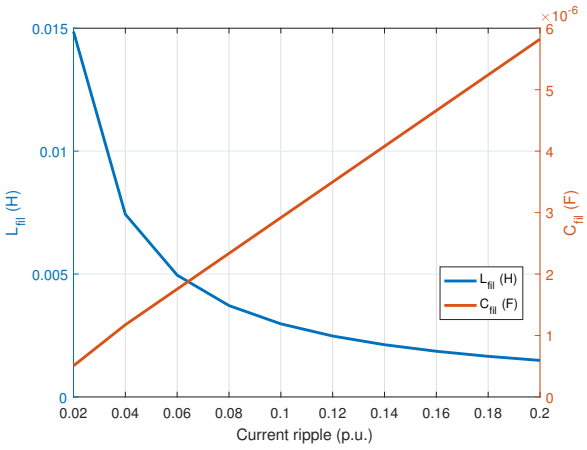


Figure 4.44: Output LC filter inductance and capacitance for desired inverter line output current ripple.

The output filters failure rate vs mass is plotted in 4.45. The mass includes the three inductors, the three capacitors, and the case enclosure. The dark-brown to light-brown lines indicate a designs' capacitor voltage rating where darker lines represents

lower voltage ratings and lighter lines represent higher voltage ratings. The blue to green coloured lines indicate a designs' allowable current ripple ΔI where blue represents lower current ripple and green represents higher current ripple. The intersection between the capacitor voltage rating lines and the inductor current ripple lines are discrete designs with its own corresponding mass and failure rate. As ΔI increases for a fixed capacitor voltage rating, mass decreases. As $V_{c,rated}$ increases for a fixed current ripple, failure rate reduces and mass increases. This effect is more pronounced at higher allowable current ripple. The maximum allowable current ripple is set to 0.2 p.u.. The pareto-frontier of these designs is determined and coincides with the designs of $\Delta I = 0.2$ p.u..

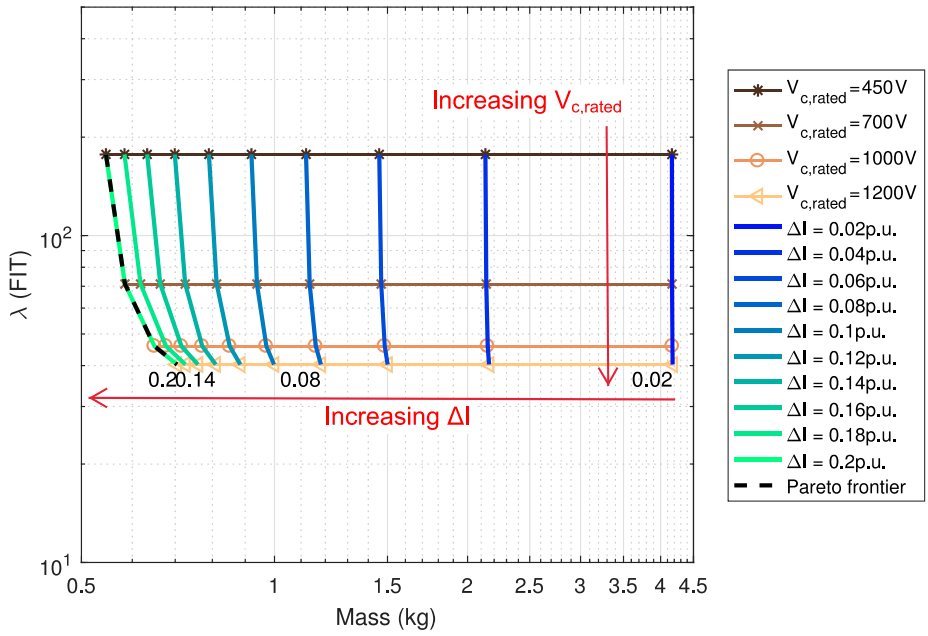


Figure 4.45: LC output filter failure rate vs. mass for capacitor voltage rating and current ripple.

The LC output filter's mass breakdown with respect to inverter output current ripple and capacitor voltage rating is shown in Figure 4.46. The total mass proportion due to the inductor decreases as inverter output current ripple increases. The total mass proportion due to the capacitor increases as output current ripple decreases and capacitor voltage rating increases.

4.9 Inverter sizing - static and low band

The components considered in the inverter sizing are its power module, heat sink, and input filter. The prerequisites for inverter sizing are that the downstream electric drive components (the machine, cable, and inverter output filter) have been sized. From that,

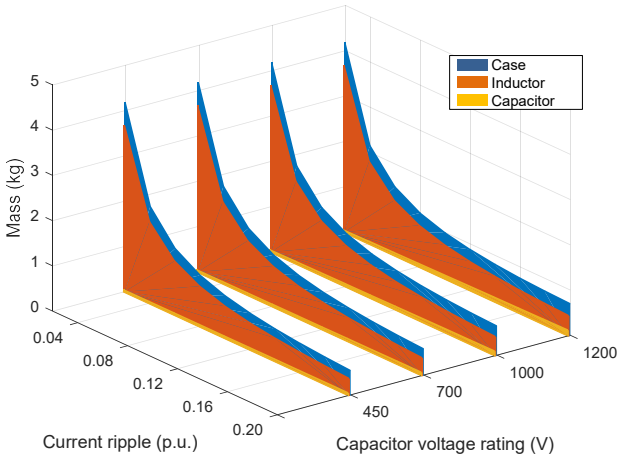


Figure 4.46: LC output filter's mass breakdown with respect to current ripple and capacitor voltage rating

the voltage and current demand are determined. The duty cycle has been defined from the application specification. The power module is selected empirically from a data base for the given voltage and current demand. The switching and conduction losses are determined from the data sheet information. The heat sink is sized based on a lumped parameter thermal network and operating environment. Finally, the inverter input filter is sized to ensure dc-link capacitance ripple voltage limits, and source side current peak to peak ripple, THD, and distortion limits are not exceeded.

4.9.1 Power electronics losses

The conduction and switching losses of the PWM voltage inverter are calculated according to [100]. The equations and explanation refer to IGBT modules but can also be applied to MOSFET modules by replacement of subscript "ce" (collector-emitter) with "ds" (drain-source). MOSFET do not have an on-state voltage, such that $V_{DS0} = 0$.

The following assumptions and simplifications are made,

- Sinusoidal pulse width modulation,
- Negligible switching times for transistors and diodes,
- Modulation is linear ($m \leq 1$),
- Sinusoidal current with negligible switching frequency ripple,
- Switching frequency f_c is much higher than that of fundamental f_o.

The modulation m is determined as follows for the peak fundamental output voltage $\hat{V}_{o(1)}$, and dc link voltage V_{dc},

$$m = \frac{\hat{V}_{o(1)}}{\frac{V_{dc}}{2}}. \tag{4.188}$$

The on-state voltage/current characteristics is linearised as follows,

$$V_{CEsat}(t) = V_{CE0} + r_{CE} i_c(t) = V_{CE0} + r_{CE} \hat{I}_1 \sin \omega_o t \tag{4.189}$$

where $\hat{I}_1$ is the fundamental current amplitude, with frequency of ω_o, V_{CE0} is the threshold votlage of the on-state characteristic, r_{CE} is the bulk resistance of the on-state characteristic. The transistor's on-state conduction losses $P_{cond(T)}$ is determined as follows for junction temperature T_j and current phase ϕ,

$$P_{cond(T)} = \left(\frac{1}{2\pi} + \frac{m \cos(\phi)}{8} \right) V_{ce0}(T_j) \hat{I}_1 + \left(\frac{1}{8} + \frac{m \cos(\phi)}{3\pi} \right) r_{ce}(T_j) \hat{I}_1^2. \tag{4.190}$$

The transistor's switching losses is as follows where E_{on+off} is the combined per switching instance turn on and turn off losses,

$$P_{sw(T)} = f_c E_{on+off} \frac{\sqrt{2}}{\pi}. \tag{4.191}$$

The on-state voltage/current characteristic of the diode is linearised as follows where V_{F0} is the diode's threshold on-state characteristic, r_F is the bulk resistance of the on-state characteristic, $\hat{I}_1$ is the fundamental current amplitude, with frequency of ω_o,

$$v_F(t) = V_{F0} + r_F i_F(t) = V_{F0} + r_F \hat{i}_1 \sin(\omega_o t) \tag{4.192}$$

The on-state diode conduction losses is determined,

$$P_{cond(D)} = \left(\frac{1}{2\pi} - \frac{m \cos(\phi)}{8} \right) V_{f0}(T_j) \hat{I}_1 + \left(\frac{1}{8} - \frac{m \cos(\phi)}{3\pi} \right) r_f(T_j) \hat{I}_1^2 \tag{4.193}$$

The diode switching losses are determined as,

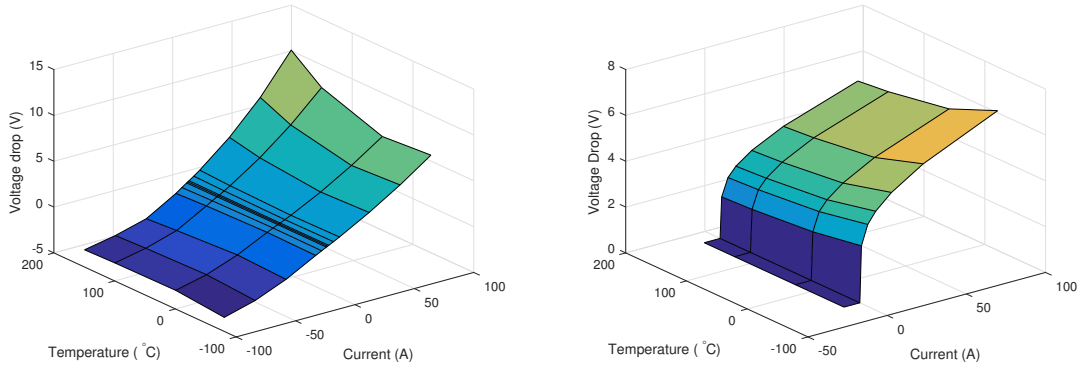
$$P_{sw(D)} = f_c E_{rr} \frac{\sqrt{2}}{\pi} \tag{4.194}$$

The transistors' and diodes' on-state voltage/current characteristics as a function of temperature, and switching losses as a function of voltage, current, and temperature are typically provided by the semiconductor component's manufacturers. These values have been provided for Microsemi's silicon carbide (SiC) power MOSFET MSC080SMA120S in Figures 4.47 and Figure 4.48.

The total transistor losses $P_{tot(T)}$ and total diode losses $P_{tot(D)}$ are as follows,

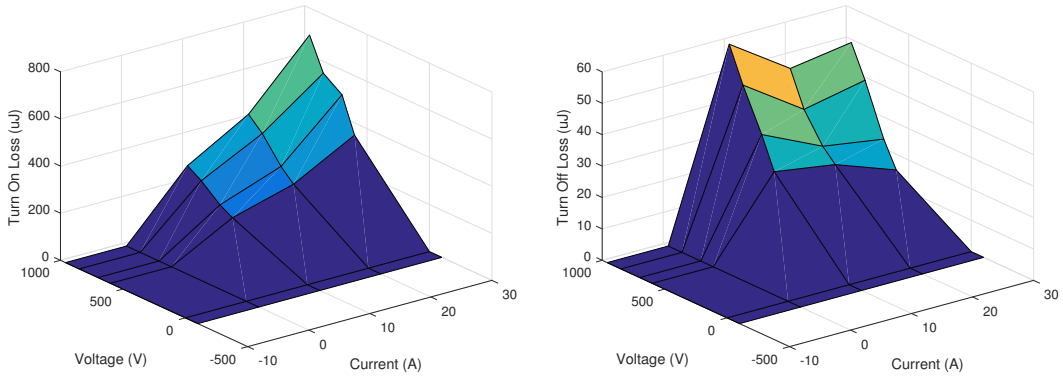
$$P_{tot(T)} = n_T (P_{cond(T)} + P_{sw(T)}), \tag{4.195}$$

$$P_{tot(D)} = n_D (P_{cond(D)} + P_{sw(D)}). \tag{4.196}$$

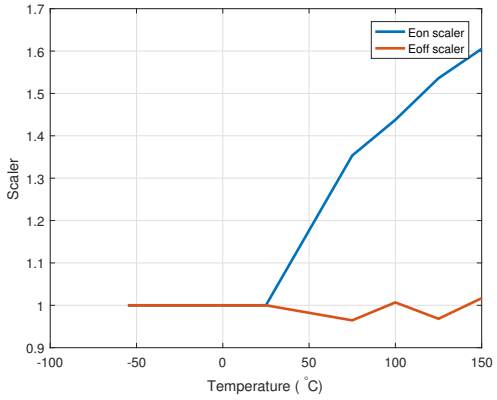


(a) MOSFET. **(b)** Diode.

Figure 4.47: On-state voltage/current characteristics with respect to temperature for Microsemi's silicon carbide power MOSFET MSC080SMA120S.



(a) Turn on loss. **(b)** Turn off loss.



(c) Turn on and turn off loss scalers with respect to temperature.

Figure 4.48: Turn on and turn off losses for Microsemi's silicon carbide power MOSFET MSC080SMA120S.

where n_T and n_D are the number of transistors and diodes. For a three-phase two-level inverter, $n_T = n_D = 6$.

The inverter's equivalent thermal network is shown in Figure 4.49 where one heat

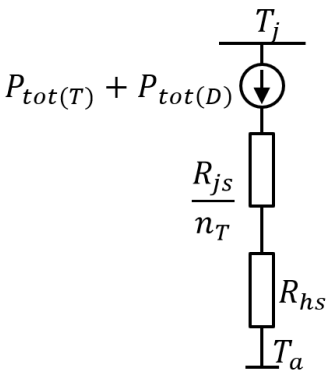


Figure 4.49: Equivalent inverter thermal network.

sink of thermal resistance R_{hs} is used to dissipate all of the heat from n devices. The considered package is a D3Pak where the transistor and diode are in the same package. The variable R_{js} is the junction to case surface thermal resistances. Using this thermal network, the required heat sink thermal resistance is determined for a desired junction temperature T_j, total transistor loss $P_{tot(T)}$, and diode loss $P_{tot(D)}$.

$$R_{hs} = \frac{T_j - T_a}{P_{tot(T)} + P_{tot(D)}} - \left(\frac{n}{R_{js}}\right)^{-1} \tag{4.197}$$

The heat sink's base temperature T_b can be calculated as follows,

$$T_b = (P_{tot(T)} + P_{tot(D)})R_{hs} + T_a. \tag{4.198}$$

4.9.2 Heat sink sizing

Parallel plate natural convection heat sink is considered for power electronics cooling. The utilised heat sink sizing technique and governing heat transfer equations are found in [101], [102].

The relationship between equivalent base to ambient thermal resistance R_{hs}, base temperature T_b, ambient temperature T_a, and total heat flow rate from heat sink to ambient q is as follows,

$$R_{hs} = \frac{T_b - T_a}{q} \tag{4.199}$$

The total heat transfer rate q from heat sink to ambient is the sum of heat transfer by natural convection q_c and by radiation q_r,

$$q = q_c + q_r. \tag{4.200}$$

Natural convection heat transfer rate q_c is a function of ambient air conditions. Radiation heat transfer of an object is dependent on its surface temperature. The goal is determine

the relationship between heat sink mass and equivalent base to ambient thermal resistance as a function of base temperature, ambient air temperature and pressure. Knowing this relationship allows the creation of a heat sink look-up table to be utilised in power electronics losses thermal management.

4.9.2.1 Geometry

Consider parallel plate natural convection heat sink with the following dimensions and geometry as shown in Figure 4.50, where H, W, d, L, t, and s are the fin height, heat sink width, base thickness, heat sink length, fin thickness, and spacing respectively.

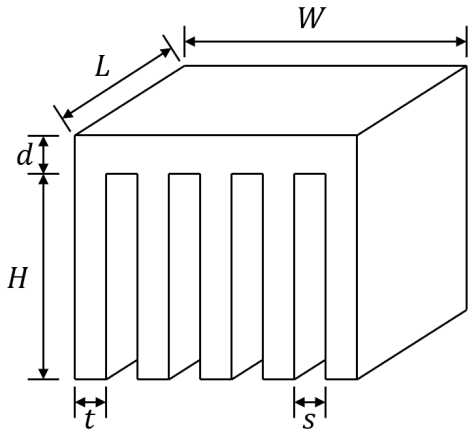


Figure 4.50: Parallel plate natural convection heat sink geometry.

4.9.2.2 Convection

The total convection heat transfer is expressed as a function of total heat transfer from the fins, and heat transfer from the base plate,

$$q_c = n_{fin} q_{fin} + (n_{fin} - 1) h_{base} s L \Delta T, \tag{4.201}$$

where n_{fin} is the total number of fins, q_{fin} is the heat flow from each fin, h_{base} is the heat transfer coefficient of the base, A_b is the base area, and ΔT is the temperature difference between base T_b and ambient T_a.

$$\Delta T = T_b - T_a \tag{4.202}$$

The heat dissipation of a fin q_{fin}, assuming insulated tip is as follows [103],

$$q_{fin} = L k_{fin} t \Delta T m \tanh(mH), \tag{4.203}$$

where m is the fin parameter for fin heat transfer coefficient h_{fin}, fin material thermal

conductivity k_s, and fin thickness t,

$$m = \sqrt{\frac{2h_{fin}}{k_s t}}. \tag{4.204}$$

The geometric ratio for parallel plate fin heat sink of minimum material is,

$$t = \frac{0.993 h_{fin} H^2}{k_s} \tag{4.205}$$

Equation (4.205) is solved for h_{fin} and then substituted into (4.204) to get,

$$m = \sqrt{\frac{2}{0.993 H^2}}, \tag{4.206}$$

The fin efficiency η_{fin} is as follows for fin height H,

$$\eta_{fin} = \frac{\tanh(mH)}{mH}. \tag{4.207}$$

Ambient air properties must be calculated with respect to temperature and pressure.

The optimum fin spacing s is as follows [104],

$$s = 2.66 \left(\frac{L v_a^2}{g \beta_a \eta_{fin} \Delta T P_{r,a}} \right)^{\frac{1}{4}} \tag{4.208}$$

where v_a, β_a, and $P_{r,a}$ are the viscosity, expansion coefficient, and Prandtl number of air respectively. The heat sinks width W is calculated as,

$$W = (n_{fin} - 1) \left(\frac{n_{fin} t}{n_{fin} - 1} + s \right) \tag{4.209}$$

The Elenbaas number E_l is given by,

$$E_l = \frac{\rho_a^2 \beta_a g c_{p,a}}{\mu_a k_a L} s^4 \Delta T, \tag{4.210}$$

where ρ_a, g, $c_{p,a}$ μ_a, k_a, are the air density, acceleration due to gravity, air's specific heat capacity, air's dynamic viscosity, and air's thermal conductivity respectively.

The fin's convective heat transfer coefficient h_{fin} is as follows [105],

$$h_{fin} = \frac{k_a}{s} \left(\frac{576}{E_l^2} + \frac{2.873}{\sqrt{E_l}} \right)^{-0.5} \tag{4.211}$$

The expression for fin's heat transfer rate q_{fin} is as follows,

$$q_{fin} = \sqrt{2h_{fin}k_s t}L\Delta T \tanh\left(\sqrt{\frac{2h_{fin}}{k_s t}}H\right) \tag{4.212}$$

The base heat transfer coefficient h_{base} is as follows,

$$h_{base} = \frac{Ck_a}{L}R_a^{1/4} \tag{4.213}$$

where $C = 0.59$ is an empirical constant, and R_a is the Rayleigh number,

$$R_a = \frac{\rho_a^2 \beta_a g L^3 \Delta T c_{p,a}}{\mu_a k_a}. \tag{4.214}$$

Thus (4.201) can be solved for q_c after determining q_{fin} and h_{base}.

4.9.2.3 Radiation

The expression for radiation heat transfer of a parallel plate heat sink considering channel view are as follows [106],

$$q_r = (n_{fin} - 1)q_{r,ch} + \left(n_{fin}t(L + 2H) + 2HL + d(LW)\right)\epsilon_s\sigma(T_b^4 - T_a^4). \tag{4.215}$$

where the first group of terms are the sum of all channel radiation heat transfer $q_{r,ch}$ and the second group of terms are the radiation heat transfer of the remaining surfaces.

The channel view factor F_s is as follows,

$$F_s = 1 - \frac{2H'\sqrt{1 + L'} - 1}{2H'L' + \sqrt{1 + L'^2} - 1} \tag{4.216}$$

for normalised height $H' = H/s$ and length $L' = L/s$.

The expression for per channel radiation $q_{r,ch}$ for an isothermal heat sink is as follows,

$$q_{r,ch} = \frac{\sigma(s + 2H)L(T_b^4 - T_a^4)}{\frac{1-\epsilon_s}{\epsilon_s} + \frac{1}{F_s}}. \tag{4.217}$$

Temperature variation of fins need to be taken into consideration. An equivalent heat transfer coefficient of radiation h_r is defined as,

$$h_r = \frac{q_r}{A_{hs}(T_b - T_a)}, \tag{4.218}$$

where A_{hs} is the total surface area of the heat sink,

$$A_{hs} = (n_{fin} - 1)sL + n_{fin}(t(L + 2H) + 2HL) + d(W + L) \tag{4.219}$$

Thus, the total radiation heat transfer is as follows,

$$q_{r,ch} = \eta_{hs} A_{hs} h_r (T_b - T_a) \tag{4.220}$$

where η_{hs} is the heat sink efficiency, A_f is the fin area,

$$\eta_{hs} = 1 - \frac{n_{fin} A_f}{A_{hs}} (1 - \eta_f), \tag{4.221}$$

$$A_f = 2(L + t)H + Lt, \tag{4.222}$$

$$\eta_f = \frac{\tanh\left((H + t/2)\sqrt{\frac{2h_r(L+t)}{k_s Lt}}\right)}{(H + t/2)\sqrt{\frac{2h_r(L+t)}{k_s Lt}}}. \tag{4.223}$$

4.9.2.4 Equivalent thermal resistance

The base's equivalent conductive thermal resistance is as follows, assuming isothermal conditions,

$$R_b = \frac{d}{LWk_s} \tag{4.224}$$

The total equivalent thermal resistance of the heat sink R_{hs} with respect base and ambient temperature T_b and T_a are as follows,

$$R_{hs} = \frac{\Delta T}{q_c + q_r} + R_b. \tag{4.225}$$

4.9.2.5 Mass and volume

The mass and "box" volume of the heat sink, M_{hs} and V_{hs}, are as follows,

$$M_{hs} = \rho_s (n_{fin} HtL + dLW), \tag{4.226}$$

$$V_{hs} = LW(d + H), \tag{4.227}$$

where ρ_s is the density of the heat sink material. Here, the material is assumed to be aluminium.

4.9.2.6 Heat sink look-up table generation

The procedure for determining a parallel plate natural convection heat sinks' equivalent base to ambient thermal resistance R_{hs} as a function of ambient air temperature T_a, ambient air pressure P_a, base temperature T_b, fin height H, heat sink length L, number of fins n_{fin}, and base thickness d has been presented in sections 4.9.2.2 to 4.9.2.4. As a by-product of this procedure, the geometric dimensions fin thickness t, fin spacing s,

and heat sink width W are determined from which the heat sinks' mass and volume are calculated by (4.226) and (4.227) in Section 4.9.2.5. This procedure is compiled into a script function f_{hs} that returns both R_{hs} and M_{hs},

$$(R_{hs}, M_{hs}) = f_{hs}(H, L, n_{fin}, d, T_a, P_a, T_b). \tag{4.228}$$

For fixed T_a, P_a, T_b, and d, the inputs H, L, n_{fin} of function f_{hs} are iterated for which corresponding outputs R_{hs} and M_{hs} are determined. The relationship between the resultant designs' respective mass and thermal resistance is illustrated in Figure 4.51. As heat sink mass increases, equivalent thermal resistance reduces. The Pareto frontier of heat sink designs is determined. Thus, it has been shown for fixed T_a, P_a, T_b, and d, a set of Pareto efficient heat sink designs is generated.

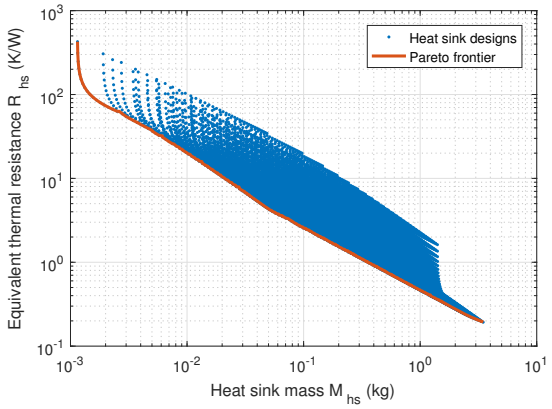


Figure 4.51: Equivalent thermal resistance vs. heat sink mass for ambient temperature 70°C, equivalent pressure at an altitude of 20,000ft, base temperature 120°C, base thickness = 5mm.

Assuming d is fixed, the values T_a, P_a, and T_b are iterated for which corresponding sets of Pareto efficient heat sink designs are generated. This is done to create a look-up table function $f_{LUT,hs}$ that provides the R_{hs} and M_{hs} relationship of Pareto efficient heat sinks for given inputs T_a, P_a, and T_b.

$$R_{hs}(M_{hs}) = f_{LUT,hs}(T_a, P_a, T_b) \tag{4.229}$$

4.9.3 Inverter failure rate vs. heat sink mass

In this section, the relationship between inverter failure rate and heat sink mass is shown. The results in the presented graphs refer to a case study of the following specifications in Table 4.23.

1. λ vs. T_j - In section 4.3.4, the power electronics's lifetime profile is defined from which the discrete semiconductor failure rate λ with respect to junction temperature T_j is determined for a semiconductor component as seen in Figure 4.52. Two

Table 4.23: Case study for inverter failure rate vs. heat sink mass.

Parameter	Value
Internal lifetime profile	Table 4.1
External lifetime profile	Table 4.2
Discrete semiconductor	Microsemi SiC MSC080SMA120S
DC voltage	270V
Modulation index	1
Power factor	0.9866
Output current	5.0Apk
Fundamental frequency	400Hz
Switching frequency	15kHz

different lifetime profiles were considered, "internal" referring to that of the avionics bay of a civil medium haul aircraft in Table 4.1, and "external" referring to in the wing, at the point of actuation environment in Table 4.2. The lifetime profile also defines the ambient temperature T_a and ambient pressure P_a which are relevant to inverter thermal management calculations.

For the same discrete semiconductor junction temperature, the predicted failure rate for the external lifetime profile is higher than that of the internal. Externally located discrete semiconductor junction temperatures would need to operate at ≈25°C lower than that of internally located components to achieve the same predicted failure rate.

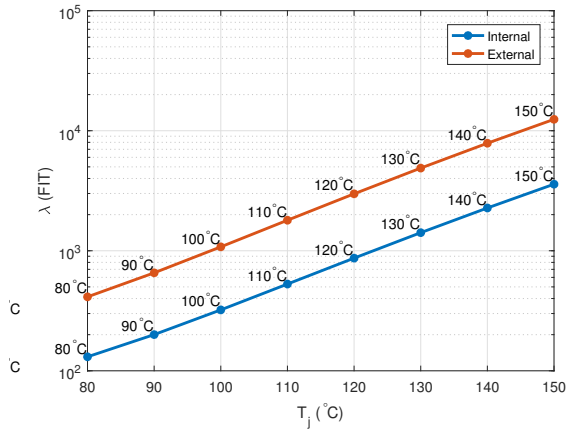


Figure 4.52: Inverter failure rate vs. junction temperature.

2. R_{hs} vs. T_j - In section 4.9.1, the required heat sink thermal resistance R_{hs} and resultant heat sink base temperature T_b is determined as a function of junction and ambient temperatures T_j and T_a, total transistor and diode power losses $P_{tot(T)}$ and $P_{tot(D)}$. This relationship is illustrated in 4.53.

   The required heat sink thermal resistance is lower for the external case than that of the internal case. This is due to the higher ambient temperature for the external design case (T_a = 70°C) compared to the internal case (T_a = 40°C). Higher

ambient temperature results in a smaller relative temperature differential between semiconductor junction and ambient. Thus, a lower thermal resistance is required to dissipate the same amount of heat.

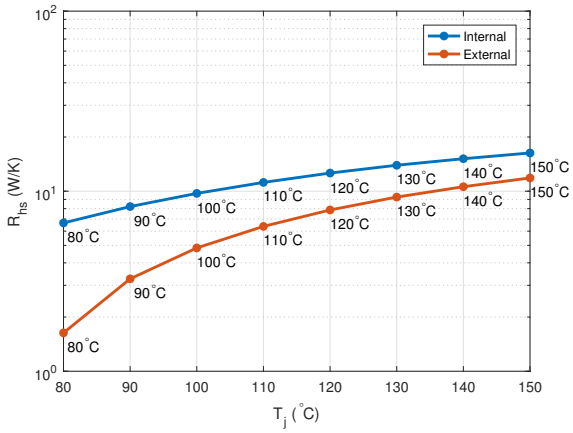


Figure 4.53: Heat sink thermal resistance vs. junction temperature.

3. R_{hs} vs. M_{hs} - In section 4.9.2, a look-up table of heat sink designs has been created that gives the relationship between heat sink equivalent thermal resistance R_{hs} and heat sink mass M_{hs} of Pareto-efficient heat sinks for given inputs T_a, P_a, and T_b. This relationship has been shown in Figure 4.54.
   A heavier heat sink with a lower thermal resistance is required for the same junction temperature in the external case compared to that of the internal case. For the same mass, heat sinks of the external case have higher thermal resistance than that of the internal case. This is due to higher ambient temperature and lower ambient pressure at higher equivalent altitudes in the external case, than that of the internal case.

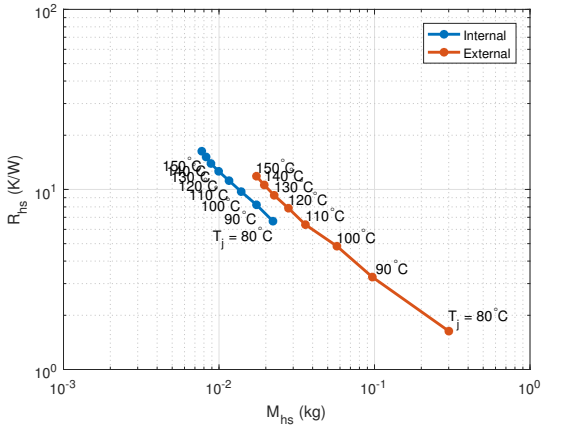


Figure 4.54: Corresponding heat sink thermal resistance vs. mass.

4. λ vs. M_{hs} - Knowing the relationships λ vs. T_j, R_{hs} vs. T_j, and R_{hs} vs. M_{hs}, the relationship between inverter failure rate and heat sink mass λ vs. M_{hs} can be

determined for each of the design cases and is plotted in Figure 4.55.
For the same predicted failure rate, the heat sink mass of the internal case is lower than that of the external case. The internal design cases range from (0.0077kg, 3586FIT) at a junction temperature of 150°C to (0.022kg, 3586FIT) at 80°C. The external design cases range from (0.0174kg, 12440FIT) at junction temperature of 150°C to (0.301kg, 413.2FIT) at 80°C. For the same failure rate, a heavier heat sink is required for the external case compared to that of the internal case.

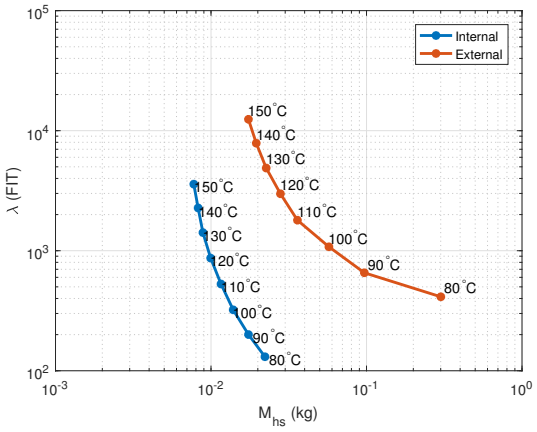


Figure 4.55: Inverter failure rate in time vs. heat sink mass.

4.10 Input EMI filter design

A multi-stage LC inverter input EMI filter is considered. First, the EMI design requirements are outlined. The proposed EMI filter topology is presented. The mixed-mode, DM and CM equivalent circuits are shown. Finally, the parameter selection procedure steps are outlined. The inverter input filter are designed for the following considerations:

- To minimise EMI filter's mass or volume.
- Ensure MIL-STD-461F's CE101 and CE102 conducted emissions limits are adhered to.

4.10.1 Conducted Emissions Requirements - MIL-STD-461F

MIL-STD-461's CE101 and CE102 limits [107] define the power leads conducted emissions requirements for subsystems and equipment used in/with ships, ground devices, and aircraft as shown in Figure 4.56. The conducted emissions are measured using a MIL-STD-461 specific line impedance stabilisation network (LISN) as shown in Figure 4.57. The LISN is connected between the power source via the "IN" port and the EUT via the "OUT" port for each power lead. The reference port "REF" is connected to ground.

The voltage is measured at the "MEAS" port with 50Ω impedance termination and its spectrum is plotted and compared with the appropriate emissions requirements. The LISN is connected to the equipment under test (EUT) as shown in Figure 4.58 to measure u_+ and u_- for the outgoing and return lead.

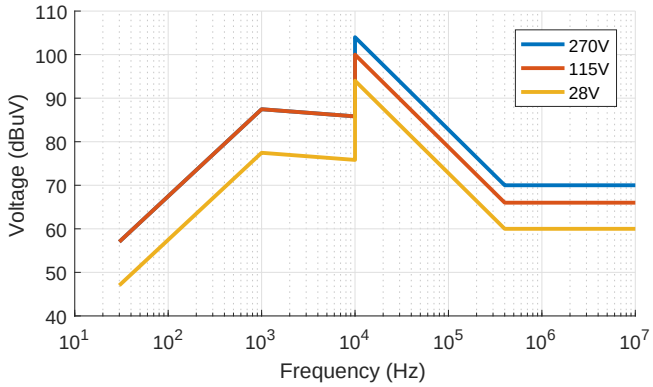


Figure 4.56: MIL-STD-461 CE101 and CE102 conducted emissions, power leads, limits for aircraft applications at different operating voltages (AD or DC).

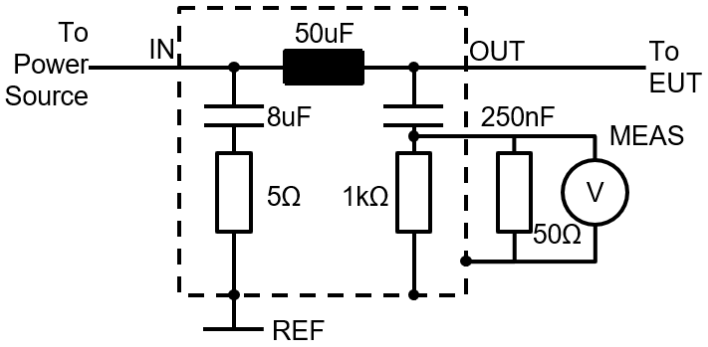


Figure 4.57: MIL-STD-461 Line impedance stabilisation network (LISN).

4.10.2 Multi-stage LC inverter topology

The proposed multi-stage LC EMI filter topology is shown in Figure 4.59. The EMI filter is placed between the source via a linear impedance stabilisation network (LISN) and the inverter's dc-link. The EMI filter consists of n LC branch stages sized for the DM attenuation requirement [108]. The DM voltage u_{dm} is calculated as,

$$u_{dm} = \frac{u_+ - u_-}{2}. \tag{4.230}$$

The EMI filter's simplified DM equivalent circuit is shown in Figure 4.60 where i_{dc} is the inverter current demand and u_{dm} is the equivalent DM measured voltage. Inverter current i_{dc} harmonics is analytically determined for a given phase current, inverter

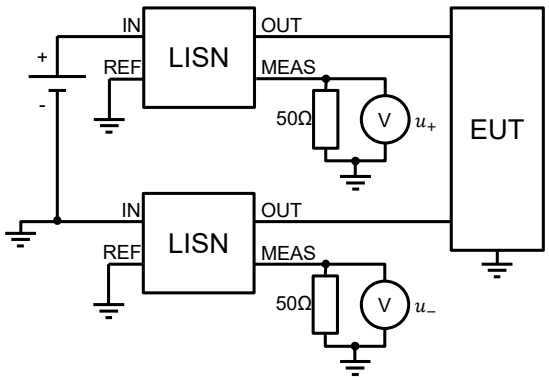


Figure 4.58: Line impedance stabilisation network (LISN) connection to power source and equipment under test (EUT).

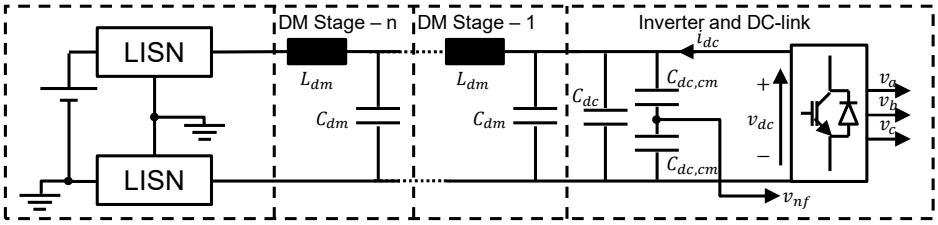


Figure 4.59: Proposed multi-stage LC EMI filter consisting of n differential mode (DM) stages.

switching scheme and frequency, modulation index, and dc-link voltage as discussed in section 4.10.3. Knowing the inverter current harmonics of i_{dc}, the DM measured voltage u_{dm} harmonics is solved using the equivalent circuit and plotted against the MIL-STD-461F limits in Figure 4.56 to check the effectiveness of the DM attenuation. The current harmonics of i_{dc} are determined in section 4.10.3.

4.10.3 Determination of common mode voltage and dc-link current harmonics

Consider a two-level dc to ac inverter as shown in Figure 4.61. Pulse width modulated switched voltages of amplitude equal to that of the dc-link's voltage V_{dc} are applied to the output voltages v_a, v_b, and v_c at a given switching carrier frequency f_c, modulation index M, and baseband frequency ω_o. The relationship between modulation index M and the desired first harmonic baseband $\hat{v}_{a1}$ for a given dc-link V_{dc} is,

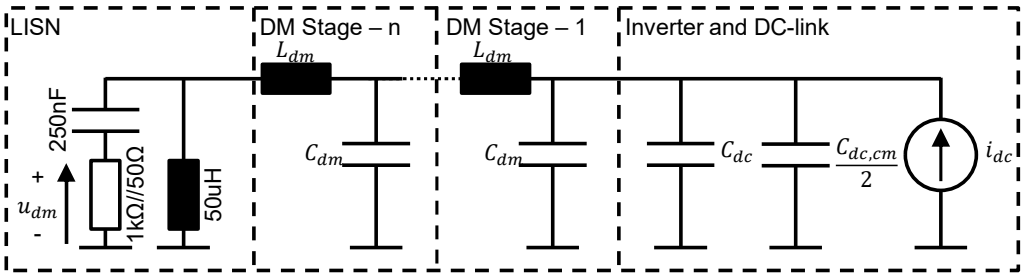


Figure 4.60: Multi-stage LC EMI filter, differential mode (DM) equivalent circuit.

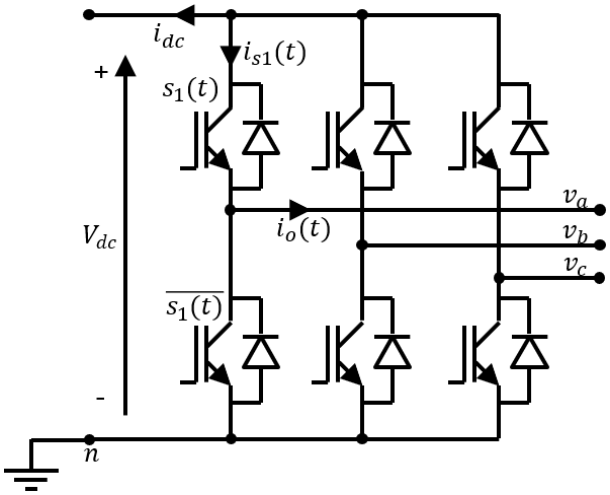


Figure 4.61: Two-level inverter diagram.

$$M = \frac{\hat{v}_{a1}}{V_{dc}/2}. \tag{4.231}$$

Holmes and Lipo in [109] have derived a double Fourier-series solution for the switched output voltage waveform's harmonic spectrum. Its general form $f(t)$ consists of a dc component, harmonics of the baseband fundamental frequency ω_o, carrier frequency ω_c and carrier side bands, as shown below,

$$\begin{aligned} f(t) =& \frac{A_{00}}{2} + \sum_{n=1}^{\infty}[A_{0n}\cos(n\omega_o t) + B_{0n}\sin(n\omega_o t)] \\ &+ \sum_{m=1}^{\infty}\sum_{n=-\infty}^{\infty}[A_{mn}\cos(m\omega_c t + n\omega_o t) + B_{mn}\sin(m\omega_c t + n\omega_o t)], \end{aligned} \tag{4.232}$$

where m and n are the carrier and baseband index variables respectively.

The double Fourier integral defined spectral coefficients A_{mn} and B_{mn} for different switching schemes are provided in [109].

The harmonic solution for symmetrical regular sampled modulation is expressed as [109, p. 137],

$$\begin{aligned} v_{an}(t) =& \frac{V_{dc}}{2} + \frac{2V_{dc}}{\pi}\sum_{n=1}^{\infty}\frac{J_n(n\frac{\omega_o}{\omega_c}\frac{\pi}{2}M)}{n\frac{\omega_o}{\omega_c}}\sin\left(n\left[1+\frac{\omega_o}{\omega_c}\right]\frac{\pi}{2}\right)\cos(n[\omega_o t+\theta_o]) \\ &+ \frac{2V_{dc}}{\pi}\sum_{m=1}^{\infty}\frac{1}{m}J_0\left(m\frac{m}{2}M\right)\sin\left(m\frac{\pi}{2}\right)\cos(m[\omega_c t+\theta_c]) \\ &+ \frac{2V_{dc}}{\pi}\sum_{m=1}^{\infty}\sum_{n=-\infty}^{\infty}\frac{J_n((m+n\frac{\omega_o}{\omega_c})\frac{\pi}{2}M)}{m+n\frac{\omega_o}{\omega_c}}\sin\left(\left[m+n\frac{\omega_o}{\omega_c}+n\right]\frac{\pi}{2}\right) \\ &\times\cos(m[\omega_c t+\theta_c]+n[\omega_o t+\theta_o]). \end{aligned} \tag{4.233}$$

The harmonic coefficients for naturally sampled space vector modulation are taken from [109, p. 282] as follows,

$$A_{00} = V_{dc}, \tag{4.234}$$

$$A_{01} = \frac{MV_{dc}}{2}, \tag{4.235}$$

$$\begin{aligned} A_{0n}+jB_{0n}|_{n>1} =& \frac{\sqrt{3}MV_{dc}}{2\pi}\times \\ &\left[\frac{1}{n+1}\left[\sin\left((n+1)\frac{\pi}{6}\right)\cos\left((n+1)\frac{\pi}{2}\right)\right.\right. \\ &\left.\times\left(\sqrt{3}+2\cos\left((n+1)\frac{\pi}{3}+\frac{\pi}{6}\right)\right)\right] \\ &+\frac{1}{n-1}\left[\sin\left((n-1)\frac{\pi}{6}\right)\cos\left((n-1)\frac{\pi}{2}\right)\right. \\ &\left.\left.\times\left(\sqrt{3}+2\cos\left((n-1)\frac{\pi}{3}-\frac{\pi}{6}\right)\right)\right]\right], \end{aligned} \tag{4.236}$$

$$
\begin{aligned}
A_{mn}+jB_{mn} &= \frac{4V_{dc}}{m\pi^2} \\
&\times \left[\frac{\pi}{6}\sin\left([m+n]\frac{\pi}{2}\right)\left(J_n\left(m\frac{3\pi}{4}M\right)+2\cos\left(n\frac{\pi}{6}\right)J_n\left(m\frac{\sqrt{3}\pi}{4}M\right)\right)\right. \\
&+\frac{1}{n}\sin\left(m\frac{\pi}{2}\right)\cos\left(n\frac{\pi}{2}\right)\sin\left(n\frac{\pi}{6}\right)\left(J_0\left(m\frac{3\pi}{4}M\right)J_0\left(m\frac{\sqrt{3}\pi}{4}M\right)\Big|_{n\neq 0}\right) \\
&+\sum_{k=1}^{\infty}\left(\left(\frac{1}{n+k}\sin([m+k]\frac{\pi}{2})\cos([n+k]\frac{\pi}{2})\sin([n+k]\frac{\pi}{6})\right)\right. \\
&\times\left.\left.\left(J_k\left(m\frac{3\pi}{4}M\right)+2\cos\left([2n+3k]\frac{\pi}{6}\right)J_k\left(m\frac{\sqrt{3}\pi}{4}M\right)\right)\right) \\
&+\sum_{k=1}^{\infty}\left(\frac{1}{n-k}\sin\left((m+k)\frac{\pi}{2}\right)\cos\left([n-k]\frac{\pi}{2}\right)\sin\left([n-k]\frac{\pi}{6}\right)\right. \\
&\times\left.\left.\left(J_k\left(m\frac{3m}{4}M\right)+2\cos\left((2n-3k)\frac{\pi}{6}\right)J_k\left(m\frac{\sqrt{3}\pi}{4}M\right)\right)\right)\right].
\end{aligned}
\tag{4.237}
$$

To determine the inverter output common mode voltage spectrum harmonics $v_{cm,mn}$, the A-, B-, and C- phase contributions are summed up and divided by the number of phases (in this case three). B- and C- phases' fundamental have a phase shift of $n2\pi/3$.

$$v_{cm,mn} = (A_{mn} + jB_{mn})(1 + 2\cos(n2\pi/3)) \tag{4.238}$$

[110] presents a general analytical method for determining the dc-link current harmonics for voltage source switching topologies. The inverter dc-link current is the sum of each phase legs' respective switched currents. For a two level inverter, the switched current of a given phase leg $i_{s1}(t)$ is the product of the phase leg's load current $i_o(t)$ and phase leg PWM binary switching function $s_1(t) \in \{1, 0\}$,

$$i_{s1}(t) = s_1(t) \times i_o(t). \tag{4.239}$$

The product of two time dependent functions is evaluated in the frequency domain by the convolution of the time dependent functions' spectra. As the PWM switching function is defined by a discrete frequency spectrum, the convolution evaluates to an infinite summation in the frequency domain. If sinusoidal load current is assumed, the infinite summation reduces to that of a simple phase shift of the PWM switching function's spectrum.

The waveform harmonics of the switching function $s_1(t)$ can be represented by a double Fourier-series solution whose general form is the same as that of the inverter

output voltage spectrum as shown in (4.232).

Assuming sinusoidal load current of magnitude I_o, fundamental frequency ω_o and phase ϕ,

$$i_o(t) = I_o \cos(\omega_o t + \phi), \tag{4.240}$$

the Fourier series for the phase leg's switched current is,

$$\begin{aligned} i_{s1}(t) =& \frac{\hat{A}_{00}}{2} + \sum_{n=1}^{\infty} [\hat{A}_{0n} \cos(n\omega_o t) + \hat{B}_{0n} \sin(n\omega_o t)] \\ & \sum_{m=1}^{\infty} \sum_{n=-\infty}^{\infty} [\hat{A}_{mn} \cos(m\omega_c t + n\omega_o t) + \hat{B}_{mn} \sin(m\omega_c t + n\omega_o t)], \end{aligned} \tag{4.241}$$

where the harmonic coefficients are,

$$\hat{A}_{00} = \frac{I_o}{2}[A_{01} \cos(\phi) + B_{01} \sin(\phi)], \tag{4.242}$$

$$\hat{A}_{mn} = \frac{I_o}{2}[(A_{m,n-1} + A_{m,n+1}) \cos(\phi) + (B_{m,n-1} - B_{m,n+1}) \sin(\phi)], \tag{4.243}$$

$$\hat{B}_{mn} = \frac{I_o}{2}[(B_{m,n-1} + B_{m,n+1}) \cos(\phi) - (A_{m,n-1} - A_{m,n+1}) \sin(\phi)]. \tag{4.244}$$

The switching function's harmonic coefficients A_{mn} and B_{mn} are determined for a given switching scheme using the expressions derived for the switched voltage waveform harmonic coefficients by setting $V_{dc} = 1$ as $s_1(t) \in \{1, 0\}$. Harmonic coefficients for symmetrical regular sampled modulation are shown in (4.233) and for naturally sampled space vector modulation in (4.234 - 4.237).

These coefficients are substituted into (4.242 - 4.244) to solve for $\hat{A}_{mn}$ and $\hat{B}_{mn}$ and then substituted into (4.241) to give the Fourier series for the phase leg's switched current.

To determine the inverter dc-link current harmonics $\hat{I}_{dc,mn}$, the A-, B-, and C- phase contributions are summed up. B- and C- phase's fundamental current have a $n2\pi/3$ and $-n2\pi/3$ phase shift respectively thus,

$$\hat{I}_{dc,mn} = (\hat{A}_{mn} + j\hat{B}_{mn})(1 + 2\cos(n2\pi/3)). \tag{4.245}$$

4.10.4 EMI filter parameter selection

The analytical EMI filter parameter selection process is as follows and are based on the design steps presented by [111],

1. Define the inverter operating point - modulation index M, DC-link voltage V_{dc}, output phase current i_o at baseband frequency f_o, switching carrier frequency f_c, and inverter switching scheme.
2. Calculate inverter input current spectrum i_{dc} and voltage spectrum v_{cm}.

3. Determine DM voltage spectrum at LISN measurement port u_{dm}.
4. Compare u_{dm} to MIL-STD-461F emission limits to determine baseline required DM attenuation $A_{tt,dm}$.
5. Determine DM filter parameters L_{cm}, C_{dm} for n stages.
6. Compare u_{dm} to MIL-STD-461F emission limits to determine effectiveness of DM filter.
7. Increase/decrease baseline required $A_{tt,dm}$ until realised attenuation is achieved.

The baseline DM attenuation $A_{tt,dm}$ is determined using the DM equivalent circuit shown in Figure. 4.62 for a total dc-link capacitance C_{dc}. The inverter current demand's i_{dc} spectrum is calculated using (4.245) from which the DM voltage spectrum u_{dm} is calculated and plotted against the MIL-STD-461F limits with a -6dBuV margin as shown in Figure 4.63. The

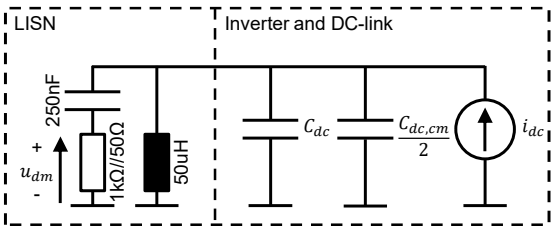


Figure 4.62: Equivalent circuit to determine baseline differential mode (DM) attenuation requirement.

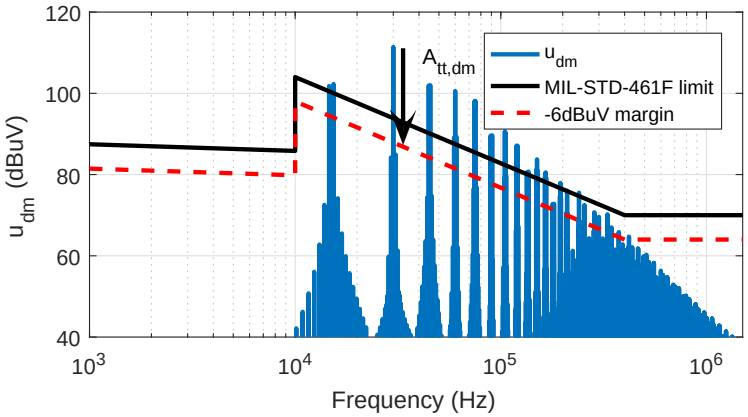


Figure 4.63: Differential mode (DM) baseline voltage spectrum, MIL-STD-461F limits, -6dBuV margin, $V_{dc} = 270$V, $M = 0.39$, $f_o = 150$Hz, $f_c = 15$kHz, $C_{dc} = 40$uF, attenuation $A_{tt,dm}$ of -23.535dBuV at 30kHz.

Raggal *et al.* presents a model based EMI filter design procedure for minimal volume and desired DM attenuation in [84]. Heldwein and Kolar [112] have shown that a multi-

stage LC filter of the same inductance and capacitance for each stage gives the minimal volume. Consider the differential mode equivalent circuit in Figure 4.60. The relationship between the LC filter's DM attenuation $A_{tt,dm}$ at a frequency f_D with n stages of inductance L_{dm} and capacitance C_{dm} is,

$$A_{tt,dm} = \frac{1}{(2\pi f_D)^{2n} L_{dm}^n C_{dm}^n}. \tag{4.246}$$

Empirical equations for inductor volume V_L and mass M_L, as a function of operating current $\hat{I}_{in}$ and inductance L, and capacitor volume V_C and mass M_C, as function of voltage $\hat{U}_{in}$ and capacitance C, have been derived as follows,

$$V_L(L, \hat{I}_{in}) = k_{L1} L \hat{I}_{in}^2 + k_{L2} L + k_{L3} \hat{I}_{in}, \tag{4.247}$$

$$V_C(C, \hat{U}_{in}) = k_{C1} C \hat{U}_{in}^2 + k_{C2}, \tag{4.248}$$

$$M_L(L, \hat{I}_{in}) = m_{L1} L \hat{I}_{in}^2 + m_{L2} L + m_{L3} \hat{I}_{in}, \tag{4.249}$$

$$M_C(C, \hat{U}_{in}) = m_{C1} C \hat{U}_{in}^2 + m_{C2}, \tag{4.250}$$

where k_{L1}, k_{L2}, k_{L3}, and k_{C1}, k_{C2} are inductor and capacitor specific volume parametric constants and m_{L1}, m_{L2}, m_{L3}, and m_{C1}, m_{C2} are inductor and capacitor specific mass parametric constants as described in sections 4.4.1.7 and 4.4.2.

Consider filter topology presented in Figure 4.59. Each stage consists of an inductor L_{dm} and a capacitor C_{dm}. Thus, the total volume V_{DM} and mass M_{DM} of the EMI filter's DM portion are,

$$V_{DM} = (n)(V_L(L_{dm}, \hat{I}_{in}) + V_C(C_{dm}, \hat{U}_{in})), \tag{4.251}$$

$$M_{DM} = (n)(M_L(L_{dm}, \hat{I}_{in}) + M_C(C_{dm}, \hat{U}_{in})). \tag{4.252}$$

Substituting (4.247) and (4.248) into (4.251) for $L = L_{dm}$, $C = C_{dm}$, gives the following expression,

$$V_{DM} = n(k_{L1} L_{dm} \hat{I}_{in}^2 + k_{L2} L_{dm} + 2k_{L3} \hat{I}_{in} + k_{C1} C_{dm} \hat{U}_{in}^2 + k_{C2}) \tag{4.253}$$

Equation (4.246) is solved with respect to L_{dm},

$$L_{dm} = \frac{1}{(2\pi f_D)^2 (A_{tt,dm}^{\frac{1}{n}} C_{dm})}, \tag{4.254}$$

and substituted into (4.253) to get an expression of V_{DM} absent of L_{dm},

$$V_{DM} = n\left(\frac{(k_{L1}\hat{I}_{in}^2 + k_{L2})}{(2\pi f_D)^2 C_{dm}^2 A_{tt,dm}^{\frac{1}{n}}} + k_{L3}\hat{I}_{in} + k_{C1}C_{dm}\hat{U}_{in}^2 + k_{C2}\right). \tag{4.255}$$

To minimise the DM filter volume, V_{DM} is differentiated with respect to C_{dm},

$$\frac{dV_{DM}}{dC_{dm}} = n\left(-\frac{\left(k_{L1}\hat{I}_{in}^2 + k_{L2}\right)}{4\pi^2 {f_D}^2 {C_{dm}}^2 {A_{tt,dm}}^{\frac{1}{n}}} + k_{C1}\hat{U}_{in}^2\right), \tag{4.256}$$

and set equal to zero and solved for the capacitance $C_{dm,\min(V)}$ for minimal volume of the EMI filter with n stages for desired DM attenuation $A_{tt,dm}$,

$$C_{dm,\min(V)} = \sqrt{\frac{\left(k_{L1}\hat{I}_{in}^2 + k_{L2}\right)}{(2\pi f_D)^2 k_{C1}\hat{U}_{in}^2 {A_{tt,dm}}^{\frac{1}{n}}}}. \tag{4.257}$$

Equation (4.257) is substituted back into (4.254),

$$L_{dm,\min(V)} = \sqrt{\frac{k_{C1}\hat{U}_{in}^2}{(k_{L1}\hat{I}_{in}^2 + k_{L2})(2\pi f_D)^2 A_{tt,dm}^{\frac{1}{n}}}} \tag{4.258}$$

This model based procedure is repeated to minimise EMI filter's mass with n stages for a desired DM attenuation $A_{tt,dm}$ by appropriately substituting the specific volume parametric constants k_{L1}, k_{L2}, k_{L3}, k_{C1}, k_{C2} with the specific mass parametric constants m_{L1}, m_{L2}, m_{L3}, m_{C1}, m_{C2} in (4.257) and (4.258), and then solving for capacitance $C_{dm,\min(M)}$ and inductance $L_{dm,\min(M)}$.

$$C_{dm,\min(V)} = \sqrt{\frac{\left(m_{L1}\hat{I}_{in}^2 + m_{L2}\right)}{(2\pi f_D)^2 m_{C1}\hat{U}_{in}^2 {A_{tt,dm}}^{\frac{1}{n}}}}. \tag{4.259}$$

$$L_{dm,\min(V)} = \sqrt{\frac{m_{C1}\hat{U}_{in}^2}{(m_{L1}\hat{I}_{in}^2 + m_{L2})(2\pi f_D)^2 A_{tt,dm}^{\frac{1}{n}}}} \tag{4.260}$$

The minimised EMI filter mass is determined,

$$M_{DM} = (n)(M_L(L_{dm,\min(M)}, \hat{I}_{in}) + M_C(C_{dm,\min(M)}, \hat{U}_{in})). \tag{4.261}$$

4.10.4.1 Example EMI filter design

The following two-stage ($n = 2$) EMI filter design case for operating conditions $V_{dc} =$ 270V, $M = 0.9$, $f_o = 483.3$Hz, $f_c = 15$kHz, $I_o = 9.29$A, centralised topology is considered. Inductance $L_{dm} = 278$uH and capacitance $C_{dm} = 3.265$uF were calculated. The resultant simulated voltage spectrum u_+, u_- are plotted in Figure 4.64. Both u_+, u_- spectrums are below the MIL-STD-461F emissions limit and -6dBuV margin.

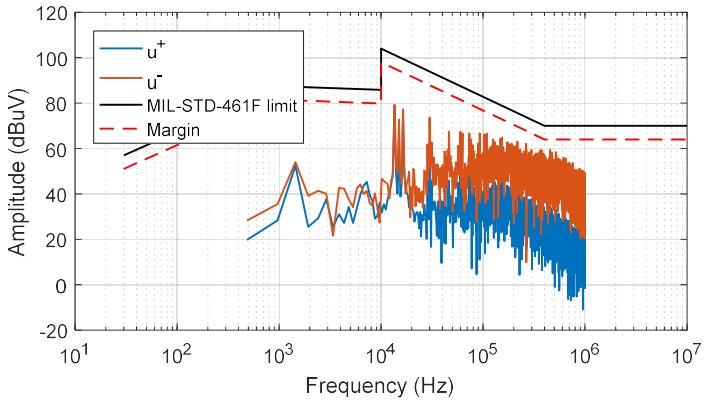


Figure 4.64: Simulated power lead voltage spectrum, MIL-STD-461F limits, -6dBuV margin, $n = 2$, $L_{dm} = 278$uH, $C_{dm} = 3.265$uF, $V_{dc} = 270$V, $M = 0.9$, $f_o = 483.3$Hz, $f_c = 15$kHz, $I_o =$ 9.29A, $C_{dc} = 1$uF, $C_{dc,cm} = 47.1$uF.

4.10.5 Inverter input EMI filter and dc-link capacitor - failure rate vs. mass

The inverter input EMI filter and dc-link capacitor design process is presented in Figure 4.65. Each key step is indexed with a letter and its corresponding section is referenced in Table 4.24. Subscripts "L, dm" and "C, dm" refer to the EMI filter's inductors and capacitors respectively. Subscript "C, dc" refer to dc-link capacitor. A general component sum equation is defined as follows,

$$X_\Sigma = n(X_{L,dm} + X_{C,dm}) + X_{C,dc} \tag{4.262}$$

where X can represent volume V, mass M, or failure rate λ. Regarding shorthand notation for inductor and capacitor empirical sizing constants, $x_{y\{1,2,\ldots,N\}} = \{x_{y,1}, x_{y,2}, \ldots, x_{y,N}\}$ where x represents volume constant k or mass constant m, and y represents inductor L or capacitor C.

For a given lifetime profile (internal/external), inductor temperature rise T_r, and capacitor voltage rating $V_{c,rated}$; the failure rate $\lambda_{L,dm}$, $\lambda_{C,dm}$, and $\lambda_{C,dc}$ are determined at

steps (a)-(c) in Figure 4.65. The total EMI-filter and dc-link capacitor failure rate λ_{total} is determined at step (d) using (4.262), given number of stages n.

The lifetime profile defines ambient temperature and pressure T_a and P_a for either internal/external conditions. These parameters, along with T_r, and desired core material are provided to the inductor parameter LUT at step (d), from which inductor empirical volume and mass equation constants $k_{L\{1,2,3\}}$ and $m_{L\{1,2,3\}}$ respectively are provided.

For given modulation index m, dc-link voltage V_{dc}, inverter output current magnitude I_o, current fundamental frequency f_o, inverter switching carrier frequency f_c, current phase ϕ, dc-link capacitor C_{dc}, and switching scheme; the dc-link current spectrum i_{dc} is determined at step (f). The LISN equivalent differential mode voltage u_{dm} is determined from the LISN equivalent circuit at step (g). This is compared with the distortion spectrum limit from which the required attenuation $A_{tt,dm}$ at frequency f_D is determined.

For "n" stages, $k_{L\{1,2,3\}}$, $k_{C\{1,2\}}$, $A_{tt,dm}$, f_D, $\hat{U}_{in}$, and $\hat{I}_{in}$; the optimal inductance L_{dm} and capacitance C_{dm} is calculated for minimum EMI filter volume at step (h). The value $\hat{U}_{in}$ is set equal to the capacitor voltage rating $V_{c,rated}$. The inductor's rated current $\hat{I}_{in}$ is calculated from M, V_{dc}, I_o as follows,

$$\hat{I}_{in} = \frac{3MV_{dc}I_o}{4}. \tag{4.263}$$

The effectiveness of the designed filtering is double checked by numerically solving its equivalent circuit at step (i) to ensure desired attenuation $A_{tt,dm}$ is achieved. LISN differential voltage u_{dm} is compared to the distortion spectrum limits using the EMI filter circuit and calculated i_{dc}. If u_{dm} exceeds this limit, the discrepancy attenuation $A'_{tt,dm}$ is calculated. The input $A_{tt,dm}$ is compensated by $A'_{tt,dm}$ and L_{dm}, C_{dm} are calculated again at step (h). This is repeated until u_{dm} no longer exceeds its distortion spectrum limits.

Once, L_{dm} and C_{dm} have been finalised and the desired attenuation is achieved, the EMI filter inductors' and capacitors' mass and volume (i.e., $M_{L,dm}$, $M_{C,dm}$, $V_{L,dm}$, $V_{C,dm}$) are determined at step (j).

The dc-link capacitor's mass $M_{C,dc}$ and volume $V_{C,dc}$ are calculated from $V_{c,rated}$ and C_{dc} at step (k)

The total component volume V_Σ is determined from $V_{C,dc}$, $V_{C,dm}$, $V_{L,dm}$, and n at step (l). The case volume V_{case} is determined at step (m) from V_Σ, followed by the case mass M_{case} at step (n).

The total component mass M_Σ is determined from $M_{C,dc}$, $M_{C,dm}$, $M_{L,dm}$ and n at step (n) using (4.262). The total mass M_{total} is the sum of total component mass M_Σ and case mass M_{case} and determined at step (p).

The inverter input EMI filter and dc-link capacitor design process of Figure 4.65 is utilised to determine how the capacitor voltage rating $V_{c,rated}$, inductor material, number of stages, dc-link capacitor C_{dc}, and lifetime profile influences resultant design's overall

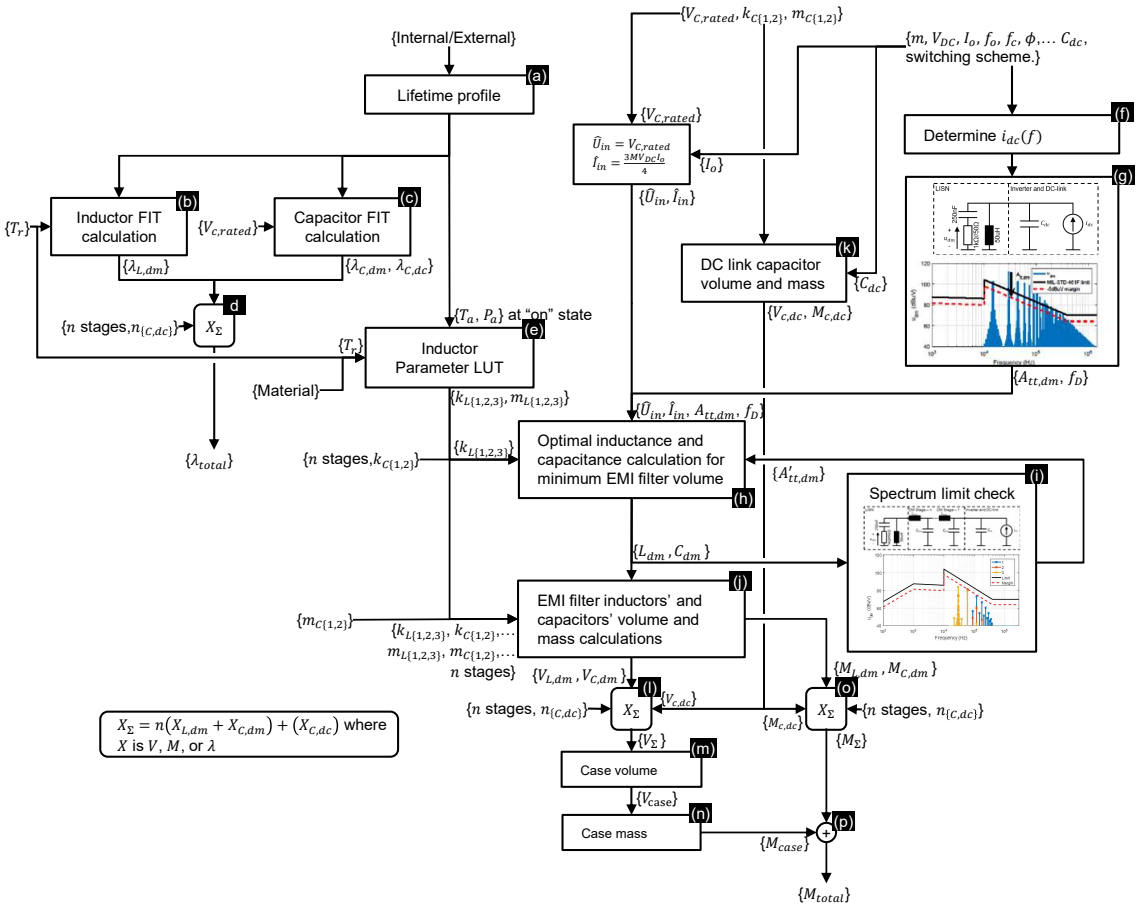


Figure 4.65: Inverter input EMI filter and dc-link capacitor design process.

Table 4.24: Section references for the Figure 4.65.

Index	Reference	Index	Reference
(a)	§4.3.2	(i)	§4.10.2
(b)	§4.3.3	(j)	§4.4.1.7, §4.4.2
(c)	§4.3.3	(k)	§4.4.2
(d)	(4.262)	(l)	(4.262)
(e)	§4.4.1.7	(m)	§4.5
(f)	§4.10.3	(n)	§4.5
(g)	§4.10.4	(o)	(4.262)
(h)	§4.10.4	(p)	n/a

mass and failure rate for a fixed electrical power demand. The input variable sets for a considered 1.1kVA inverter case study is shown in Table 4.25.

For each of the five inductor core materials, the EMI filter and dc-link capacitor designs' failure rate and mass are determined. The results for silicon steel as the inductor core material and internal/external lifetime profiles is shown in Figure 4.66. The failure rate vs. mass Pareto-frontier for internal and external lifetime profiles have been determined. Internal designs generally have a lower failure rate and higher mass compared to that of external designs. The lower failure rate is due to the more hospitable internal operating environment. The higher mass is due to requirement of two dc-link capacitors

Table 4.25: Input variables of input EMI filter and dc-link capacitor design process for 1.1kVA inverter case study.

Variable	Value	Units
M	1	
V_{dc}	270	V
I_o	5.54	Apk
f_o	400	Hz
f_c	15	kHz
Power factor	0.98	
Switching scheme	Sinusoidal PWM	
T_r	30	°C
C_{dc}	{1, ..., 400}	uF
n stages	{1, 2, 3}	
$V_{c,rated}$	{450, 700, 1000, 1200}	V
Lifetime profile	{Internal, External}	
Inductor core material	{Silicon Steel, Amorphous, Iron-powder, Nanocrystalline, Ferrite}	

of double the capacitance for the equivalent external dc-link design.

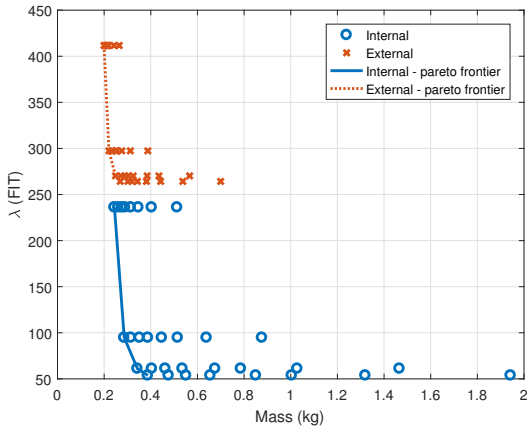
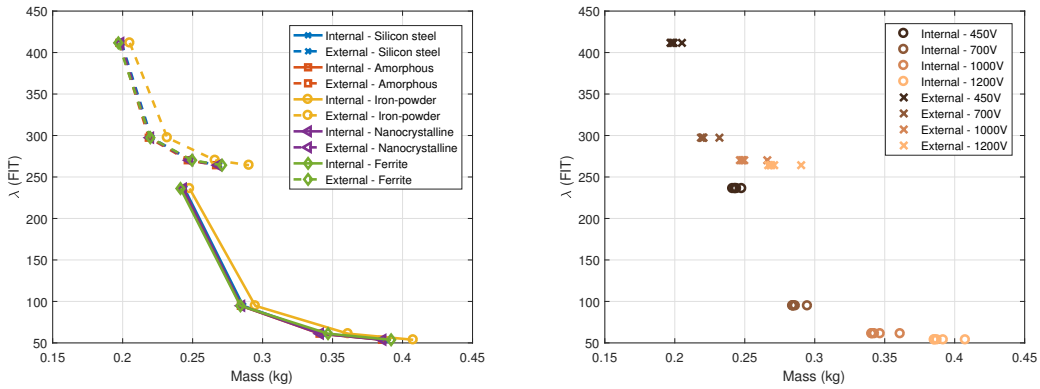


Figure 4.66: EMI filter and dc-link capacitor with silicon steel core inductors for 1.1kVA inverter - failure rate vs. mass.

The Pareto-efficient designs for the five inductor core materials and internal/external lifetime profiles is plotted in Figure 4.67 (a). Inductor material has small-influence on overall mass. Designs with iron-powder and ferrite cores are slightly heavier compared to that of silicon steel, amorphous, and nano-crystalline. Designs with iron-powder inductors are 8% heavier than that of the lightest design with comparable failure rates.

The Pareto-efficient designs are labelled by capacitor voltage ratings and plotted as shown in Figure 4.67 (b). As capacitor rating increases, overall failure rate decreases and mass increases. Higher voltage rated capacitors have greater volume and mass. Greater capacitor volume contributes to greater case volume and greater case mass.

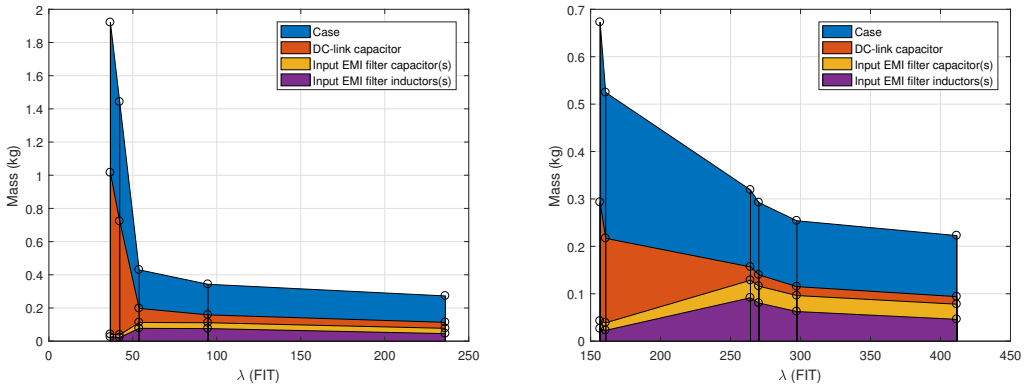
The total mass breakdown of internal and external lifetime profile designs and silicon steel core inductors with respect to failure rate is shown in Figure 4.68. For most designs,



(a) Inductor core material. **(b)** Capacitor voltage rating.

Figure 4.67: Failure rate vs. mass of Pareto-efficient 1.1kVA inverter designs.

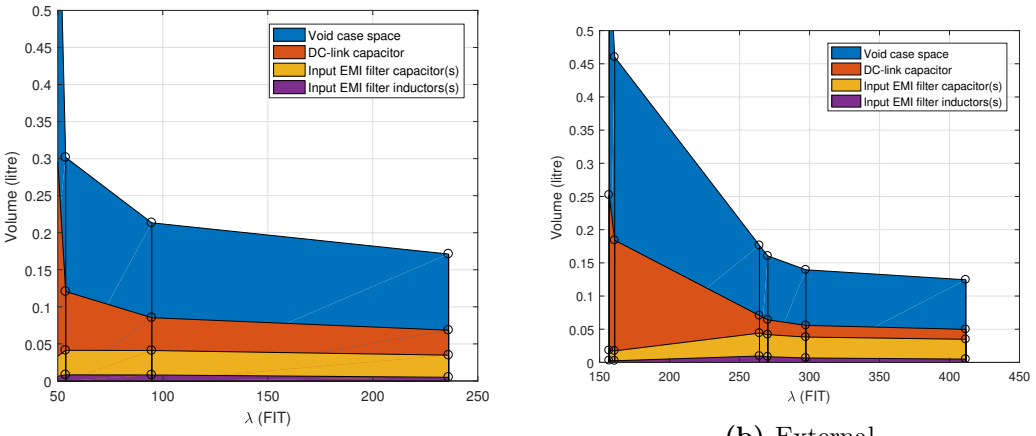
nearly 60% of the total mass is that of the case. This emphasises the significance of EMI filter and dc-link capacitor volume minimisation, as this would lead to minimum case volume and overall case mass.



(a) Internal **(b)** External

Figure 4.68: Mass breakdown by failure rate for internal and external lifetime profiles with silicon steel, 1.1kVA inverter.

The total volume breakdown of internal and external lifetime profile designs and silicon steel core inductors with respect to failure rate is shown in Figure 4.69. It can be seen that inductors contribute a small proportion (at most 10%) to the total volume of passive components. The majority of it is contributed by capacitors.



(a) Internal

(b) External

Figure 4.69: Volume breakdown by failure rate for internal lifetime profiles, 1.1kVA inverter.

4.11 Conclusion

In this chapter, the toolbox realisation for optimal sizing of aerospace electric drive systems was presented. The toolbox consisted of design procedures and models fro different system components and modelling domains. The considered components were inductors, capacitors, heat sinks, semiconductors, electric machine, and cable. These components make up electric drive subsystems such as the inverter, output LC filter, and input EMI filter. The modelling domains were electrical, electromechanical, power quality, mass, volume, thermal, and failure rate.

The high-level design concept for the optimal aerospace electric drive system sizing is as follows. For a given topology, actuation requirement, and set of constraints; generate a set of Pareto optimal designs with respect to mass and failure rate for each of the component of the electrical drive system. Each component is designed using its own respective design algorithm. The inputs and constraints of each components' respective design algorithm are coordinated at a system level such that all resultant components are intercompatible. When sets of optimal designs for each system component have been generated, they are mixed and matched in every permutation iteratively to generate unique combinations of components and thus a set of unique designs. Each unique design's system mass and failure rate is determined from which Pareto-efficient designs are identified and down-selected. These designs will go through an additional level of refinement, including controller tuning and controllability testing as described in Chapter 5, and high-frequency analysis in Chapter 6.

Failure rates of inductors, capacitors, and semiconductors were determined using FIDES guide 2009 for a typical lifetime profile of a medium haul civil aviation aircraft. The guide provided the failure rate equations as function of voltage, current, temperature, application, vibration, and environmental stressors. Insulation lifetime was determined

as function of temperature and life time profile.

Inductors were sized for inductance and current rating. The core geometry, and ratios were defined and fixed. The magnetic operating point was determined considering core geometry, material properties, and gap fringing effect. Copper losses and core losses were determined. The temperature rise was calculated for natural convection and radiation. Inductors design were optimised using the bisection method for minimal mass for an allowed temperature rise. The inductor design procedure was repeated for different values of inductance and current rating to generate an inductor design look-up table. The system level design process pull designs from the look-up table, thus reducing computational load. Capacitors were sized empirically as a function of rated voltage and capacitance.

The enclosure's volume and mass is estimated by scaling with respect to the total volume of the passives. A case scale factor of 2.5 was assumed as estimated from an in-house demonstrator inverter. One may consider this scale factor as dubious as the space required for cable-routing, PCB, connectors, and mounting solutions have not been factored in. Future work and further investigation looking at a wide range of demonstrator inverters will provide a more representative case scale factor.

A design procedure for optimal sizing of a surface mounted permanent magnet synchronous machine was implemented. The main steps of the procedure are: 1) initial stator and rotor sizing, 2) phase resistance, phase inductance, and magnetic flux linkage calculation, 3) air-gap, magnet and tooth-tip sizing, and 4) thermal calculation. Initial stator and rotor sizing was done using fundamental electric machine equations where the main dependent variables are torque per rotor volume and current density. The stator inner/outer diameters, back iron thickness, rotor diameter, stack length were determined. The stator resistance is determined from the stator slot geometry and copper fill factor. For a given nominal torque/speed, switching frequency, dc-link voltage, and current ripple requirement, the required stator inductance and magnetic flux linkage were solved. These are the target stator inductances and magnet flux linkage for which the magnet and stator teeth dimensions were sized. The stator flux permanence paths were identified and quantified to determine the relationship between stator teeth geometry and stator inductance. A simplified open-circuit magnet reluctance circuit is utilised to represent the relationship between magnetic flux linkage, magnet operating point, and magnet/air-gap dimensions. The air-gap, tooth-tip, and magnet dimensions were determined to provide the required stator inductance and magnetic flux linkage. An error function was defined with respect to calculated over required stator inductance, calculated over required magnetic flux linkage, and dimensions of the air-gap, stator tooth tip, and magnet. This error function was minimised using pattern search algorithm. A lumped parameter thermal network was utilised to determine the temperature of the machine. The machine's components' geometry are approximated by cylinders where axial and radial heat flows are assumed to be independent of one another. The equivalent thermal resistance from

frame to ambient was determined considering natural convection, radiation, and conduction. Ambient conditions at altitude were accounted for in calculating frame to ambient thermal resistance.

Cable's were sized from manufacturer brochures. The sourced cables were aerospace standard cables. De-rating factors were determined considering altitude and bundle number.

The LC output filter is sized to condition the inverter's output such that transmission line effects are reduced by reducing its effective dv/dt, attenuate the output phase voltage harmonics so they don't exceed MIL-STD-704F distortion spectrums, and limit output phase current ripple to ensure current control stability. The common mode and differential mode equivalent impedance networks were utilised. The LC filter's cut-off frequency was determined from the required attenuation to bring the main switching harmonic below that of the MIL-STD-704F distortion spectrum limit. The inductor was selected for a given allowable output phase current ripple. The relationship between LC filter mass, failure rate, allow phase current ripple, and capacitor voltage rating was determined. Increase in voltage rating leads to a reduction in failure rate but an increase volume. Increasing the allowable current ripple decreases required inductance and decreases inductor mass.

The inverter's transistor and diode conduction and switching losses were determined for a given modulation index, dc-link voltage, output phase current, phase, and switching frequency. The power module's steady state thermals were modelled using an equivalent thermal network. Junction to case thermal resistances were provided by the manufacturer.

Parallel plate finned heat sink is used to dissipate heat from the inverter's power module to ambient. The heat sinks are optimally sized considering natural convection, operating environment, and radiation. A look-up table was generated of optimally heat-sink designs from which the system level design process can pull from, alleviating computational load. The relationship between heat-sink mass and failure rate is determined. An increase in heat sink mass lead to a decrease in both semiconductor junction temperatures and failure rates.

The multi-stage LC inverter was determined to ensure MIL-STD-461F's CE101 and CE102 conducted emissions limits are adhered to. The dc-link current and voltage was analytically determined from Holmes and Lipo's double Fourier-series solution for switching output voltage waveform's harmonic spectrum for a given inverter operating point. The DM voltage spectrum at LISN measurement port was determined from which the required attenuation is calculated. The inductance and capacitance for a n-stage input EMI filter was determined. The achieved attenuation was rechecked with respect to distortion spectrum limits. If attenuation is not achieved, the required attenuation is readjusted a new inductance and capacitance values are calculated. This process is repeated until the

desired attenuation is achieved.

Chapter 5

Drive level - dynamic modelling and control

5.1 Overview

In this chapter, the dynamic modelling and automated controller tuning of designed electric drive system of chapter 4 is presented. The main purpose of the presented automated controller tuning procedure is validate that the designed system is controllable, stable, and meets desired dynamics. It is of no use designing an optimal system of minimal mass within failure rate constraints if it's uncontrollable or its dynamic performance does not meet criteria. Prefer back to Figure 4.1 to see how dynamic modelling and control fits into the overall system sizing; it is catalogued under "Refinement and Validation". Dynamic modelling and control is not directly integrated in the optimal electric drive design and sizing process as time based control simulations are relatively computational demanding.

An overview of the full system control scheme is shown in Figure 5.1. The flap position θ^* is set by the slats flap control computer SFCC. Each flap is controlled by its corresponding actuator control electronics (ACE). Each flap actuation system consists of two identical drive lanes, labelled L1 and L2 respectively. Both lanes drive the actuator via a differential gearbox DGB, transmission torque tube, and gear box GB to move the flap.

The ACE takes position and operating mode set points from the slats flaps control computer (SFCC) and reports back status updates from its actuator and PCU lanes. The ACE has three operating modes,

1. Hold - the default state when flap position is fixed, both lanes' EB are locked and the machines are idle. This occurs if the actuator's position is equal to that of the SFCC's set point or if both PCU lanes are faulted.
2. Move - if no faults are present and SFCC's actuator position's set point does not

equal to measured actuator's position, both E/B are unlocked and both lanes drive the actuator load via the differential gearbox to the desired position.

3. Fault - if a fault develops in one PCU lane, that lane's EB is locked. The none-faulted lane's EB is unlocked and the lane drives the actuator load via the differential gearbox. This fault is reported back to the SFCC.

Each lanes' PCU is responsible for speed control, current control with state observer, and generating the correct switching scheme for desired voltage command. The PCU monitors the inverter and machine's operating status.

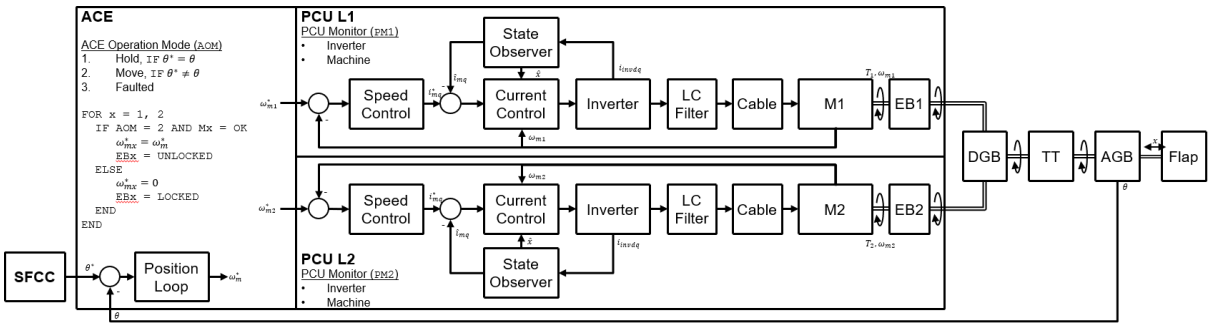


Figure 5.1: Full actuator overview for control analysis.

The two system models that need to be realised are:

1. Electrical model - represents the electrical dynamics of each PCU lane consisting of the inverter, LC filter, cable and machine.
2. Mechanical model - represents the mechanical dynamics of each machine of the two PCU lanes, E/B, the differential gear box, torque tube, actuator, and flap.

The three control loops that need to be realised are:

1. Current loop - controls the dq currents $i_{m,dq}$ of each machine in their respective lane such that it matches the desired current set point $i^*_{m,dq}$ as determined by the speed loop. The current controller outputs voltage commands $v_{inv,dq}$ to the inverter.
2. Speed loop - controls the speed of each machine ω_m in their respective lane such that it matches the desired speed set point ω^*_m as determined by the position loop. It outputs the current set point $i^*_{m,dq}$ to the inner current control loop.
3. Position loop - controls actuator position θ for a given actuator such that it matches the desired position set point θ^* as determined by the SFCC. The position controller outputs speed set points ω^*_m to the inner speed control loops.

The presence of the LC sine-wave output filter can lead to unstable resonance if not accounted for in the control design. Thus, a robust full state feedback gain-scheduled linear quadratic regulator (LQR) controller has been used to ensure stable machine current control and attenuation of the output filter's intrinsic resonance. To reduce the number of additional sensors required in hardware implementation for the full state feedback

control scheme, a full state-space gain-schedule observer is used in conjunction with the controller.

5.2 Electrical system dq representation

The dq equivalent circuit of the inverter, output filter, and machine is shown in Figure 5.2.

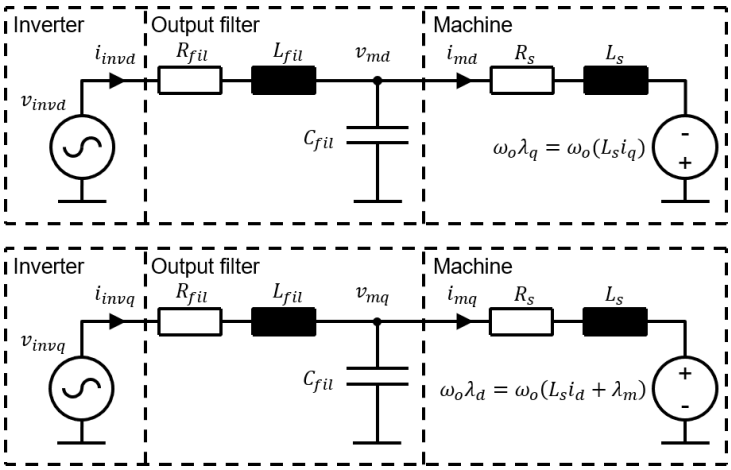


Figure 5.2: System dq equivalent circuit considering inverter, LC output filter, and machine.

The dq voltage equations v_{md}, v_{mq} for a non-salient permanent magnet synchronous machine are as follows where R_s and L_s are the stator resistance and inductance, ω_o is the electrical frequency, λ_m is the machine's magnetic flux constant,

$$v_{md} = R_s i_{md} + L_s \frac{di_{md}}{dt} - \omega_o L_s i_{mq}, \tag{5.1}$$

$$v_{mq} = R_s i_{mq} + L_s \frac{di_{mq}}{dt} + \omega_o \left(L_s i_{md} + \lambda_m\right). \tag{5.2}$$

The machine electromagnetic torque T_{em} is as follows where p is the number of pole pairs,

$$T_{em} = \frac{3}{2} p \lambda_m i_{mq}. \tag{5.3}$$

The dq inverter voltage equations v_{invd}, v_{invq} are as follows where R_{fil} and L_{fil} are the output filter's inductors' series resistance and inductance, and C_{fil} is the output filter's phase-to-neutral capacitor's capacitance and i_{invd}, i_{invq} are the inverter's dq output current,

$$v_{invd} = R_{fil} i_{invd} - \omega_o L_{fil} i_{invq} + L_{fil} \frac{di_{invd}}{dt} + v_{md}, \tag{5.4}$$

$$v_{invq} = R_{fil} i_{invq} + \omega_o L_{fil} i_{invd} + L_{fil} \frac{di_{invq}}{dt} + v_{mq}. \tag{5.5}$$

Applying KCL at the nodes v_{md}, v_{mq} gives the inverter output current equations,

$$i_{invd} = -\omega_o C_{fil} v_{mq} + C_{fil}\frac{dv_{md}}{dt} + i_{md}, \tag{5.6}$$

$$i_{invq} = \omega_o C_{fil} v_{md} + C_{fil}\frac{v_{mq}}{dt} + i_{mq}. \tag{5.7}$$

The equivalent circuit shown in Figure 5.2 is modified to include the dq low-frequency cable characteristics using a single branch Γ-type lumped parameter cable model as shown in Figure 5.3. The use of a single branch lumped parameter cable model is sufficient for controller design as only control and observation of system states' base band harmonic component is considered. The cable's phase to ground capacitance C_{cpg} is parallel with the output filter's capacitance C_{fil}. The cable phases' series resistance R_{cs} and L_{cs} are in series with stator resistance R_s and inductance L_s. The values R_{cs}, L_{cs}, and C_{cpg} are determined by multiplying the cable length l_c by their respective per unit length value, as indicated with the ' superscript,

$$\begin{aligned} R_{cs} &= l_c R'_{cs}, \\ L_{cs} &= l_c L'_{cs}, \\ C_{cpg} &= l_c C'_{cpg}. \end{aligned} \tag{5.8}$$

Equations (5.1 - 5.7) are modified to include the cable characteristics as shown,

$$v_{fd} = (R_s + R_{cs})i_{md} + (L_s + L_{cs})\frac{di_{md}}{dt} - \omega_o(L_s + L_{cs})i_{mq}, \tag{5.9}$$

$$v_{fq} = (R_s + R_{cs})i_{mq} + (L_s + L_{cs})\frac{di_{mq}}{dt} + \omega_o\left((L_s + L_{cs})i_{md} + \lambda_m\right), \tag{5.10}$$

$$v_{invd} = R_{fil} i_{invd} - \omega_o L_{fil} i_{invq} + L_{fil}\frac{di_{invd}}{dt} + v_{fd}, \tag{5.11}$$

$$v_{invq} = R_{fil} + \omega_o L_{fil} i_{invd} + L_{fil}\frac{di_{invq}}{dt} + v_{fq}, \tag{5.12}$$

$$i_{invd} = -\omega_o(C_{fil} + C_{cpg})v_{mq} + (C_{fil} + C_{cpg})\frac{dv_{md}}{dt} + i_{md}, \tag{5.13}$$

$$i_{invq} = \omega_o(C_{fil} + C_{cpg})v_{md} + (C_{fil} + C_{cpg})\frac{v_{mq}}{dt} + i_{mq}. \tag{5.14}$$

Using a single branch Γ-type cable model means the number of system states remain the same. The system is described with three pairs of dq voltage and currents equations.

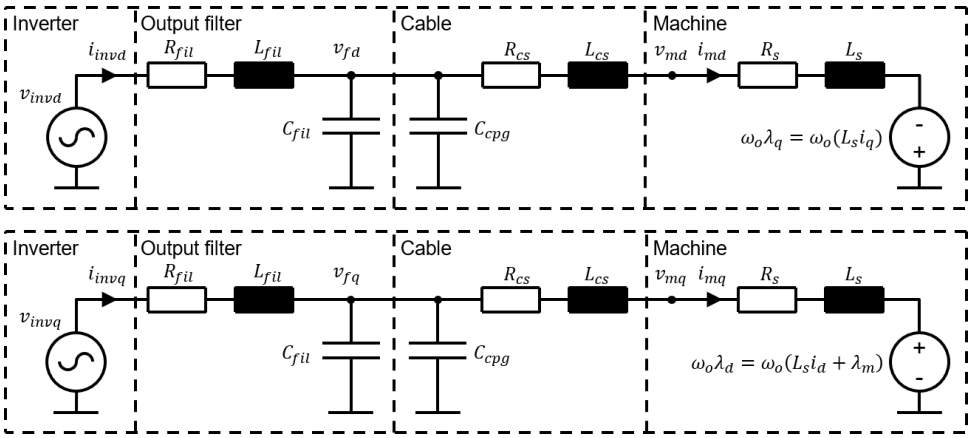


Figure 5.3: System dq equivalent circuit considering inverter, LC output filter, cable, and machine.

5.3 Electrical system state-space representation

5.3.1 Continuous state-space representation

The generalised state-space representation equations in the continuous domain for an n^{th} order linear time invariant (LTI) system with r inputs, m outputs, and u disturbances are as follows,

$$\dot{\mathbf{x}}(t) = \mathbf{A}\mathbf{x}(t) + \mathbf{B}\mathbf{u}(t) + \mathbf{E}\mathbf{d}(t), \tag{5.15}$$

$$\mathbf{y}(t) = \mathbf{C}\mathbf{x}(t), \tag{5.16}$$

where,

- $\mathbf{x}$ is the $n \times 1$ time-varying state vector,
- $\dot{\mathbf{x}}$ is the derivative of the $n \times 1$ time-varying state vector $\mathbf{x}$,
- $\mathbf{A}$ is the $n \times n$ constant state matrix,
- $\mathbf{B}$ is the $n \times p$ constant input matrix,
- $\mathbf{u}$ is the $p \times 1$ time-varying input vector,
- $\mathbf{C}$ is the $m \times n$ constant output matrix,
- $\mathbf{E}$ is the $n \times w$ constant disturbance matrix,
- $\mathbf{d}$ is the $w \times 1$ time-varying disturbance vector,
- $\mathbf{y}$ is the $m \times 1$ constant output matrix,

Equations (5.15) is solved with respect to $\mathbf{x}$ and substituted into (5.16) to get the following transfer function representation,

$$\mathbf{y}(s) = \mathbf{C}(s\mathbf{I} - \mathbf{A})^{-1}\mathbf{B}\mathbf{u}(s) + \mathbf{C}(s\mathbf{I} - \mathbf{A})^{-1}\mathbf{E}\mathbf{d}(s), \tag{5.17}$$

where s is the continuous transfer function.

For the reader's convenience, equations (5.15 - 5.16) have been rewritten as follows

where the matrices' and vectors' subscripts represent their respective dimensions,

$$\dot{\mathbf{x}}_{n\times1}(t) = \mathbf{A}_{n\times n}\mathbf{x}_{n\times1}(t) + \mathbf{B}_{n\times p}\mathbf{u}_{p\times1}(t) + \mathbf{E}_{n\times w}\mathbf{d}_{w\times1}(t), \tag{5.18}$$

$$\mathbf{y}_{m\times1}(t) = \mathbf{C}_{m\times n}\mathbf{x}_{n\times1}(t). \tag{5.19}$$

The system dq voltage and current equations of (5.9 - 5.14) are solved with respect to their respective differential terms and then arranged into state-space representation (5.15 - 5.16) where,

$$\mathbf{A} = \begin{pmatrix} -\frac{(R_s+R_{cs})}{(L_s+L_{cs})} & \omega_o & 0 & 0 & \frac{1}{(L_s+L_{cs})} & 0 \\ -\omega_o & -\frac{(R_s+R_{cs})}{(L_s+L_{cs})} & 0 & 0 & 0 & \frac{1}{(L_s+L_{cs})} \\ 0 & 0 & -\frac{R_{fil}}{L_{fil}} & \omega_o & -\frac{1}{L_{fil}} & 0 \\ 0 & 0 & -\omega_o & -\frac{R_{fil}}{L_{fil}} & 0 & -\frac{1}{L_{fil}} \\ -\frac{1}{(C_{fil}+C_{cpg})} & 0 & \frac{1}{(C_{fil}+C_{cpg})} & 0 & 0 & \omega_o \\ 0 & -\frac{1}{(C_{fil}+C_{cpg})} & 0 & \frac{1}{(C_{fil}+C_{cpg})} & -\omega_o & 0 \end{pmatrix}, \tag{5.20}$$

$$\mathbf{B} = \begin{pmatrix} 0 & 0 & \frac{1}{L_{fil}} & 0 & 0 & 0 \\ 0 & 0 & 0 & \frac{1}{L_{fil}} & 0 & 0 \end{pmatrix}^T, \tag{5.21}$$

$$\mathbf{E} = \begin{pmatrix} 0 & -\frac{\lambda_m}{(L_s+L_{cs})} & 0 & 0 & 0 & 0 \end{pmatrix}^T, \tag{5.22}$$

$$\mathbf{x} = \begin{pmatrix} i_{md} & i_{mq} & i_{invd} & i_{invq} & v_{fd} & v_{fq} \end{pmatrix}^T, \tag{5.23}$$

$$\mathbf{u} = \begin{pmatrix} v_{invd} & v_{invq} \end{pmatrix}^T, \tag{5.24}$$

$$\mathbf{d} = (\omega_o). \tag{5.25}$$

Output matrix $\mathbf{C}$ can have different variants depending on the desired system output $\mathbf{y}$ that is observed, tracked, and/or controlled. Two variants of $\mathbf{C}$ are presented, $\mathbf{C}_{im}$ which returns the machine dq current states i_{md}, i_{mq}, and $\mathbf{C}_{inv}$ which returns the inverter current states i_{invd}, i_{invq} when multiplied by state vector $\mathbf{x}$,

$$\mathbf{C}_{im} = \begin{pmatrix} 1 & 0 & 0 & 0 & 0 & 0 \\ 0 & 1 & 0 & 0 & 0 & 0 \end{pmatrix}, \tag{5.26}$$

$$\mathbf{C}_{inv} = \begin{pmatrix} 0 & 0 & 1 & 0 & 0 & 0 \\ 0 & 0 & 0 & 1 & 0 & 0 \end{pmatrix}. \tag{5.27}$$

5.3.2 Discrete state-space representation

The discrete state-space representation is as follows where $\mathbf{A}_z$, $\mathbf{B}_z$, $\mathbf{E}_z$ are the discrete state-space coefficient matrices of the continuous state-space coefficient matrices $\mathbf{A}$, $\mathbf{B}$, $\mathbf{E}$ respectively, z is the discrete transfer function, and $\mathbf{I}$ is the identity matrix,

$$z\mathbf{x} = \mathbf{A}_z\mathbf{x} + \mathbf{B}_z\mathbf{u} + \mathbf{E}_z\mathbf{d}, \tag{5.28}$$

$$\mathbf{y} = \mathbf{C}\mathbf{x}, \tag{5.29}$$

$$\mathbf{y} = \mathbf{C}(z\mathbf{I} - \mathbf{A}_z)^{-1}\mathbf{B}_z\mathbf{u} + \mathbf{C}(z\mathbf{I} - \mathbf{A}_z)^{-1}\mathbf{E}_z\mathbf{d}. \tag{5.30}$$

Discrete state-space coefficient matrices $\mathbf{A}_z$, $\mathbf{B}_z$, $\mathbf{E}_z$ are calculated as follows,

$$\mathbf{A}_z = \mathbf{exp}_m(\mathbf{A}T_s), \tag{5.31}$$

$$\mathbf{B}_z = \mathbf{A}^{-1}(\mathbf{A}_z - \mathbf{I})\mathbf{B}, \tag{5.32}$$

$$\mathbf{E}_z = \mathbf{A}^{-1}(\mathbf{A}_z - \mathbf{I})\mathbf{E}, \tag{5.33}$$

where T_s is the time step and $\mathbf{exp}_m$ is the matrix exponential function. Note that the output matrix $\mathbf{C}$ is the same for continuous and discrete state-space representation. The time step T_s is set equal to the inverse of the inverter switching carrier frequency f_c,

$$T_s = 1/f_c. \tag{5.34}$$

5.4 Gain-scheduled state feedback current controller

In this section, the gain tuning and selection procedure for a discrete full state feedback current controller with integral action is presented.

5.4.1 The need for gain-scheduling

It can be seen in (5.20) that $\mathbf{A}$, and therefore system dynamics, vary with ω_o. Thus, gain-scheduling of state feedback and observer gains as function of operating speed ω_o is required to ensure stable operation and the same closed loop dynamics for all operating speeds. The dynamic bandwidth of ω_o is equal to that of the speed control loop.For conventional cascaded control where the speed loop's bandwidth is designed to be at least one order of magnitude slower than that of the current control loop, ω_o is approximated as a constant during current controller design. Gain-scheduling with respect to ω_o will be addressed in more detail in successive sections.

5.4.1.1 State-feedback controller with integral action reference tracking

Consider the system described in (5.28-5.29). It is desired to synthesise a current control system with integral action such that at steady state, the output vector $\mathbf{y}$ asymptotically approaches a desired set point vector $\mathbf{y}^*$. The proposed discrete state-space model and state feedback controller with integral action is shown in Figure 5.4 and its accompanying state-space representation is as follows,

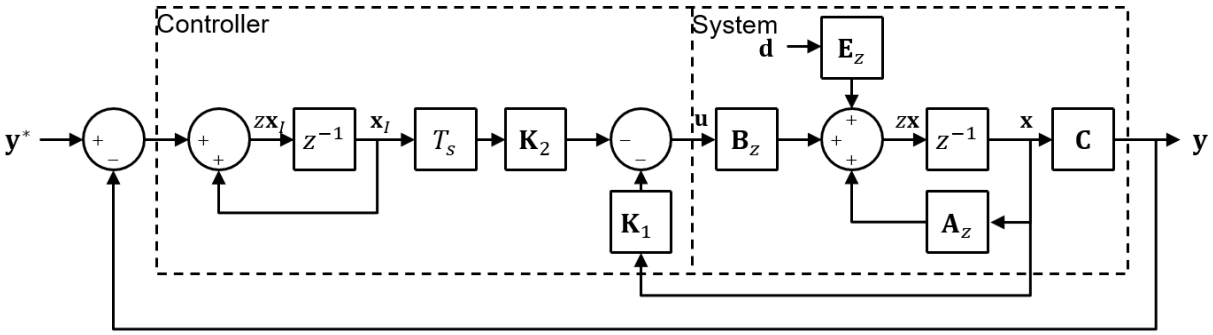


Figure 5.4: Discrete state-space system representation and state feedback controller with integral action.

$$z\left(\frac{\mathbf{x}}{\mathbf{x}_I}\right) = \left(\begin{array}{c|c} \mathbf{A}_z - \mathbf{B}_z\mathbf{K}_1 & -\mathbf{B}_z \\ \hline -T_s\mathbf{K}_2\mathbf{C}_{im} & \mathbf{I} \end{array}\right)\left(\frac{\mathbf{x}}{\mathbf{x}_I}\right) + \left(\frac{\mathbf{0}}{T_s\mathbf{K}_2}\right)\left(\frac{\mathbf{0}}{\mathbf{y}^*}\right) + \left(\frac{\mathbf{E}}{\mathbf{0}}\right)\left(\frac{\mathbf{d}}{\mathbf{0}}\right), \tag{5.35}$$

$$\mathbf{y} = \left(\begin{array}{c|c} \mathbf{C}_{im} & \mathbf{0} \end{array}\right)\left(\frac{\mathbf{x}}{\mathbf{x}_I}\right), \tag{5.36}$$

where $\mathbf{x}_I$ are the integral action states vector, and $\mathbf{y}^*$ is the desired output set point vector,

$$\mathbf{x}_I = \begin{pmatrix} x_{Id} & x_{Iq} \end{pmatrix}^T, \tag{5.37}$$

$$\mathbf{y}^* = \begin{pmatrix} i^*_{md} & i^*_{md} \end{pmatrix}^T. \tag{5.38}$$

The discrete closed loop transfer function is derived,

$$\mathbf{y} = \left(\begin{array}{c|c} \mathbf{C}_{im} & \mathbf{0} \end{array}\right)\left(z\mathbf{I} - \left(\begin{array}{c|c} \mathbf{A}_z - \mathbf{B}_z\mathbf{K}_1 & -\mathbf{B}_z \\ \hline -T_s\mathbf{K}_2\mathbf{C}_{im} & \mathbf{I} \end{array}\right)\right)^{-1}\left(\frac{\mathbf{0}}{T_s\mathbf{K}_2}\right)\left(\frac{\mathbf{0}}{\mathbf{y}^*}\right) + \left(\begin{array}{c|c} \mathbf{C}_{im} & \mathbf{0} \end{array}\right)\left(z\mathbf{I} - \left(\begin{array}{c|c} \mathbf{A}_z - \mathbf{B}_z\mathbf{K}_1 & -\mathbf{B}_z \\ \hline -T_s\mathbf{K}_2\mathbf{C}_{im} & \mathbf{I} \end{array}\right)\right)^{-1}\left(\frac{\mathbf{E}}{\mathbf{0}}\right)\left(\frac{\mathbf{d}}{\mathbf{0}}\right). \tag{5.39}$$

Consider the following expression derived from the expansion of the bottom portion

of (5.35),

$$z\mathbf{x}_I = -T_s\mathbf{K}_2\mathbf{C}_{im}\mathbf{x} + \mathbf{x}_I + T_s\mathbf{K}_2\mathbf{y}^*. \tag{5.40}$$

At steady-state, $z\mathbf{x}_I$ and $\mathbf{x}_I$ are the same and both equal to their respective steady state value $\mathbf{x}_{I,ss}$. Substituting $\mathbf{x}_{I,ss}$ into (5.40), it is shown that output $\mathbf{y}$ will match that of a constant set point $\mathbf{y}^*$ at steady-state conditions,

$$T_s\mathbf{K}_2\mathbf{C}_{im}\mathbf{x}_{ss} = T_s\mathbf{K}_2\mathbf{y}_{ss} = T_s\mathbf{K}_2\mathbf{y}^*, \tag{5.41}$$

$$\mathbf{C}_{im}\mathbf{x}_{ss} = \mathbf{y}_{ss} = \mathbf{y}^*, \tag{5.42}$$

where subscript "ss" means steady-state.

5.4.1.2 Linear quadratic regulator design and gain selection

The optimal feedback gain matrix $\mathbf{K}$ is determined by minimising the following quadratic cost function for given positive definite diagonal weighting matrices $\mathbf{Q}$ and $\mathbf{R}$,

$$J(\mathbf{u}) = \sum_{n=0}^{\infty}(\mathbf{x}_a^T\mathbf{Q}\mathbf{x}_a + \mathbf{u}^T\mathbf{R}\mathbf{u}), \tag{5.43}$$

$$\mathbf{x}_a = \left(\begin{array}{c}\mathbf{x}\\ \hline \mathbf{x}_I\end{array}\right), \tag{5.44}$$

$$\mathbf{Q} = \mathrm{diag}(q_1 \quad q_2 \quad ... \quad q_{n+p}), \tag{5.45}$$

$$\mathbf{R} = \mathrm{diag}(r_1 \quad r_2 \quad ... \quad r_p). \tag{5.46}$$

The optimal gain matrix $\mathbf{K}$ that minimises the quadratic cost function (5.43) is,

$$\mathbf{K} = \left(\begin{array}{c|c}\mathbf{K}_1 & \mathbf{K}_2\end{array}\right) = (\mathbf{B}^T\mathbf{S}\mathbf{B} + \mathbf{R})^{-1}\mathbf{B}^T\mathbf{S}\mathbf{A}, \tag{5.47}$$

where $\mathbf{S}$ is the stabilizing solution of the discrete time algebraic Riccati equation,

$$\mathbf{A}_a^T\mathbf{S}\mathbf{A}_a - \mathbf{S} - \mathbf{A}_a^T\mathbf{S}\mathbf{B}_a(\mathbf{B}_a^T\mathbf{S}\mathbf{B}_a + \mathbf{R})^{-1}\mathbf{B}_a^T\mathbf{S}\mathbf{A}_a + \mathbf{Q} = 0, \tag{5.48}$$

and $\mathbf{A}_a$ and $\mathbf{B}_a$ are the augmented matrices,

$$\mathbf{A}_a = \left(\begin{array}{c|c}\mathbf{A}_z & \mathbf{0}\\ \hline -\mathbf{C}_{im}T_s & \mathbf{I}\end{array}\right), \tag{5.49}$$

$$\mathbf{B}_a = \left(\begin{array}{c}\mathbf{B}_z\\ \hline \mathbf{0}\end{array}\right). \tag{5.50}$$

This is implemented in MATLAB using $\mathbf{K} = \texttt{lqr}(\mathbf{A}_a, \mathbf{B}_a, \mathbf{Q}, \mathbf{R})$.

The design problem of finding the feedback gains in $\mathbf{K}$ is considered as a design problem of finding constants in the weighting matrices $\mathbf{Q}$ and $\mathbf{R}$ for a desired closed loop performance criteria. Weighting constants q_1, q_2, ..., q_{n+p} in $\mathbf{Q}$ of (5.45) assign the relative significance of each system state in x_1, x_2, ..., x_{n+p} in $\mathbf{x}_a$ of (5.44). Weighting constants r_1, r_2, ..., r_p in $\mathbf{R}$ of (5.46) assign the relative energy expenditure of each system input in u_1, u_2, ..., u_p in $\mathbf{u}$.

Consider the presented current controller design problem. The augmented state matrix $\mathbf{x}_a$ is constructed by substitution of $\mathbf{x}$ of (5.23) and $\mathbf{x}_I$ of (5.37) into (5.44),

$$\mathbf{x}_a = \left(\begin{array}{c|c} \mathbf{x} & \mathbf{x}_I \end{array} \right)^T = \left(\begin{array}{cccccc|cc} i_{md} & i_{mq} & i_{invd} & i_{invq} & v_{fd} & v_{fq} & x_{I1} & x_{I2} \end{array} \right)^T \tag{5.51}$$

The primary objectives of the current controller design problem are to tune the dynamics of machine's dq currents i_{md} and i_{mq} to a desired bandwidth f_{bw} and to ensure their steady state values match that of i^*_{md} and i^*_{mq} respectively though the integral action of states x_{Id} and x_{Iq}. Since the dynamics of i_{invd}, i_{invq}, v_{fd}, and v_{fq} are not considered in these objectives (in other words, have no weighting/significance in the design problem), weights q_3, q_4, q_5, and q_6 are set to zero. This makes the parameter tuning procedure easier by reducing the number of unknowns from ten to six. Thus, the weighting matrices $\mathbf{Q}$ and $\mathbf{R}$ are structured accordingly as shown,

$$\mathbf{Q} = \text{diag}\begin{pmatrix} q_1 & q_2 & 0 & 0 & 0 & 0 & q_7 & q_8 \end{pmatrix}, \tag{5.52}$$

$$\mathbf{R} = \text{diag}\begin{pmatrix} r_1 & r_2 \end{pmatrix}. \tag{5.53}$$

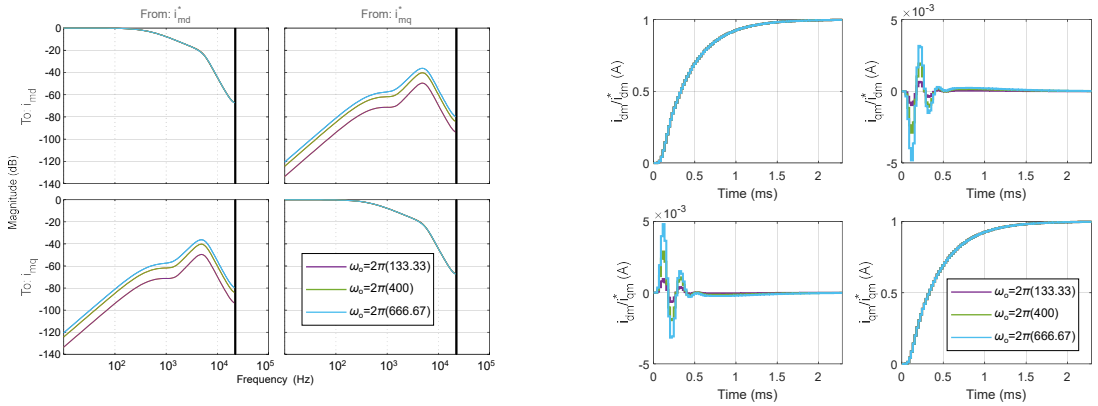
The number of unknowns are further reduced from six to three by setting $q_1 = q_2 = q_a$, $q_7 = q_8 = q_b$, and $r_1 = r_2 = r_a$. The justification for this simplification is that the system's d-axis and q-axis small signal dynamics are the same for a drive system with a symmetrical load (i.e. a non-salient PMSM). Weights q_1, q_7, and r_1 correspond to i_{md}, x_{I1}, and y^*_1. Weights q_2, q_8, and r_2 correspond to i_{mq}, x_{I2}, and y^*_2. Machine currents i_{md} and i_{mq} have the same significance, thus $q_1 = q_2 = q_a$. Similarly, $q_7 = q_8 = q_b$ because integral action states x_{I1} and x_{I2} have the same significance and $r_1 = r_2 = r_a$ because set point values i^*_{md} and i^*_{mq} have the same significance. Thus,

$$\mathbf{Q}(q_a, q_b) = \text{diag}\begin{pmatrix} q_a & q_a & 0 & 0 & 0 & 0 & q_b & q_b \end{pmatrix}, \tag{5.54}$$

$$\mathbf{R}(r_a) = \text{diag}\begin{pmatrix} r_a & r_a \end{pmatrix}. \tag{5.55}$$

The state feedback gain matrix $\mathbf{K}$ consisting of sub-matrices $\mathbf{K}_1$ and $\mathbf{K}_2$ is solved for given $\mathbf{Q}$, $\mathbf{R}$, $\mathbf{A}_a$, and $\mathbf{B}_a$ using (5.47 - 5.50). The closed loop discrete transfer function is formulated using (5.39) by substituting in feedback matrices $\mathbf{K}_1$ and $\mathbf{K}_2$, and system

coefficient matrices $\mathbf{A}_z$, $\mathbf{B}_z$, $\mathbf{E}_z$ and $\mathbf{C}$. The closed loop transfer function's dc gain and bandwidth are determined from its bode plots as shown in Figure 5.5 (a) for three different fixed speeds. The closed loop transfer function's step response in the time domain is shown in Figure 5.5 (b). DC gain and bandwidth from i^*_{md} to i_{md} and from i^*_{mq} to i_{mq} are 0dB (unity gain) and 450Hz. Minimal cross-coupling is observed from i^*_{md} to $i_{mq}*$ and from i^*_{mq} to i^*_{md}.



(a) **(b)**

Figure 5.5: Calculated (a) bode and (b) step responses for gain-scheduled closed loop current control at fixed electrical speeds $\omega_o = \{2\pi(133.33), 2\pi(400), 2\pi(666.67)\}$, with unity dc gain and 450Hz bandwidth for $i^*_{md} \rightarrow i_{md}$ and $i^*_{mq} \rightarrow i_{mq}$.

The procedure's key steps are shown in the enumerated list below.

1. The system is mathematically described by the system's dq voltage and current equations from (5.9 - 5.14).
2. The continuous state-space representation's matrix coefficients $\mathbf{A}$, $\mathbf{B}$, $\mathbf{E}$, and $\mathbf{C}$ are synthesized from the dq voltage and current equations (5.20 - 5.25) for a given operating baseband electrical speed ω_o.
3. The discrete state-space representation's matrix coefficients $\mathbf{A}_z$, $\mathbf{B}_z$, and $\mathbf{E}_z$ are calculated from $\mathbf{A}$, $\mathbf{B}$, and $\mathbf{E}$ for a time-step T_s equal to the inverse of the inverter carrier switching frequency f_c using (5.31 - 5.34).
4. Augmented matrix $\mathbf{A}_a$ and $\mathbf{B}_a$ are constructed from the discrete state-space matrix coefficients using (5.49 - 5.50).
5. Weighting matrices $\mathbf{Q}(q_a, q_b)$ and $\mathbf{R}(r_a)$ in (5.54 - 5.55) are declared from which the gain feedback matrix $\mathbf{K}$ can be solved for $\mathbf{Q}$, $\mathbf{R}$, $\mathbf{A}_a$, and $\mathbf{B}_a$ using (5.47 - 5.50).
6. $\mathbf{K}$ is separated into $\mathbf{K}_1$ and $\mathbf{K}_2$ and are substituted into (5.35) from which the closed loop discrete transfer function can be derived using (5.39).
7. The output's bandwidth f_{bw} of and dc gain K_{dc} can be determined from the closed loop discrete transfer function's bode plot.

The above design procedure is compiled into a function f_1 which directly determines the

closed loop bandwidth f_{bw}, dc gain K_{dc} and feedback gain matrix $\mathbf{K}$, when provided the variables ω_o, q_a, q_b, and r_a.

$$(f_{bw}, \mathrm{K}_{dc}, \mathbf{K}) = \mathrm{f}_1(\omega_o, q_a, q_b, r_a) \tag{5.56}$$

Let's propose a performance error function $\mathrm{f}_{\min}$ to be minimised for desired closed loop bandwidth f^*_{bw}, and dc gain K^*_{dc} where $\mathrm{f}_{\min}$ approaches 0 when f_{bw} approaches f^*_{bw} and K_{dc} approaches K^*_{dc},

$$\mathrm{f}_{\min} = \left| \frac{f_{bw} - f^*_{bw}}{f^*_{bw}} \right| + \left| \frac{\mathrm{K}_{dc} - \mathrm{K}^*_{dc}}{\mathrm{K}^*_{dc}} \right|. \tag{5.57}$$

Using (5.56 - 5.57), the performance error function is plotted with respect q_a and q_b for $\omega_o = 2\pi(400)$ and $r_a = 1$ in Figure 5.6. A valley of small $\mathrm{f}_{\min}$ values can be seen from which its minimum can be found.

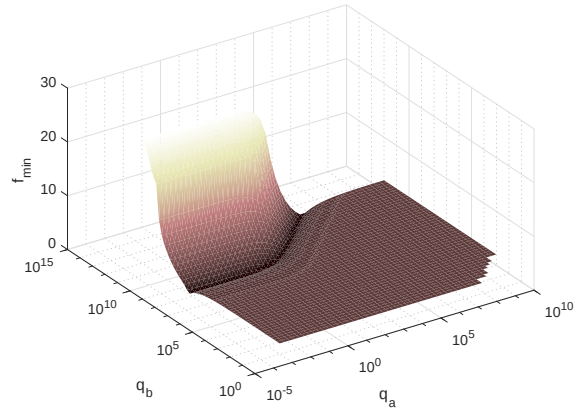


Figure 5.6: Performance error function $\mathrm{f}_{\min}$ versus q_a and q_b for $\omega_o = 2\pi(400)$ and $r_a = 1$.

Numerical methods are used to find the solution of q_a, q_b, r_a, and respective gain matrix $\mathbf{K}$ for a given constant operating electrical speed ω_o to minimise performance error function $\mathrm{f}_{\min}$. [113] presented a LQR tuning procedure by particle swarm optimisation of a full car suspension system. Pattern search optimisation [80] was utilised in the author's own implementation as this method is suitable for multi-variable functions which are not continuous or differentiable.

5.4.2 Gain-scheduling

Gain-scheduling with respect to electrical speed ω_o is realised by repeating the gain tuning procedure for a discrete set of electrical speed test points spanning the machine's operating range and generating a respective $\mathbf{K}$ matrix for each electrical speed. The index of gain

matrix $\mathbf{K}$ and their association with sub-matrices $\mathbf{K}_1$ and $\mathbf{K}_2$ are as follows,

$$\begin{aligned}\mathbf{K} &= \left(\begin{array}{c|c} \mathbf{K}_1 & \mathbf{K}_2 \end{array} \right) \\ &= \begin{pmatrix} K_{(1,1)} & \dots & K_{(1,6)} & K_{(1,7)} & K_{(1,8)} \\ K_{(2,1)} & \dots & K_{(2,6)} & K_{(2,7)} & K_{(2,8)} \end{pmatrix} \\ &= \begin{pmatrix} K_{1(1,1)} & \dots & K_{1(1,6)} & K_{2(1,1)} & K_{2(1,2)} \\ K_{1(2,1)} & \dots & K_{1(2,6)} & K_{2(2,1)} & K_{2(2,2)} \end{pmatrix}.\end{aligned} \tag{5.58}$$

An example with six electrical speed test points linearly spaced between $-2\pi(666.67)$ to $2\pi(666.67)$ rad/s is shown in Figure 5.7. The test points are represented by "x" markers for $\mathbf{K}_1$ and "o" markers for $\mathbf{K}_2$. Two y axes are present as values in $\mathbf{K}_1$ are much smaller than that of $\mathbf{K}_2$.

Second degree polynomials as a function of electrical speed ω_o in the following form are fitted in a least square manner to each gain in matrices $\mathbf{K}_1$ and $\mathbf{K}_2$,

$$\begin{pmatrix} K_{1(1,1)} \\ K_{1(1,2)} \\ \vdots \\ K_{1(1,6)} \\ K_{1(2,1)} \\ K_{1(2,2)} \\ \vdots \\ K_{1(2,6)} \\ \hline K_{2(1,1)} \\ K_{2(1,2)} \\ K_{2(2,1)} \\ K_{2(2,2)} \end{pmatrix} = \begin{pmatrix} p''_{1(1,1)} & p'_{1(1,1)} & p_{1(1,1)} \\ p''_{1(1,2)} & p'_{1(1,2)} & p_{1(1,2)} \\ \vdots & \vdots & \vdots \\ p''_{1(1,6)} & p'_{1(1,6)} & p_{1(1,6)} \\ p''_{1(2,1)} & p'_{1(2,1)} & p_{1(2,1)} \\ p''_{1(2,2)} & p'_{1(2,2)} & p_{1(2,2)} \\ \vdots & \vdots & \vdots \\ p''_{1(2,6)} & p'_{1(2,6)} & p_{1(2,6)} \\ \hline p''_{2(1,1)} & p'_{2(1,1)} & p_{2(1,1)} \\ p''_{2(1,2)} & p'_{2(1,2)} & p_{2(1,2)} \\ p''_{2(2,1)} & p'_{2(2,1)} & p_{2(2,1)} \\ p''_{2(2,2)} & p'_{2(2,2)} & p_{2(2,2)} \end{pmatrix} \begin{pmatrix} \omega_o^2 \\ \omega_o \\ 1 \end{pmatrix} \tag{5.59}$$

This is shown in Figure 5.7 where the line plot represents a second degree polynomial fit.

5.5 Gain-scheduled full state observer

The gain-scheduled full state-space feedback current controller requires feedback of dq inverter currents i_{invd}, i_{invq}, dq filter output voltages v_{fd}, v_{fq}, and dq machine currents i_{md}, i_{mq}. To minimise the number of voltage and current sensors, a gain-scheduled full-state observer is utilised to estimate voltages v_{fd}, v_{fq} and currents i_{md}, i_{mq}.

The gain-scheduled full state feedback machine current controller with gain-scheduled full-state observer are shown in Figure 5.8. The "$\hat{}$" accent represents estimated values. Consider the plant's continuous state-space representation in (5.20 - 5.25) and observe

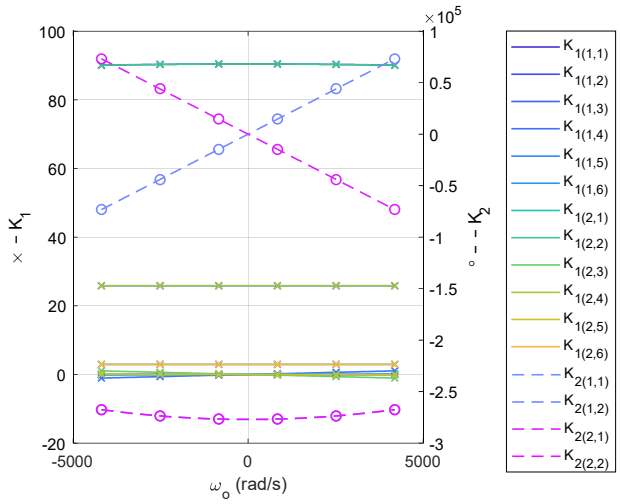


Figure 5.7: Gain-scheduled $\mathbf{K}_1$ and $\mathbf{K}_2$ matrix parameters with respect to operating electrical speed ω_o, "x" and "o" markers represent test points for matrix parameters of $\mathbf{K}_1$ and $\mathbf{K}_2$ respectively, line plots represent second degree polynomial fit.

that $\mathbf{A}$ (and with that, the system dynamics) vary with ω_o. Consider the discrete state-space matrices $\mathbf{A}_z$, $\mathbf{B}_z$, and $\mathbf{E}_z$ in (5.31 - 5.33) are a function of $\mathbf{A}$ and therefore, also vary with ω_o.

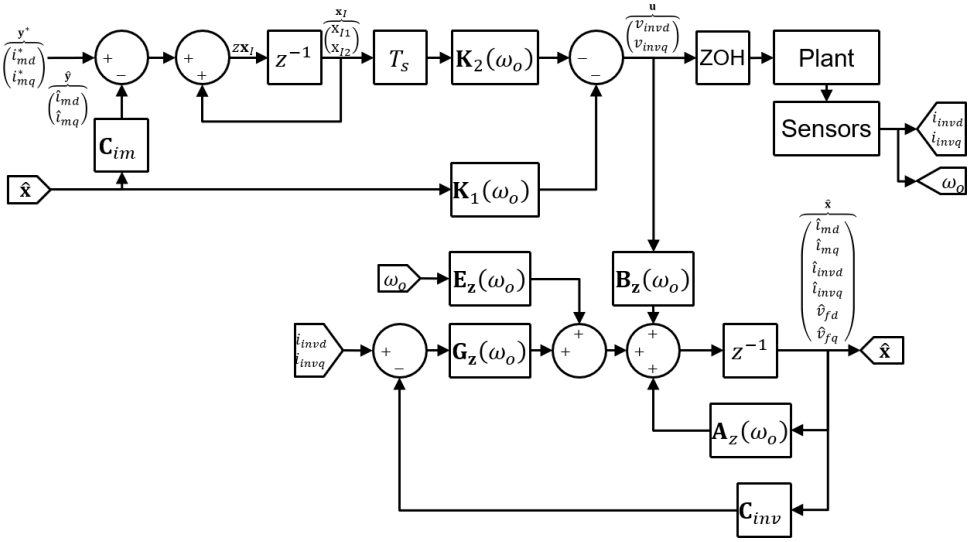


Figure 5.8: Gain-scheduled full state feedback machine current controller with gain-scheduled full-state observer.

The state-space representation of the observer is as follows,

$$z\hat{\mathbf{x}} = \mathbf{A}_z\hat{\mathbf{x}} + \mathbf{B}_z\mathbf{u} + \mathbf{E}_z\omega_o + \mathbf{G}_z\mathbf{C}_{inv}(\mathbf{x} - \hat{\mathbf{x}}). \tag{5.60}$$

The error dynamics of the observer is described by the poles of $\mathbf{A}_z - \mathbf{G}_z\mathbf{C}_{inv}$,

$$z\mathbf{e} = z(\mathbf{x} - \hat{\mathbf{x}}) = \mathbf{A}_z - \mathbf{G}_z\mathbf{C}_{inv}. \tag{5.61}$$

The total system discrete state-space representation consisting of the plant, the current controller with integral action, and the observer is as follows,

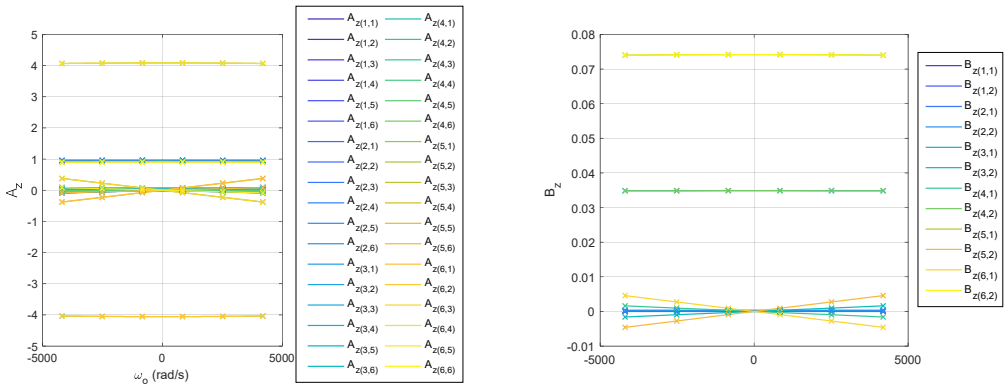
$$
\begin{aligned}
z\overbrace{\begin{pmatrix}\mathbf{x}\\ \mathbf{x}_I\\ \hat{\mathbf{x}}\end{pmatrix}}^{\mathbf{x}_t} &= \overbrace{\begin{pmatrix}\mathbf{A}_z & -\mathbf{B}_z & -\mathbf{B}_z\mathbf{K}_1\\ \mathbf{0} & \mathbf{0} & -\mathbf{K}_2\mathbf{C}_{im}T_s\\ \mathbf{G}_z\mathbf{C}_{inv} & -\mathbf{B}_z & \mathbf{A}_z-\mathbf{B}_z\mathbf{K}_1-\mathbf{G}_z\mathbf{C}_{inv}\end{pmatrix}}^{\mathbf{A}_t}\overbrace{\begin{pmatrix}\mathbf{x}\\ \mathbf{x}_I\\ \hat{\mathbf{x}}\end{pmatrix}}^{\mathbf{x}_t}\\
&\quad + \overbrace{\begin{pmatrix}\mathbf{K}_2T_s\\ \mathbf{0}\\ \mathbf{0}\end{pmatrix}}^{\mathbf{B}_t}\overbrace{(\mathbf{y}^*)}^{\mathbf{u}_t} + \overbrace{\begin{pmatrix}\mathbf{E}_z\\ \mathbf{0}\\ \mathbf{E}_z\end{pmatrix}}^{\mathbf{E}_t}\overbrace{(\mathbf{d})}^{\mathbf{d}_t},
\end{aligned}
\tag{5.62}
$$

$$
\overbrace{\begin{pmatrix}\mathbf{y}\\ \hat{\mathbf{y}}\end{pmatrix}}^{\mathbf{y}_t} = \overbrace{\begin{pmatrix}\mathbf{C}_{im} & \mathbf{0} & \mathbf{0}\\ \mathbf{0} & \mathbf{0} & \mathbf{C}_{im}\end{pmatrix}}^{\mathbf{C}_t}\overbrace{\begin{pmatrix}\mathbf{x}\\ \mathbf{x}_I\\ \hat{\mathbf{x}}\end{pmatrix}}^{\mathbf{x}_t}. \tag{5.63}
$$

MATLAB's pole-placement function `place`, which utilises a robust pole assignment algorithm described in [114], is used to determine the observer state-feedback matrix $\mathbf{G}_z$ such that the poles p_G of $(\mathbf{A}_z - \mathbf{G}_z\mathbf{C}_{inv})$ match that of desired poles p_G^*. A general rule of thumb is that the desired observer poles p_G^* is set to be at least $\times 10$ faster than the dynamics of the controlled state (i.e. the machine currents).

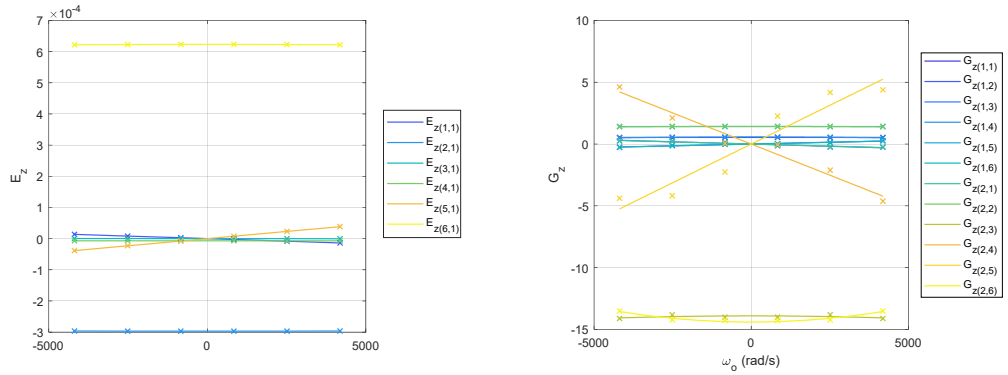
Section 5.4.2 describes the process of gain-scheduling by second degree polynomial fit applied to gain matrices $\mathbf{K}_1$ and $\mathbf{K}_2$. The same procedure is repeated for observer state-feedback matrix $\mathbf{G}_z$ for a discrete set of electrical speed test points spanning the machine's operating range. Second degree polynomials as a function of electrical speed ω_o are fitted in a least square manner to each of parameters in $\mathbf{A}_z$, $\mathbf{B}_z$, $\mathbf{E}_z$, and $\mathbf{G}_z$. This process is completed for six electrical speed test points linear spaced between $-2\pi(666.67)$ to $2\pi(666.67)$ rad/s and is shown in Figure 5.9 and Figure 5.10. The "x" markers show the test points and the line plots show the second degree polynomial fit.

The total system poles are determined from eigenvalues of (5.62) for three different operating electrical speeds ω_o and plotted in the z-domain as shown in Figure 5.11. The poles at (0.9,0) correspond to the desired machine current closed loop dynamics of 250Hz bandwidth. The observer poles were selected to be at least $\times 10$ faster than that of the machine current closed loop dynamics which, in this case, places them as a cluster at centre of the unit-circle.



(a) **(b)**

Figure 5.9: State-space matrix values (a) $\mathbf{A}_z$ and (b) $\mathbf{B}_z$ with respect to operating speed ω_o, "x" markers represent discrete test points, line plots represent second degree polynomial fit.



(a) **(b)**

Figure 5.10: State-space matrix values (a) $\mathbf{E}_z$ and observer state feedback gains matrix (b) $\mathbf{G}_z$ with respect to operating speed ω_o, "x" markers represent discrete test points, line plots represent second degree polynomial fit.

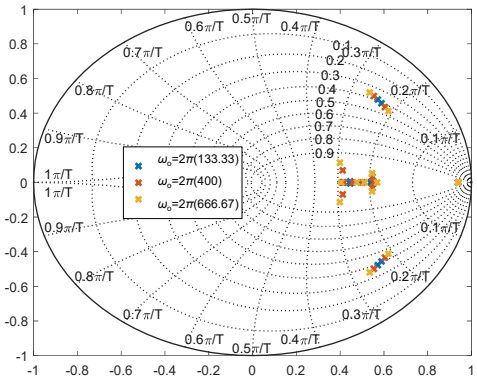


Figure 5.11: Poles of total system considering plant, controller, and observer plotted in z-domain for different operating electrical speeds ω_o.

5.6 Controller and observer simulation with switching model

Simulation results of the proposed gain-scheduled current control with state observer scheme are presented here. The simulation is implemented in PLECS and Simulink. An

Table 5.1: Controller and observer simulation with switching model and transmission line parameters.

R_s	0.503Ω	R_{cs}	0.785Ω	R_{fil}	9mΩ
L_s	1.847mH	L_{cs}	305.4uH	L_{fil}	0.62mH
λ_m	25.1mWb	C_{cpg}	90.17nF	C_{fil}	5.27uF
p	5	f_c	45kHz	l_c	10m

inverter switching model with sinusoidal PWM switching scheme is utilised. A distributed transmission line models the long feeder cable. The simulation parameters are shown in Table 5.1.

The real and estimated system's states time series are plotted in Figure 5.12 for a speed ramp from zero to 8000RPM and current command of $i^*_{md} = 0$A, $i^*_{mq} = 7$A at $t = 0.02$s. The estimated states track the real values closely. Reference tracking is achieved as i_{md} , i_{mq} tracks reference values i^*_{md}, i^*_{mq}. The corresponding phase voltage and currents are shown in Figure 5.13. By comparing the source side phase voltage v_{fa}, and machine side phase voltage v_{ma}, it can be seen that no overshoot is present and transmission line effects are mitigated.

Discrepancy is present between the observed and realised states and becomes more pronounced as speed increases. This is due to a mismatch between the inverter output voltage fundamental amplitude and the commanded dq voltage of the current controller. It is proposed the modulation index can be scaled up as a function of speed to compensate for this mismatch. Correction of this mismatch has not been investigated further.

5.7 Cascaded speed and position control loop

The proposed cascaded speed and position loop is shown in Figure 5.14 for nominal operation. PI controllers with integral clamping are utilised for both speed and position control. The machine speed is ω_m, the reference crank arm position is θ, and machine electromechanical torque is T_m. The "*" superscript represent set points. The closed loop torque/current controller dynamics are approximated by a first order transfer function $G_{cc}(s)$ of bandwidth b_{cc} where,

$$G_{cc}(s) = \frac{b_{cc}}{s + b_{cc}}. \tag{5.64}$$

The speed control loop bandwidth is a tenth that of the current controller. The position control loop bandwidth is a tenth that of the speed control loop.

A continuous PI controller of the following form is designed using bode plot analysis,

$$C(s) = K_p + K_i \frac{1}{s}. \tag{5.65}$$

The machine speed open loop and closed loop bode plots are shown in Figure 5.15. The

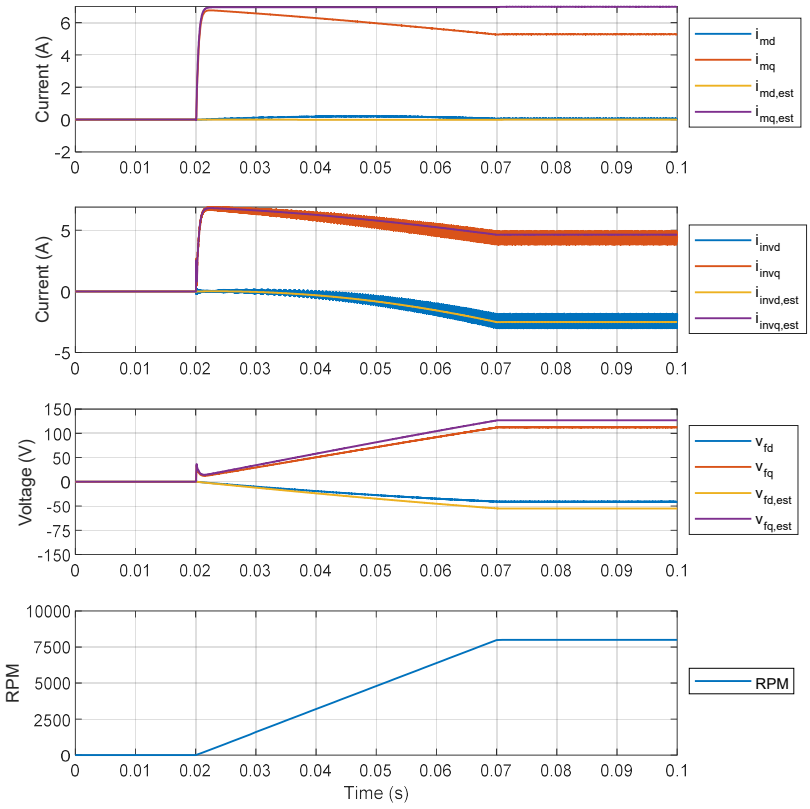


Figure 5.12: Real and estimated states with rotor speed ramp and step current command i^*_{md} = 0A, i^*_{mq} = 7A.

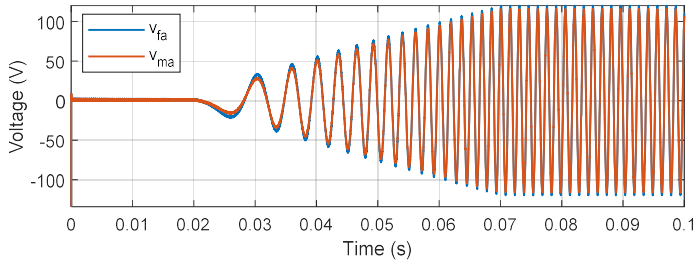


Figure 5.13: Phase voltage for rotor speed ramp and step current command $i^*_{md} = 0$A, $i^*_{mq} =$ 7A.

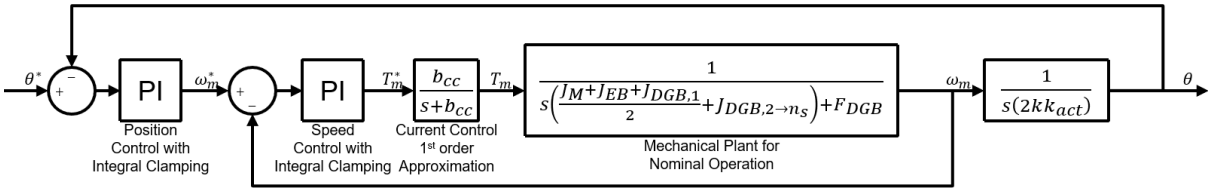


Figure 5.14: Cascaded speed and position loop for mechanical system.

open loop phase margin and cross over frequency are around 78deg and 42Hz respectively for both nominal and faulted operation.

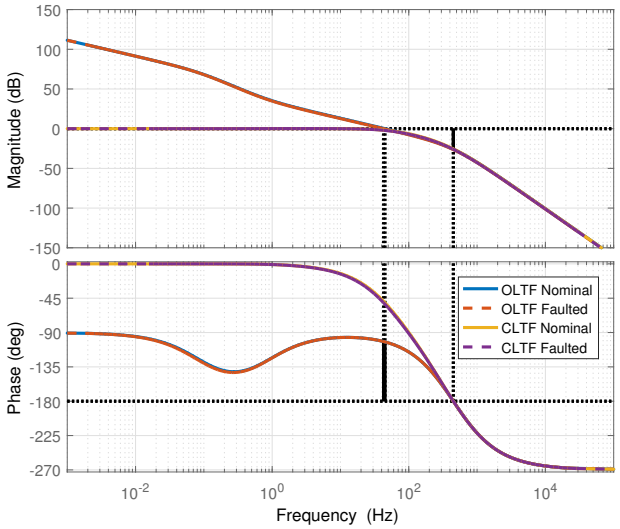


Figure 5.15: Open loop and closed loop bode plot of the machine speed for nominal and faulted operation.

The output of the PI controller is a torque command T_m^*. Torque command's maximum absolute value is limited by the controller to that of the machine's maximum torque. Large changes in position set point can lead to significant accumulation of error in the integrator, known as integrator windup. This effect causes excessive overshoot, oscillations and long settling times of both the controller output and system output during the integral unwind period. Integral windup is particularly apparent in systems where the input effort of the plant (in this case, the machines) saturates to a maximum limit. To deal with integrator windup, clamping anti-windup is utilised as seen in Figure 5.16 where the input to the integral term is set to zero when the plant's input effort saturates (i.e. $u \neq u^*$) and the input effort u and error e have the same sign (i.e. $u \times e > 0$) [115].

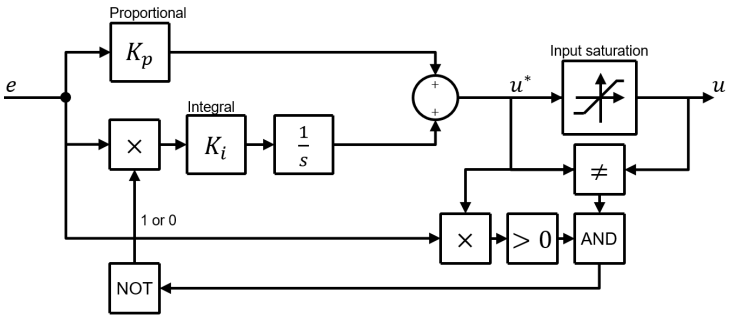


Figure 5.16: PI controller with integral clamping anti-windup.

The outer position loop is then designed. The speed closed loop transfer functions $G_{nom}(s)$ and $G_{flt}(s)$ are considered from which the plant models $L_{nom}(s)$ and $L_{flt}(s)$ for

which the position loop control is designed.

$$L_{nom}(s) = \frac{\theta(s)}{T_m(s)} = \left(\frac{C(s)G_{cc}(s)G_{nom}(s)}{1 + C(s)G_{cc}(s)G_{nom}(s)}\right)\left(\frac{1}{2(kk_{act})}\right), \tag{5.66}$$

$$L_{flt}(s) = \frac{\theta(s)}{T_m(s)} = \left(\frac{C(s)G_{cc}(s)G_{flt}(s)}{1 + C(s)G_{cc}(s)G_{flt}(s)}\right)\left(\frac{1}{kk_{act}}\right). \tag{5.67}$$

The closed loop speed transfer function is multiplied by a free integrator to determine position from speed and then scaled by the product of the gear ratios to determine actuator crank arm position angle θ as shown.

A PI position controller is designed considering the described nominal plant model. The position loop's open loop transfer function's cross over frequency is a tenth that of speed loop's. As with the speed controller, integrator clamping is also utilised.

The mechanical system response for actuator arm position, slider positions, and machine speed for the cascaded speed-position control loops are shown in Figure 5.17. The actuator position set point started from fully extended to fully retracted. The current, speed, and position controller bandwidths are 450Hz, 45Hz, and 4.5Hz respectively. The phase margin for both speed and position control loops were set at 80°. The time it takes to reach the desired positions are 13.7s and 26.5s for nominal and faulted operation respectively. The absolute speed limit of 8000RPM is set for the machine.

5.8 Conclusion

This chapter presented a discrete state feedback gain-schedule LQR current controller for the distributed topology. The objective of the current controller is to control the machine's current by appropriate adjusting the voltage command of the inverter. The LC filter in the distributed topology is required to reduce the inverter's output voltage's dv/dt such that transmission line and voltage overshoot does not occur on the load side, and to ensure MIL-STD-704F's distortion spectrum is adhered to. However, the LC filter is inherently a resonator. A control scheme is required to ensure machine current is controllable and the inherent resonance of the LC filter is dampened.

The electrical system's dq equivalent circuit considering the inverter, LC filter, cable, and machine was presented from which the discrete state-space representation was derived. The cable is modelled by a single-branch γ-type lumped parameter circuit. Reference tracking was realised using state-feedback with integral action. Gain tuning for desired closed-loop performance steady state tracking and bandwidth was done through minimisation of LQR based performance error cost function using pattern search. An observer was implemented to estimate machine side voltages and currents. Gain scheduling for both the state feedback controller and observer was implemented using second order polynomials as a function of electrical speed.

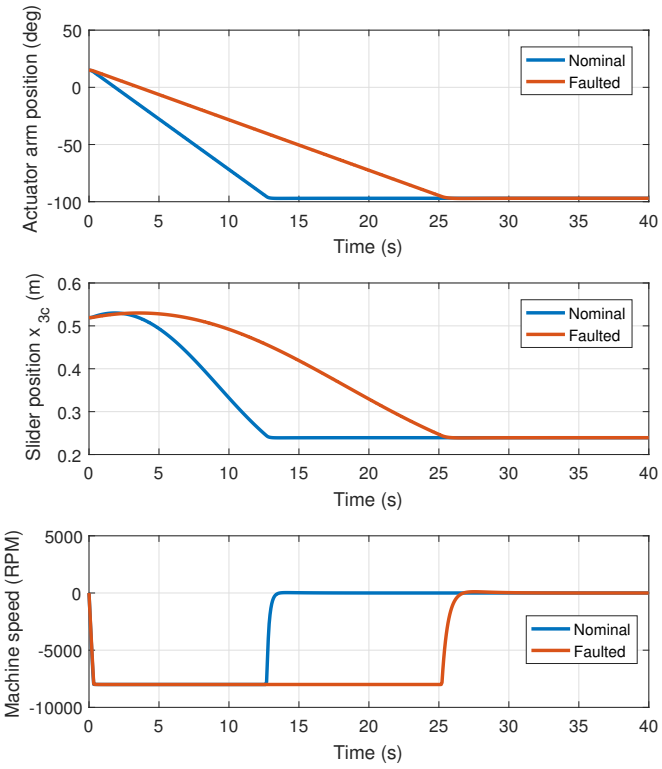


Figure 5.17: Mechanical system response for actuator arm, slider positions, and machine speed with respect to time for nominal and faulted operation.

The designed controller is simulated in MATLAB Simulink and PLECS with switching inverter model. Sinusoidal switching was utilised. The controller is stable and dynamic performance was achieved for a constant current command during a speed ramp. Discrepancy was present between the observed and actual machine current. This is due to the a mismatch between commanded voltage output of the current controller and the achieved voltage output of the inverter. This discrepancy increased with electrical speed. This issue can be resolved by a speed dependent compensation method however, a solution was not pursued further.

Chapter 6

Drive level - high-frequency

6.1 Overview

In this chapter, high-frequency modelling of the designed electric drive system of chapter 4 is presented. High-frequency modelling is not directly integrated in the optimal electric drive design and sizing process as simulations are relatively computational demanding. What is considered high-frequency and what related phenomenons of interest is discussed as follows.

High frequency drive level analysis considers electrical dynamics equal to or greater than the inverter switching frequency. Particular focus is placed on modelling transmission line phenomenon. Switched voltages with high dv/dt i.e. short rise times and fall times, applied on long feeder cables, whose surge impedance matches poorly with that of the machine, can cause high-amplitude high-frequency voltage oscillations throughout the cable, at the machine terminals, and extending into the first few turns of the machine windings. Analysis of this phenomenon can inform a designer for a given system, topology, rise/fall time, cable properties, cable length, and load impedance:

- If transmission line phenomenon poses an issue with load side over-voltage. For example, if a short feeder cable is used, transmission line phenomenon may not be of a concern and additional filtering or voltage shape conditioning does not need to be added.
- If transmission line phenomenon does pose an issue, what filter solution can be used to deal with this issue. Increasing the rise and fall time on the source side can also reduce the over-voltage phenomenon.
- Can the distance between the switched inverter and the load be reduced such that the assumption of short transmission line length is sufficient.

Consider a given candidate electric drive design consisting of inverter, transmission line cable, and machine. Each component has been designed by their respective sizing methods. Each component design, as defined by their geometry, material, electrical

parameters, and characteristics are known and set. From each component's design, a corresponding high frequency model can be synthesized. Each component high frequency model is combined to synthesize a drive level high frequency model. The high frequency model consists of the source (which models inverter switching characteristics), output filter (if present), and transmission line (which models the feeder cable), and load (which represents the machine impedance). How these are modelled and represented is shown in the following sections.

The analysis and calculations are done predominately in the frequency domain. Each voltage pulse of the inverter's output is approximated as a trapezoidal waveform from which the Fourier expansion coefficients are derived, and the spectra is determined. The cable's impedance characteristics as a function of frequency is derived from FEA and modelled as a single line transmission line. Parameters of a per-turn equivalent circuit of the machine winding are determined using FEA.

Given the input voltage waveform's Fourier expansion coefficients and the impedance characteristics of the cable and the load, the load side voltage waveform's Fourier expansion coefficients are derived. Then the load side voltage is plotted in the time domain.

Note on output filter requirement: For a centralised topology whereby the switched inverter is located centrally (e.g. in the fuselage) and connected to the machine that is located at the point of actuation (e.g. on the wing), a sine-wave output filter must be used to ensure MIL-STD-704F's distortion spectrum and power quality limits are respected. Thus, the applied inverter side voltage on the cable is sinusoidal, its effective dv/dt is low and transmission line effects can be ignored.

6.2 Single-line transmission line model

Consider any conventional three-phase two-level inverter switching scheme. At any switching instance, two of the three-phases are connected to one polarity of the DC-link while the remaining phase is connected to the opposite polarity. At this instance, the three-phase output inverter can be considered as a two port source as two phases are effectively shorted together. Similarly, a single-line transmission line model is used to represent the feeder cable where the two parallel lines connected to the same polarity are lumped into one line. The load impedance of the three-phase machine is also simplified to a two-port equivalent impedance. Thus, each switching instance of a two-level three-phase inverter is modelled by a voltage pulse applied on the source side of a single-line transmission line model and equivalent load impedance.

6.2.1 Source

Each individual voltage pulse of the inverter output is represented as a trapezoidal waveform defined by rise time τ_r, fall time τ_f, period T, pulse width τ and amplitude A [116]. The duty cycle d is equal to τ/T. The base frequency in radians is $\omega_0 = 2\pi/T$. The trapezoidal waveform's Fourier series expansion coefficients c_n at harmonic n are as follows,

$$c_n = \frac{A}{T(jn\omega_0)^2}\left(\frac{1}{\tau_r}\left(1 - e^{-jn\omega_0\tau_r}\right) + \frac{1}{\tau_f}\left(e^{-jn\omega_0\left(\tau+\frac{\tau_r+\tau_f}{2}\right)} - e^{-jn\omega_0\left(\tau+\frac{\tau_r-\tau_f}{2}\right)}\right)\right). \quad (6.1)$$

The amplitudes of the Fourier series expansion coefficients are plotted in Figure 6.1 for a switching frequency f_0 of 15kHz, DC bus of 270V, duty cycle of 0.4 and for different combinations of rise time τ_r and τ_f.

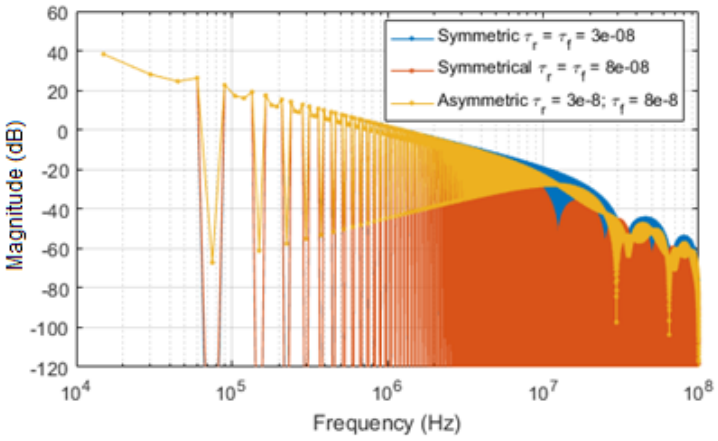


Figure 6.1: Spectrum of symmetric and asymmetric trapezoidal waveform for f_0 = 15kHz, d = 0.4, A = 270V.

The amplitude of the Fourier series expansion coefficients fall within a maximum magnitude spectrum envelope E_{trap}. For symmetrical trapezoidal waveforms (i.e. rise and fall time are equal) it is expressed as a function of the switching frequency and inverse of the rise time,

$$E_{trap} = 2A\frac{\tau}{T}\left|\text{sinc}\left(\pi\tau\frac{n}{T}\right)\right|\left|\text{sinc}\left(\pi\tau_r\frac{n}{T}\right)\right|. \quad (6.2)$$

For short duty cycles where,

$$\frac{1}{\pi\tau} > \frac{2\pi}{T}, \quad (6.3)$$

$$\tau < \frac{T}{2}, \quad (6.4)$$

the spectrum envelope would have a slope of 0dB/decade from the f_0 to associated frequency $\frac{1}{\pi\tau}$ as shown by the blue line in Figure 6.2. An envelope slope of -20dB/decade exists between $\frac{1}{\pi\tau}$ and $\frac{1}{\pi\tau_r}$. An envelope slope of -40dB/decade exists beyond $\frac{1}{\pi\tau_r}$.

For longer duty cycles such that $\tau > \frac{T}{2}$, the envelope starts with a -20dB/decade slope at switching frequency $\frac{1}{\pi T}$ which continues up to $\frac{1}{\pi\tau_r}$ and -40dB/decade slope beyond $\frac{1}{\pi\tau_r}$. This is shown by the red line in Figure 6.2.

Increasing the switching frequency and decreasing the rise time pushes this envelope to the right, thus increasing the high frequency harmonics. With the adoption of SiC inverters comes faster switching, steeper switched voltage wave-fronts, and thus, higher frequency harmonics.

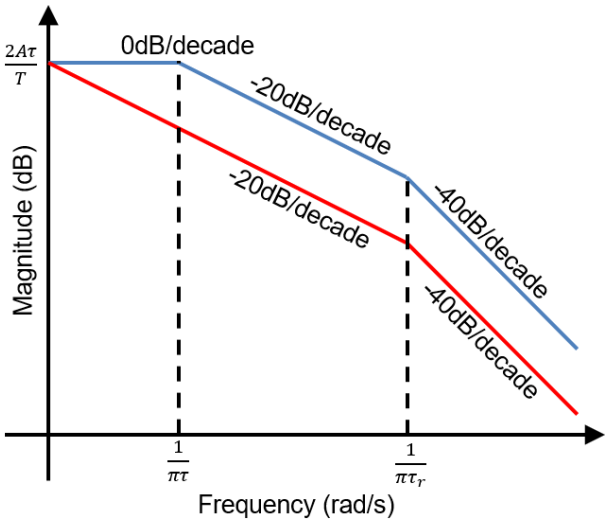


Figure 6.2: Fourier series expansion coefficient maximum magnitude envelope for symmetrical trapezoid waveform, blue line where $\tau < \frac{T}{2}$, red line where $\tau > \frac{T}{2}$.

6.2.2 Differential mode model

Single-line lumped parameter multi-branch network models are used to model three-phase transmission line effects. The following lumped parameter multi-branch Γ-type transmission line model is considered as shown in Figure 6.3. Each Γ-type branch consists of series resistance R_{dm}, series inductance L_{dm} and line to reference capacitance C_{dm},

$$R_{dm}(\omega) = \frac{R'_{dm} l_c}{N+1}, \tag{6.5}$$

$$L_{dm}(\omega) = \frac{L'_{dm} l_c}{N+1}, \tag{6.6}$$

$$C_{dm} = \frac{C'_{dm} l_c}{N}, \tag{6.7}$$

where R'_{dm}, L'_{dm}, and C'_{dm} are per unit length series resistance, series inductance, and line to reference capacitance, and N is the number of branches. The voltage source v_0 represents the trapezoidal voltage waveform. The voltage across the load is v_{Ldm}.

As frequency increases, current density near the conductor outer boundary increases while current density in the centre reduces due to the skin effect and proximity effect.

With that, resistance increases and inductance decreases. These non-linear effects need to be considered in the analysis as both R_{dm} and L_{dm} are a function of ω.

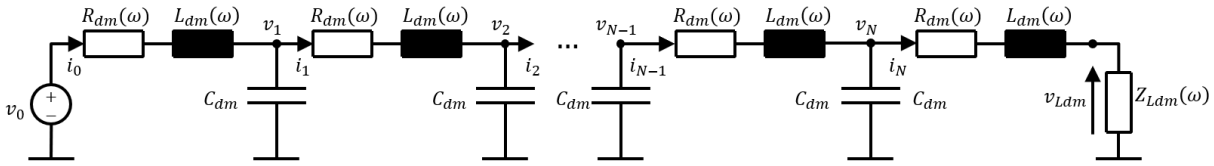


Figure 6.3: Γ-type single-line transmission line model.

The relationship between the source side voltage v_0 and the node voltages from 1 to N is presented in matrix form as follows for conductance terms G_s, G_g, and G_l,

$$\begin{pmatrix} (\frac{G_g}{G_s}+2) & -1 & 0 & 0 & 0 \\ -1 & (\frac{G_g}{G_s}+2) & -1 & 0 & 0 \\ 0 & \ddots & \ddots & \ddots & 0 \\ 0 & 0 & -1 & (\frac{G_g}{G_s}+2) & -1 \\ 0 & 0 & 0 & -1 & (\frac{G_g+G_l}{G_s}+1) \end{pmatrix} \begin{pmatrix} v_1 \\ v_2 \\ \vdots \\ v_{N-1} \\ v_N \end{pmatrix} = \begin{pmatrix} v_0 \\ 0 \\ \vdots \\ 0 \\ 0 \end{pmatrix}, \tag{6.8}$$

$$G_s = \left(\frac{1}{R'_{dm}+j\omega L'_{dm}}\right)\left(\frac{N+1}{l_c}\right), \tag{6.9}$$

$$G_g = j\omega C'_{dm}\left(\frac{N}{l_c}\right), \tag{6.10}$$

$$G_l = \frac{1}{Z_{ldm}}. \tag{6.11}$$

Node voltage vector of v_1 to v_N is solved by multiplying the inverse of the conductance matrix with input voltage vector as follows,

$$\begin{pmatrix} v_1 \\ v_2 \\ \vdots \\ v_{N-1} \\ v_N \end{pmatrix} = \begin{pmatrix} (\frac{G_g}{G_s}+2) & -1 & 0 & 0 & 0 \\ -1 & (\frac{G_g}{G_s}+2) & -1 & 0 & 0 \\ 0 & \ddots & \ddots & \ddots & 0 \\ 0 & 0 & -1 & (\frac{G_g}{G_s}+2) & -1 \\ 0 & 0 & 0 & -1 & (\frac{G_g+G_l}{G_s}+1) \end{pmatrix}^{-1} \begin{pmatrix} v_0 \\ 0 \\ \vdots \\ 0 \\ 0 \end{pmatrix}. \tag{6.12}$$

Knowing v_N, an expression for v_{Ldm} is derived,

$$v_{Ldm} = v_N\left(\frac{Z_{Ldm}}{R_{dm}+j\omega L_{dm}+Z_{Ldm}}\right). \tag{6.13}$$

Consider the trapezoidal waveform's Fourier series expansion coefficients c_n of fundamental frequency f_0 at harmonic n as described by (6.1). For $v_0 = 1$, v_{Ldm} is solved at each harmonic of frequency nf_0. This is plotted in blue as shown in Figure 6.4. Coefficients c_n are plotted in orange. Coefficients c_n are then multiplied by v_{Ldm} to determine

the load side voltage's Fourier series expansion coefficients and are plotted in yellow. The influence of v_{Ldm}'s resonant peaks on the trapezoidal spectrum's coefficients c_n is shown on the resultant $c_n v_{Ldm}$ plot.

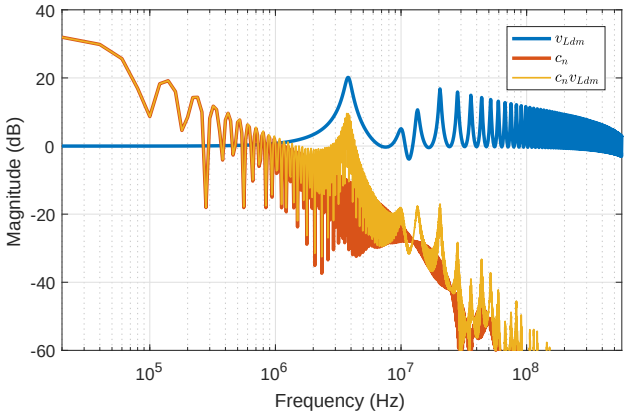


Figure 6.4: Bode response plot of source side to load side voltage v_{Ldm}, source side trapezoidal waveform's Fourier expansion coefficients c_n, and resultant product of $c_n v_{Ldm}$ for a 10m long cable, fundamental frequency of $f_0 = 20$kHz, DC bus voltage of $A = 100$V, source side trapezoidal rise time $\tau_r = 0.03$us and fall time $\tau_f = 0.08$ns.

The respective time series $a(t)$ of Fourier series expansion coefficients a_n is determined as follows,

$$a(t) = \frac{1}{2}a_0 + \sum_{n=1}^{\infty} |a_n| \cos\left(2\pi n f_0 t + \angle(a_n)\right). \tag{6.14}$$

The time series of load side voltage response for a source side trapezoidal voltage input is determined and plotted as shown in Figure 6.5. For the reader's convenience, the amplitude A of the source side trapezoid is set to 100 so the percentage voltage overshoot on the load side can be easily determined. Here, the load side voltage peaked at a value of 98.8% greater than that of the source side voltage's amplitude.

6.3 Transmission line model parameter extraction

In this section, the method to determine the variation of line resistance and inductance of cables with frequency due to skin effect and proximity effect is described. Analytical methods of determining the cable parameters were initially considered. Equations for three-phase cable series resistance considering proximity effect and skin effect have been found [117]. Equations for per phase line inductance for high and low frequency conditions have been found [118]. Phase-to-ground and phase-to-phase capacitance expressions as derived using the mirror image method have been found for three conductors within a round shield [118].

However, large discrepancies were observed between reviewed analytically determined and their respective measured values. The main limitation of the reviewed analytical

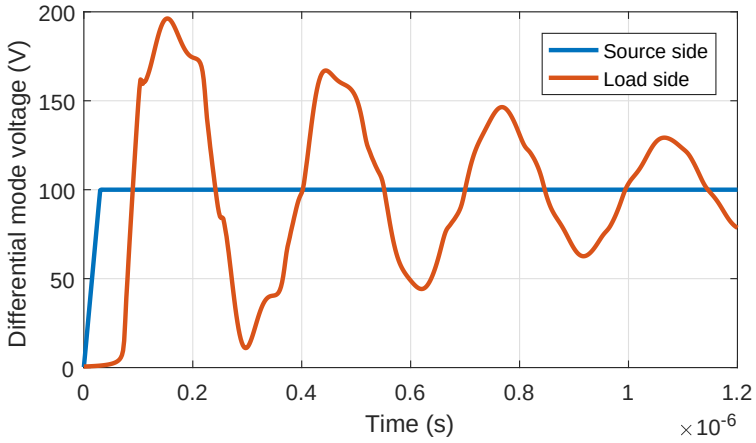
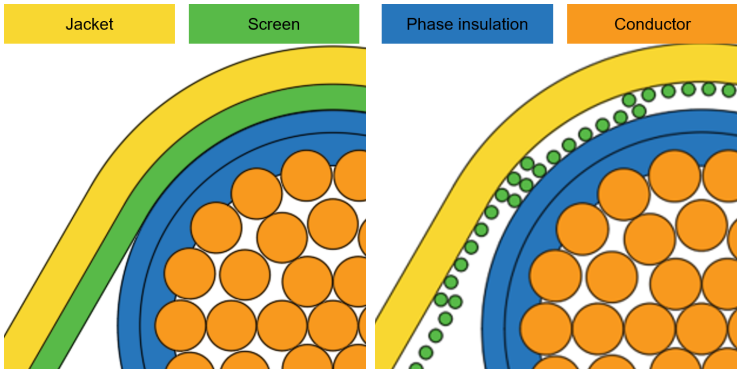


Figure 6.5: Time series of source side and load side voltages for a 10m long cable, fundamental frequency of $f_0 = 20$kHz, DC bus voltage of $A = 100$V, source side trapezoidal rise time $\tau_r = 0.03$us.

equations is their approximation of each cable's phase conductor to that of a single solid homogeneous cylinder. In reality, the conductors are stranded, consisting of numerous individual smaller solid cylinders. At high frequencies, the current density increases at the outer boundaries of each conductor. Thus, precise representation of these outer boundaries of each cable phase conductor is critical to the accurate determination of resistance and inductance variation with frequency due to skin and proximity effect. Phase-to-ground and phase-to-phase capacitance equations for three conductors assuming a lumped continuous shield can be inaccurate as the shield in real three-phase cables tend to be stranded as shown in Figure 6.6. For these reasons, FE methods are preferred and have been used in the determination of cable parameters.



(a) Lumped continuous shield. **(b)** Stranded shield.

Figure 6.6: Lumped continuous shield and stranded shield representation.

FEMM was used to calculate the equivalent resistance and inductance of a metre long portion of cable connected in a three-phase differential mode arrangement as shown in Figure 6.7 where IA stands for impedance analyser.

The governing equations for this analysis are as follows. For a steady-state operating

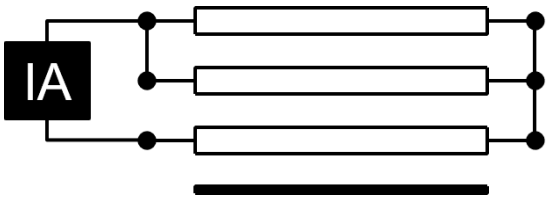


Figure 6.7: Cable differential mode single phase measurement arrangement.

frequency, the magnetic vector potential A is represented as,

$$A = \mathrm{Re}[a(\cos(\omega_t) + j\sin(\omega t))], \tag{6.15}$$

where a is the magnetic vector potential magnitude. FEMM solves the governing harmonic magnetic problem,

$$\nabla \times \left(\frac{1}{\mu_{eff}\,(B)} \nabla \times a \right) = -j\omega\sigma a + \hat{J}_{src} + \sigma \nabla V, \tag{6.16}$$

where μ_{eff} is the effective permeability, B is the flux density, σ is the conductivity, $\hat{J}_{src}$ is the phasor transform of the applied current source [119].

The resultant flux and current density plots at three different frequencies, determined using FEMM, are shown in Figure 6.8. At low frequency, current density is evenly distributed throughout the conductors. As frequency increases, current density increases at the outer boundary of each conductor, and decreases in the middle of the conductors due to skin and proximity effect. In the absence of current density in the centre of the conductors at high frequency, flux density reduces, leading to a reduction in inductance.

The FEE calculated PUL common mode three-phase equivalent capacitance $C'_{eq,cm3ph}$ is 977pF/m. The FEE calculated PUL common mode single phase equivalent capacitance $C'_{eq,cm1ph}$ is 416pF/m. The PUL phase to ground, phase to phase, single-line equivalent differential mode, and single-line equivalent common mode capacitances C'_g, C'_m, C'_{cm} can be determined as follows,

$$C'_g = \frac{C'_{eq,cm3ph}}{3}, \tag{6.17}$$

$$C'_m = \frac{C'_{eq,cm1ph} - C'_g}{2}, \tag{6.18}$$

The equivalent three-phase cable capacitance network is shown in Figure 6.9. It consists of the three conductors and the shield.

Cable phase-to-phase and phase-to-ground capacitance are determined using finite element electrostatics (FEE). The electrostatic potential plots are shown in Figure 6.10, for the given XL-ETFE insulator's dielectric constant of 2.6.

For cable conductor's gauges AWG#10 to AWG#24, the equivalent three-phase differential-mode per unit length cable resistance and inductance with respect to frequency is de-

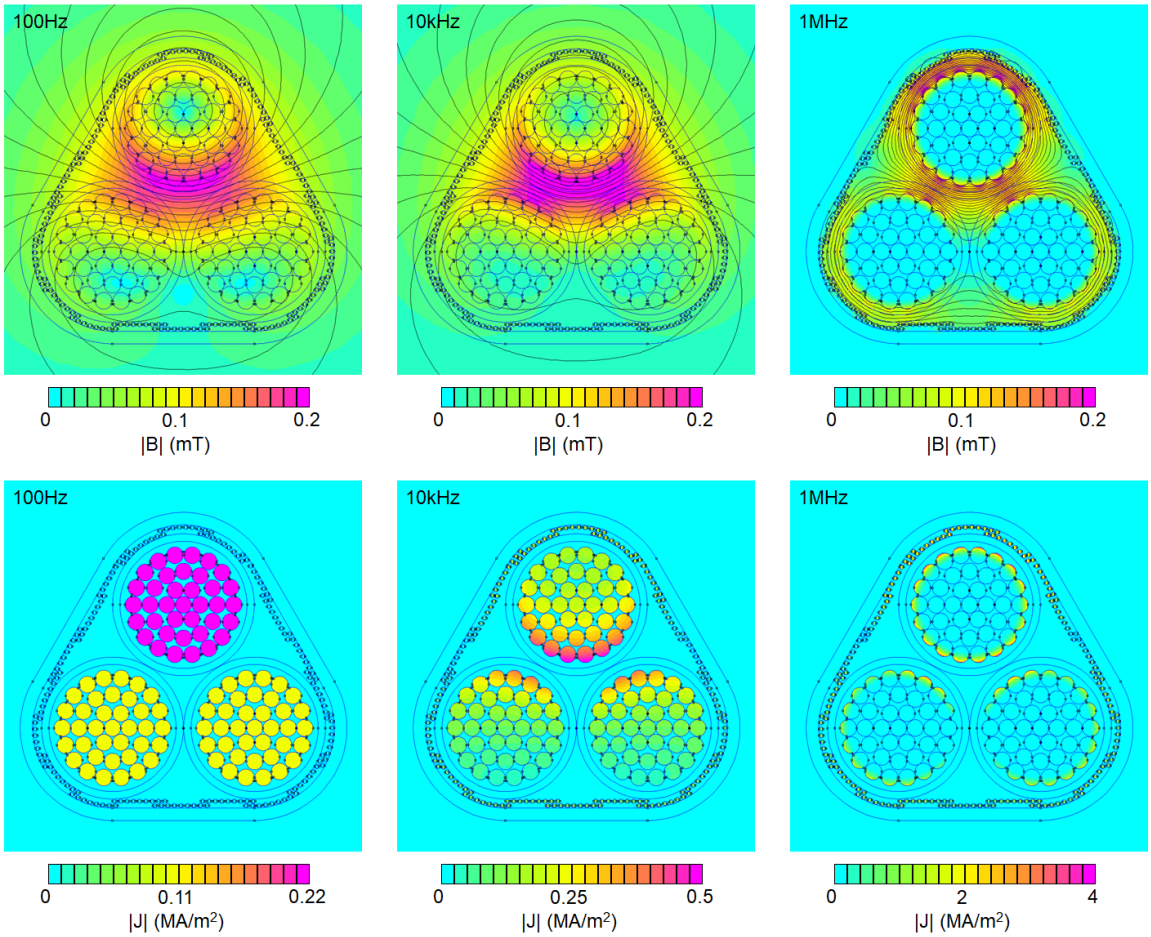


Figure 6.8: Flux density $|B|$ and current density $|J|$ plots for different frequencies of M27500-10SD3T23 cable's cross section in three-phase differential model arrangement determined using FEMM.

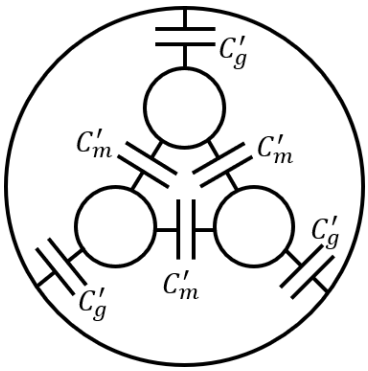
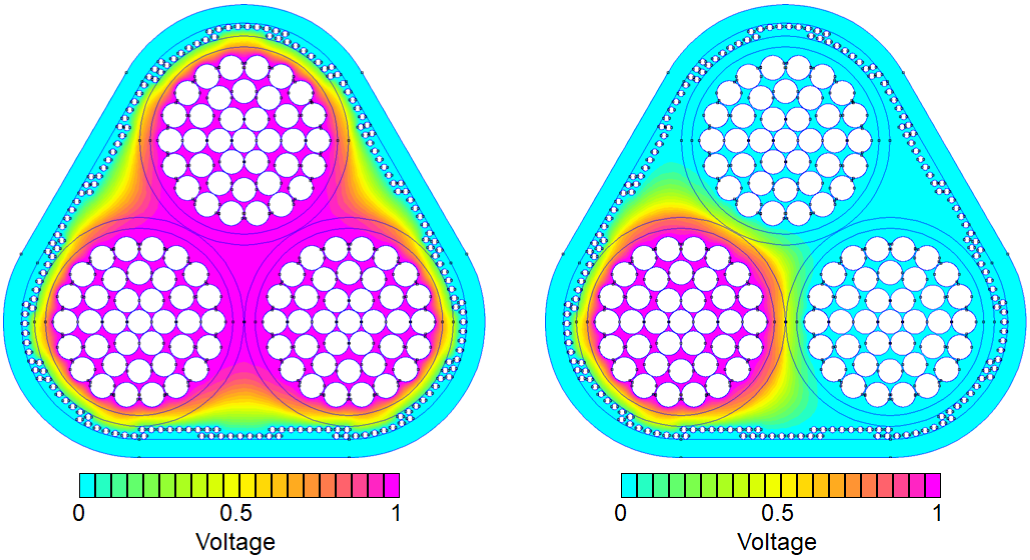


Figure 6.9: Equivalent three-phase cable capacitance network.

termined using FEM. These results are shown in Figure 6.11. The equivalent per unit length common-mode three-phase and single-phase cable capacitance is determined for cable conductor's gauges in Table 6.1. It is assumed that phase insulation outer and inner layer thickness, shield strand diameter and all component material properties remain the same for all cable gauges.



(a) Common mode three-phase. **(b)** Common mode single phase.

Figure 6.10: Finite element electrostatic voltage plot for common mode three-phase and single phase arrangements of M27500-10SD3T23 cable.

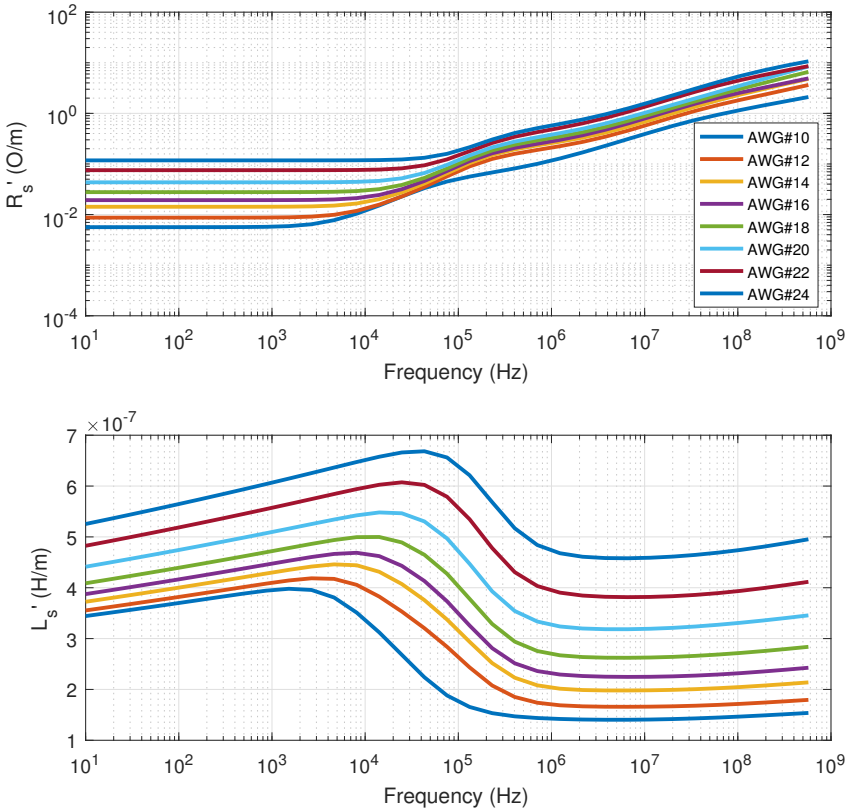


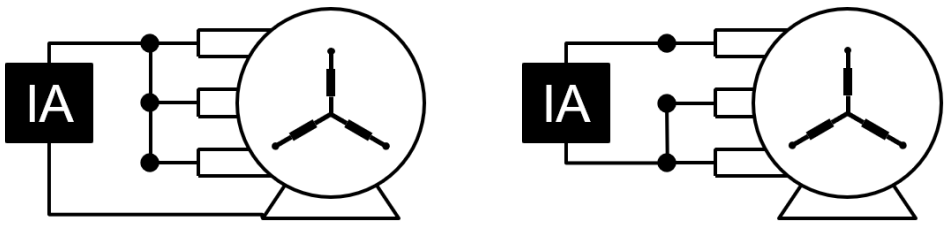
Figure 6.11: Per unit length FEM calculated resistance and inductance with respect to frequency for three-phase differential mode cable arrangement for different conductor gauges.

Table 6.1: Per unit length FEE determined cable capacitance with respect to cable gauge.

AWG	Stranding (No. × mm)	$C'_{eq,cm3ph}$ (pF/m)	$C'_{eq,cm1ph}$ (pF/m)
10	37 × 0.40	770.7	367.0
12	37 × 0.32	691.0	308.2
14	37 × 0.25	571.2	260.3
16	19 × 0.30	521.6	233.5
18	19 × 0.25	452.4	201.8
20	19 × 0.20	379.8	167.0
22	7 × 0.25	324.7	143.9
24	7 × 0.20	270.5	119.6

6.4 High-frequency machine model

A three-phase non-salient permanent magnet machine's common mode and differential mode impedance is experimentally determined using an impedance analyser under the measurement arrangement shown in Figure 6.12 where IA stands for impedance analyser.



(a) Common mode. **(b)** Differential mode.

Figure 6.12: Three-phase permanent magnet machine's common mode and differential mode impedance measurement arrangements.

However a physical machine from which one can measure the DM and CM equivalent impedance with respect to frequency is of course not available during preliminary design stage. Thus, methods of determining DM and CM equivalent impedance up to/beyond 10MHz from machine geometry, material data, and operating point need to be investigated and developed. Broadly speaking, these methods can fall into one of two categories, analytically/mathematically or finite element analysis FEA.

It has been shown in section 4.6 that equivalent per phase resistance and inductance can be determined analytically for low frequencies. However this method is not appropriate for determination of high frequency resistance considering skin effect, proximity effect, and complex geometry. As frequency increases, resistance increases and inductance reduces. Equivalent turn-to-ground, turn-to-turn, and coil capacitance can be determined for form-wound windings with tight packing. However, it cannot determine equivalent capacitance terms for randomly distributed windings or assess how significant the variance is on the equivalent DM and CM impedance.

Thus, the focus of determining HF impedance is FEA based. A per turn equivalent circuit is presented for which the parameters would be determined using FEMM.

6.4.1 Machine winding per-turn equivalent circuit

The **per turn equivalent circuit** of turn 1 of a coil is shown in Figure 6.13. The turn-to-stator winding is presented by $C_{1.0}$. The per turn frequency dependent variation of the resistance and inductance is modelled by the three parallel RL branches consisting of $\{R_{l1}, L_{l1}\}$, $\{R_{l2}, L_{l2}\}$, and $\{R_{l3}, L_{l3}\}$. The per turn eddy current loss resistor is represented by R_{et}. The inter-turn capacitance between turn 1 and turn 2 is $C_{1.2}$ and between 1 and 3 is $C_{1.3}$. This extends to any inter-turn capacitance between turn n and m for $C_{n.m}$.

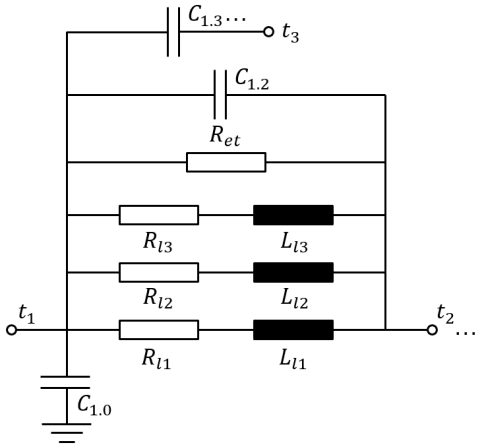


Figure 6.13: Equivalent machine winding per-turn network.

Each turn's $\{R_{l1}, L_{l1}\}$, $\{R_{l2}, L_{l2}\}$, $\{R_{l3}, L_{l3}\}$, and R_{et} is approximated to be equal. How these terms are determined and the justification for approximation is explained in section 6.4.2. The inter-turn and turn-to-stator capacitances is determined for a given stator geometry and conductor placement and is presented in section 6.4.3.

6.4.2 Per-turn resistance and inductance

The per turn resistance and inductance with respect to frequency is determined using FEMM magnetodynamic analysis for given stator and rotor geometry, material data, winding scheme and conductor definition.

Instead of explicit conductor representation in a coil, each wound coil and its conductors as a whole is represented as a continuum via an equivalent foil approach [120, 121]. This is both for the sake of simplicity and to improve computational efficiency by reducing the number of mesh finite elements to solve. This approach determines the equivalent conductivity and permeability of a region filled with packed round wires, from which skin and proximity effects can be considered in the magnetodynamic field computation.

Three circuits, A, B, and C are defined, representing each phase. Circuit A's current magnitude a is set to 1A, while the magnitude of B, and C are both set to -0.5A. Each phase circuit's phasor voltage $\bar{V}_{A,B,C}$ is determined with respect to frequency. Knowing each phase circuit's phasor voltage and current, the complex impedance is determined of

which its real term equates to an equivalent per phase resistance $R_{A,B,C}$ and imaginary term equates to the product of equivalent inductance $L_{A,B,C}$ and ω,

$$\frac{\bar{V}_{A,B,C}(\omega)}{\bar{I}_{A,B,C}(\omega)} = \bar{Z}_{A,B,C}(\omega) = R_{A,B,C}(\omega) + j\omega L_{A,B,C}(\omega). \tag{6.19}$$

The equivalent differential mode impedance $\bar{Z}_{DM}(\omega)$ is of the following sum,

$$\bar{Z}_{DM}(\omega) = R_a(\omega) + \frac{R_b(\omega)R_c(\omega)}{R_b(\omega) + R_c(\omega)} + j\omega\left(L_a(\omega) + \frac{L_b(\omega)L_c(\omega)}{L_b(\omega) + L_c(\omega)}\right). \tag{6.20}$$

FEMM determined $\bar{Z}_{DM}(\omega)$ for 12s/10p machine is shown in Figure 6.14 for which its real, imaginary, and calculated inductance are plotted with respect to frequency. As frequency increases, resistance increases, and inductance decreases due to skin effect, proximity effect, and core losses.

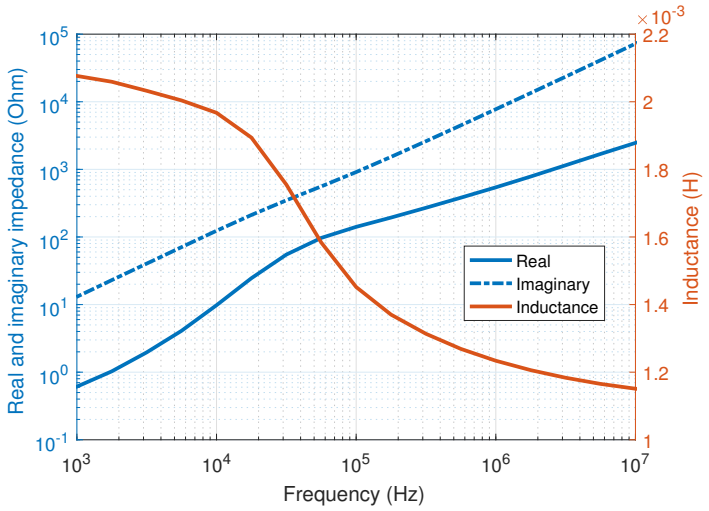


Figure 6.14: FEMM determined real, imaginary impedance and inductance with respect to frequency for 12s10p HEMAS machine.

The per turn equivalent impedance $\bar{Z}_t$ as a function of frequency is determined from the $\bar{Z}_{DM}$ as follows,

$$\bar{Z}_t(\omega) = \frac{2}{3N_{ph}}\bar{Z}_{DM}(\omega). \tag{6.21}$$

Next, parameters $\{R_{t1}, L_{t1}\}$, $\{R_{t2}, L_{t2}\}$, and $\{R_{t3}, L_{t3}\}$ of the three RL parallel branch that model $\bar{Z}_t(\omega)$ need to be determined. This is done using a technique known as vector-fitting [122] [123] which determines a rational least squares approximation $Y_{fit}(s)$ of a frequency response $Y(s)$ of the following form,

$$Y(s) \approx Y_{fit}(s) = \sum_{m=1}^{N} \frac{c_m}{s - a_m} + D + sE, \tag{6.22}$$

where c_m and a_m are residues and pole respectively and D and E are constants to be

fitted. For the presented case, $N = 3$.

Next, passivity of the admittance's rational approximation $Y_{fit}(s)$ in pole-residue form is enforced [124]. Passivity implies that the real part of its eigen values are positive for all frequencies,

$$\text{eig}(\text{Re}\{\sum_{m=1}^{N} \frac{c_m}{s - a_m} + D + sE\}) > 0. \tag{6.23}$$

Passivity enforcement ensures that any energy applied by a voltage would be absorbed, ensuring stable simulation.

Passivity enforcement is done by minimum variation of difference ΔY to the original model,

$$\Delta Y = \sum_{m=1}^{N} \frac{c_m}{s - a_m} + D + sE \approx 0. \tag{6.24}$$

while ensuring real part of eigenvalues are positive as governed by (6.23).

Passive admittance in pole-residue form as expressed in (6.22) is synthesised into an equivalent RLC circuit as shown in Figure 6.15 where,

$$R_m = -a_m/c_m, \tag{6.25}$$

$$L_m = 1/c_m, \tag{6.26}$$

$$R_D = 1/D, \tag{6.27}$$

$$C_E = E. \tag{6.28}$$

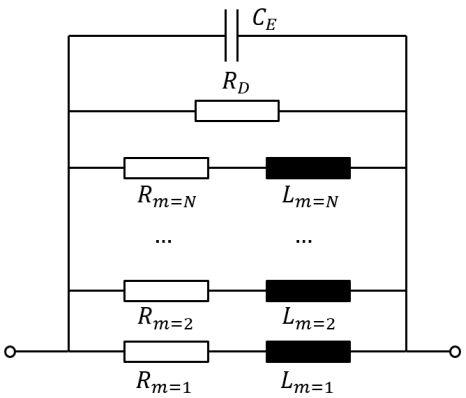


Figure 6.15: RLC equivalent circuit from vector fitting admittance.

The FEMM determined differential mode complex admittance as calculated from Figure 6.14 is vector-fitted for $N = 3, D = 0$, and $E = 0$. The parameters of an equivalent RL parallel ladder are determined and shown in Table 6.2.

The per turn RL parameters $\{R_{t1}, L_{t1}\}$, $\{R_{t2}, L_{t2}\}$, and $\{R_{t3}, L_{t3}\}$, is determined from the respective differential mode RL fitted parameters $\{R_1, L_1\}$, $\{R_2, L_2\}$, and $\{R_3, L_3\}$

Table 6.2: Vector-fitted RL parameters for FEMM determined differential mode complex admittance

Subscript	$x_{m=1}$	$x_{m=2}$	$x_{m=3}$
$x = R$	1689	929	0.368
$x = L$	0.00495	0.0549	0.00205

by scaling the differential mode parameters by $2/(3N_{ph})$, where N_{ph} is the number of turns per phase.

$$R_{tm}|_{m=1\ldots N} = \frac{2}{3N_{ph}} R_m|_{m=1\ldots N}, \tag{6.29}$$

$$L_{tm}|_{m=1\ldots N} = \frac{2}{3N_{ph}} L_m|_{m=1\ldots N}. \tag{6.30}$$

6.4.3 Inter-turn and turn-to-stator capacitance

Consider the conductor turns of a coil in a stator slot. For any given conductor turn of index n, parasitic capacitance is present between itself and the stator slot wall of value $C_{0.n}$, and between itself and other conductor of index m of value $C_{n.m}$. Trivially, $C_{m.n} = C_{n.m}$. All conductor turns' turn-to-stator and inter-turn capacitances is represented as a capacitance matrix and determined for given slot geometry, conductor turn placement, conductor geometry, and material data using electrostatic FEA.

FEMM is used to solve the electrostatic field problem. The governing electric field [119] equation for which the program solves for voltage V, charge density ρ and electric permittivity ϵ is,

$$-\epsilon \nabla^2 V = \rho. \tag{6.31}$$

A system with three conductors surrounded by a grounded box as shown in Figure 6.16 is used to explain the capacitance matrix solving method. The conductors are analogous to coil conductors and the grounded box is analogous to the stator slot wall. The circular conductors are indexed 1, 2, and 3. The inter-conductor capacitances are $C_{1.2}$, $C_{1.3}$, and $C_{2.3}$. The conductor to ground capacitances are $C_{0.1}$, $C_{0.2}$, and $C_{0.3}$.

Given relationship $Q = CV$, the net charge Q on each conductor of a voltage V is,

$$\begin{pmatrix} Q_1 \\ Q_2 \\ Q_3 \end{pmatrix} = \begin{pmatrix} C_{0.1} + C_{1.2} + C_{1.3} & -C_{1.2} & -C_{1.3} \\ -C_{1.2} & C_{0.2} + C_{1.2} + C_{2.3} & -C_{2.3} \\ -C_{1.3} & -C_{2.3} & C_{0.3} + C_{1.3} + C_{2.3} \end{pmatrix} \begin{pmatrix} V_1 \\ V_2 \\ V_3 \end{pmatrix} \tag{6.32}$$

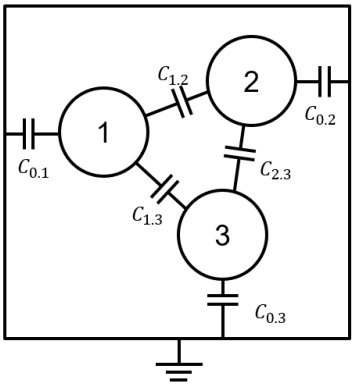


Figure 6.16: Three conductor in grounded box example with labelled inter-conductor and conductor to ground capacitances.

A matrix G is defined as inverse of matrix C,

$$\begin{pmatrix} G_{11} & G_{12} & G_{13} \\ G_{21} & G_{22} & G_{23} \\ G_{31} & G_{32} & G_{33} \end{pmatrix} \triangleq \begin{pmatrix} C_{0.1}+C_{1.2}+C_{1.3} & -C_{1.2} & -C_{1.3} \\ -C_{1.2} & C_{0.2}+C_{1.2}+C_{2.3} & -C_{2.3} \\ -C_{1.3} & -C_{2.3} & C_{0.3}+C_{1.3}+C_{2.3} \end{pmatrix}^{-1}. \tag{6.33}$$

An expression of V with respect to G and Q is made,

$$\begin{pmatrix} V_1 \\ V_2 \\ V_3 \end{pmatrix} = \begin{pmatrix} G_{11} & G_{12} & G_{13} \\ G_{21} & G_{22} & G_{23} \\ G_{31} & G_{32} & G_{33} \end{pmatrix} \begin{pmatrix} Q_1 \\ Q_2 \\ Q_3 \end{pmatrix} \tag{6.34}$$

The conductor charge excitations are set as follows,

$$\begin{pmatrix} Q_1 & Q_2 & Q_3 \end{pmatrix}^T = \begin{pmatrix} 1 & 0 & 0 \end{pmatrix}^T \tag{6.35}$$

Substituting (6.35) into (6.34) gives,

$$\begin{pmatrix} V_1 \\ V_2 \\ V_3 \end{pmatrix} = \begin{pmatrix} G_{11} & G_{12} & G_{13} \\ G_{21} & G_{22} & G_{23} \\ G_{31} & G_{32} & G_{33} \end{pmatrix} \begin{pmatrix} 1 \\ 0 \\ 0 \end{pmatrix}. \tag{6.36}$$

Voltages V_1, V_2, and V_3 are solved using FEMM for $Q_1 = 1$, and $Q_2 = Q_3 = 0$. Thus, the following G matrix terms is equated to the voltage vector,

$$\begin{pmatrix} G_{11} & G_{12} & G_{13} \end{pmatrix}^T = \begin{pmatrix} V_1 & V_2 & V_3 \end{pmatrix}^T. \tag{6.37}$$

This process is repeated by setting the charge of each conductor equal to 1 coulomb and the other conductors to zero. The voltage of all conductors are determined us-

ing FEMM, and each row of the G matrix is solved. For charges $\begin{pmatrix} Q_1 & Q_2 & Q_3 \end{pmatrix}^T = \begin{pmatrix} 0 & 1 & 0 \end{pmatrix}^T$, G parameters are solved by equating $\begin{pmatrix} G_{21} & G_{22} & G_{23} \end{pmatrix}^T = \begin{pmatrix} V_1 & V_2 & V_3 \end{pmatrix}^T$. For charges, $\begin{pmatrix} Q_1 & Q_2 & Q_3 \end{pmatrix}^T = \begin{pmatrix} 0 & 0 & 1 \end{pmatrix}^T$, G parameters are solved by equating, $\begin{pmatrix} G_{31} & G_{32} & G_{33} \end{pmatrix}^T = \begin{pmatrix} V_1 & V_2 & V_3 \end{pmatrix}^T$ Once all terms of G are determined, capacitance matrix terms C is determined using (6.33).

This capacitance matrix solving technique is demonstrated on the 12s/10p HEMAS machine. Each of its three-phases consists of two concentrated coils with 46 turns per coil. Each coil occupies two slots exclusively. The per slot geometry has been provided as shown in Figure 6.17. The slot-liner material is 0.2mm insulation paper with a dielectric constant of 3.0. The wire's inner and outer diameters are 0.95mm and 1.0mm respectively.

Conductors were uniformly randomly distributed within the slot region. This is done using a random number generator to generate a series of candidate conductor centre coordinates. The geometric constraint criterion by which eligible conductor centre coordinates are selected are that the distance between centres are greater than that of the conductor's outer diameter and the centre's perpendicular distance to the slot-liner inner wall is greater than that of the conductor's outer radius. What this does is that it ensures conductors don't overlap with each other or with the boundary wall.

The outer boundary's voltage is set to zero. The charge of one conductor is set to 1 coulomb while the charge of the other conductors are set to 0. The geometric depth of the problem is set equal to the machine's stack length L_{stk}. The electrostatic field problem is solved, the voltage of each conductor is determined using FEMM and the corresponding row of G matrix's parameters are solved. This is repeated for all conductor until all rows of G are solved. The capacitance matrix is then determined by inversion of G from which all conductors' inter-turn and turn to stator capacitances is equated.

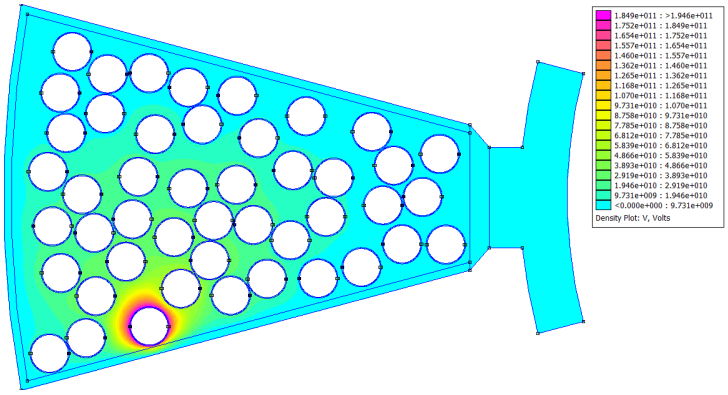


Figure 6.17: Resultant voltage field plot of conductor filled stator slot where charge of one conductor is set to 1 coulomb.

The conductor capacitance values determined in Figure 6.17 relate to a single slot of depth equal to that of the stack length. One turn consists of two in-slot portions and two

end-winding portions. Thus, to determine the equivalent turn-to-stator capacitance, the conductor turn-to-stator capacitance is simply doubled. The inter-conductor capacitance is multiplied by l_{mlt}/L_{stk} to get the inter-turn capacitance where l_{mlt} is the mean length per turn.

The results of the turn to stator and inter-turn capacitances are shown in Figure 6.18. The diagonal represents turn to stator capacitance values $C_{0.1}, C_{0.2} \ldots C_{0.46}$. All off-diagonal values are inter-turn capacitances. Note the symmetry of the off-diagonal parameters as $C_{n.m} = C_{m.n}$.

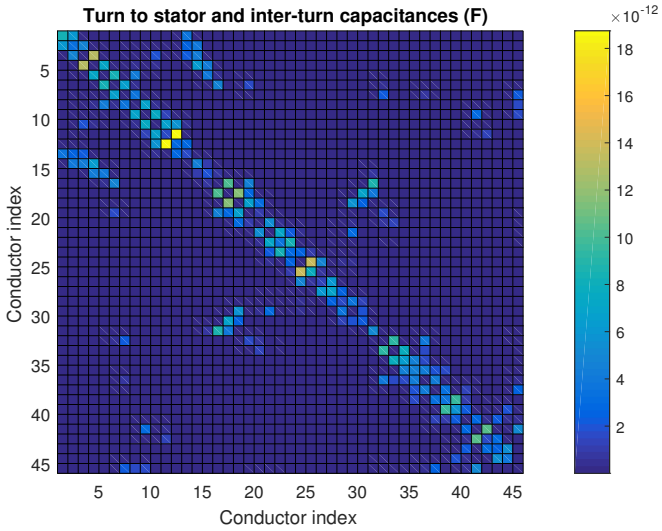


Figure 6.18: FEMM determined turn to stator (diagonal) and inter-turn (off-diagonal) capacitances.

6.4.4 Eddy current resistor

Per turn eddy current losses are represented by the resistor R_{et}. Methods of determining this experimentally have been investigated in [25]. An empirical power fit of equivalent eddy current resistance vs. machine power rating was derived for the following per phase HF equivalent circuit as shown in Figure 6.19.

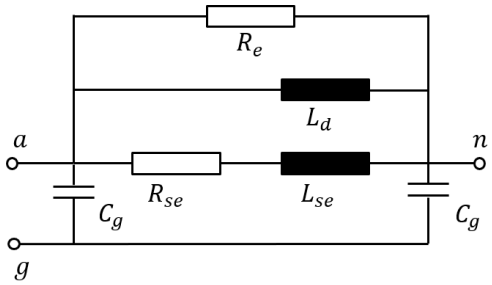


Figure 6.19: Per-phase equivalent circuit considering eddy current resistor [25].

The equivalent eddy current resistor of this machine is determined using vector-fitting of measured differential mode impedance. The RLC equivalent circuit of Figure 6.15 is

assumed. Observe the similarities between this circuit and that presented in [25]. Both have an RL circuit in parallel with an eddy current resistor and terminal-to-terminal capacitance.

For three RL branches, the following parameters were determined from RLC equivalent circuit in Figure 6.15 by vector-fitting and shown in Table 6.3. The vector-fitted impedance is plotted alongside the measured data with respect to frequency in Figure 6.20.

Table 6.3: Vector-fitted RL parameters for measured differential mode impedance.

R_1	1689Ω	L_1	4.95mH
R_2	929.4Ω	L_2	54.88mH
R_3	0.368Ω	L_3	2.05mH
R_D	1174Ω	C_E	121.56pF

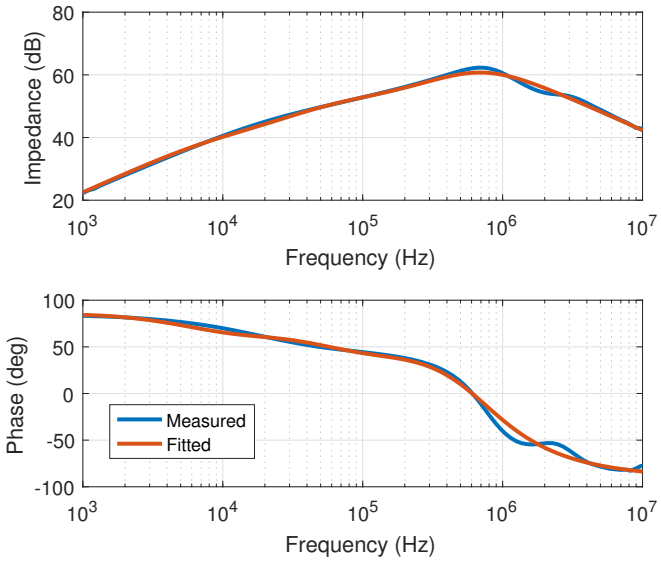


Figure 6.20: Vector-fitting of measured differential mode impedance.

The per turn eddy current resistor R_{et} is determined from vector fitted R_D as follows,

$$R_{et} = R_D \frac{2}{3N_{ph}}. \tag{6.38}$$

Here, N_{ph} is 92.

6.4.5 HF machine model from measurement

If the considered machine under test has been physically realised/built, its differential and common mode impedance can be measured and an equivalent high-frequency circuit can be used to model it. The considered high-frequency equivalent circuit non-salient

permanent magnet machine model is shown in Figure 6.21 and is presented in [26]. It builds upon the conventional low-frequency per-phase equivalent circuit by adding parameters to model high-frequency impedance characteristics. The per-phase low-frequency equivalent circuit portion consists of stator resistance R_s, magnetising and leakage inductances L_M and L_{ls} respectively, and a back-EMF term $K\sin(\omega_r + \phi)$ where K is the back-emf constant, ω_r is the rotor electrical speed and ϕ is the rotor's electrical position. The high-frequency impedance is modelled by phase inter-turn winding capacitance C_{sw}, mid-frequency stator resistance R_{swm}, high-frequency stator resistance R_{swh}, effective HF stator inductance ηL_{ss} where L_{ss} is the sum of L_M and L_{ls}, and effective stator-to-frame capacitances and resistances C_{sf} and R_{sf} respectively. The ports a, g, and n represent phase input, grounded frame, and neutral respectively.

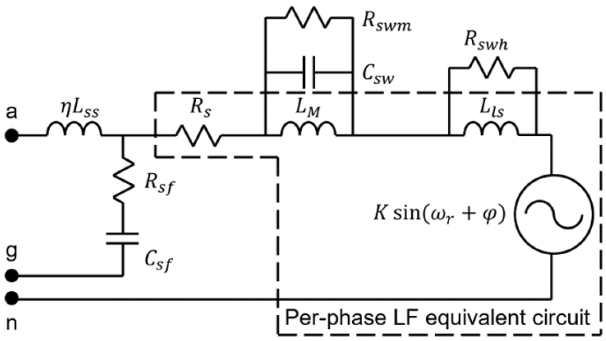


Figure 6.21: Per phase high frequency permanent machine model. [26]

The per-phase high frequency permanent machine model's parameters were fitted to measured differential mode and common mode plots in a least square manner [125] using particle swarm optimisation. The fitness function f_{error} to be minimised is the sum of integral of the absolute errors between measured and fitted common mode and differential mode impedances e_{cm} and e_{dm} across the considered frequency range f_1 to f_2 such that,

$$f_{error} = \int_{f_1}^{f_2} |e_{cm}|df + \int_{f_1}^{f_2} |e_{dm}|df. \tag{6.39}$$

The measured and fitted differential mode and common mode impedance plots of a 1kW test machine is shown in Figure 6.22. The machine's phases are connected in star.

6.5 Experimental validation

Experiments to validate the high frequency cable model, common- and differential-mode impedance models of the machine are presented in this section. Details of the experimental hardware is shown in section 4.6.10.1.

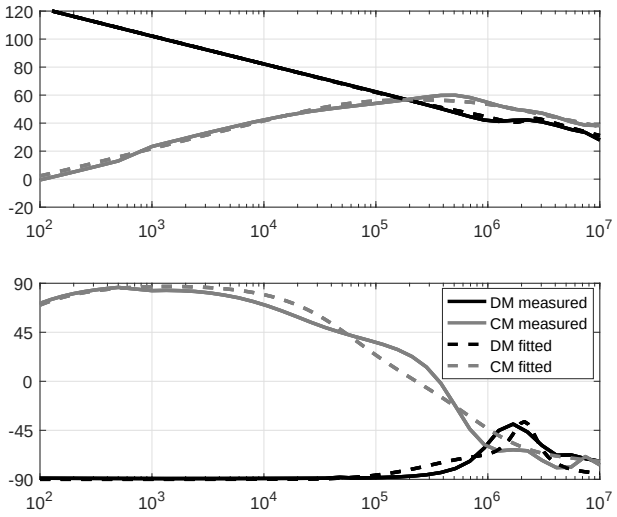


Figure 6.22: Measured vs. fitted differential mode and common mode impedance.

6.5.1 Cable

The FE cable parameter extraction process is demonstrated on the M27500-10SD3T23 three-phase 10AWG shielded aerospace cable, the cross section of which is shown in Figure 6.23 and its dimensions and material construction are shown in Table 6.4 and 6.5 respectively. The FE calculated values are then compared with measured values.

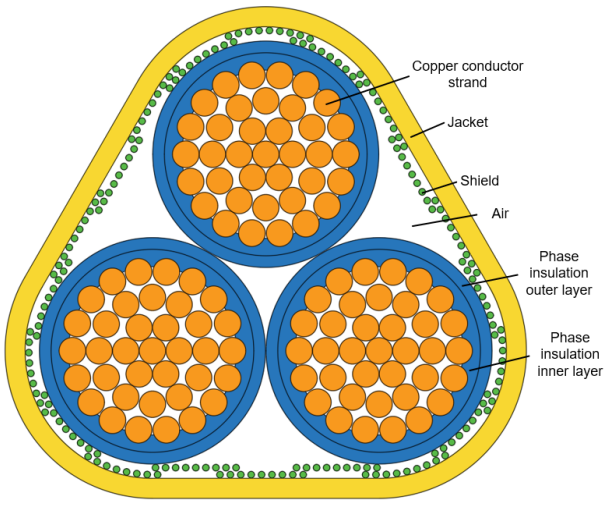


Figure 6.23: M27500-10SD3T23 10AWG cable cross section.

The equivalent three-phase differential mode per unit length (PUL) cable resistance and inductance as a function of frequency are calculated using FEMM for both the stranded shield and lumped continuous shield. The results are plotted against measured values in Figure 6.24. Resistance increases with frequency due to skin and proximity effect, while inductance decreases. Explicit strand representation of the shield leads to more accurate three-phase DM PUL FEMM determined resistance and inductance values

Table 6.4: M27500-10SD3T23 10AWG dimensions.

Parameter	Value
No. of conductors	3
No. of strands per conductor	37
Conductor strand diameter	0.4mm
Conductor outer insulation thickness	0.18mm
Conductor inner insulation thickness	0.26mm
Conductor diameter with insulation	3.4mm
Screen strand thickness	0.1mm
Outer jacket thickness (single layer)	0.3mm

Table 6.5: M27500-10SD3T23 10AWG materials.

Component	Material
Conductor outer insulation	XL-ETFE
Conductor inner insulation	XL-ETFE
Outer jacket	XL-ETFE
Conductor	Tin-coated copper

compared to that of a simplified lumped continuous screen representation.

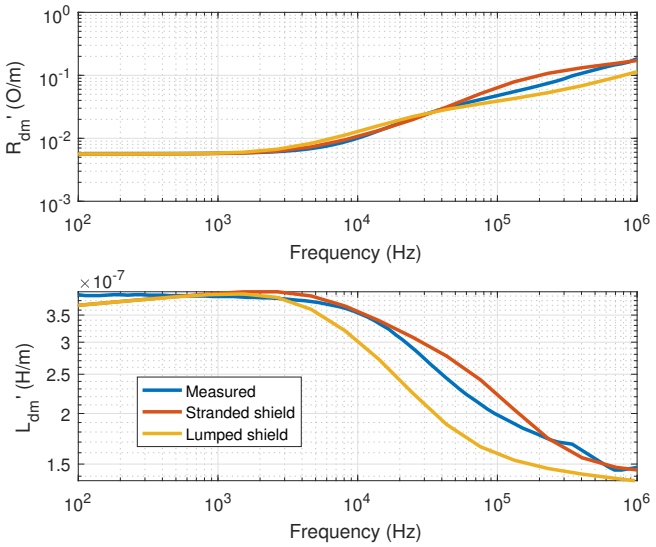
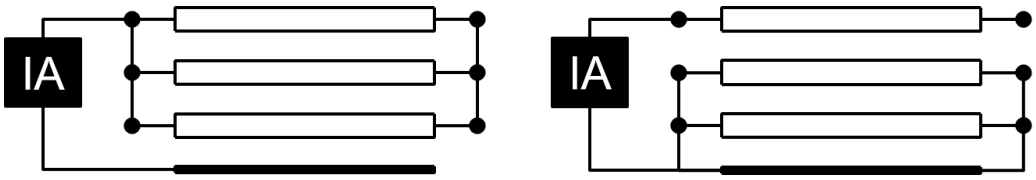


Figure 6.24: Per unit length FEM-calculated vs. measured resistance and inductance with respect to frequency for three-phase differential mode cable arrangement.

These capacitances were calculated from two different measurement arrangements, common mode three-phase and common-mode single phase as shown in Figure 6.25.

C_g' and C_m' have been determined and compared with measured values in Table 6.6. The percentage error is calculated as the ratio of the difference of the calculated value and the measured value to the measured value.



(a) Common mode three-phase. **(b)** Common mode single phase.

Figure 6.25: Cable common mode three-phase and single phase measurement arrangements.

Table 6.6: Per unit length measured and FEE determined cable capacitances for M27500-10SD3T23 cable.

PUL	Measured (pF/m)	FEE stranded screen (pF/m)	FEE lumped screen (pF/m)
$C'_{eq,cm3ph}$	770.7	814.4 (5.7%)	977.7 (26.9%)
$C'_{eq,cm1ph}$	367.0	367.6 (0.1%)	412.6 (12.4%)
C'_g	256.9	271.5 (5.7%)	325.9 (26.9%)
C'_m	905.3	916.1 (1.2%)	1042.4 (15.1%)

6.5.2 Differential mode and common mode machine impedance

The considered the machine for analysis is the HEMAS-SL, its details are shown in 4.6.10.2. The differential and common-mode impedance was determined using an impedance analyser. The calculated and experimentally determined differential and common mode impedances are plotted with respect to frequency alongside their respective measured impedances in Figure 6.26. Good match is observed for the measured and calculated differential mode impedance first resonant frequency at 0.61MHz and 0.67MHz respectively. Calculated DM impedance amplitude at frequencies greater than the first resonance is overestimated. The common mode impedance amplitude is overestimated for frequencies below that of the first anti-resonance point of 1MHz but matches closer for values beyond its first resonance point of 2MHz.

6.5.3 High frequency cable and machine model - time domain comparison

The calculated and measured differential mode voltages of both source and load side for 10m long cable have been plotted in Figure 6.27. For the calculated response, the finite element determined values for differential mode resistance, inductance as a function of frequency, and capacitance were utilised for the cable modelling. The calculated per-turn high-frequency equivalent circuit is used to model the load impedance.

For the measured case, the DC link voltage is set to 100Vdc. It is observed that the measured source side line-to-line voltage climbs from 0V to an initial voltage of 86.44V in 24.83ns. Then it climbs from 86.44V to 100V in the next 102ns. Thus the source side line-to-line voltage wave front is modelled as the sum of two time-shifted trapezoids to consider for the two different slope portions

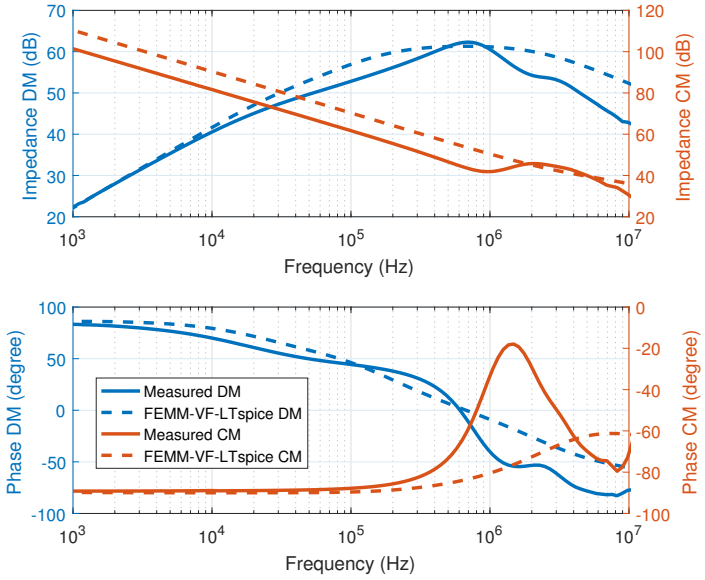


Figure 6.26: Comparison between measured and FEMM, vector fitted, LTspice calculated differential and common mode impedances.

The voltage peak for the calculated and measured load side line-to-line voltages are 182V and 171V respectively. The calculated and measured oscillation frequency are 3.49MHz and 3.87MHz respectively. The discrepancy between calculated and measured values are due to modelling errors in the cable and machine impedance characteristics, as shown in Figure 6.24 and 6.27.

6.6 Conclusion

High-frequency drive level analysis was completed using a developed high-frequency model. The model considers the source, the transmission line, and the load. The source represents the inverter, the transmission line represents the cable, and the load represents the electrical machine. The analysis is completed in the frequency domain.

Each individual voltage pulse of the inverter is represented as a trapezoidal waveform, from which its Fourier series expansion coefficients as a function of harmonic number was calculated. The three phase feeder cable is represented by a Γ-type single-line transmission line model. The frequency dependent per unit length series resistance, inductance, and capacitance were determined using FEA. The shield and conductors, and individual conductor strands were explicitly represented. Flux density and current density plots were determined with respect to frequency. Resistance increase with frequency due to skin and proximity effect while inductance decreases. Current density increases near the outer boundary of the conductors and decrease away towards the centre of the conductors with an increase in frequency.

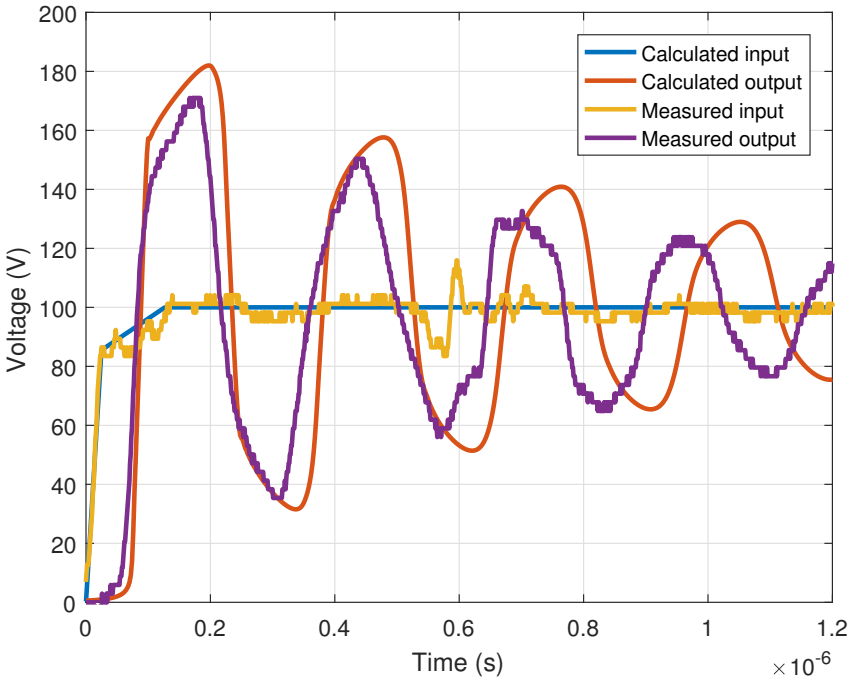


Figure 6.27: Calculated and measured differential mode voltages of source and load side for 10m cable.

A machine winding per-turn equivalent circuit was utilised to represent the machine's differential model and common mode impedance. The per-turn equivalent circuits maybe connected in series to create coils, the coils are connected to form phases, and phase are connected to form equivalent differential and common-mode impedance measurement set ups. The per-turn resistance and inductance with respect to frequency is determined using FEA. Each wound coil and its conductors was represented as a continuum via an equivalent foil approach. The inter-turn and turn-to-ground capacitance is determined using electrostatic analysis considering random placement of conductors for a mush wound winding.

The source, line, and load models representing the inverter, feeder cable, and machine respectively were combined together from which the load-side line-to-line voltage time series is calculated.

The per unit length FEM-calculated and measured resistance and inductance with respect to frequency for three-phase differential mode cable arrangement were determined and compared. Impedance values determined from two different cable representations were compared to measured values; stranded shield and lumped shield. The stranded shield model explicitly represented the conductor strands of the cable. Lumped shield lumps all shield conductors and represents them as one conductor. More accurate results are achieved by explicit representation of the individual conductor strands in the cable shield. The high-frequency machine model was validated against measured differential-

and common-mode impedances. The frequency of the first resonance point of differential-mode impedance was determined with acceptable accuracy using the presented method, with measured and calculate resonance frequencies 0.61MHz and 0.67MHz respectively. Larger discrepancies were observed between the measured and model-calculated common-mode impedance plots. The cable, and machine models were combined to generate a high-frequency cable-machine model. This is used to determine load-side line-to-line voltage for a given source-side voltage step. Peak voltage for calculated and measured load-side line-to-line voltages are 182V and 171V respectively with a 6% error in oscillation frequency.

Chapter 7

Topology Comparison

The flap actuation design problem is described in Chapter 3. The full electric drive design and sizing algorithm toolbox has been presented in Chapter 4. The toolbox is used to generate two optimal designs for flap actuation, one with centralised topology, the other with a distributed topology. The resultant designs are compared with each other and discussed.

7.1 Introduction

In section 4.1.1, the electric drive design sizing algorithm concept and scope was presented. The system consists of subsystems and components with their respective design procedures. The details of component and system level design procedures are shown in Chapter 4. The relevant inputs for each component's design procedure have been coordinated at a system level to ensure that components are inter-compatibility, the functional definition is met, and design constraints are adhered to. The resultant output from each of the design procedures were sets of feasible designs of known mass and failure rate. These designs were mixed and matched in every possible combination. For each combination, the system level mass and failure rate is determined from which the optimal designs were selected. Optimal designs in this case are designs with minimum mass within the failure rate constraint.

The full electric drive design and sizing algorithm toolbox, as presented in Chapter 4, is utilised to generate optimal system designs of different topologies . A comparison between the centralised and distributed topologies for trailing edge flap actuation is made. The considered system components are the gearbox, machine, cable, inverter LC output filter (if present), power electronics, heat sink, and EMI LC input filter. The centralised topology has the inverter and its associated passives inside the fuselage and the machine is located in the wing, near the point of actuation. An inverter LC output filter both conditions the output voltage, such that its distortion spectrum is within MIL-STD-

704F limits, and mitigates transmission-line over-voltage and oscillation effects. The distributed topology has the inverter and its associated passives out in the wing, next to the machine. No output filter is present because the inverter to machine feeder cable is short, thus making transmission line effects a non-issue.

7.2 Design search space

The system level functional definition, design variables' respective search space limits and resolution for this case study are listed in Table 7.1. The mechanical functional requirement for the electric drive actuation system is outlined in section 3.2.1. The per lane machine's mechanical output power is 1.1kW corresponding to the per flap high-lift trailing edge device power requirements of an Airbus A320-200. The nominal gear box low speed side's speed is 25RPM. The per lane failure rate constraint is 1375FIT as determined in section 3.3. A reminder that 1FIT is equal to 1 failure per 10^9 hours. The inverter's dc-link's voltage is equal to aerospace standard 270V power supply. For the centralised topology, the LC filter is designed such that its output voltage spectrum is within MIL-STD-704F distortion limits for variable frequency systems. The inverter input EMI filter's design targets are that of the MIL-STD-461F distortion limits. A -6dB safety margin is introduced to all distortion spectrum limits. The nominal inverter modulation index upper limit is set to 0.9 for sinusoidal PWM and 1 for the space vector modulation. This provides a safety margin and gives the current controller some additional voltage head room to utilise during transient high speed/high torque operation. The considered semiconductor technology is SiC MOSFET as its base predicted failure rate is an order of magnitude lower than that of IGBT's as shown in Table 4.4, assuming that SiC MOSFETs has the same base failure rate as a Si MOSFET. The internal and external lifetime profiles are utilised to determine component's failure rates are shown in Table 4.1 and 4.2 respectively. The internal lifetime profile applies to the EMI filter, power electronics, and LC output filter for centralised topology as they are located in the fuselage. The external lifetime profile applies to the same listed components for distributed topology as they would be located external of the fuselage, near the point of actuation.

The machine design procedure input variables' search space limits and resolution are listed in Table 7.2. Mechanical output power is equal to that of the system level's functional definition. The RPM speed search space is between 4000 and 8000RPM. An increase in speed typically leads to a decrease in machine mass and size. The mass of the gearbox needs to be considered as its mass is a function of gear ratio, number of gear stages, and output torque. Variation of machine speed varies both the gear ratio and the number of gear stages, thus the minimum combined mass of the gear box and the machine may not be the machine of maximum speed. Phase current search space

Table 7.1: Centralised vs. distributed topology - system level functional definition and design search space.

Parameter	Value	Unit
Application	High-lift trailing edge actuation	
Aircraft	Airbus A320-200	
Mechanical output power	1.1	kW
Nominal gear box low speed side	25	RPM
Per-lane failure rate limit	1375	FIT
DC bus voltage	270	V
Inverter switching frequency	{15, 30, 45, 60}	kHz
Inverter output LC filter design targets	MIL-STD-704F	
Inverter input EMI filter design targets	MIL-STD-461F	
Distortion spectrum safety margin	-6	dB
Inverter nominal modulation index limit	0.9	
Semiconductor technology	SiC MOSFET	
Internal lifetime profile	Table 4.1	
External lifetime profile	Table 4.2	

lower and upper limits are 3.85A and 7.59A respectively. The lower phase current limit corresponds to delivering 1.1kW from 270V dc-link at unity power factor, 100% efficiency, and modulation index of 1. The upper phase current limit corresponds to the delivering the same 1.1kW from 270V dc-link at 0.75 power factor, 75% efficiency, and modulation index of 0.9. The geometric limits for air gap, magnet, slot opening width, and height of slot depression are defined either in absolute values (such as a lower limit of 0.5mm for the air gap) or relative limits (such as air gap distance must be less than 25% of the stator bore diameter). Slot opening's lower limit is equal to double that of its winding wire thickness. The maximum ambient temperature of 70°C is considered for nominal steady state winding temperature calculation though typically, ambient temperature in this environment is lower than 70°C, and is highly dependent on the aircraft's operating climate. This can lead to over-sizing of machine.

The inverter's EMI LC input filter design procedure input variables' search space limits and resolution are listed in Table 7.3. The modulation index, output current, fundamental frequency, and power factor are dependent on the inverter load (i.e. LC output filter, cable, machine for desired steady state operating current and electrical speed). The dc-link voltage is the same as the system level defined 270V. The switching frequency search range is {15, 30, 45, 60} kHz, same as the system level defined switching frequency set. Sinusodial PWM and space vector modulation are the utilised switching schemes for centralised and distributed topologies respectively. Space vector modulation cannot be utilised in the centralised topology due to the presence of the third harmonic in the output voltage, causing common mode resonance in the LC output filter and dc-link mid-point. The inductor's temperature rise is 30°C. This is suggested as a typical value in FIDES guide [15]. The set of dc-link capacitor capacitances and rated voltages are typical values found in manufacturer's datasheets [85] [86]. The search set for number

Table 7.2: Centralised vs. distributed topology - machine functional definition and design search space.

Parameter	Value	Units
Mechanical output power P_o	1.1	kW
RPM	{4000, 4250, ..., 8000}	
DC-link voltage V_{dc}	270	V
Phase current I_{ph}	{3.85, ..., 7.59}	A_{rms}
Torque per rotor volume TRV	{3, ..., 100}	kNm/m^3
Rotor aspect ratio x_r	{0.5, 1, 2}	
Current density J	{10, 10.1, ..., 20}	A/mm^2
Tooth peak flux density $B_{t(pk)}$	1.6	T
Slots/poles N_{sl}/N_p	{12/10, 12/14}	
Switching carrier frequency f_c	{15, 30, 45, 60}	kHz
Relative tooth width τ	0.5	
Air gap d_a	$\{0.5 \times 10^{-3}, \ldots, 0.25 r_{ra}\}$	m
Magnet thickness d_m	$\{1 \times 10^{-3}, \ldots, 0.25 r_{ra}\}$	m
Width of slot opening w_d	$\{2 d_{wire}, \ldots, 0.9 w_{si}\}$	m
Height of slot opening depression h_d	$\{1 \times 10^{-3}, \ldots, 0.5 w_{si}\}$	m
Maximum ambient temperature	70	°C
Magnet material	Recoma 32	
Laminated steel	Vacoflux 50	

of EMI stages is limited to {1, 2, 3}. It was observed in preliminary design cases that increasing the number of stages further for this power level and these components, leads to an increase in component count and failure rate without a significant decrease in volume and mass.

Table 7.3: Centralised vs. distributed topology - EMI LC input filter functional definition and design search space.

Parameter	Value	Unit
Modulation index M	Load dependent	
Output current I_o	Load dependent	Apk
Output fundamental frequency f_o	Load dependent	Hz
Power factor	Load dependent	
DC-link voltage V_{dc}	270	V
Switching frequency f_c	{15, 30, 45, 60}	kHz
Switching scheme	Space vector modulation	
Inductor temperature rise T_r	30	°C
DC-link capacitance C_{dc}	{3, 5, 7, 10, 15, 20, 30, 50}	uF
Capacitor voltage rating $V_{c,rated}$	{450, 700, 1000, 1200}	V
EMI filter n stages number	{1, 2, 3}	
Lifetime profile	{Internal, External}	
Inductor core material	{Silicon Steel, Amorphous, Iron-powder, Nanocrystalline, Ferrite}	
Inverter input EMI filter design targets	MIL-STD-461F	

Inductor mass and volume is determined using empirical sizing equations. The constants of these empirical equations are determined by fitting to a set of optimised inductor designs with respect to current rating, inductance, switching frequency, temperature rise, and ambient conditions. The inductor design procedure's input variables' search space

limits and resolution utilised to generate the optimised inductor designs from which the empirical inductor mass and volume equations are fitted is presented in Table 7.4. Five different core materials are considered. An EI core is assumed, its geometry is shown in Figure 4.6 and geometric ratios are shown in (4.29-4.37). The inductor's temperature rise is 30°C, as suggested as a typical value in FIDES guide [15].

Table 7.4: Centralised vs. distributed topology - inductor functional definition and design search space.

Parameter	Value	Unit
Core material	{Silicon Steel, Amorphous, Iron-powder, Nanocrystalline, Ferrite}	
Core geometry	EI core Figure 4.6	
Core dimension D	0.1, ..., 10	cm
Gap length l_g	{0, 0.05, ..., 0.5}	cm
Temperature rise	30	°C
Ambient temperature {internal/external}	{40/70}	°C
Ambient altitude {internal/external}	{8000/20000}	ft
Switching frequency	{15, 30, 45, 60}	kHz
Current ripple for EMI filter	0.05	p.u.

The LC output filters design procedure's input variables' search space limits and resolution can be seen in Table 7.5. The LC output filter is only applicable for centralised topology, thus the internal lifetime profile is utilised. The inverter output current limit is limited to between 0.02 and 0.2 p.u., ensuring controller and observer stability. The distortion limits are that of MIL-STD-704F. Switching frequencies correspond to system level selected values. The LC output filter's inductor's core geometry, core material, temperature rise, and ambient conditions match that of Table 7.4.

Table 7.5: Centralised topology - LC output filter definition and design search space.

Parameter	Value	Unit
Inverter output current ripple	{0.02,0.04,...,0.2}	p.u.
Lifetime profile	Internal	
Distortion spectrum limit	MIL-STD-704F	
Switching frequency	{15, 30, 45, 60}	kHz
Inductor core material	{Silicon Steel, Amorphous, Iron-powder, Nanocrystalline, Ferrite}	
Core geometry	EI core Figure 4.6	
Inductor temperature rise	30	°C
Ambient temperature	40	°C
Ambient altitude	8000	ft

The control stability and filter effectiveness of the designed systems are checked in simulation. The control stability test involves a simulation with step command of rated current during a speed ramp from stand still to nominal speed. When the system is running at steady state nominal torque and speed, the source power leads' conducted emission distortion spectrum is determined and compared with the MIL-STD-461F limits. The

LC output voltage distortion spectrum is compared to the MIL-STD-704F limits in simulation. A designed system is considered feasible if current control stability is maintained during speed ramp, and input and output conducted emission spectra are compliant with their respective limits, MIL-STD-461F and MIL-STD-704F limits respectively.

7.3 Results - Centralised topology

7.3.1 System level

Consider a set of machine designs with known mass and failure rate. For each machine design which is an element of the Pareto frontier with respect to failure rate and mass, sets of inter-compatible cable, LC output filter, LC input filter, power electronics, and heat sink designs were created. These designs were iteratively mixed and matched in every possible combination from which one optimal combination is selected. The optimal combination is considered to be a system design of minimum mass and a per-lane failure rate below the 1375FIT threshold.

The full set of machine designs with known mass and failure rate are shown in Figure 7.1. The considered slot/pole combinations are 12s/10p and 12s/14p. The design search space is defined in Table 7.2. The pareto frontier is plotted with respect to both slot/pole combinations. It can be seen that 12s/10p's pareto frontier is below that of the 12s/14p, and thus are considered better designs. The designs which are an element of the 12s/10p's pareto frontier were selected from the full set. These machine designs were utilised for full system sizing.

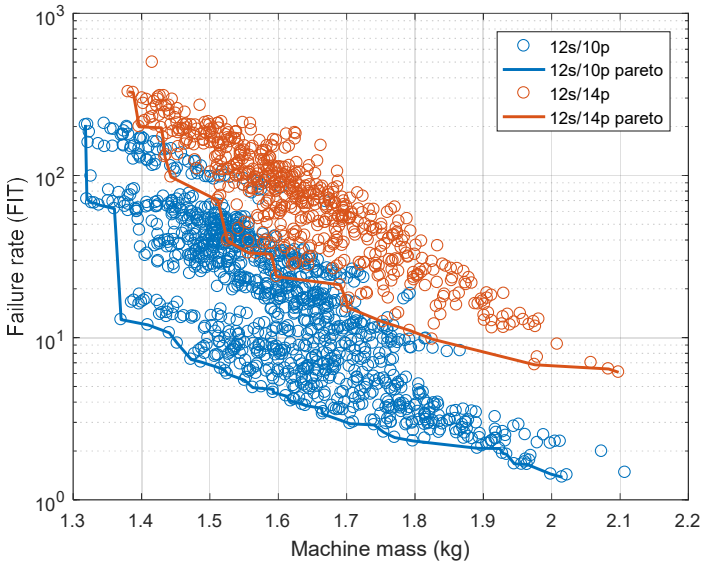


Figure 7.1: Machine designs 12s/10p, 12s/14p with respect to failure rate and mass.

The results of the system level sizing designs are shown in Figure 7.2. The colour of the markers indicate the systems' switching frequency. The mass includes all of the electrical components and half the mass of the differential gearbox. A reminder that two electrical lanes drive one differential gear/box, thus doubling this mass value would give the total per flap gearbox and electrical lanes' mass. It is shown that as failure rates increase, mass decreases.

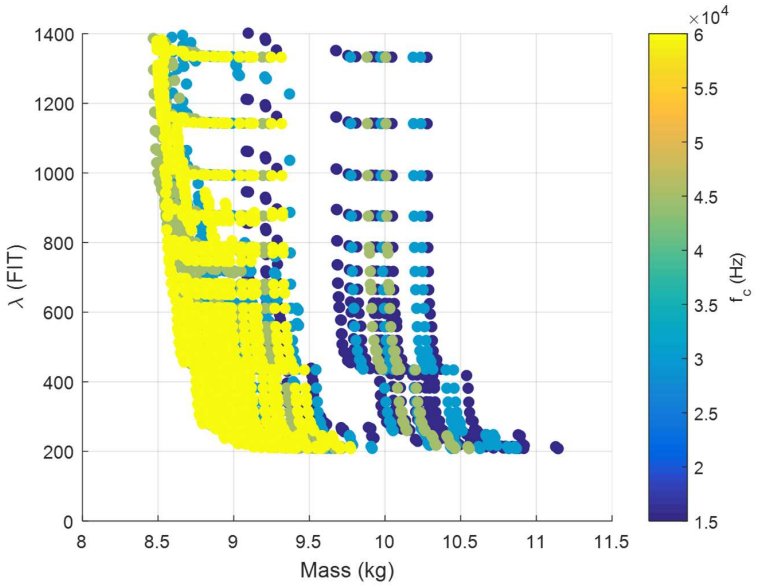
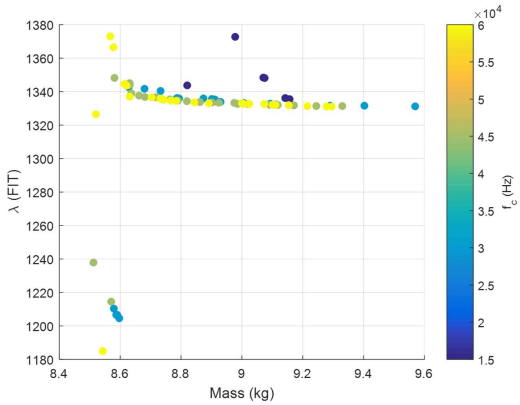


Figure 7.2: All system designs for centralised topology - per lane failure rate vs. mass.

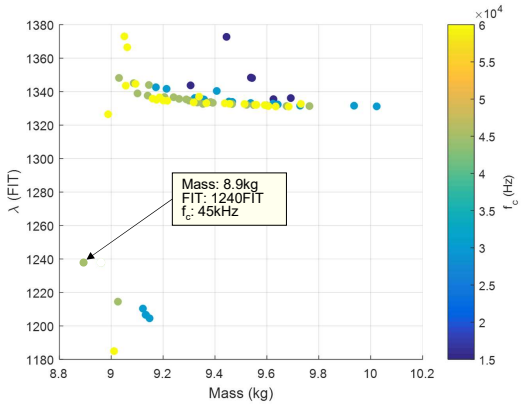
For each Pareto efficient machine design, the best combination of cable, LC output filter, LC input filter, power electronics and heat sinks is selected. The best combination has both a minimum per lane total mass and a failure rate below the 1375FIT threshold. These designs are shown in Figure 7.3 (a). This removes the majority of the sub-optimal designs of 7.2.

The mass and volume of inductors in the LC output filter and inverter input EMI filter were initially determined using empirical equations. Discrepancies are observed between the empirically determined values and their corresponding calculated data set values are shown in Figure 4.10. Thus, the exact mass and volume of all inductors were recalculated using Sections 4.4.1.1-4.4.1.6 for their current rating and inductance. Total system mass is recalculated to correct for the discrepancy caused by empirical mass and volume determination of inductor components. The results of this correction are shown in Figure 7.3 (b). The optimal system design of per-lane minimum mass is marked. Its mass is 8.963kg, failure rate is 1240FIT, and inverter switching frequency is 45kHz. Two groupings of designs can be seen; a small group with failure rate less than 1250FIT and a large group with failure rates greater than 1250FIT.

For each of these designs, their per component failure rate is plotted with respect to



(a) Preliminary designs with empirical inductor sizing.



(b) Refined designs with exact inductor sizing.

Figure 7.3: Centralised systems, down-selected designs' failure rate vs. mass.

the per-lane failure rate as shown in Figure 7.4. The failure rate for the LC output filter and LC input filter remain constant for all designs. Both output and input filters consist of inductors and capacitors, all of which were designed with the same target inductor temperature rise, mission profile, and capacitor voltage rating, thus resulting in the same failure rate across all designs. System designs with per-lane failure rates <1320FIT have PE failure rates of 677.5FIT and semiconductor junction temperature of 115°C, and designs with per-lane failure rates >1320FIT have PE failure rates of 868.3FIT and semiconductor junction temperature of 120°C. This discrete 190.8FIT difference in PE failure rate between the two design groups is the main reason for the segregation of these two groups.

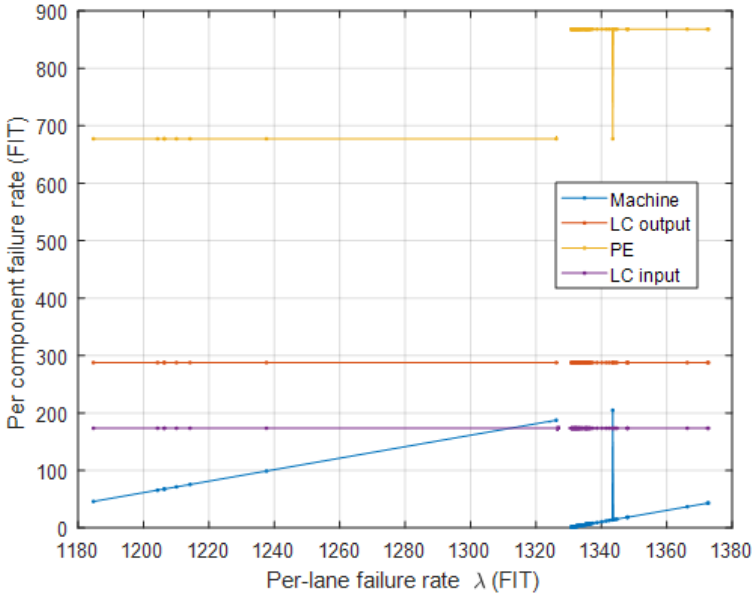


Figure 7.4: Per-lane failure rate vs. per component failure rate for centralised systems.

The mass and failure rate for each system component of the optimum solution is shown in Figure 7.5. The total per lane mass is 8.9kg. The gear box contributes 71% to the total per lane mass followed by machine at 15%, LC output filter at 11%, cable at 2%, LC input filter at 2%, and power electronics heat sink at <1%.

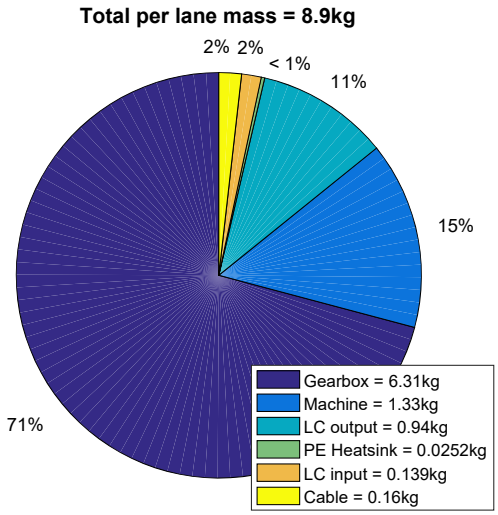


Figure 7.5: Optimal system design for centralised topology - per-lane component mass breakdown.

The per lane electrical component mass and failure rate breakdown are shown in Figure 7.6. The total per lane electrical component mass is 2.59kg and total per lane failure rate is 1240FIT. The machine contributes 51% to the total electrical component mass and less than 8% to total failure rate. This is due to its large mass and low steady state operating temperature. The LC output filter contributes 36% to the total electrical component mass, followed by the LC input filter at 6%, cable at 5%, and power electronics and heat sink at 1%. Power electronics are the largest contributor to the total failure rate at 55%, followed by LC output filter at 23%, LC input filter at 14% and machine at 8%. Power electronics and heat sink contributes minimally to total mass but the power electronics themselves contribute a large amount to the total failure rate. Increasing heat sink would lead to lower operating temperatures and lower failure rates. There is an opportunity to save additional mass as the total per lane failure rate is below the 1375FIT threshold. The inverse relationship between failure rate and mass has already been well established. There is particular opportunity in mass savings for the LC output filter as its inductors contribute to a large proportion of the LC output filter's mass while contributing a small proportion to the total failure rate.

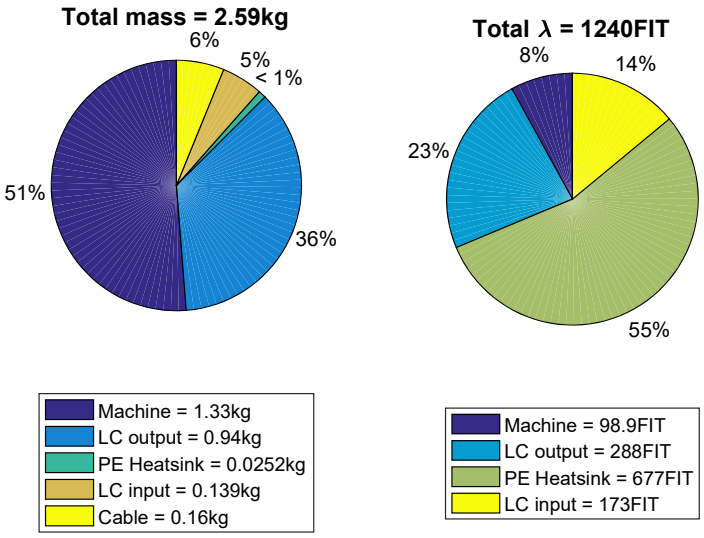


Figure 7.6: Optimal system design for centralised topology - per-lane mass and failure rate of each electrical component.

7.3.2 Machine

The optimal system's machine design specification is shown in Table 7.6. It is a 1.1kW, 8000RPM nominal, 12/10 slot/pole design. The steady state temperature rise is 99.9°C when operating at 20,000ft, ambient temperature of 70°C.

The optimal system's machine design was checked in FEMM. The machine's winding scheme and flux density plot at nominal operating condition is shown in Figure 7.7. Torque as a function of electrical loading angle, and torque ripple with respect to electrical angle were determined with FEMM and plotted in Figure 7.8. The FEMM determined torque of 1.35Nm is close to the desired torque of 1.31Nm. Peak-to-peak torque ripple amplitude is 5.5% with respect to the mean torque value.

Values for analytically determined and FEMM determined stator inductance, magnetic flux linkage, and percentage peak-to-peak torque ripple with respect to nominal torque are shown in Table 7.7. FEMM determined d-axis and q-axis inductances are 1.869mH and 1.879mH respectively while the analytically determined value is 1.847mH. Magnetic flux linkage is calculated from torque at rated current using (4.107). Both FEMM and analytically determined magnetic flux linkage are close. Torque ripple is not determined in the analytical method however the magnet arc has been selected as a function of slot/pole combination to minimise torque ripple. The FEMM determined peak-to-peak torque ripple is 5.5% of the nominal torque value.

Table 7.6: Optimal system design for centralised topology - machine specifications.

Parameter	Value	Units
Nominal torque	1.31	Nm
Nominal speed	8000	RPM
Slots	12	
Poles	10	
Winding scheme	Single layer	
Stator diameter	68.8	mm
Stator bore	35.7	mm
Tooth width	4.7	mm
Slot depth	14.3	mm
Tooth tip depth	1.5	mm
Slot opening	3.8	mm
Stack length	34.7	mm
Magnet thickness	3	mm
Magnet arc	120	ED
Air gap	0.71	mm
Shaft diameter	20	mm
Turns per phase	134	
Stator core material	Vacoflux-50	
Rotor core material	Vacoflux-50	
Magnet material	Recoma 32	
Stator resistance	0.503	Ohm
Stator inductance	1.847	mH
Magnetic flux linkage	0.0251	Wb
Steady state winding temp	169.9	°C
Steady state temp rise	99.9	°C
Thermal resistance	1.407	K/W
Mass	1.326	kg
Failure rate	98.9	FIT

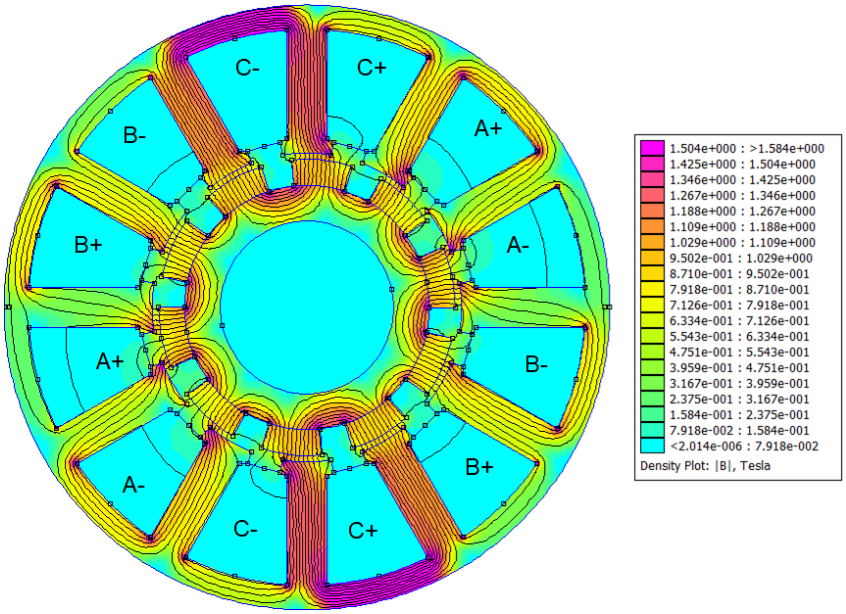


Figure 7.7: Optimal system design for centralised topology - machine winding scheme and flux density plot at nominal load.

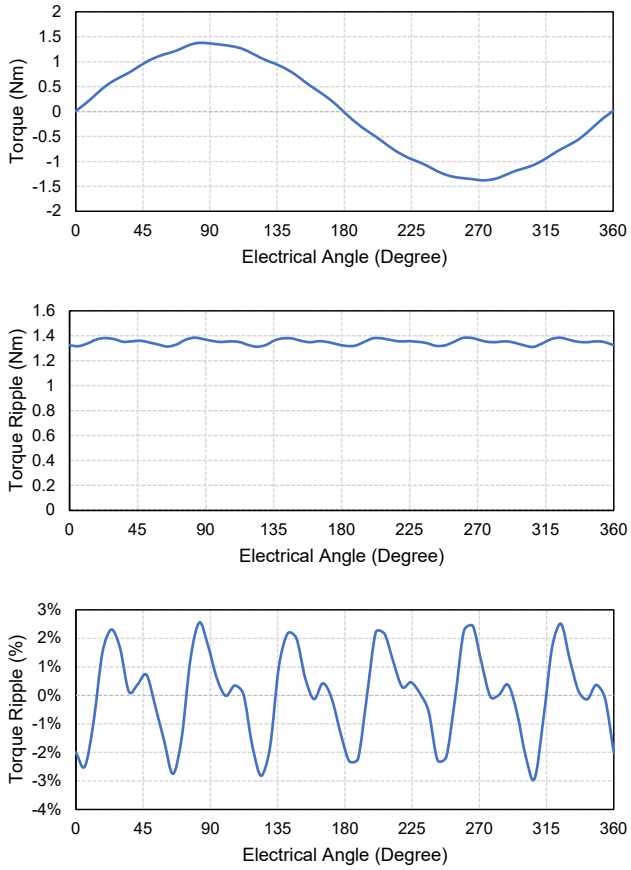


Figure 7.8: Optimal system design for centralised topology - FEMM calculated torque and torque ripple vs electrical angle.

Table 7.7: Optimal system design for centralised topology - FEMM determined machine specifications.

Parameter	Analytical	FEMM calculated	Units
Stator inductance	1.847	1.869/1.879	mH
Magnetic flux linkage	0.0251	0.0259	Wb
Peak-to-peak torque ripple	n/a	5.5%	p.u.

7.3.3 Gearbox

The gearbox specifications are shown in Table 7.8. A per stage gear ratio limit of 10 is assumed. The gearbox's input torque and speed is equal to the nominal output torque and speed of the machine. The gearbox's output speed is 25RPM. The total gear ratio is calculated as 320. The per stage gear ratio is 6.84 for each of the three stages. Each stages' equivalent torque loading is calculated and shown in ascending order from which the stage's mass, moment of inertia, and high-speed side equivalent moment of inertia's are determined. The total mass is the sum of all the stages. Note that two machines connect to one gearbox. Thus, the per lane gearbox mass is half that of the total gearbox mass.

Table 7.8: Optimal system design for centralised system - gearbox specifications.

Parameter	Value	Unit
Mass	11.49	kg
Equivalent moment of inertia	8.12×10^{-6}	kgm^2
Equivalent friction	3.25×10^{-4}	Nms/rad
Number of gear stages	3	
Per stage gear ratio	6.84	
Input torque	1.31	Nm
Input speed	8000	RPM
Stage torque output	{31.32, 109.46, 382.59}	Nm
Stage mass	{0.688, 2.403, 8.399}	kg
Stage moment of inertia	$\{6.741 \times 10^{-6}, 5.485 \times 10^{-5}, 4.462 \times 10^{-4}\}$	kgm^2
Equivalent per stage moment of inertia	$\{6.741 \times 10^{-6}, 1.172 \times 10^{-6}, 2.039 \times 10^{-7}\}$	kgm^2

7.3.4 Cable

The selected cable specifications are show in Table 7.9. The current rating is 4.937Arms which is the same as the machine's nominal current rating. The conductor's altitude and bundle de-rating factors were determined as 0.8459 and 0.5937 respectively for 20000ft and a conductor number of three. The conductor AWG number is 24 and cable diameter is 1.887mm and mass of 0.1598kg. The line resistance, line inductance, phase-to-phase and phase-to-ground capacitances were determined in Figure 6.11 at the machines fundamental electrical frequency and from Table 6.1.

Table 7.9: Optimal system design for centralised system - cable specifications.

Parameter	Value	Unit
RMS Voltage rating	600	Vrms
RMS current rating	4.937	Arms
Cable length	10	m
Altitude	20000	ft
Altitude de-rating factor	0.8459	
Bundle number	3	
Bundle de-rating factor	0.5937	
Conductor gauge	24	AWG
Line resistance	0.0785	Ohm
Line inductance	0.3054	uH
Phase to phase capacitance	0.0147	nF
Phase to ground capacitance	0.0902	nF
Cable radius	1.887	mm
Mass	0.1598	kg

7.3.5 LC output filter

7.3.5.1 Initial design parameters

The parameters of the optimal system design for centralised topology's LC output filter and the dc-link mid-point capacitor are shown in Table 7.10. Its mass and failure rate

values are 0.94kg and 287.8FIT respectively. Capacitor voltage rating of 450V was selected. The selected inductor core material is nanocrystalline, its specifications are shown in Table 4.5. Total case volume is 0.382litres, assuming a 2.5× scaling with respect to the total passive component volume.

Table 7.10: Optimal system design for centralised topology - LC output filter and dc-link mid-point capacitor parameters.

Parameter	Value	Units
Mass	0.94	kg
Failure rate	287.8	FIT
Inductance	0.622	mH
Capacitance	5.266	uF
Mid point capacitance	26.16	uF
Capacitor voltage rating	450	V
Per inductor mass	0.186	kg
Per capacitor mass	0.011	kg
Per mid point capacitor mass	0.039	kg
Per inductor volume	0.016	litre
Per capacitor volume	0.01	litre
Per mid point capacitor volume	0.038	litre
Case volume	0.382	litre
Case mass	0.272	kg
Inductor core material	Nanocrystalline	
Per inductor failure rate	3.7	FIT
Per capacitor failure rate	55.3	FIT

7.3.5.2 Filtering effectiveness

The filter output voltage and its distortion spectrum are shown in Figure 7.9. The fundamental switching harmonic at 45kHz is visible. The distortion spectrum is below the MIL-STD-704F limit for variable frequency systems. This illustrates the effectiveness of the designed LC output filter to generate sinusoidal output voltage and mitigate inverter switching harmonics to below the MIL-STD-704F distortion spectrum limit.

LC output filter and machine side terminal phase a voltages, v_{fa} and v_{ma} respectively, are plotted together in Figure 7.10. A 10m cable separates the LC output filter source side and the machine load side. The cable is modelled by a distributed transmission line. Transmission line effects are mitigated as smooth sinusoidal voltages are applied on the source side of the cable and no overshoot on the load side is observed. Voltages v_{fa} and v_{ma} are a close match, with v_{ma} having a slightly smaller amplitude due to voltage drop across the cable. The inverter output current is plotted. The design goal of 0.2 p.u. amplitude current ripple with respect to fundamental nominal output current is achieved.

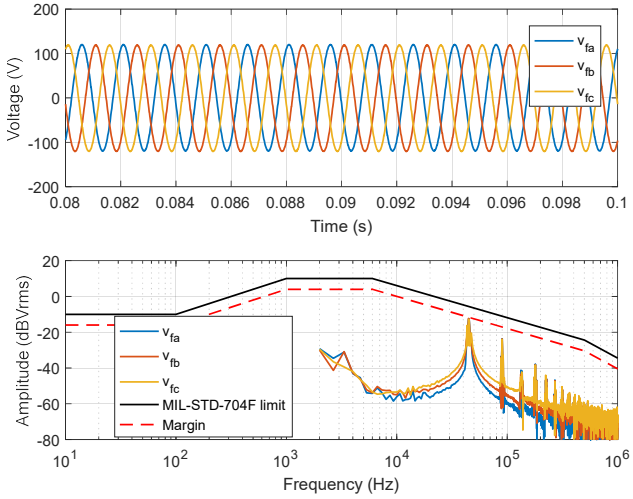


Figure 7.9: LC output filter phase voltage at nominal operating condition and distortion spectrum.

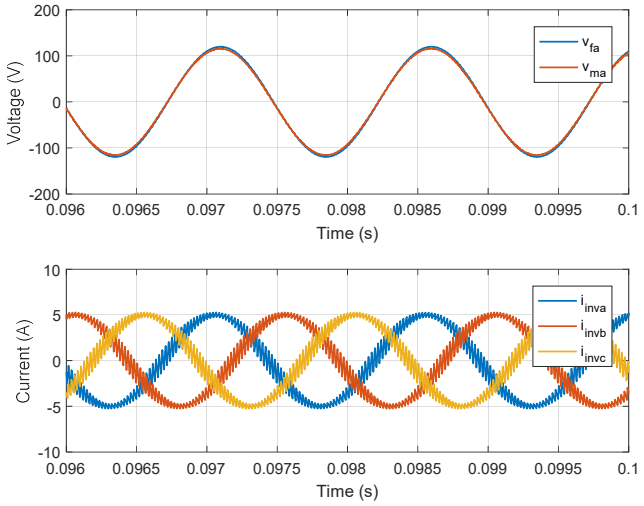


Figure 7.10: Source-side vs. load-side phase voltage and inverter output current.

7.3.5.3 Inductor design

The specification of the designed inductor utilised in the LC output filter is shown in 7.11. The dimensions D, E, F, G are shown in Figure 4.6. The inductor's mass and volume are 0.186kg and 0.016litres respectively for a desired temperature rise of 30°C at steady state operating conditions.

The inductor design of Table 7.11 is realised in FEMM and an inductance value of 6.33mH was calculated. This value is 1.8% greater than the desired inductance value of 0.622mH, showing a close match between FEMM calculated and desired inductance. The FEMM inductor's flux density plot is shown in Figure 7.11.

Table 7.11: Optimal system design for centralised topology - LC output filter inductor specifications.

Parameter	Value	Unit
Inductance	0.622	mH
RMS current	4.937	Arms
Peak current	8.378	A
Fundamental frequency	666.667	Hz
Ripple frequency	45000	Hz
Turn number	42	
D	15	mm
E	15	mm
F	7.7	mm
G	23.1	mm
Gap length	1	mm
Mass	0.186	kg
Volume	0.016	litre
Material	Nanocrystalline	
Steinmetz constant k	3.47×10^{-6}	W/cm3
Steinmetz constant α	1.71	
Steinmetz constant β	2.09	
Copper loss	0.792	W
Core loss	0.034	W

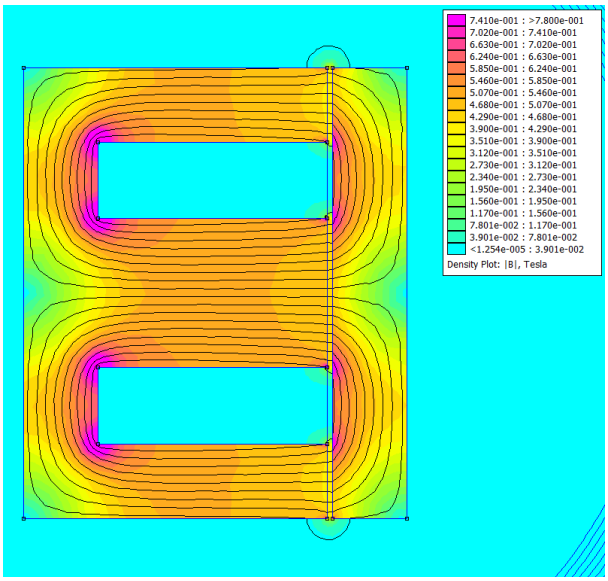


Figure 7.11: LC output filter inductor design FEMM determined flux density plot.

7.3.6 Power electronics

The power electronics and heat sink specifications are shown in Table 7.12. The switching frequency is 45kHz, modulation index is 0.9 and output current is 5Arms. The total semiconductor losses is 14.06W. For a junction temperature of 115°C, a heat sink of equivalent thermal resistance of 5.291K/W is required. The heat sink mass of 0.025kg and volume of 0.0891litre were determined from the heat sink look up table of Section 4.9.2. The total semiconductor failure rate is 677.5FIT for this junction temperature and

internal operating environment.

Table 7.12: Optimal system design for centralised topology - power electronics and heat sink specifications.

Parameter	Value	Unit
Manufacturer	Microsemi	
Model Number	MSC080SMA120S	
Ambient temperature	40	°C
Equivalent ambient altitude	8000	ft
Junction temperature	115	°C
Transistor conduction losses	0.661	W
Transistor switching losses	1.329	W
Diode conduction losses	0.354	W
Total transistor and diode losses	14.06	W
Heat sink equivalent thermal resistance	5.291	K/W
Heat sink mass	0.025	kg
Heat sink volume	0.0891	litre
Failure rate	677.5	FIT

7.3.7 LC input filter

The designed EMI LC input filter's specifications are shown in Table 7.13. It is a two-stage LC design. The per stage differential mode inductance and capacitance are 0.011mH and 1uF respectively. The dc-link capacitance is 1uF. Note that dc-link mid point capacitors needed for the LC output filter contributes to the total dc-link capacitance. The total passive mass is 0.065kg and the total mass including the case is 0.139kg. Considering a 30°C inductor temperature rise, and capacitor rating of 450V, the determined EMI filter failure rate is 173.4FIT.

Table 7.13: Optimal system design for centralised topology - EMI LC input filter specifications.

Parameter	Value	Unit
Inductance L_{dm}	0.011	mH
Capacitance C_{dm}	1	uF
DC-link capacitance C_{dc}	1	uF
Capacitor rating	450	V
Number of stages	2	
Passive mass	0.065	kg
Passive volume	0.022	litre
Total mass	0.139	kg
Failure rate	173.4	FIT

The effectiveness of the EMI filter design is determined in simulation. The input leads conducted emissions were simulated and its corresponding spectrum is determined as shown in Figure 7.12. The harmonics of largest amplitude correspond to the side bands of the fundamental switching harmonic around 45kHz. Both the source and return lead

distortion spectrums u^+ and u^- are below both the MIL-STD-461F limit with a margin of at least 6dB.

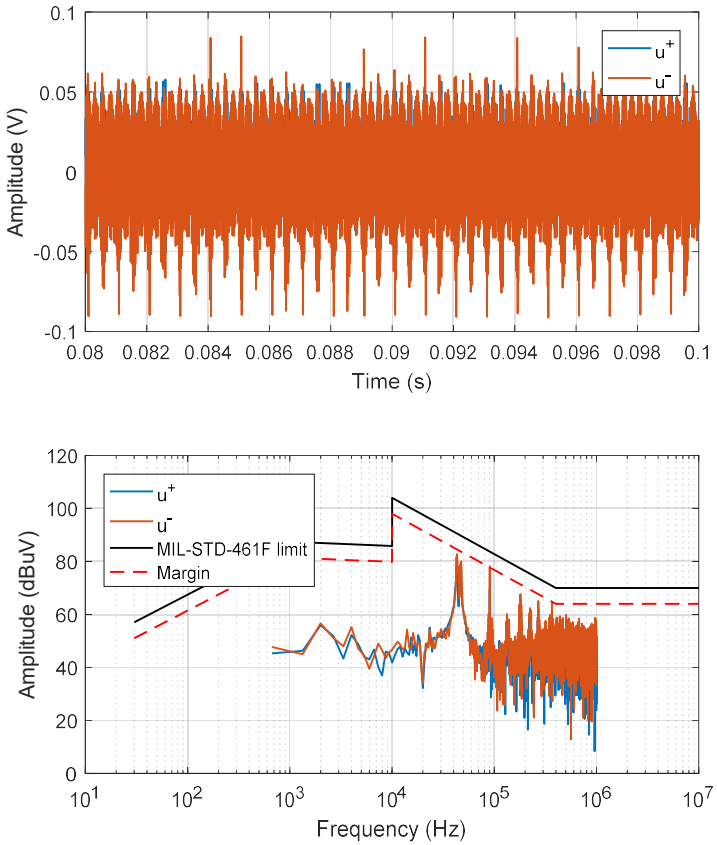
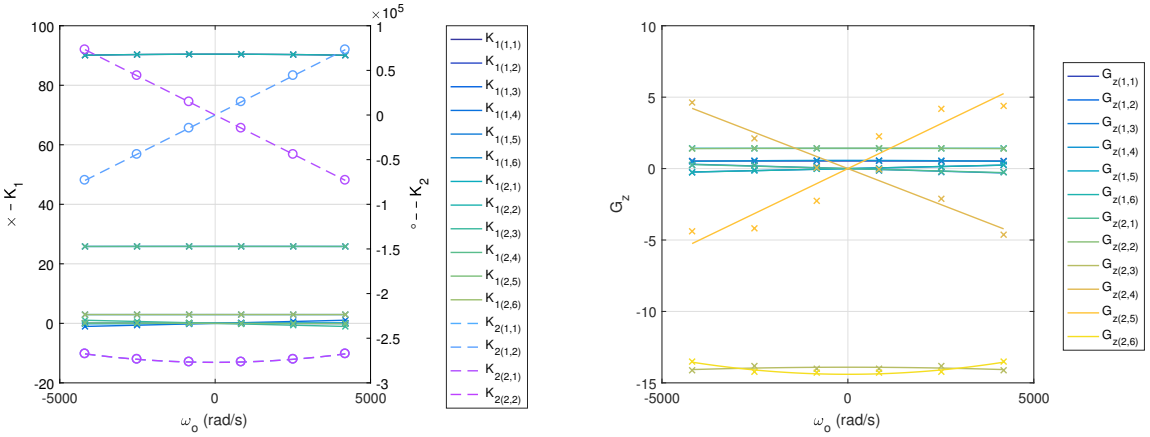


Figure 7.12: Optimal system design for centralised topology - EMI filter spectrum.

7.3.8 Current control

A gain-scheduled LQR controller and observer was realised and tested in simulation. The switching scheme utilised is sinusoidal PWM. The current controller and observer bandwidths are 450Hz and 4.5kHz respectively. The second-order polynomially fitted gain-scheduled controller feedback and observer gains are shown in Figure 7.13. Refer to Figure 5.8 for the full state-feedback and observer block diagram.

To test the stability of the current control, the current set point is stepped from zero to rated while the speed is ramped from zero to rated as shown in Figure 7.14. Both the real and observer-estimated states for dq machine current, inverter output current, and filter output voltages are plotted. The q-axis current command is stepped at 0.02 seconds from 0A to 7A, at same time as the speed ramps up. Control stability is maintained from 0RPM to 8000RPM. Discrepancy is present between the observed and realised states and becomes more pronounced as speed increases. This is due to a mismatch between the inverter output voltage fundamental amplitude and the commanded dq voltage of the



(a) State-feedback current controller gains. **(b)** Observer gains.

Figure 7.13: Optimal system design for centralised topology - current controller second-order polynomial gain-scheduled state feedback and observer gains.

current controller. It is proposed the modulation index can be scaled up as a function of speed to compensate for this mismatch. Correction of this mismatch has not been investigated further.

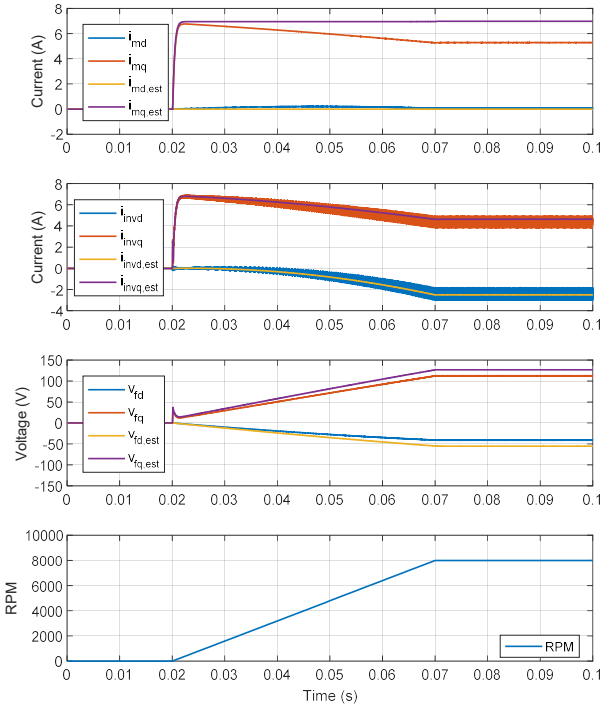


Figure 7.14: Optimal system design for centralised topology - current control test for step current step and speed ramp.

7.3.9 Summary

The optimal system design of a centralised electric drive topology for a given defined search space has been generated. The total per-lane mass and failure rate are 8.9kg and 1240FIT respectively. The inverter's switching frequency is 45kHz. The majority of the total per lane mass contribution is from the gearbox at 71%, followed by the machine 15%, LC output filter 11%. The remaining components consisting of the cable, inverter heat sink and inverter input LC filter together contribute <5% to the total per lane mass.

The machine design has 12 slots, 10 poles, and nominally outputs 1.1kW at 8000RPM. Its mass and failure rate are 1.326kg and 98.9FIT respectively. The machine design was validated in FEMM, with a small error of 1.5% and 3.2% between the desired and FEMM-calculated inductance and magnetic flux linkage values respectively. The achieved peak-to-peak torque ripple is 5.5%.

The cable was sized considering operating current, altitude, and bundle derating factor. The cable length considered is 10m. Its conductor AWG number is 24, its cable total diameter is 1.887mm, and total mass is 0.1598kg. Its line resistance, line inductance, phase-to-phase and phase-to-ground capacitances were determined in Figure 6.11 at the machines fundamental electrical frequency and from Table 6.1 with respect to AWG gauge and insulation thickness appropriate for the 600Vrms voltage rating.

The inverter's LC output filter is sized to mitigate the voltage distortion spectrum below MIL-STD-704F limits and filter out high switching harmonics such that a sinusoidal voltage is applied on the source side of the feeder cable. Its mass and failure rates respectively are 0.94kg and 287.8FIT. The filtering effectiveness of designed LC filter is validated in simulation. The filter output voltage distortion spectrum is below that of the MIL-STD-704F limit for variable frequency systems. No voltage overshoot due to transmission line effects was observed on the load side voltage. The dimensions of the LC output filter inductors were determined and its design was validated using FEMM.

Silicon carbide switches were considered for the inverter semiconductor technology. The total semiconductor losses, consisting of switching and conduction losses, were determined as a function of modulation index, switching frequency, output current and dc-link voltage for nominal conditions. The relationship between junction temperature, failure rate, and heat sink mass has been established in section 4.9.3 for which an appropriate heat sink is selected for desired junction temperature. Total inverter losses are 14.1W. The junction temperature, equivalent heat sink thermal resistance, heat sink mass, and failure rate are 115°C, 5.291K/W, 0.025kg, and 677.5FIT respectively.

The inverter input EMI filter is a 2 stage LC design, its effectiveness in mitigating source and return leads' conducted emissions distortion spectrum below that of MIL-STD-461F was validated by simulation for nominal operating conditions. Its mass and failure rate are 0.139kg and 173.4FIT respectively.

The current controller's scheduled state feedback and observer gains were tuned for 450Hz and 4.5kHz bandwidth respectively. Control stability was maintained for a q-axis current command step from zero to rated 7A peak current at the start of a speed ramp from 0RPM to 8000RPM in 0.05 seconds. Discrepancy is observed between the actual and observer-estimated states which increase with respect to operating speed. This is caused by mismatch between the inverter output voltages' fundamental voltage and the current controller's commanded voltage. A compensation technique for this speed dependent voltage discrepancy was not investigated further.

7.4 Results - Distributed topology

7.4.1 System level

The design process described in section 7.3.1 for the centralised topology is repeated for the distributed topology. A set of machine designs with known mass and failure rate is generated. For each machine which is an element of the Pareto frontier with respect to mass and failure rate, an optimum combination of cable, LC input filter, power electronics and heat sink designs is generated. Due to discrepancies between analytically calculated, and empirically determined inductor mass and volume, all inductors are re-sized and recalculated analytically for its specific operating condition. Inductors are present in the EMI LC input filter and its mass is recalculated for the new inductor parameters, followed by the per-lane mass. Each of these design's per-lane mass and failure rate are plotted in Figure 7.15. The optimum design of minimum mass and a failure rate <1375FIT is highlighted and has a per lane mass of 8kg, failure rate of 1300FIT, and an inverter switching frequency of 45kHz.

The per lane component mass breakdown of the optimum design is shown in Figure 7.16. The gearbox mass contributes the most to the total per lane mass of 8kg with 79%, followed by the machine with 14%, LC input filter with 3%, and power electronics heat sink with 2%, and cable with 1%. The non-gearbox mass is only 21% of the total per lane mass.

The electrical component mass and failure rate breakdown is shown in Figure 7.17. The machine contributes 69% to the total electrical component mass value of 1.15kg, followed by the EMI LC input filter with 16%, power electronics heat sink with 9% and cable with 6%. Power electronics contribute the highest proportion of 64% to the per lane failure rate value of 1300FIT, followed by the LC input filter with 27% and the machine with 8%.

More details of the individual components are outlined in successive sections.

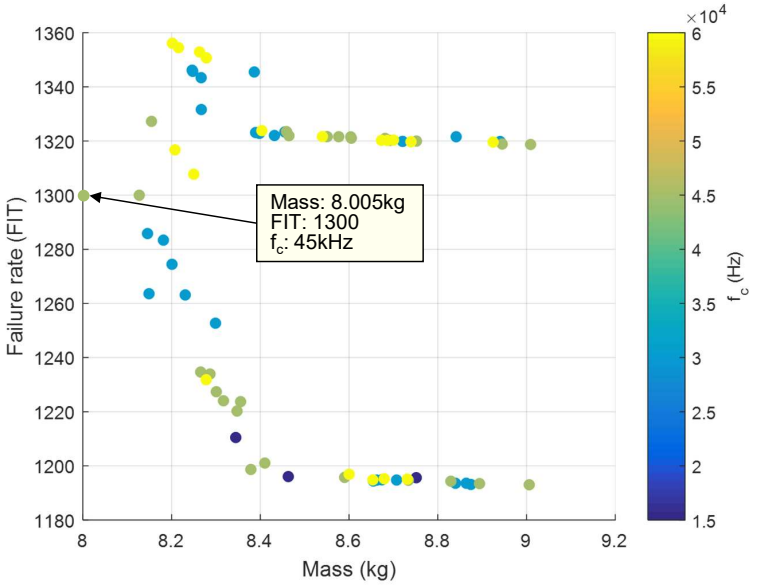


Figure 7.15: Distributed topology system designs - per lane mass vs. failure rate.

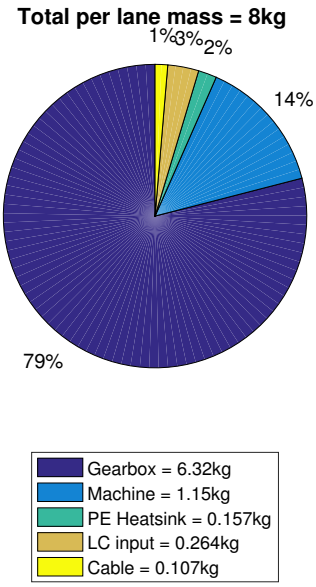


Figure 7.16: Optimised distributed system - per-lane component mass breakdown.

7.4.2 Machine

The optimal distributed system's machine design specifications are shown in Table 7.14. Three sets of values are shown, corresponding to column headings "Analytical design", "FEMM calculated", and "Refined design". "Original design" corresponds to the values calculated by the machine sizing script. This design is realised in FEMM from which the torque, stator inductance, magnetic flux linkage, and torque ripple values are calculated and are shown in the "FEMM calculated" column. The "Original design" is refined such

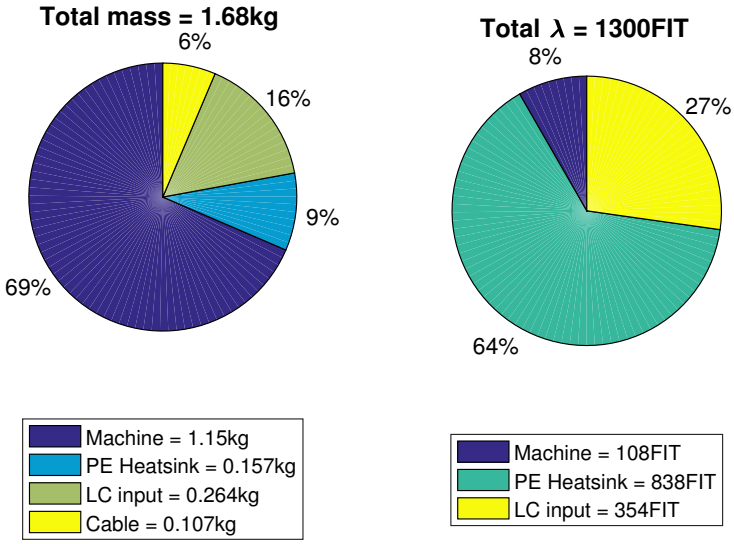


Figure 7.17: Optimised distributed system - electrical component mass and failure rate breakdown.

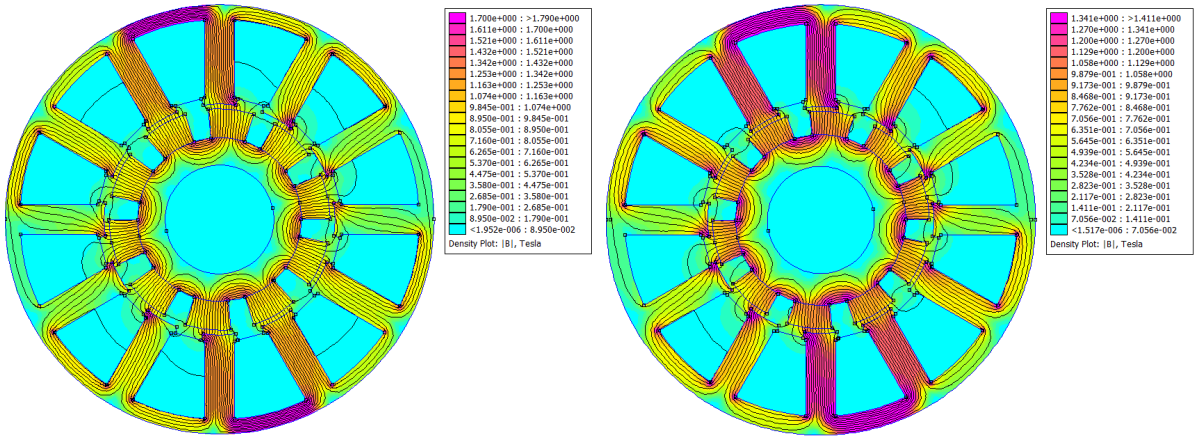
that FEMM calculated inductance, magnetic flux linkage, torque values match closer to their respective desired values of the "Original design". The double dots represent repeated row values, making it easier to identify which dimensions were changed. The refined design has thinner magnets, smaller diameter shaft, larger stator diameter, and smaller number of turns per phase. Overall mass of the refined design is 1.149kg, compared to the original mass of 1.278kg. The stator resistance is marginally reduced due to the refined design having four fewer turns per phase than the original design. The flux density plots of both the original and refined designs are shown in Figure 7.18. The refined design's stator diameter was increased, effectively increasing the back iron thickness such that peak flux density in the teeth and back iron are approximately equal. The FEMM calculated torque and torque ripple vs. electrical angle for both original and refined designs are shown in Figure 7.19. Peak-to-peak torque ripple for original and refined designs are 4.9% and 5.6% respectively.

7.4.3 Gearbox

The gearbox specifications are shown in Table 7.15. A per stage gear ratio limit of 10 is assumed. The gearbox's input torque and speed is equal to the nominal output torque and speed of the machine. The gearbox's output speed is 25RPM. The total gear ratio is calculated as 310. The per stage gear ratio is 6.77 for the total of three stages. Each stage's equivalent torque loading is calculated and shown in ascending order, from which

Table 7.14: Optimal system design for distributed topology - machine specifications

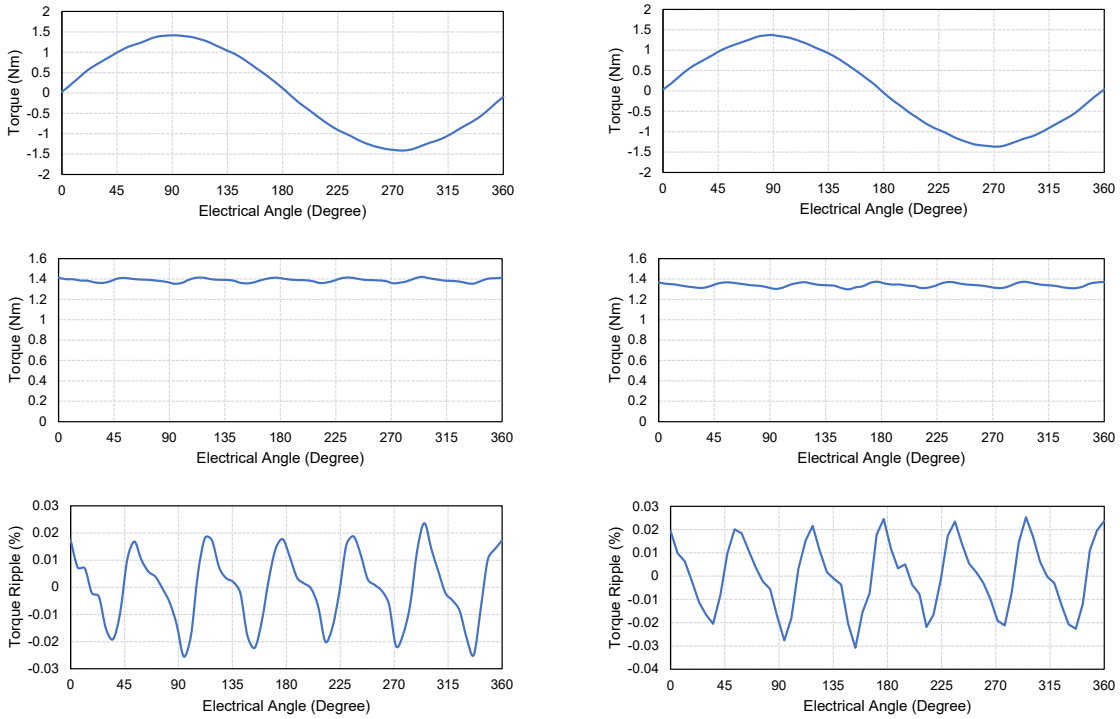
Parameter	Original design	FEMM calculated	Refined design	Units
Mass	1.278	..	1.149	kg
Failure rate	108.4	..	..	FIT
Nominal torque	1.355	1.41 [+4%]	1.366 [+1%]	Nm
Nominal speed	7750	..	..	RPM
Slots	12	..	..	
Poles	10	..	..	
Winding scheme	Single layer	..	..	
Stator diameter	67	..	68.4	mm
Stator bore	36	..	..	mm
Tooth width	4.7	..	..	mm
Slot depth	13.2	..	..	mm
Tooth tip depth	1	..	..	mm
Slot opening	4.2	..	..	mm
Stack length	35	..	..	mm
Magnet thickness	4.5	..	3.7	mm
Magnet arc	120	..	..	ED
Air gap	0.75	..	..	mm
Shaft diameter	22.2	..	17	mm
Turns per phase	158	..	154	
Stator core material	Vacoflux-50	..	..	
Rotor core material	Vacoflux-50	..	..	
Magnet material	Recoma 32	..	..	
Stator resistance	0.749	..	0.73	Ohms
Stator inductance	2.160	2.127/2.134 [-1.3%]	2.117/2.126 [-1.8%]	mH
Magnetic flux linkage	0.0301	0.0313 [+4%]	0.0304 [+1%]	Wb
Steady state winding temp	170.7	..	169.2	°C
Steady state temp rise	100.7	..	99.2	°C
Thermal resistance	1.414	..	..	K/W
Peak-to-peak torque ripple	n/a	4.9	5.6	%



(a) Original design. **(b)** Refined design.

Figure 7.18: Optimised distributed system - machine designs.

the stages' mass, moment of inertia, and high-speed side equivalent moment of inertia are determined. The total mass is the sum of mass of all stages. Note that two machine connect to one gearbox. Thus, the per lane gearbox mass is half that of the total gearbox mass.



(a) Original design. **(b)** Refined design.

Figure 7.19: Optimal system design for distributed topology - FEMM calculated torque nd torque ripple vs electrical angle.

Table 7.15: Optimal system design for centralised system - gearbox specifications.

Parameter	Value	Unit
Mass	11.63	kg
Equivalent moment of inertia	8.47×10^{-6}	kgm^2
Equivalent friction	3.35×10^{-4}	Nms/rad
Number of gear stages	3	
Per stage gear ratio	6.77	
Input torque	1.36	Nm
Input speed	7750	RPM
Stage torque output	{32.09 111.36 386.48}	Nm
Stage mass	{0.704 2.445 8.485}	kg
Stage moment of inertia	$\{7.020 \times 10^{-6}, 5.645 \times 10^{-5}, 4.539 \times 10^{-4}\}$	kgm^2
Equivalent per stage moment of inertia	$\{6.741 \times 10^{-6}, 1.232 \times 10^{-6}, 2.163 \times 10^{-7}\}$	kgm^2

7.4.4 Cable

The selected cable specifications are show in Table 7.16. The current rating is 4.937Arms which is the same as the machine's nominal current rating. The conductor's altitude and bundle de-rating factors were determined as 0.8459 and 0.74 respectively for 20000ft and a conductor number of two. The conductor AWG number is 24 and cable diameter is 1.887mm and mass of 0.107kg. The line resistance, line inductance, phase-to-phase and phase-to-ground capacitances were determined in Figure 6.11 at the machines fundamental electrical frequency and from Table 6.1.

Table 7.16: Optimal system design for distributed system - cable.

Parameter	Value	Unit
RMS Voltage rating	600	V
RMS current rating	4.16	A
Cable length	10	m
Altitude	20000	ft
Altitude de-rating factor	0.8459	
Bundle number	2	
Bundle de-rating factor	0.74	
Conductor gauge	24	AWG
Line resistance	0.0785	Ohm
Line inductance	0.3054	uH
Phase to phase capacitance	0.0147	nF
Phase to ground capacitance	0.0902	nF
Cable radius	1.887	mm
Mass	0.107	kg

7.4.5 Control

A standard PI current controller configuration with cross decoupling terms is utilised, as shown in Figure 7.20. How it was integrated into the system is shown in Figure 7.21. The control scheme was realised and tested in simulation. The switching scheme utilised is space vector modulation. The switching frequency is 45kHz. The current controller close loop bandwidth is 2250Hz. The proportional gain K_p and integral gain K_I are 30.36 and 7553 respectively.

To test the current control stability, the current set point is stepped from zero to rated while the speed is ramped from zero to rated as shown in Figure 7.22. The machine dq currents (i_{md}, i_{mq}), commanded currents (i^*_{md}, i^*_{mq}), and rotor speed (RPM) are plotted. The q-axis current command is stepped from 0 to 6A at 0.02 seconds while the d-axis current command is held at zero. A constant speed ramp from 0 to 7750RPM is introduced at the same time. The current controller attempts to maintain the machine currents to their respective commanded values. The commanded and actual machine current values match at steady state constant speed.

7.4.6 Power electronics and heat sink

The power electronics and heat sink specifications are shown in Table 7.17. The switching frequency is 45kHz, modulation index is 1, and output current is 4.25Arms. The total semiconductor losses is 10.827W. For a junction temperature of 95°C, a heat sink with equivalent thermal resistance of 2.266°K/W is required. The heat sinks' mass of 0.157kg and volume of 0.872 litres is determined from the heat sink look up table of Section 4.9.2. The total semi-conductor failure rate is 837.7FIT for this junction temperature and external operating environment.

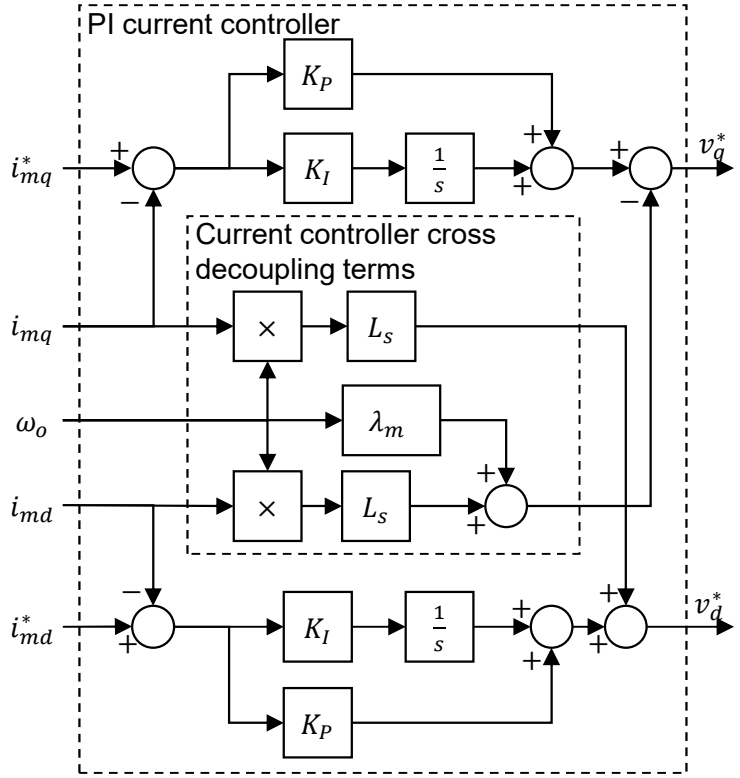


Figure 7.20: PI current controller with cross decoupling terms.

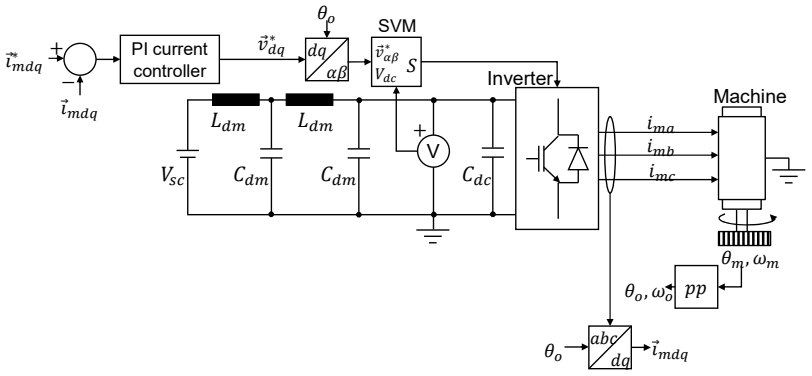


Figure 7.21: PI current controller with system diagram.

7.4.7 LC input filter

The designed EMI LC input filter specifications are shown in Table 7.18. It is a two-stage LC design. The per stage differential mode inductance and capacitances are 0.113mH and 1.182uF respectively. The dc-link capacitance is 10uF. The total passive mass is 0.153kg and the total mass including the case is 0.139kg. Considering a 30°C inductor temperature rise, capacitor voltage rating of 450V, and external lifetime profile, the determined EMI LC input filter's failure rate is 353.6FIT.

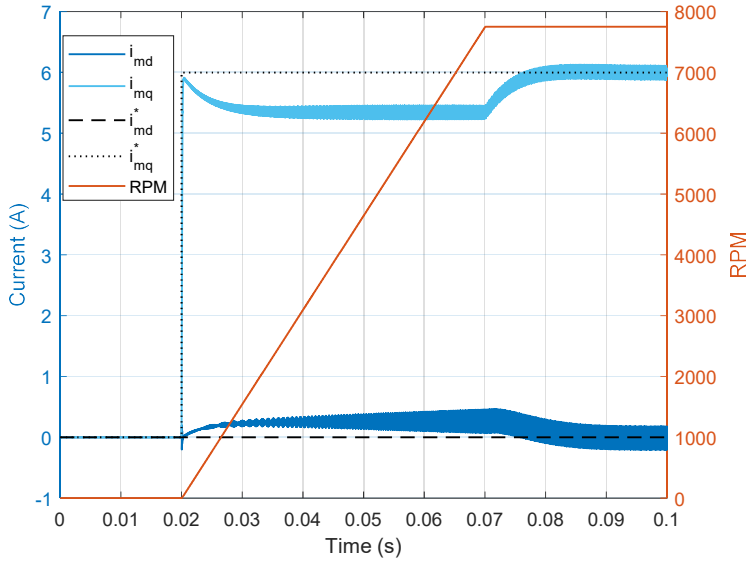


Figure 7.22: Optimised design for a distributed topology - current control test for current command step and speed ramp.

Table 7.17: Optimal system design for a distributed topology - power electronics and heat sink specifications.

Parameter	Value	Unit
Manufacturer	Microsemi	
Model Number	MSC080SMA120S	
Ambient temperature	70	°C
Equivalent ambient altitude	20000	ft
Junction temperature	95	°C
Transistor conduction losses	0.514	W
Transistor switching losses	1.129	W
Diode conduction losses	0.162	W
Total transistor and diode losses	10.827	W
Heat sink equivalent thermal resistance	2.266	°K/W
Heat sink mass	0.157	kg
Heat sink volume	0.872	litre
Failure rate	837.7	FIT

The effectiveness of the EMI filter design is determined in simulation and shown in Figure 7.23. The source and return lead conducted emissions were simulated at nominal steady state conditions and its corresponding spectrum is determined. The harmonics of largest amplitude correspond to side bands of the fundamental switching harmonic around 45kHz. Both source and return lead distortion spectrums u^+ and u^- are below both the MIL-STD-461F limit and -6dB margin.

Table 7.18: Optimal system design for distributed topology - EMI LC input filter specifications.

Parameter	Value	Units
Inductance	0.113	mH
Capacitance	1.182	uF
DC-link capacitance	10	uF
Capacitor rating	450	V
Number of stages	2	
Passive mass	0.153	kg
Passive volume	0.04	litre
Total mass	0.264	kg
Failure rate	353.6	FIT

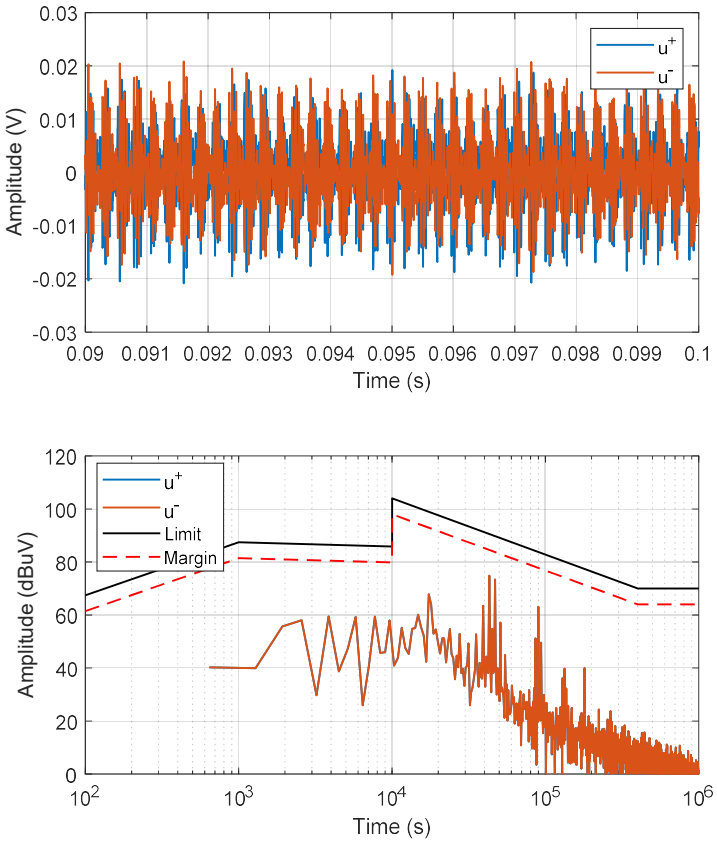


Figure 7.23: Optimal design for distributed system - EMI filter spectrum.

7.4.8 Summary

The optimal system design of a distributed electric drive topology for a given search space has been generated. The total per-lane mass and failure rate are 8kg and 1300FIT respectively. The inverter's switching frequency is 45kHz. The majority of the total per lane mass contribution is from the gearbox at 79%, followed by the machine with 14%, the LC output filter with 3%, the power electronics heat sink at 2% and cable at 1%.

The machine design has 12 slots, 10 poles, and nominally outputs at 1.1kW at

7750RPM. Its mass and failure rate are 1.149kg and 108.4FIT respectively. The machine design is validated and refined in FEMM. A smaller error of -1.8% and 3.2% between the desired and FEMM-calculated inductance and magnetic flux linkage values was observed. The achieved peak-to-peak torque ripple is 5.6%.

The cable was sized considering operating current, altitude, and bundle derating factor. The cable length is 10m. Its conductor AWG number is 24, its cable total diameter is 1.887mm, and total mass is 0.107kg.

Silicon carbide switches were considered for the inverter semiconductor technology. The total semiconductor losses, consisting of switching and conduction were determined as a function of modulation index, switching frequency, output current and dc-link voltage for nominal conditions. The total switching losses are 10.827W. The junction temperature, equivalent heat sink thermal resistance, heat sink mass, and failure rate are 95 FIT, 2.266°K/W, 0.157kg, and 837.7FIT respectively.

The inverter input EMI filter is a 2 stage LC design, its filtering effectiveness in attenuating source and return leads' conducted emissions distortion spectrum below that of MIL-STD-461F limits was validated by simulation for nominal operating conditions. Its mass and failure rate are 0.139kg and 173.4FIT respectively.

A PI current controller with cross decoupling terms was implemented. It was tuned to have a bandwidth of 2250Hz. Control stability was maintained for a q-axis current command step from zero to rated 6A peak at the start of a speed ramp from 0RPM to 7750RPM in 0.05 seconds. The machine currents tracked that of the commanded and no steady state error was present.

7.5 Centralised vs. distributed topology

The optimal design for centralised topology was presented in section 7.3. The optimal design for distributed topology was presented in section 7.4. These designs and their components are compared with respect to each other.

7.5.1 System level

The total per lane mass and failure rate composition of the two optimal designs of each topology are shown together in Table 7.19. The centralised topology's EMI LC input filter, power electronics, and LC output filter are located inside the fuselage of the aircraft. The distributed topology's EMI LC input filter, and inverter located outside of the fuselage, next to the point of actuation. The operating environment and lifetime profile effects component sizing and its failure rate.

The distributed topology's per lane mass of 8kg is 0.9kg less than that of the centralised topology of 8.9kg. The distributed topology lacks an LC output filter which

its mass of 0.94kg is comparable to the total per lane mass difference between the two topologies. The distributed topology has a lower part count by virtue of not having an LC output filter. The distributed topology has higher failure rates for LC input filter and power electronics compared to the centralised topology. The cable mass for the distributed topology is less as only two conductors instead of three are required.

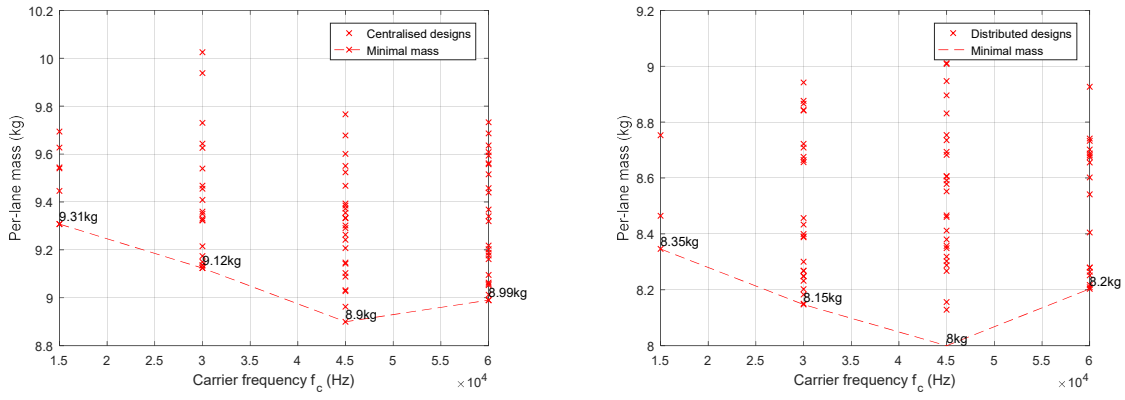
Table 7.19: Centralised vs. distributed topology comparison - system level mass and failure rate.

	Mass (kg)		Failure rate (FIT)	
Component	Centralised	Distributed	Centralised	Distributed
Gearbox	6.31	6.32	-	-
Machine	1.33	1.15	98.9	108
LC output	0.94	-	288	-
PE heat sink	0.0252	0.157	677	838
LC input	0.139	0.264	173	354
Cable	0.16	0.107	-	-
Electrical component total	2.59	1.68	1236.9	1300.0
Total per-lane	8.90	8.00	1236.9	1300.0

The per-lane mass is plotted against carrier frequency for centralised and distributed designs in Figure 7.24. A line is plotted through the design of minimal per-lane mass at each unique carrier frequency. As seen in both Table 7.19 and Figure 7.24, the optimal solution of both centralised and distributed topologies happens to operate at 45kHz. It is known that as switching frequency increases, the required inductance and capacitance for passive filters tend to decrease for a fixed level of attenuation and specified frequency at the expense of increased switching losses, and core losses. For the presented functional definition and presented design constraints, the optimal solution of the 45kHz switching frequency leads to the optimal compromise between the minimal mass of passive components at the expanse of increased switching and core losses. If the functional description were to change, the optimal solution may lie somewhere else. Thorough sensitivity analysis is required to definitively determine the relationship between switching frequency and mass of optimal solution.

7.5.2 Machine

The machine designs for the centralised and distributed topologies are compared in Table 7.20. Both designs have 12 slots and 10 poles. Their nominal line current values are 4.77Arms and 4.24Arms respectively. The centralised topology machine designs' mass and failure rate are 1.326kg and 98.9FIT respectively. The distributed topology machine designs' mass and failure rate are 1.15kg and 108.4FIT. Their stator diameter and stack length are similar, 68.8mm to 68.4mm for stator diameter, 34.7mm to 35mm for stack length. Magnet thickness is greater in the distributed topology machine at 3.7mm, com-



(a) Centralised topology - per-lane mass vs. carrier frequency.

(b) Distributed topology - per-lane mass vs. carrier frequency.

Figure 7.24: Centralised vs. distributed topology comparison - per-lane mass vs. carrier frequency.

pared to 3.0mm for the centralised topology machine. Permanent magnets are one of the most expensive components on a per kilogram basis. The peak-to-peak torque ripple of both machines are quite similar, 5.5% to 5.6%.

7.5.3 Cable

The selected cable designs for the centralised and distributed topologies are compared in Table 7.21. The cable bundle conductor number is different for the centralised and distributed. For the centralised topology, a three-phase cable transmits ac power from the inverter to the machine. For distributed topology, a two phase cable transmits dc power from the aircraft's grid to the inverters input. It is assumed the distance between the inverter and the machine is negligibly short for distributed topology. The cable mass for the distributed topology is lower as it has one less conductor. Conductor gauge is selected to the nearest AWG number.

7.5.4 LC output filter

The LC output filter design of the centralised topology is shown in Table 7.21. No LC output filter is present in the distributed topology, thus no comparison can be made. The LC output filter weighs 0.94kg and 287.8FIT. Its mass is significant if compared to the 2.59kg total electrical components mass of the distributed topology . The inductors contribute the most to the LC output filters mass, each weighing 0.186kg. There are three inductors per LC output filter, making the total inductor mass equal to 0.558kg, equivalent to 59% of the total LC output filter mass.

Table 7.20: Centralised vs. distributed topology comparison - machine design.

Parameter	Centralised	Distributed	Units
Nominal torque	1.31	1.366	Nm
Nominal speed	8000	7750	RPM
Nominal line current	4.77	4.24	Arms
Slots	12	12	
Poles	10	10	
Winding scheme	Single layer	Single layer	
Stator diameter	68.8	68.4	mm
Stator bore	35.7	36	mm
Tooth width	4.7	4.7	mm
Slot depth	14.3	13.2	mm
Tooth tip depth	1.5	1	mm
Slot opening	3.8	4.2	mm
Stack length	34.7	35	mm
Magnet thickness	3	3.7	mm
Magnet arc	120	120	ED
Air gap	0.71	0.75	mm
Shaft diameter	20	17	mm
Turns per phase	134	154	
Stator core material	Vacoflux-50	Vacoflux-50	
Rotor core material	Vacoflux-50	Vacoflux-50	
Magnet material	Recoma 32	Recoma 32	
Stator resistance	0.503	0.73	Ohms
Stator inductance	1.869/1.879	2.117/2.126	mH
Magnetic flux linkage	0.0259	0.0304	Wb
Steady state winding temp	169.9	169.2	°C
Steady state temp rise	99.9	99.2	°C
Thermal resistance	1.407	1.414	K/W
Mass	1.326	1.15	kg
Failure rate	98.9	108.4	FIT
Peak to peak torque ripple	5.5	5.6	%

Table 7.21: Centralised vs. distributed topology comparison - cable design.

Parameter	Centralised	Distributed	Unit
RMS voltage rating	600	600	Vrms
RMS current rating	4.77	4.16	Arms
Cable length	10	10	m
Altitude	200000	200000	ft
Altitude derating factor	0.846	0.846	
Bundle conductor number	3	2	
Bundle derating factor	0.594	0.74	
Conductor gauge	24	24	AWG
Mass	0.16	0.107	kg

7.5.5 Power electronics and heat sink

The power electronics and heat sink designs of the centralised and distributed topology are shown in Table 7.23. Silicon carbide switches are utilised. The total semiconductor losses are calculated for centralised and distributed topologies are 14.06W and 10.87W respectively. The inverter's output current for centralised and distributed topologies are

Table 7.22: Centralised vs. distributed topology comparison - LC output filter design.

Parameter	Centralised	Distributed	Units
Mass	0.94	-	kg
Failure rate	287.8	-	FIT
Inductance	0.622	-	mH
Capacitance	5.266	-	uF
Mid-point capacitance	26.16	-	uF
Capacitor voltage rating	450	-	V
Per inductance mass	0.186	-	kg
Per capacitor mass	0.011	-	kg
Per mid point capacitor mass	0.039	-	kg
Per inductor volume	0.016	-	litre
Per capacitor volume	0.01	-	litre
Per mid point capacitor volume	0.038	-	litre
Case volume	0.382	-	litre
Case mass	0.272	-	kg
Inductor core material	Nanocrystalline	-	
Per inductor failure ratee	3.7	-	kg
Per capacitor failure rate	55.3	-	kg

4.77Arms and 4.24Arms. A reduction in the required output current leads to a reduction in the semiconductor losses.

Consider the factors that affect power electronics/semiconductor failure rate. These are described by the component lifetime profile that is associated with its operation and environment. The distributed topology's power electronics are located external of the fuselage in the wing. This operating environment is harsher with increased vibration, larger temperature and ambient pressure cycling compared to the internal operating environment of the centralised topology. The distributed topology's power electronics/semiconductor's associated lifetime profile leads to greater component failure rate compared to that of the centralised topology. Semiconductor failure rate reduces with a reduction in operating junction temperature. The increase in semiconductor failure rate due to its associated lifetime profile is offset by lowering its junction temperature with a larger heat sink of smaller thermal resistance. Reduced pressure at higher altitude increases the effective heat sink thermal resistance, leading to a further increase in heat sink sizing. The distributed and centralised topology's optimal design's heat sinks designs are determined and compared. The distributed topology's heat sink's 0.157kg mass and 0.872 litres volume is greater than the centralised topology's heat sinks 0.025kg mass, 0.089 litre volume. The centralised and distributed junction temperatures are 115°C and 95°C respectively. The distributed topology's heat sink mass is 6.3 times that of the centralised topology's. This mass is still small compared to the total per lane mass of 8.0kg and total per lane electrical mass of 1.68kg. The centralised and distributed failure rates are 677.5FIT and 837.7FIT respectively.

Table 7.23: Centralised vs. distributed topology comparison - power electronics and heat sink design.

Parameter	Centralised	Distributed	Unit
Ambient temperature	40	70	°C
Equivalent ambient altitude	8000	20000	ft
Output current	4.77	4.16	Arms
Junction temperature	115	95	°C
Transistor conduction losses	0.661	0.514	W
Transistor switching losses	1.329	1.129	W
Diode conduction losses	0.354	0.162	W
Total transistor and diode losses	14.06	10.827	W
Heat sink equivalent thermal resistance	5.291	2.266	°K/W
Heat sink mass	0.025	0.157	kg
Heat sink volume	0.089	0.872	litre
Failure rate	677.5	837.7	FIT

7.5.6 EMI LC input filter

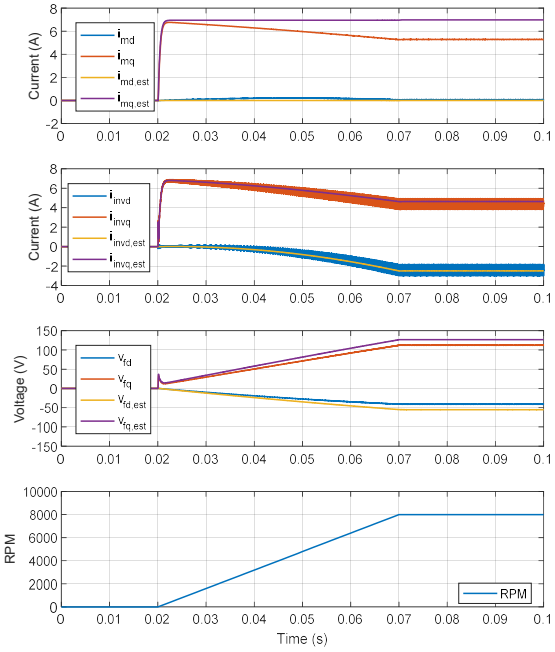
The EMI LC input filter designs of the centralised and distributed topologies are shown in Table 7.24. Both designs are two stage LC input filters. Smaller differential mode capacitors are required for the centralised topology design compared to that of the distributed topology. In the centralised topology, two dc link mid-point balancing capacitors are utilised for the LC outputs filter's neutral point connection. These balancing capacitors contribute to the overall dc-link capacitance. The inductance term is higher for the distributed topology with a value of 0.113mH compared to the 0.011mH of the centralised topology. Both designs utilised the same 450V capacitor voltage rating and assumed 30°C inductor temperature rise but have different operating environments and lifetime profiles. The failure rate of the distributed topology's EMI filter is higher than that of the centralised due solely to its harsher external operating environment and lifetime profile. The mass of the centralised and distributed topology EMI LC input filters are 0.139kg and 0.264kg respectively while the failure rates are 173.4FIT and 353.6FIT respectively.

Table 7.24: Centralised vs. distributed topology comparison - EMI LC input filter design.

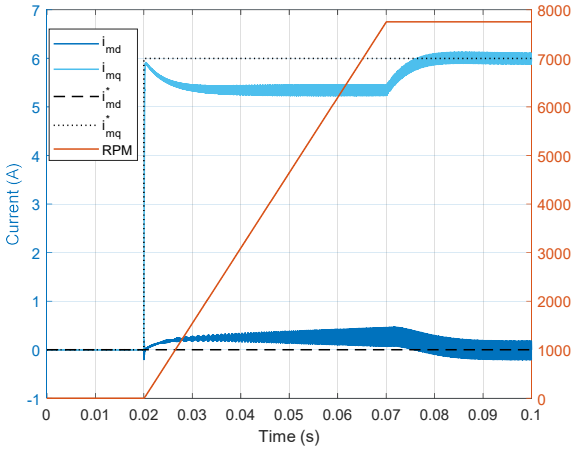
Parameter	Centralised	Distributed	Units
Inductance	0.011	0.113	mH
Capacitance	1	1.182	uF
Inductor core material	Amorphous	Amorphous	
DC-link capacitance	1	10	uF
Capacitor rating	450	450	V
Number of stages	2	2	
Passive mass	0.065	0.153	kg
Passive volume	0.022	0.04	litre
Total mass	0.139	0.264	kg
Failure rate	173.4	353.6	FIT

7.5.7 Control

The current control step responses during speed ramp is shown for centralised and distributed topologies are shown in Figure 7.25 (a) and (b) respectively. A gain-scheduled state feedback current controller with state observer is utilised in the centralised system. The current controller's bandwidth is 450Hz and the observer is 4.5KHz. A PI current controller with cross decoupling terms is utilised in the distributed topology. Its bandwidth is 2250Hz. Control stability is achieved throughout the speed range for both control schemes. For the centralised topology, discrepancy is present between the observed and realised states and becomes more pronounced as speed increases. This is due to mismatch between the inverter output voltage's fundamental amplitude and the commanded dq voltage of the current controller. For the distributed topology, the actual current lagged behind the commanded current during the speed ramp but zero error is observed at steady state.



(a) Centralised topology - gain-scheduled LQR current controller and observer.



(b) Distributed topology - PI current controller with cross decoupling terms.

Figure 7.25: Centralised vs. distributed topology comparison - current control step response during speed ramp.

7.5.8 Conclusion

For a given design search space, optimal designs for centralised and distributed topologies were generated. The considered components are the gearbox, machine, cable, LC output

filter for the centralised topology only, power electronics and heat sink, and EMI input filter. These designs were compared on a system level with respect to total per lane mass and failure rate. Designs with a total per lane failure rate of <1375FIT are considered.

The distributed topology's optimal design's total per lane mass of 8.0kg is less than the centralised topology's optimal design's total per lane mass of 8.9kg. The majority of the total per lane mass is due to the gearbox. The mass of the LC output filter in the centralised topology, which is absent in the distributed topology, accounts for the majority of the mass discrepancy between the two topologies.

The machine designs were validated in FEMM. The desired inductance and magnetic flux linkage were achieved.

The feeder cable for the distributed system is lighter on the account that it transmits dc power with a two conductor cable and not ac power through a three conductor cable.

The power electronics heat sink mass is greater for the distributed topology. This is to compensate for the negative effects of increased ambient temperature, reduced atmospheric pressure, and reduced junction temperature to achieve a comparable failure rate to that of the centralised topology.

The EMI LC filter of the distributed system is greater than that of the centralised topology. This is due to the requirement of larger dc-link capacitors and greater differential mode attenuation due to the absence of the two mid-point balancing dc link capacitors for the LC output filter neutral point, present in the centralised topology.

Stable current control is achieved for both topologies. Control is implemented in the synchronous dq domain. Gain-scheduled LQR state feedback current control and observer is required for the centralised topology due to the presence of the LC output filter. Discrepancy is observed between actual and estimated system states, leading to an overestimation of machine current and reduced torque output. This is due to the mismatch between the desired and the attained inverter output fundamental voltage which appear to increase with operating speed. A compensation technique for this issue was not investigated further. A standard PI current controller with cross-decoupling terms is utilised for the distributed topology and zero steady state error is achieved at steady state.

It is concluded that for the given design search space and flap actuation requirement, the distributed topology is superior to the centralised topology. This is due to the distributed topology's optimal design having less mass than that of the centralised system. It lacks an LC output filter which both reduces overall systems mass and makes the control scheme more straightforward.

Chapter 8

Conclusion

A summary of the work completed is presented. The work is critiqued, its shortcomings are identified, and opportunities for future work are suggested. The novel contributions from the author's work are listed.

8.1 Summary

The aviation industry is moving towards more electric aircraft with the replacement of conventional pneumatic and hydraulic systems with electric solutions. Recent trends have shown an increase in commercial aircraft's electric generation capacity. European wide collaborations such as Actuation2015 and ACARE2020 show the aviation industry's intention to develop an all electric aircraft with the full elimination of all hydraulic and pneumatic systems. Thus, new design tools are required to develop the future more electric, and all electric aircraft.

The aim was to develop a design toolbox which optimally sizes the electric drive system for aerospace actuation considering centralised or distributed topology. The optimal design has the minimum mass within a failure rate constraint. The actuation requirement is defined by its motion type, control scheme, life time profile, power capability, dynamics, operating environment, power quality, and failure rate. The system consists of basic components and subsystems. A multi-domain design approach is required. The considered basic components are inductors, capacitors, gearbox, machine, cable, heat sink, semiconductor, and enclosure. The considered domains are electrical, electromagnetic, high-frequency, losses, thermal, mass, volume, and failure rate. The domains for which each basic component was modelled for are marked with a ✓in Table 8.1. The considered subsystems are the LC output filter, inverter, and EMI input filter. These subsystems are built from some combination of inductors, capacitors, heat sinks, semiconductors, and enclosures. Each subsystem and their contributing components are shown in Table 8.2. Pareto optimal (with respect to mass and failure rate) sizing algorithms were developed

for each basic component and subsystem.

Table 8.1: Modelling of basic components and their relevant domains.

Component \ Domain	Electrical	Electromagnetic	High-frequency	Losses	Thermal	Mass	Volume	Failure rate
Inductor	✓	✓		✓	✓	✓	✓	✓
Capacitor	✓					✓	✓	✓
Gearbox						✓		
Machine	✓	✓	✓	✓	✓	✓	✓	✓
Cable			✓	✓		✓	✓	
Heat sink					✓	✓	✓	
Semiconductor	✓		✓	✓	✓			✓
Enclosure						✓	✓	

Table 8.2: Subsystems and their contributing basic components.

Sub-system \ Component	Inductor	Capacitor	Heat sink	Semiconductor	Enclosure
LC output filter	✓	✓			✓
Inverter			✓	✓	✓
EMI input filter	✓	✓			✓

The relevant inputs of each basic component and subsystems' respective design algorithm are coordinated at a system-level to ensure that designed components and subsystems are inter-compatible, the functional definition is met, and design constraints are adhered to. The basic components' and subsystems' designs are mixed and matched in every possible combination. For each combination, the system level mass and failure rate is determined from which optimal designs of minimum mass within a given failure rate limit is selected. The optimal designs go through an intermediate refinement stage whereby inductors and subsystems with inductors are resized in an analytical manner to account for the discrepancy in its initially empirically-determined mass and volume. Power quality and control stability were validated by simulation. The considered power quality standards are MIL-STD-461 for the conducted source/return leads emission spectrums and MIL-STD-704F for the LC output filter's spectrum. A gain-scheduled LQR state feedback current controller and state observer was implemented for the centralised topology. A PI current controller with cross de-coupling terms is utilised in the distributed topology.

The tool was utilised to design and size the electric drive system for flap actuation of an Airbus A320. For each flap, a "2×3" dual-lane velocity summing topology is utilised.

This consists of two machines driving one differential gearbox, its output drives the rotary actuators on either side of the flap via a transmission shaft. Each lane is powered by two isolated networks to avoid common-mode failure. Each lane has an electric brake which locks each lane when the commanded flap position has been reached or to mechanically isolate a faulted lane. The power requirement is 1.1kW and the per-lane fault constraint is <1375FIT. Optimal designs for the centralised and distributed topologies were generated and compared against each other. The per-lane mass for the optimal centralised and distributed designs are 8.9kg and 8.0kg respectively. The mass difference of 0.9kg is mainly attributed to the lack of an LC output filter in the distributed design. A speed dependent discrepancy is seen in the estimated system states for the centralised topology. This is due to mismatch between the desired voltage command and the realised inverter output voltage. A compensation method for this discrepancy was not investigated.

From the analysis using the realised optimal design tool and outlined design requirements and constraints, it is concluded that the distributed topology is superior to the centralised topology for electric drive flap actuation as it has reduced mass, less components, and a more straightforward current control scheme.

8.2 Critiques and future work

In this section, a critique of the accomplished work is presented. This in turn outlines future work opportunities to address the accomplished work's shortcomings.

A holistic approach considering all domains for all basic components and subsystems was desired and the ✓'s in Table 8.1 show to what extent that goals was achieved. Table 8.1 is modified with the addition of extra components, domains, and ∘ markers to indicate the component/domain model upgrades that can be addressed in future work. The modified table is shown in Table 8.3.

The ways in which the existing model can be upgraded are as follows:

- High-frequency inductor modelling is desired. Just as machine differential mode impedance varies as function of frequency, so too does the impedance of inductors. Both inductors and machines have multi-turn windings about magnetic core material. As frequency increases, series resistance increases due to skin effect, proximity effect, and core losses while inductance decreases. The impedance of turn-to-turn and turn-to-ground capacitive parasitic paths reduce as frequency increases. The inductor sizing algorithm utilised is only suitable for relatively "lower" switching frequencies. This "lower" threshold is arbitrarily defined.
- Capacitor losses and thermal modelling is desired considering voltage ripple and ambient conditions. Capacitors tend to have lower operating temperatures compared to the inductor and particular attention is required to ensure their thermal

Table 8.3: Modelling of basic components and their relevant domains.

Component \ Domain	Electrical	Electromagnetic	High-frequency	Losses	Thermal	Mass	Volume	Failure rate	Non-linear mechanical
Inductor	✓	✓	○	✓	✓	✓	✓	✓	
Capacitor	✓			○	○	✓	✓	✓	
Gearbox				○		✓	○	○	○
Machine	✓	✓	✓	✓	✓○	✓	✓	✓	○
Cable			✓	✓		✓	✓		
Heatsink					✓	✓	✓		
Semiconductor	✓		✓	✓	✓			✓	
Enclosure					○	✓	✓		
Bearing				○	○	○	○	○	
Electric brake	○	○		○	○	○	○	○	

limits are respected.

- More detail regarding the gearbox and bearing modelling is desired. Bearing failure rate is dependent on loading, vibrations, number of rotations, and bearing temperature. Temperature is related to gearbox losses and bearing losses. Non-linear mechanical model is desired which considers effects like backlash, compliance, friction.
- The machine's thermal model is a steady state model. An attempt was made by the author to develop a transient thermal model to estimate a machine's design equivalent thermal time constant. Results from the author developed transient thermal model matched poorly with that of the experimentally determined values and were not included in the thesis. Actuation operation is intermittent and not continuous. Intermittent operation allows time for the machine to heat up and cool down. It may not get a chance to reach steady state nominal temperature. The failure rate due to thermal stresses on winding insulation has been overestimated as it was determined for steady state conditions. An accurate determination of the machines transient thermal response can enable further machine mass minimisation.
- The effects of cogging torque can also be included as a part of the non-linear mechanical model component of the machine. Cogging torque can be determined using FEA methods and then be included in the simulation as a rotor-position dependent torque source.
- The enclosure volume was determined by multiplying the total volume of contained passives by a scaling factor. The accuracy of this is questionable as inductors and capacitors can vary in height and required spacing. Thus, enclosure utilisation can vary substantially. The enclosure also consists of PCB, upon which other circuitry,

amplifiers, microcontroller, DSP etc are mounted. The mass, required spacing, and losses of these components have not been considered. Internal temperature within the enclosure needs to be determined considering enclosure geometry, material, internal losses and ambient conditions. The thermal characteristics of one component can effect the temperature of neighbouring component, which in turn can effect its failure rate.

- All components were assumed to be thermally isolated with respect to each other. Depending on the degree with which the inverter may be integrated with the machine or the machine is integrated with the gearbox, substantial heat flow can occur between these components. This can be beneficial as the large mass of the gearbox may act as an alternative heat sink for the machine's losses or detrimental if heat from the machine increases the inverter switch temperature.
- The electric brake's physical specifications, power electronics, and failure rate have not been considered. Electric brake's mass, volume, moment of inertia may be determined using scaling laws.

More accurate and representative results will be achieved if all of these modelling upgrade options are implemented. It is believed that the same conclusion regarding distributed being lighter than centralised topology for this application will still be reached. Bearings and electric brakes are present in both centralised and distributed topologies and will contribute an equivalent amount to the respective topology's mass and failure rate.

The inductors were designed assuming a 30°C temperature rise with respect to ambient during operation, as recommended by FIDES guide 2009. Increasing the allowable temperature rise will lead to more power dense, and thus lighter results. The thermal interaction between the hotter inductors and other neighbouring components may need to be considered and assessed.

The high-frequency drive modelling considering transmission line effects is not well integrated or utilised in system level optimisation. High-frequency cable models may not be necessary if an inverter LC output filter is used whose cut-off frequency is less than that of the inverter switching frequency (as is the case in the centralised topology) or the if the inverter-machine cable length is short (as is the case for the distributed topology). Transmission line effects do not occur if the conditions for them occurring (i.e. source side voltage with high dv/dt and long feeder cable) have been removed.

The per-lane failure rate was determined by the sum of all of its components' failure rats. This is equivalent to using fault-tree analysis. As an alternative, Markov analysis can be used to determine a more representative failure rate as it allows the inclusion of scheduled maintenance effects on the per-lane failure rate.

For the experimental setup, the prototype optimal inverter has limited similarity with the optimised designs presented in Chapter 7. The experimental inverter's power stage is

the IGBT based FS50R12KT4P_B11 power module while the proposed inverter is based on the Microsemi's silicon carbide power MOSFET MSC080SMA120S. Silicon carbide is being developed aerospace applications. One example is Microchip's MAIPDMC40X120 SiC 5kVA power module which was designed with typical aviation mission profiles in mind [126]. As of time of writing this, detailed specifications for the MAIPDMC40X120 is limited. The justification with not going with IGBT in the proposed optimal inverter is IGBT's relatively high base failure rate as shown in Table 4.4. The base failure rate for Silicon MOSFET and IGBT is 0.0202FIT and 0.3021FIT. The base failure rate of SiC MOSFETs was not provided by FIDES guide 2009. In the presented work, it is assumed the SiC and Si MOSFETs have the same failure rate.

In spite of this, the experimental inverter was still used to effectively validate the high-frequency models for inverter, cable, and machine to model specifically transmission line effects. The basis of the inverter modelling is to consider dv/dt and dc-link voltage. These input variables for my proposed modelling scheme are readily adjustable to account for different inverter technologies with different dv/dt.

Outstanding experimental verification include LC output filter and assessing its effectiveness in phase voltage harmonic attenuation, controller stability and dynamics of the gain scheduled LQR control with LC output filter, inverter loss and operating temperature, and EMI conducted emissions. Should this work to be continued in earnest, a completed system would be designed, realised in hardware, and experimental validated as a whole instead of a model-by-model basis as presented here.

Sensitivity analysis is absent. Design process implementation requires further streamlining and optimisation for meaningful sensitivity analysis can be done. Insight gained from this analysis may include identification of key variables that have a major impact on system mass and failure rate.

8.3 Contributions

The following novel contributions were generated by the author,

- Permanent magnet machine sizing algorithm from drive level requirements.
  - Conventional machine sizing algorithms start with the machine geometry and then checks if the design satisfies the drive requirements.
  - The presented algorithm starts with the drive level requirements and designs a machine for it. It directly calculates appropriate machine electrical parameters considering voltage limit, current ripple, nominal torque/speed, and then designs the machine to fit those requirements.
- Optimal design for mass and failure rates.

  - Existing publications have either a high focus on electrical, electromechanical, models with low focus on failure rate analysis or high focus failure rate analysis with low focus on electrical, electromechanical models.
  - Presented a detailed optimal design tool that explicitly considers the relationship between electrical, electromechanical, power quality, thermal, mechanical and failure rate. High-detailed inter-domain dependent models were developed and utilised. This allows for the determination of Pareto-efficient designs with respect to mass and failure rate of electric drive systems.

- Investigation and comparison between centralised and distributed electric drive system for flap actuation.
  - Utilised the presented optimal design toolbox to compare optimised electric drive designs for both centralised and distributed topologies.
  - Concluded that distributed topology to be superior due to lighter mass, less components, and more straight forward control scheme.

Bibliography

[1] T. S. Lampl, S. Muschkorgel, and M. Hornung, "Parameterized flight mission for secondary power requirement estimations of commercial transport aircraft," in *17th AIAA Aviation Technology, Integration, and Operations Conference*, p. 3066, 2017.

[2] M. Sinnett, "787 no-bleed systems: saving fuel and enhancing operational efficiencies," *Aero Quarterly*, vol. 18, pp. 6–11, 2007.

[3] Airbus SAS, "A350-900 flight deck and systems briefing for pilots," Sep 2011.

[4] Q. Chao, J. Zhang, B. Xu, H. Huang, and M. Pan, "A review of high-speed electrohydrostatic actuator pumps in aerospace applications: challenges and solutions," *Journal of Mechanical Design*, vol. 141, no. 5, 2019.

[5] R. Navarro, *Performance of an electro-hydrostatic actuator on the F-18 systems research aircraft*. Citeseer, 1997.

[6] Moog Inc., "Airbus A350 aftermarket services," 2016.

[7] D. Van Den Bossche, "The a380 flight control electrohydrostatic actuators, achievements and lessons learnt," in *25th international congress of the aeronautical sciences*, pp. 1–8, 2006.

[8] M. A. Davis, "High performance electromechanical servoactuation using brushless dc motors," *Technical bulletin*, vol. 150, 1984.

[9] J. W. Bennett, B. C. Mecrow, A. G. Jack, and D. J. Atkinson, "A prototype electrical actuator for aircraft flaps," *IEEE Transactions on Industry Applications*, vol. 46, no. 3, pp. 915–921, 2010.

[10] W. Cao, B. C. Mecrow, G. J. Atkinson, J. W. Bennett, and D. J. Atkinson, "Overview of electric motor technologies used for more electric aircraft (mea)," *IEEE transactions on industrial electronics*, vol. 59, no. 9, pp. 3523–3531, 2011.

[11] J. Bennett, B. Mecrow, D. Atkinson, and G. Atkinson, "Safety-critical design of electromechanical actuation systems in commercial aircraft," *IET Electric Power Applications*, vol. 5, no. 1, pp. 37–47, 2011.

[12] F. Y. Annaz, "Fundamental design concepts in multi-lane smart electromechanical actuators," *Smart materials and structures*, vol. 14, no. 6, p. 1227, 2005.

[13] M. Rottach, C. Gerada, and P. Wheeler, "Evaluation of motor-drive segmentation strategies for fault-tolerance," in *2013 IEEE ECCE Asia Downunder*, pp. 530–536, IEEE, 2013.

[14] Lufthansa Technical Training, "Training manual a319/a320/a321," 1997.

[15] F. Group *et al.*, "Fides guide 2009-reliability methodology for electronic systems," *Edition A, September*, 2010.

[16] I. Christou, A. Nelms, I. Cotton, and M. Husband, "Choice of optimal voltage for more electric aircraft wiring systems," *IET Electrical Systems in Transportation*, vol. 1, no. 1, pp. 24–30, 2011.

[17] D. Vechtel, B. Hauber, and G. Looye, "Analysis of a multi-functional high-lift system driven by an active differential gear box," *CEAS Aeronautical Journal*, vol. 5, no. 3, pp. 227–238, 2014.

[18] D. Zaccai, "Design framework for trailing edge high-lift systems: a knowledge based engineering application," 2014.

[19] I. APEX DYNAMICS, 2018.

[20] E. Furukawa, "Essex furukawa magnet wire winding wire gp/mr-200 datasheet," Nov 2020.

[21] C. W. T. McLyman, *Transformer and inductor design handbook*. CRC press, 2017.

[22] B. N. Cassimere, S. D. Sudhoff, and D. H. Sudhoff, "Analytical design model for surface-mounted permanent-magnet synchronous machines," *IEEE Transactions on Energy Conversion*, vol. 24, no. 2, pp. 347–357, 2009.

[23] T. J. Miller, "Brushless permanent-magnet and reluctance motor drives," 1989.

[24] P. Mellor, D. Roberts, and D. Turner, "Lumped parameter thermal model for electrical machines of tefc design," in *IEE Proceedings B (Electric Power Applications)*, vol. 138, pp. 205–218, IET, 1991.

[25] A. Boglietti, A. Cavagnino, and M. Lazzari, "Experimental high-frequency parameter identification of ac electrical motors," *IEEE Transactions on Industry Applications*, vol. 43, pp. 23–29, Jan 2007.

[26] M. A. Gries and B. Mirafzal, "Permanent magnet motor-drive frequency response characterization for transient phenomena and conducted emi analysis," in *2008 Twenty-Third Annual IEEE Applied Power Electronics Conference and Exposition*, pp. 1767–1775, Feb 2008.

[27] P. K. Rudolph, "High-lift systems on commercial subsonic airliners," 1996.

[28] A. Hilal and B. Cougo, "Optimal inductor design and material selection for high power density inverters used in aircraft applications," in *2016 International Conference on Electrical Systems for Aircraft, Railway, Ship Propulsion and Road Vehicles & International Transportation Electrification Conference (ESARS-ITEC)*, pp. 1–6, IEEE, 2016.

[29] T. J. E. Miller, *Speeds electric motors: an outline of some of the theory in the SPEED software for electric machine design: with problems and solutions.* Magna Physics, 2004.

[30] Nexans, "Nexans aircraft wires and cables," 2007.

[31] T. Sawata, P. Sangha, M. Benarous, and C. Maxwell, "Thermal modeling of brushless dc motor and brake solenoid in electro-mechanical actuators for the more electric aircraft engine," in *2007 IEEE International Symposium on Industrial Electronics*, pp. 1236–1241, IEEE, 2007.

[32] M. Jean-Charles and F. Jian, "Review on signal-by-wire and power-by-wire actuation for more electric aircraft," *Chinese Journal of Aeronautics*, vol. 30, no. 3, pp. 857–870, 2017.

[33] J. C. Mankins, "Technology readiness levels," *White Paper, April*, vol. 6, no. 1995, p. 1995, 1995.

[34] J.-C. Derrien, P. Tieys, D. Senegas, and M. Todeschi, "Ema aileron covadis development," tech. rep., SAE Technical Paper, 2011.

[35] "ACTUATION 2015: Modular Electro Mechanical Actuators for ACARE 2020 Aircraft and Helicopters," tech. rep.

[36] J. W. Bennett, *Fault tolerant electromechanical actuators for aircraft.* PhD thesis, Newcastle University, 2010.

[37] J. W. Bennett, G. J. Atkinson, B. C. Mecrow, and D. J. Atkinson, "Fault-tolerant design considerations and control strategies for aerospace drives," *IEEE Transactions on Industrial Electronics*, vol. 59, no. 5, pp. 2049–2058, 2011.

[38] Airbus, "Airbus A318/A319/A320/A321 flight crew training manual," 2011.

[39] J. Bennett, B. Mecrow, A. Jack, D. Atkinson, C. Sewell, G. Mason, S. Sheldon, and B. Cooper, "Choice of drive topologies for electrical actuation of aircraft flaps and slats," in *IEE CONFERENCE PUBLICATION*, vol. 1, pp. 332–337, IET, 2004.

[40] M. Amrhein, J. Wells, and T. Baudendistel, "Design of a high-temperature utility electromechanical actuator," tech. rep., SAE Technical Paper, 2012.

[41] M. Budinger, J. Liscouët, F. Hospital, and J. Maré, "Estimation models for the preliminary design of electromechanical actuators," *Proceedings of the Institution of Mechanical Engineers, Part G: Journal of Aerospace Engineering*, vol. 226, no. 3, pp. 243–259, 2012.

[42] J. Liscouët, M. Budinger, J.-C. Maré, and S. Orieux, "Modelling approach for the simulation-based preliminary design of power transmissions," *Mechanism and Machine Theory*, vol. 46, no. 3, pp. 276–289, 2011.

[43] M. Budinger, A. Reysset, T. E. Halabi, C. Vasiliu, and J.-C. Maré, "Optimal preliminary design of electromechanical actuators," *Proceedings of the Institution of Mechanical Engineers, Part G: Journal of Aerospace Engineering*, vol. 228, no. 9, pp. 1598–1616, 2014.

[44] M. Torabzadeh-Tari, *Dimensioning tools of MEA actuator systems, including modeling, analysis and technology comparison.* PhD thesis, KTH, 2008.

[45] "A design study of a future 10 kw converter."

[46] B. Cheong, P. Giangrande, M. Galea, P. Zanchetta, and P. Wheeler, "Integrated motor drive design for weight optimization," in *2017 IEEE Energy Conversion Congress and Exposition (ECCE)*, pp. 816–823, IEEE, 2017.

[47] M. Amrhein, T. C. O'Connell, and J. R. Wells, "An integrated design process for optimized high-performance electrical machines," in *2013 International Electric Machines & Drives Conference*, pp. 847–854, IEEE, 2013.

[48] D. C. Aliprantis, O. Wasynczuk, N. Wu, C. E. Lucas, and M. A. Masrur, "Automated evolutionary design of a hybrid-electric vehicle power system using distributed heterogeneous optimization," tech. rep., SAE Technical Paper, 2006.

[49] M. Rottach, C. Gerada, T. Hamiti, and P. Wheeler, "A computationally efficient design procedure for actuator motors using magnetic reluctance-and thermal resistance network models," in *2012 XXth International Conference on Electrical Machines*, pp. 2526–2532, IEEE, 2012.

[50] C. Gerada, K. Bradley, M. Sumner, and G. Asher, "Non-linear dynamic modelling of vector controlled pm synchronous machines," in *2005 European Conference on Power Electronics and Applications*, pp. 10 pp.–P.10, 2005.

[51] D. Gerada, A. Mebarki, N. L. Brown, K. J. Bradley, and C. Gerada, "Design aspects of high-speed high-power-density laminated-rotor induction machines," *IEEE Transactions on Industrial Electronics*, vol. 58, no. 9, pp. 4039–4047, 2011.

[52] M. Rottach, C. Gerada, and P. Wheeler, "Design optimisation of a fault-tolerant pm motor drive for an aerospace actuation application," 2014.

[53] J. Fu, J.-C. Maré, and Y. Fu, "Modelling and simulation of flight control electromechanical actuators with special focus on model architecting, multidisciplinary effects and power flows," *Chinese Journal of Aeronautics*, vol. 30, no. 1, pp. 47–65, 2017.

[54] G. Dauphin-Tanguy, A. Rahmani, and C. Sueur, "Bond graph aided design of controlled systems," *Simulation Practice and Theory*, vol. 7, no. 5-6, pp. 493–513, 1999.

[55] J. W. Kolar, U. Drofenik, J. Biela, M. L. Heldwein, H. Ertl, T. Friedli, and S. D. Round, "Pwm converter power density barriers," in *2007 Power Conversion Conference-Nagoya*, pp. P–9, IEEE, 2007.

[56] U. Drofenik, G. Laimer, J. W. Kolar, *et al.*, "Theoretical converter power density limits for forced convection cooling," in *Proceedings of the International PCIM Europe 2005 Conference*, no. 4, pp. 608–619, 2005.

[57] S. D. Sudhoff, S. D. Pekarek, and D. R. Fudge, "Multi-objective design of an unmanned underwater vehicle propulsion drive," in *2019 IEEE Electric Ship Technologies Symposium (ESTS)*, pp. 452–459, IEEE, 2019.

[58] B. Zhang, S. Sudhoff, S. Pekarek, R. Swanson, J. Flicker, J. Neely, J. Delhotal, and R. Kaplar, "Prediction of pareto-optimal performance improvements in a power conversion system using gan devices," in *2017 IEEE 5th Workshop on Wide Bandgap Power Devices and Applications (WiPDA)*, pp. 80–86, IEEE, 2017.

[59] M. Pettersson and J. Ölvander, "Drive train optimization for industrial robots," *IEEE Transactions on Robotics*, vol. 25, no. 6, pp. 1419–1424, 2009.

[60] M. Pettersson, J. Andersson, and P. Krus, "Methods for discrete design optimization," in *International Design Engineering Technical Conferences and Computers and Information in Engineering Conference*, vol. 4739, pp. 295–303, 2005.

[61] Deparment of Defense, United States of America, "Reliability prediction of electronic equipment," tech. rep., MIL-HDBK-217F, 1991.

[62] G. P. Pandian, D. Diganta, L. Chuan, Z. Enrico, and M. Pecht, "A critique of reliability prediction techniques for avionics applications," *Chinese Journal of Aeronautics*, vol. 31, no. 1, pp. 10–20, 2018.

[63] P. Charpenel, P. Cavernes, V. Casanovas, J. Borowski, and J. Chopin, "Comparison between field reliability and new prediction methodology on avionics embedded electronics," *Microelectronics Reliability*, vol. 38, no. 6-8, pp. 1171–1175, 1998.

[64] M. Nilsson and Ö. Hallberg, "A new reliability prediction model for telecommunication hardware," *Microelectronics Reliability*, vol. 37, no. 10-11, pp. 1429–1432, 1997.

[65] P. Carton, M. Giraudeau, and F. Davenel, "New fides models for emerging technologies," in *2017 Annual Reliability and Maintainability Symposium (RAMS)*, pp. 1–6, IEEE, 2017.

[66] B. Nystrom, L. Austrin, N. Ankarback, and E. Nilsson, "Fault tree analysis of an aircraft electric power supply system to electrical actuators," in *2006 international conference on probabilistic methods applied to power systems*, pp. 1–7, IEEE, 2006.

[67] A. M. Bazzi, A. Dominguez-Garcia, and P. T. Krein, "Markov reliability modeling for induction motor drives under field-oriented control," *IEEE Transactions on Power Electronics*, vol. 27, no. 2, pp. 534–546, 2011.

[68] G. Chan and S. Asgarpoor, "Optimum maintenance policy with markov processes," *Electric power systems research*, vol. 76, no. 6-7, pp. 452–456, 2006.

[69] X. Yu and A. M. Khambadkone, "Reliability analysis and cost optimization of parallel-inverter system," *IEEE Transactions on Industrial Electronics*, vol. 59, no. 10, pp. 3881–3889, 2011.

[70] D. Zhou, H. Wang, and F. Blaabjerg, "Mission profile based system-level reliability analysis of dc/dc converters for a backup power application," *IEEE Transactions on Power Electronics*, vol. 33, no. 9, pp. 8030–8039, 2017.

[71] P. Xie, G. Vakil, and C. Gerada, "Electric drive systems with long feeder cables," *IET Electric Power Applications*, vol. 14, no. 1, pp. 16–30, 2020.

[72] R. J. Kerkman, D. Leggate, and G. L. Skibinski, "Interaction of drive modulation and cable parameters on AC motor transients," *IEEE Transactions on Industry Applications*, vol. 33, pp. 722–731, May 1997.

[73] "A350 high-lift devices combine simplicity with fuel savings."

[74] R. G. Budynas, J. K. Nisbett, *et al.*, *Shigley's mechanical engineering design*, vol. 8. McGraw-Hill New York, 2008.

[75] J.-L. Ha, R.-F. Fung, K.-Y. Chen, and S.-C. Hsien, "Dynamic modeling and identification of a slider-crank mechanism," *Journal of sound and vibration*, vol. 289, no. 4-5, pp. 1019–1044, 2006.

[76] R. Anderson, C. Flora, R. Nelson, E. Raymond, and J. Vincent, "Development of weight and cost estimates for lifting surfaces with active controls," 1976.

[77] A. SAS, "A320 aircraft characteristics airport and maintenance planning," 2005.

[78] J. Rea, "Boeing 777 high lift control system," in *Proceedings of the IEEE 1993 National Aerospace and Electronics Conference-NAECON 1993*, pp. 476–483, IEEE, 1993.

[79]

[80] C. Audet and J. E. Dennis Jr, "Analysis of generalized pattern searches," *SIAM Journal on optimization*, vol. 13, no. 3, pp. 889–903, 2002.

[81] J. Kennedy and R. Eberhart, "Particle swarm optimization," in *Proceedings of ICNN'95-international conference on neural networks*, vol. 4, pp. 1942–1948, IEEE, 1995.

[82] N. Valentine, D. Das, M. Pecht, and M. Pecht, "Failure mechanisms of insulated gate bipolar transistors (igbts)," in *NREL photovoltaic reliability workshop*, Center for Advanced Life Cycle Engineering (CALCE), University of Maryland ..., 2015.

[83] V. Valchev and A. Van den Bossche, "Accurate natural convection modelling for magnetic components," *Microelectronics Reliability*, vol. 43, no. 5, pp. 795–802, 2003.

[84] K. Raggl, T. Nussbaumer, and J. W. Kolar, "Model based optimization of EMC input filters," in *2008 11th Workshop on Control and Modeling for Power Electronics*, pp. 1–6, 2008.

[85] Vishay, "Mkp1848 dc-link metallized polypropylene film capacitors dc-link capacitor," 2020.

[86] Vishay, "Mkt1820 dc film capacitors mkt radial potted type," 2018.

[87] P. Xie, R. Ramanathan, G. Vakil, and C. Gerada, "Simplified analytical machine sizing for surface mounted permanent magnet machines," in *2019 IEEE International Electric Machines & Drives Conference (IEMDC)*, pp. 751–757, IEEE, 2019.

[88] D. C. Hanselman, "Effect of skew, pole count and slot count on brushless motor radial force, cogging torque and back emf," *IEE Proceedings-Electric Power Applications*, vol. 144, no. 5, pp. 325–330, 1997.

[89] T. Li and G. Slemon, "Reduction of cogging torque in permanent magnet motors," *IEEE Transactions on magnetics*, vol. 24, no. 6, pp. 2901–2903, 1988.

[90] D. C. Hanselman, *Brushless permanent magnet motor design*. The Writers' Collective, 2003.

[91] A. M. El-Refaie, "Fractional-slot concentrated-windings synchronous permanent magnet machines: Opportunities and challenges," *IEEE Transactions on industrial Electronics*, vol. 57, no. 1, pp. 107–121, 2009.

[92] J. Pyrhonen, T. Jokinen, and V. Hrabovcova, *Design of rotating electrical machines*. John Wiley & Sons, 2013.

[93] A. Boglietti, A. Cavagnino, and M. Lazzari, "Computational algorithms for induction-motor equivalent circuit parameter determination—part i: Resistances and leakage reactances," *IEEE Transactions on Industrial Electronics*, vol. 58, no. 9, pp. 3723–3733, 2010.

[94] P. C. Krause, O. Wasynczuk, S. D. Sudhoff, and S. Pekarek, *Analysis of electric machinery and drive systems*, vol. 2. Wiley Online Library, 2002.

[95] Z. Zhu and D. Howe, "Influence of design parameters on cogging torque in permanent magnet machines," *IEEE Transactions on energy conversion*, vol. 15, no. 4, pp. 407–412, 2000.

[96] J. L. Kirtley Jr, H. W. Beaty, N. K. Ghai, S. B. Leeb, and R. H. Lyon, *Electric motor handbook*. McGraw-Hill Education, 1998.

[97] S. W. Churchill and H. H. Chu, "Correlating equations for laminar and turbulent free convection from a horizontal cylinder," *International journal of heat and mass transfer*, vol. 18, no. 9, pp. 1049–1053, 1975.

[98] S. W. Churchill and H. H. Chu, "Correlating equations for laminar and turbulent free convection from a vertical plate," *International journal of heat and mass transfer*, vol. 18, no. 11, pp. 1323–1329, 1975.

[99] S. AS50881, "Wiring aerospace vehicle," *SAE International*, pp. 1–91, 2010.

[100] A. Wintrich, U. Nicolai, W. Tursky, and T. Reimann, *Application manual power semiconductors*, vol. 7. ISLE Verlag Ilmenau, Germany, 2011.

[101] A. Bar-Cohen, M. Iyengar, and A. D. Kraus, "Design of optimum plate-fin natural convective heat sinks," *J. Electron. Packag.*, vol. 125, no. 2, pp. 208–216, 2003.

[102] S. Zulk, T. Koneke, and A. Mertens, "Analytical modeling of plate fin heat sinks for natural convection cooling in power electronics," in *2016 IEEE Vehicle Power and Propulsion Conference (VPPC)*, pp. 1–6, IEEE, 2016.

[103] A. D. Kraus, A. Aziz, J. Welty, and D. Sekulic, "Extended surface heat transfer," *Appl. Mech. Rev.*, vol. 54, no. 5, pp. B92–B92, 2001.

[104] A. Bar-Cohen and M. Jelinek, "Optimum arrays of longitudinal, rectangular fins in corrective heat transfer," *Heat Transfer Engineering*, vol. 6, no. 3, pp. 68–78, 1985.

[105] A. Bar-Cohen and W. Rohsenow, "Thermally optimum spacing of vertical, natural convection cooled, parallel plates," 1984.

[106] Y. Shabany, "Radiation heat transfer from plate-fin heat sinks," in *2008 Twenty-fourth Annual IEEE Semiconductor Thermal Measurement and Management Symposium*, pp. 132–136, IEEE, 2008.

[107] Department of Defense United States of America, "MIL-STD-461G," Dec 2015.

[108] K. Raggl, T. Nussbaumer, and J. W. Kolar, "Guideline for a simplified differential-mode EMI filter design," *IEEE Transactions on Industrial Electronics*, vol. 57, no. 3, pp. 1031–1040, 2010.

[109] D. G. Holmes and T. A. Lipo, *Pulse width modulation for power converters: principles and practice*, vol. 18. John Wiley & Sons, 2003.

[110] B. P. McGrath and D. G. Holmes, "A general analytical method for calculating inverter dc-link current harmonics," *IEEE Transactions on Industry Applications*, vol. 45, no. 5, pp. 1851–1859, 2009.

[111] T. Nussbaumer, M. L. Heldwein, and J. W. Kolar, "Differential mode input filter design for a three-phase buck-type pwm rectifier based on modeling of the EMC test receiver," *IEEE Transactions on Industrial Electronics*, vol. 53, no. 5, pp. 1649–1661, 2006.

[112] M. L. Heldwein and J. W. Kolar, "Design of minimum volume EMC input filters for an ultra compact three-phase pwm rectifier," 2007.

[113] M. Assahubulkahfi, Y. M. Sam, A. Maseleno, and M. Huda, "LQR tuning by particle swarm optimization of full car suspension system," *International Journal of Engineering & Technology (UAE)*, vol. 7, no. 2.13, pp. 328–331, 2018.

[114] J. Kautsky, N. K. Nichols, and P. Van Dooren, "Robust pole assignment in linear state feedback," *International Journal of control*, vol. 41, no. 5, pp. 1129–1155, 1985.

[115] K. J. Åström and T. Hägglund, *PID controllers: theory, design, and tuning*, vol. 2. Instrument society of America Research Triangle Park, NC, 1995.

[116] C. R. Paul, "Bandwidth of digital waveforms," *IEEE Practical Papers, Articles, and Application Notes*, pp. 58–64, 2009.

[117] N. Idir, Y. Weens, and J. J. Franchaud, "Skin effect and dielectric loss models of power cables," *IEEE Transactions on Dielectrics and Electrical Insulation*, vol. 16, pp. 147–154, February 2009.

[118] C. Purcarea, *High-frequency parasitic effects in electric drives with long cables*. PhD thesis, Technische Universität, 2011.

[119] D. Meeker, "Finite element method magnetics," *FEMM*, vol. 4, p. 32, 2010.

[120] D. C. Meeker, "An improved continuum skin and proximity effect model for hexagonally packed wires," *Journal of Computational and Applied Mathematics*, vol. 236, no. 18, pp. 4635–4644, 2012.

[121] D. Meeker, "Continuum representation of wound coils via an equivalent foil approach," *Available on 1-5-2015 at Http://www. femm. info/examples/prox/notes. pdf*, 2010.

[122] B. Gustavsen and A. Semlyen, "Rational approximation of frequency domain responses by vector fitting," *IEEE Transactions on Power Delivery*, vol. 14, pp. 1052–1061, Jul 1999.

[123] B. Gustavsen, "Improving the pole relocating properties of vector fitting," *IEEE Transactions on Power Delivery*, vol. 21, pp. 1587–1592, July 2006.

[124] B. Gustavsen and A. Semlyen, "Enforcing passivity for admittance matrices approximated by rational functions," *IEEE Transactions on Power Systems*, vol. 16, no. 1, pp. 97–104, 2001.

[125] M. Degano, P. Zanchetta, L. Empringham, E. Lavopa, and J. Clare, "HF induction motor modeling using automated experimental impedance measurement matching," *IEEE Transactions on Industrial Electronics*, vol. 59, no. 10, pp. 3789–3796, 2012.

[126] MICROCHIP, 2019.